Beiträge zur Entwicklung und Prüfung nanofaserbasierter Materialien für biomedizinische Implanttanwendungen

kumulative Dissertation
zur
Erlangung des akademischen Grades
Doktor-Ingenieur (Dr.-Ing.)
der Fakultät für Maschinenbau und Schiffstechnik
der Universität Rostock

vorgelegt von
Andreas Götz
aus Rostock

Rostock, 3. Januar 2025

https://doi.org/10.18453/rosdok_id00005120

Dekan: Prof. Dr.-Ing. Bert Buchholz
Universität Rostock
Fakultät für Maschinenbau und Schiffstechnik
Lehrstuhl für Kolbenmaschinen und Verbrennungsmotoren

1. Gutachter: Prof. Dr.-Ing. habil. Niels Grabow
Universitätsmedizin Rostock
Institut für Biomedizinische Technik

2. Gutachter: Prof. Dr.-Ing. Hermann Seitz
Universität Rostock
Fakultät für Maschinenbau und Schiffstechnik
Lehrstuhl für Mikrofluidik

Datum der Verteidigung: 7. März 2025

Gehe nicht, wohin der Weg führen mag,
sondern dorthin, wo kein Weg ist,
und hinterlasse eine Spur.

Jean Paul

Metis – Göttin des praktischen,
komplexen, impliziten Wissens
(Hauptgebäude der Universität Rostock)

Inhaltsverzeichnis

Abkürzungen und Begriffe

AE	Akustische Emission, Entstehung und Abgabe von Geräuschen
Binärbild, Binarisierung	Schwarzweißbild mit 1 Bit Farbtiefe, keine Grauwerte
Crimpen	Zusammendrücken eines Stents/Implantats auf einen kleinen Durchmesser zum Zwecke der Montage
Dilatation	morphologischer Nachbarschaftsoperator, im Binärbild werden weiße Bezugspixel durch ein definiertes Strukturelement erweitert.
EOA	Effective Orifice Area; dt.: effektive Öffnungsfläche
Erosion	morphologischer Nachbarschaftsoperator der prüft, ob ein definiertes Strukturelement Teilmenge des Bildes ist. Falls ja, gehört das jeweilige Bezugspixel zur erodierten Bildmenge.
Farbtiefe	Anzahl möglicher Grauwerte für ein Pixel, Speicherbedarf, z.B. 8 Bit Farbtiefe entsprechen 2^8 = 256 Werten mit: 0 = Schwarz … n = Grau … 255 = Weiß, bzw. Farbbilder sind je nach Farbsystem aus mehreren n-Bit-Bildern zusammengesetzt (z.B. drei Einzelbilder für ein 8 Bit tiefes RGB-Bild: 0 = Schwarz … n = dunkle Farbe … 255 = Rot/Gün/Blau)
FFT	Fast Fourier Transformation
GIFT	General Image Fiber Tool, Bezeichnung der eigenen Methode zur computergestützten Bestimmung von Nanofaserdurchmessern in REM-Bildern
KI	Künstliche Intelligenz
mmHg	Druckeinheit, Schweredruck einer Quecksilbersäule bei einer Fallbeschleunigung von 9,81 m/s^2
Öffnung/Öffnen	morphologische Bildoperation, Nacheinanderausführung der Operationen Erosion und Dilatation unter Anwendung des gleichen Strukturelements
Oversizing	ein etwas größerer Stentdurchmesser, bezogen auf den Gefäßdurchmesser; häufige klinische Verwendung zur sicheren Verankerung des Implantats.
Pixel	Bezeichnung für Bildpunkte von digitalen Bildern
PLLA	engl.: Poly(L-lactic acid), dt.: Poly (L-Milchsäure)
REM	Rasterelektronenmikroskopie
TSPCU	Thermoplastic Silicone Polycarbonate Polyurethane

1. Einleitung und Zielstellung

Viele medizinische Einsatzgebiete von Implantaten stellen besondere Anforderungen an die verwendeten Materialien. Bei innovativen kardiovaskulären Implantatanwendungen, wie Gefäßstützen (Stents) und Klappenprothesen, besteht das Bedürfnis nach zuverlässig bestimmbaren Materialeigenschaften, die wesentlichen Einfluss auf die Funktion des Implantats haben. Nanofaservliesmaterialien eröffnen aufgrund materieller und struktureller Eigenschaften ein weites Feld an Einsatzgebieten als Implantatmaterial und gewinnen zunehmende Bedeutung im medizinischen Bereich [1–16].

Die Herstellung der Nanofaservliese erfolgt üblicherweise per Elektrospinning. Dieses Verfahren ist vom Labor- bis Industriemaßstab etabliert [2] und in Abb. 1 am Beispiel des Einzelnadelemittersystems illustriert. Dabei wird eine Polymerlösung unter langsamem Vorschub durch eine Kanüle gefördert, die unter elektrischer Hochspannung gegenüber einem Kollektorsystem steht. Kollektoren können dabei in verschiedensten Formgestaltungen ausgeführt sein und während des Elektrospinnings bei Bedarf mechanisch bewegt werden. Durch die Wirkung elektrostatischer Kräfte wird die Oberflächenspannung des austretenden Tropfens überwunden. Es entsteht ein dünner Flüssigkeitsstrahl, der nach kurzem geraden Verlauf stark verwirbelt. Bei gleichzeitiger Verdunstung des Lösungsmittels wird der Strahl wesentlich im Durchmesser reduziert und schließlich in Form einer endlosen Nanofaser auf dem Kollektor als Spinnvlies wachsender Dicke abgelegt [17]. Der Gesamtprozess sowie die Faserdurchmesser werden von vielfältigen Parametern beeinflusst [18–20].

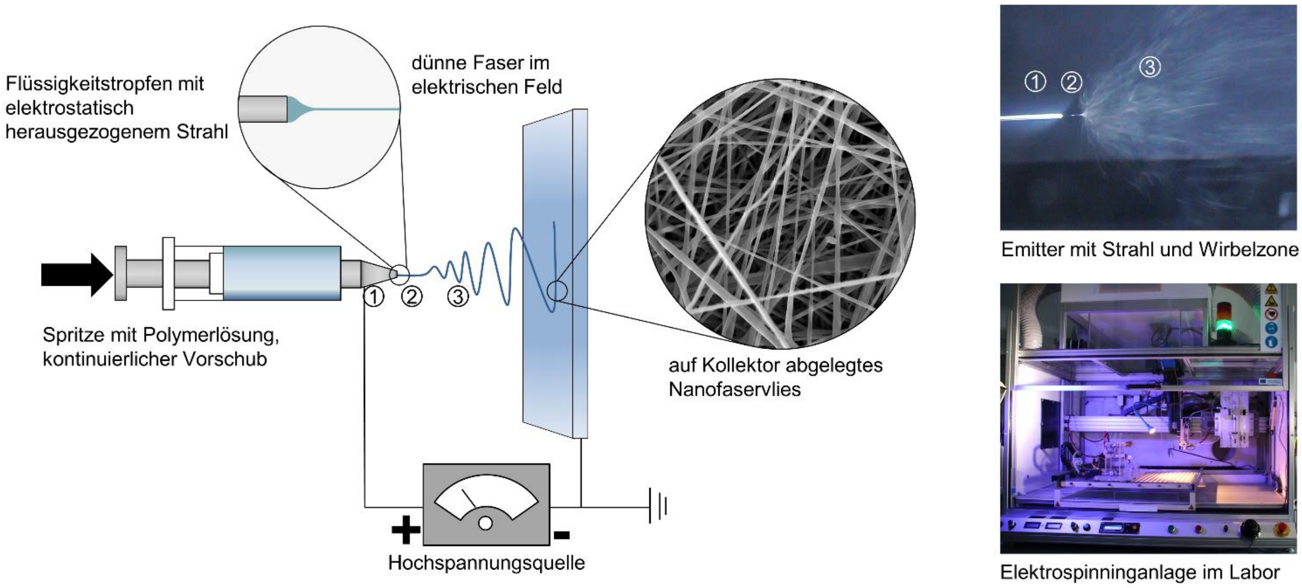

Emitter mit Strahl und Wirbelzone

Elektrospinninganlage im Labor

Abb. 1: Elektrospinning, schematische Darstellung (E-Feld im Hintergrund [21]), REM-Aufnahme Nanofaservlies, Fotos: Emitterkanüle (1) mit Flüssigkeitsstrahl (2) und Verwirbelungszone (3), Elektrospinninganlage im Labor.

Aus der zunehmenden Verwendung von Nanofasermaterialien erwächst generell ein Bedarf an Charakterisierungsmethoden hinsichtlich verschiedener Materialeigenschaften. Ein Teil allgemein etablierter Methoden wie u.a. die Rasterelektronenmikroskopie (REM) oder Transmissionselektronenmikroskopie (TEM) erfordern einigen Aufwand in der Probenaufbereitung oder Ergebnisauswertung. Bezüglich bestimmter Materialeigenschaften ist das Spektrum verfügbarer Charakterisierungsmethoden begrenzt. Daher ist es für die Material- und schließlich Implantat-Prüfung unabdingbar, die Methodenpalette mit neuentwickelten Ansätzen zu erweitern, die idealerweise auch in nicht-biomedizinischen Gebieten nutzbringend eingesetzt werden können.

Die besondere Herausforderung liegt in der Dimension von „Nano“-Fasern und den diesbezüglichen Einschränkungen gängiger Methoden: einzelne Fasern sind oft zu dünn für das menschliche Auge und herkömmliche Optiken, gravimetrisch nicht messbar, händisch oder feinmechanisch kaum manipulierbar und empfindlich gegenüber Luftzug sowie statischer Aufladung. Die Reißkraft von Einzelfasern ist nicht messbar. Nanofaservliesproben sind generell filigran und anspruchsvoll in der Handhabung. Mit technisch aufwändigen Analysemethoden (u.a. REM) sind Nanofasern zwar zugänglich, aber automatische Bildanalysen sind aufgrund wenig zuverlässiger Softwaretools kaum verbreitet. Auch sind kaum Methoden bekannt, die mit geringem technischen Aufwand Aussagen über das Versagensverhalten von Nanofaservliesen auf Mikroebene im Faserverbund bei mechanischer Belastung liefern, um beispielsweise Faserrisse zu detektieren. Für die Entwicklung eines Implantats ist schließlich das komplexe Zusammenspiel des Nanofaservliesmaterials mit makroskopischen Strukturen von Bedeutung, das am Beispiel der Venenklappenprothese in dieser Arbeit untersucht wird.

Diese kumulative Dissertation umfasst in drei Abschnitten die Entwicklung von Prüfverfahren für nanofaserbasierte Implantatmaterialien und die Entwicklung und Testung von nanofaserbasierten Venenklappenprothesen auf drei Skalen: 1 beginnend bei der computergestützten Bestimmung des Faserdurchmessers auf Nano-Skala, 2 über die Untersuchung des Versagensverhaltens unter Zugbelastung im Faserverbund auf Mikro-Skala durch die Detektion akustischer Emissionen (AE), 3 bis hin zur Entwicklung und Bauteilprüfung am Beispiel des Venenklappenimplantats auf Makro-Skala. Im Folgenden werden die Problemstellungen der jeweiligen Teilgebiete jeweils kurz eingeleitet und deren Lösungen im Zusammenhang dargestellt, siehe hierzu auch Abb. 2.

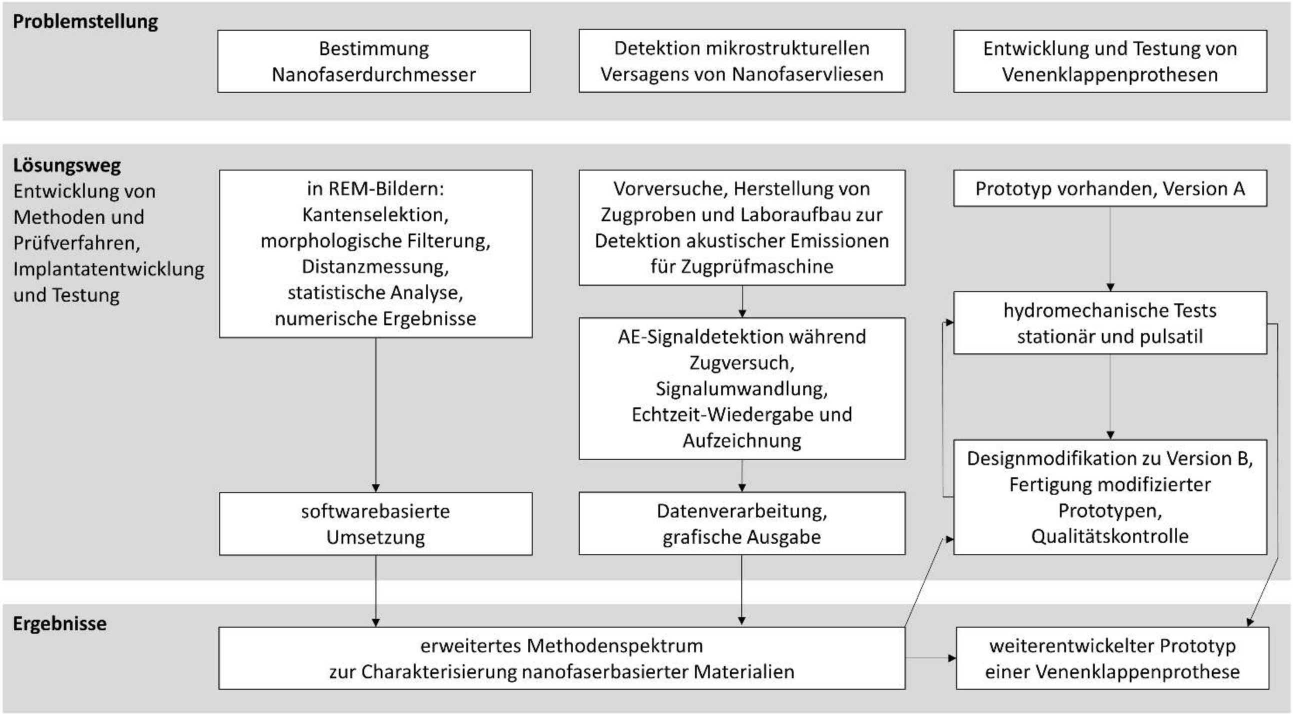

Abb. 2: Schematische Darstellung der Entwicklung von Prüfverfahren für nanofaserbasierte Implantatmaterialien sowie der Implantatentwicklung und Testung nanofaserbasierter Venenklappenprothesen.

2. Computergestützte Bestimmung von Nanofaserdurchmessern

2.1. Methodischer Entwicklungsbedarf

Der Nanofaserdurchmesser und seine statistische Verteilung sind zwei der wichtigsten Parameter, die ein Nanofaservlies charakterisieren. Stand der Technik ist das Ausmessen von Hand auf REM-Bildern am Bildschirm [22]. Dabei werden per Mausklick zwei Punkte definiert, deren Abstand von einer Software berechnet und ausgegeben wird. Die Übertragung der Messwerte in entsprechende Tabellen erfolgt händisch oder automatisch. Das Verfahren ist langsam, fehleranfällig, liefert nur wenige Messwerte und ist vom Bediener beeinflusst.

Hieraus lässt sich ein Bedarf an softwarebasierten Verfahren ableiten. Die Definition, was den Faserdurchmesser in einem Bild ausmacht, wie dieser erkennbar ist, was genau zu messen ist, wie dies in Rechenanweisungen übersetzt werden kann und welche Fehlerquellen Einfluss nehmen, stellt eine komplexe Aufgabe dar und begründet das Nichtvorhandensein einer weitgehend zuverlässigen Software (bis 2022). Die bisher verfügbaren Softwaretools sowie die in wissenschaftlicher Literatur vorgestellten Verfahren basieren meist auf prinzipiell ähnlichen Ansätzen. Grauwertbasierte Verfahren erkennen Fasern per Schwellwert (Prinzip: Faser hell, Hintergrund dunkel) und scheitern an ungleichmäßig hell abgebildeten Faseranteilen bzw. Grauwertverläufen [23–38]. Die kantenbasierten Verfahren stellen bestimmte Anforderungen an die Kanten, die eine Ausführung spezieller nachfolgender Operationen erlauben, z.B. Anpassung von Rechtecken, Fast Fourier Transformation (FFT), Radon Transformation, Nachbarschaftsmodelle, zelluläre Automaten [39–44]. Gekrümmte, kurze oder überlappende Fasern können diese Verfahren überfordern. Weitere Verfahren stellen ebenso bestimmte Anforderungen an die auszuwertenden Bilder und sind der Bandbreite realer REM-Bilder nicht umfänglich gewachsen [39,45–55]. Eine Übersicht ist in der eigenen Publikation 1 aufgeführt [Pub 1]. Unter idealen Bedingungen und mit jeweils gut geeigneten Bildern funktionieren diese Verfahren relativ gut. Reale REM-Bilder sind jedoch sehr variabel hinsichtlich deren Abbildungseigenschaften und stellen eine Herausforderung für die Analysesoftware dar.

Auf künstlicher Intelligenz (KI) basierende Verfahren sind für die Faserdurchmesserbestimmung nicht verfügbar, da hierfür weder ein ausgereiftes Konzept zur Implementierung, noch ein großer Datensatz an Trainingsdaten vorhanden ist.

Der Bedarf an einem Verfahren wurde abgeleitet, das unbeeinflusst von der Variabilität realer REM-Bilder zuverlässige Ergebnisse liefert und etablierter Software ebenbürtig oder überlegen ist. Es wurde das Ziel gesteckt, dass die Ergebnisse nicht von Abbildungseigenschaften, dem Bediener oder der Fasermorphologie selbst beeinflusst oder verfälscht werden dürfen. Wesentliche Ansprüche sind in Tab. 1 dargestellt, das Messergebnis der Faserdurchmesser darf von den genannten Einflüssen nicht beeinträchtigt werden.

Tab. 1: Anforderungen an das zu entwickelnde Bildanalyseverfahren.

Parameter/Anforderung	**Einflüsse auf die Bestimmung der Faserdurchmesser**
Anzahl der Messdaten	Manuelle Messung: wenige Messwerte, subjektive Auswahl der Fasern im Bild. Automatisierte Verfahren: tausende Messwerte, wobei die statistische Sicherheit großer Zahlen auch einen gewissen Anteil falscher Messwerte verzeiht. Bei kommerzieller Software kann die maximale Anzahl der Messwerte begrenzt sein [29].

Faserdurchmesser	In einem Bild können sehr unterschiedlich dicke Fasern abgebildet sein, teils gibt es Einschränkungen des Messbereichs bei etablierter Software [29].
Bildkontrast und Helligkeit	Unterschiedlich kontrastierte Bilder sowie sehr verschiedene Durchschnittshelligkeiten kommen vor, auch in Teilbereichen der Bilder.
Grauwertverläufe	Unterschiedlich hell abgebildete Faseranteile oder Hell-Dunkel-Verläufe treten auf.
Faserkrümmung	Fasern können in geraden bis stark gekräuselten Formen auftreten, auch in Kombination.
Überlagerung	Meist sind Fasern nur teilweise abgebildet oder verdecken sich. Tieferliegende Fasern sind oft dunkler abgebildet.
Ausrichtung	Alle Winkelorientierungen können auftreten.
Lage im Bild	Fasern können zentral oder am Bildrand liegen bzw. durch das ganze Bild verlaufen.
Bildgröße und Datenformat	Die Kantenlänge in Pixeln gängiger Bilder liegt meist im Bereich von 500 bis 2000. Teils bestehen Einschränkungen bei etablierten Softwaretools hinsichtlich verwendbarer Dateiformate und maximaler Bildgröße [29]. Das zu entwickelnde Verfahren soll ein möglichst großes Datenformatspektrum verarbeiten können.
Faktor Mensch	„Human bias“ beschreibt Einflüsse durch z.B. individuelle Unterschiede, Müdigkeit, generelle Gewissenhaftigkeit in der Arbeit, Stress, Konzentriertheit, Ablenkung und weitere Einflüsse.
Robustheit gegen „Fehlbedienung“	Auch bei nicht optimal gewählten Voreinstellungen soll ein zuverlässiges Ergebnis generiert werden.

2.2. Eigener Entwicklungsansatz für Bildanalyseverfahren - GIFT

Die Entwicklung eines Verfahrens zur automatischen Faserstärkenbestimmung unter Berücksichtigung der oben genannten Aspekte war eine zentrale Zielsetzung im Rahmen der vorliegenden Arbeit. Es wurde ein Verfahren entwickelt, das den obigen Anforderungen gerecht wird und sich als robust und zuverlässig erwiesen hat. Das **G**eneral **I**mage **F**iber **T**ool (GIFT) genannte Verfahren wird im Folgenden erläutert. GIFT basiert auf herkömmlicher Bild- und Datenverarbeitung, ohne den Einsatz von KI. Die eigene Publikation 1 [Pub 1] bezieht sich dabei auf das Verfahren als solches, die eigene Publikation 2 [Pub 2] bezieht sich auf die Entwicklung und Bereitstellung einer benutzerfreundlichen kostenlosen Software.

GIFT basiert auf einem eigens dafür entwickelten Ansatz: die Kombination der genauen Messung mit der statistischen Sicherheit großer Zahlen. Die Grundidee ist, alle möglichen Abstände von Kanten im Bild zu messen, diese nach Größe zu sortieren, nach Häufigkeit als Histogramm darzustellen und herausragende Häufungen durch Anpassung einer geeigneten Funktion zu numerischen Ergebnissen zu führen, siehe Abb. 3. Ist eine Faser im Bild (unabhängig von Durchmesser, Lage, Bildkontrast, Helligkeit, Krümmung oder Richtung), so wird der immer gleiche Abstand ihrer parallelen Kanten mehrfach mit großer Häufigkeit gemessen. Verlaufen zwei Kanten im Winkel zueinander, z.B. Zwischenraum zweier Fasern, so werden viele verschiedene Abstände mit jeweils geringer Häufigkeit gemessen. In der Histogramm-Darstellung erscheint daraus ein von zufälligen Abständen verursachter Untergrund, aus dem die Häufungen gleicher Abstände deutlich herausragen. Die Lage und Breite dieser Häufungen (Peaks) kann nach Anpassung einer Gaußfunktion direkt als Zahlenwert ausgegeben werden und entspricht der gesuchten Information von Faserdurchmesser und

Verteilung (d.h. Mittelwert und Standardabweichung). Zur zusätzlichen Sicherheit wird in der Umsetzung von GIFT bei im größeren Winkel verlaufenden Kanten mindestens eine Kante ausgefiltert und somit die Messung nichtparalleler Kantenabstände von vorn herein verhindert.

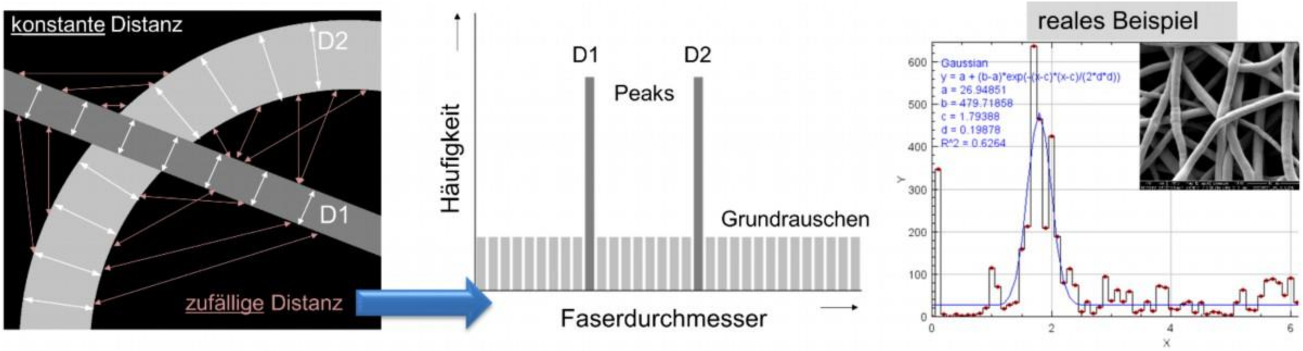

Abb. 3: Grundidee von GIFT, die Kombination der genauen Messung mit der statistischen Sicherheit großer Zahlen, links: schematische Darstellung zweier Fasern unterschiedlicher Lage, Krümmung und Helligkeit, Distanzen zwischen den Faserkanten, Mitte: schematische Häufigkeitsverteilung der Distanzen, rechts: Häufigkeitsverteilung der Distanzen von Faserkanten in einem realen REM-Bild, angepasste Gaußfunktion mit numerischen Ergebnissen im von GIFT generierten Histogramm.

Für einen Menschen sind Fasern auf einem Bild intuitiv erkennbar, ein Bild repräsentiert für einen Computer aber lediglich eine große Tabelle mit Zahlen. Daher stellt sich zunächst die Frage nach der Definition einer Faser. Ausgehend vom menschlichen Vorbild wird eine Faser hauptsächlich anhand ihrer scharfen parallelen Kanten nahezu konstanten Abstands erkannt. Grauwertverläufe oder Kontrastunterschiede führen menschliche Betrachter nicht in die Irre. Vor der eigentlichen Verarbeitung wird das Bild in ein Grauwertbild mit einer Farbtiefe von 8 Bit konvertiert, um definierte Bedingungen zu schaffen. Der erste Schritt der Verarbeitung von GIFT liegt bei einer sicheren Kantenerkennung, die mittels zweidimensionaler Sobel-Operatoren realisiert wird [56], siehe Abb. 4-B.

Es folgt ein Binarisierungsschritt, um Kanten eindeutig vom Hintergrund zu unterscheiden. Hierzu wird ein Schwellwert in Abhängigkeit des Bildkontrasts oder als prozentualer Anteil der Bildfläche festgelegt, Grauwerte ab dem Schwellwert werden auf Weiß gesetzt, kleinere Grauwerte auf Schwarz. Je höher der Schwellwert gesetzt wird, umso weniger und dünnere Kanten verbleiben im Bild. Bei diesem Schritt wird bereits ein Teil von eventuell vorhandenen Unebenheiten auf der Faseroberfläche entfernt, siehe Abb. 4-C.

Um die kürzeste Distanz zwischen den Faserkanten zu finden, muss senkrecht zu den Kanten gemessen werden, nicht schräg durch die Faser. Hierzu ist es zunächst notwendig, als Bezugspunkte, kurze parallele Kantenstücke zu selektieren, die sich gegenüberstehen, und alle schrägverlaufenden Kanten zu entfernen, um danach dann in senkrechter Richtung deren Distanzen zu messen. Mittels eines morphologischen Nachbarschaftsoperators wird pixelweise für ein Strukturelement (hier: horizontale Linie einer bestimmten Länge) geprüft, ob das Strukturelement im Bild vorhanden ist oder nicht. Ist die Bedingung erfüllt, bleibt das Pixel und die Nachbarschaft weiß, andernfalls werden Pixel und Nachbarschaft schwarz gesetzt. Somit wird erreicht, dass nur horizontale Linien einer Mindestlänge im Bild verbleiben. Die Länge dieser Linie beträgt einige Pixel. Eine zu kurze Linie würde zu viel schrägverlaufende Kanten im Bild belassen, eine zu lange Linie würde zu wenige Kantensegmente selektieren. Daher wird die experimentell ermittelte Länge von acht Pixeln als Standardeinstellung gesetzt. Dieser Filter-Schritt entspricht der morphologischen Filterung „Öffnung“, die aus den aufeinanderfolgend ausgeführten Operationen „Erosion“ und „Dilatation“ besteht, welche jeweils die horizontale Line als Strukturelement anwenden [57–60]. Durch diese morphologische Filterung werden gleichzeitig fast alle störenden Strukturen wie Verunreinigungen oder Unebenheiten der Faseroberfläche, teilweise auch Bildrauschen und Unschärfen aus dem Bild entfernt (Abb. 4-D1).

Im folgenden Schritt werden die Distanzen zwischen den verbliebenen Kantensegmenten gemessen. Zur Sicherstellung der senkrechten Messrichtung wird in den folgenden Schritten jede senkrechte Pixelreihe einzeln verarbeitet. Bei mehr als einem Pixel breiten Kantensegmenten muss zunächst deren Mitte gefunden werden. Für jede Pixelreihe im Bild werden senkrecht verlaufende Hilfslinien gesetzt und die im Verlauf auftretenden Grauwerte als Höhen interpretiert, wobei „Schwarz“ der Basislinie entspricht und „Weiß“ eine Erhebung (Peak) darstellt. Auf diesen Hilfslinien werden die Positionen der Peaks (Weiß) gesucht, entsprechend der mittleren Position der weißen Kantensegmente. Die Abstände der Mitten benachbarter Peaks entsprechen hierbei den Distanzen der Kantensegmente. Auf alle Pixelreihen wird das Verfahren nacheinander angewendet und alle gefundenen Abstände (Distanzen) registriert. Der Datensatz enthält nun Distanzdaten aus (nahezu) horizontal verlaufenden Faserabschnitten und zufälligen Abständen aus (nahezu) horizontal verlaufenden Faserzwischenräumen. Somit wird sichergestellt, dass senkrecht (nicht schräg) durch die Fasern gemessen und bei mehreren Pixeln breiten Kanten deren Mitte berücksichtigt wird. Da Fasern in allen möglichen Orientierungswinkeln im Bild auftreten können und auch vermessen werden sollen, ist es notwendig, das Verfahren für mehrere Winkel anzuwenden. Hierzu wird das binarisierte Kantenbild um einen bestimmten Winkel gedreht (ohne Interpolation von Grauwerten). Die morphologische Filterung und die Distanzmessung werden wiederholt. Danach wird das Procedere für weitere äquidistante Winkelschritte bis maximal 180° wiederholt. Größere Winkel wären den kleinen aufgrund der Symmetrie redundant. Somit wird gewährleistet, dass Fasern von beliebiger Orientierung erfasst werden, siehe Abb. 4-D2.

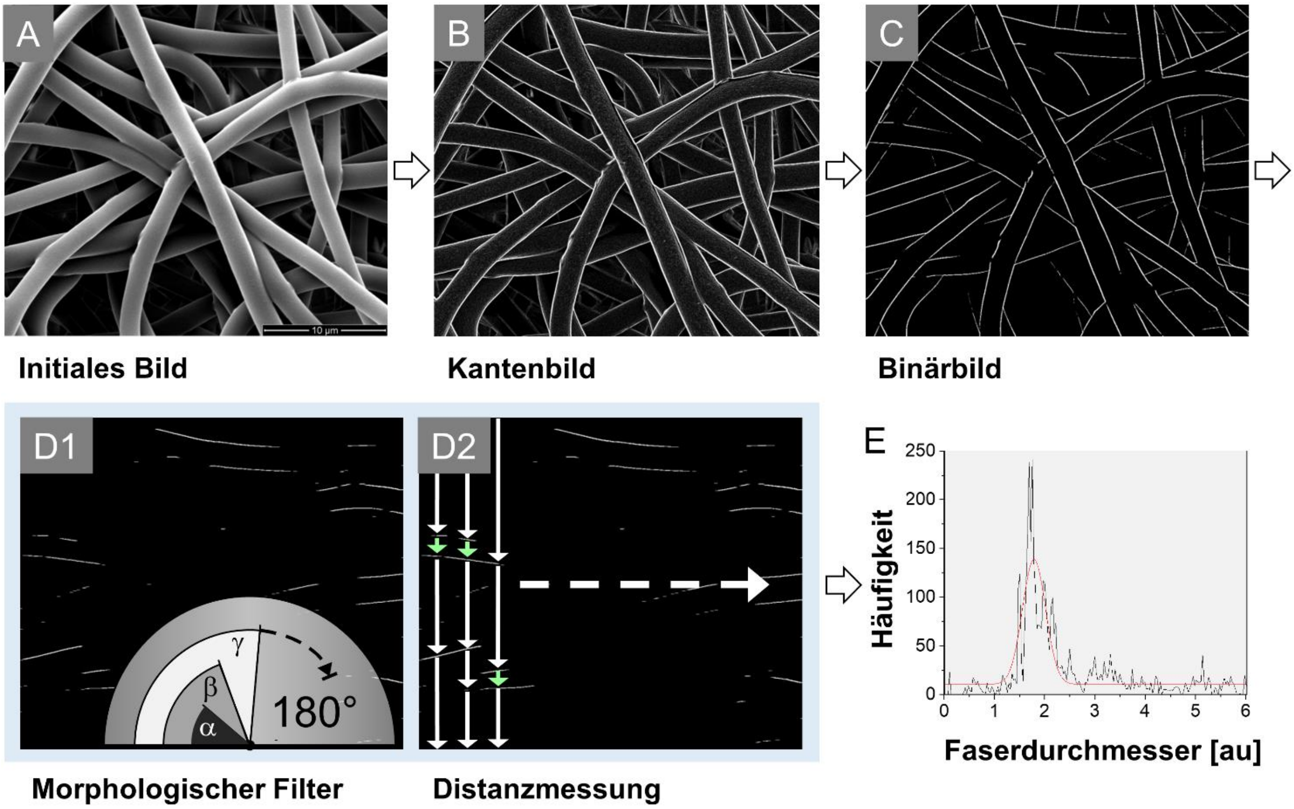

Abb. 4: Prozessschritte der Bildverarbeitung, A: REM-Bild eines Nanofaservlieses, B: Bild nach Kantenerkennung, C: Kantenbild nach Binarisierung, D1: Binärbild nach morphologischer Filterung mit einer horizontalen Linie (im Beispiel Länge 8 Pixel) als Strukturelement, D2: schematische Veranschaulichung der Distanzmessung, D gesamt: nach Rotation des Binärbildes um einen bestimmten Winkel werden diese Schritte mehrfach wiederholt (im Beispiel 0, 45, 90, 135 Grad), E: eine statistische und numerische Auswertung per Anpassungsrechnung schließt sich an.

Die gemessenen Distanzen in Pixeln werden anhand des Bildmaßstabs in metrische Einheiten umgerechnet. Im Anschluss erfolgt die statistische Aufbereitung, wobei die gemessenen Distanzen als klassifizierte Häufigkeitsverteilung dargestellt werden [61]. In einer Histogramm-Darstellung werden dabei die Häufigkeiten der einzelnen Distanzklassen aufgetragen. Eine frei wählbare Klassierung der Distanzdaten erlaubt eine beliebige Abstufung der darzustellenden Distanzbereiche. Zur Gewinnung numerischer Ergebnisse wird eine in ImageJ (National Institutes of Health, USA) implementierte Anpassungsrechnung für eine Gaußfunktion (Normalverteilung) ausgeführt, die dann die gesuchten Zahlenwerte ausgibt. Die ausgegebenen Zahlen entsprechen dabei der Gaußfunktion, somit indirekt dem ihr zugrundeliegenden Datensatz, siehe Abb. 4-E. Die Faserdurchmesser sind nicht zwingend normalverteilt, dennoch ist die Gaußfunktion als Modell für diese Anwendung gut geeignet.

2.3. GIFT – Softwarebasierte Umsetzung

Die manuelle Ausführung der oben genannten Einzelschritte ist umständlich und zeitraubend, die Entwicklung einer Software war der nächstliegende Schritt. Aufgrund der weiten Bekanntheit und Beliebtheit von ImageJ [56,62,63] in der wissenschaftlichen Community, sowie der Möglichkeit der Einbindung erweiternder Softwarepakete durch die Nutzer, wurde ImageJ als Plattform gewählt, ein darauf zugeschnittenes GIFT-Makro zu veröffentlichen. Die wesentlichen Schritte der Bild- und Datenverarbeitung sind in einem Flussdiagramm in Abb. 5 dargestellt. Das GIFT-Makro ist quelloffen und unter „https://github.com/IBMTRostock/GIFT“ incl. einer englischsprachigen Bedienungsanleitung frei verfügbar. Es kann prinzipiell auf alle Bilder angewendet werden, die sich mit der Software ImageJ bzw. Fiji verarbeiten lassen [62,64]. Außerdem ermöglicht das GIFT-Makro die schnelle Verarbeitung großer Mengen von REM-Bildern in einem einzigen Schritt (Stapelverarbeitung, engl.: batch processing), wobei der Benutzer alle Bildverarbeitungsparameter leicht einstellen kann. Das GIFT-Makro ist benutzerfreundlich gestaltet und kann mit minimalen Eingaben unter Verwendung der Standardeinstellungen ausgeführt werden. Zur Ausführung des Makros ist lediglich die Eingabe der Datei oder der Dateispeicherorte erforderlich. Alle wichtigen Verarbeitungs- und Ausgabeparameter können über eine einzige grafische Benutzeroberfläche festgelegt werden. Zusätzlich können Bildausschnitt, Skalierung und prozentualer Schwellwert interaktiv auf der Grundlage des ersten Bildes in einem bestimmten Datensatz festgelegt werden, siehe auch die eigene Publikation 2 [Pub 2]. Als weitere Zusatzfunktion sind die Plug-ins „OrientationJ“ oder „Directionality“ zur Bestimmung der Faserorientierung abrufbar.

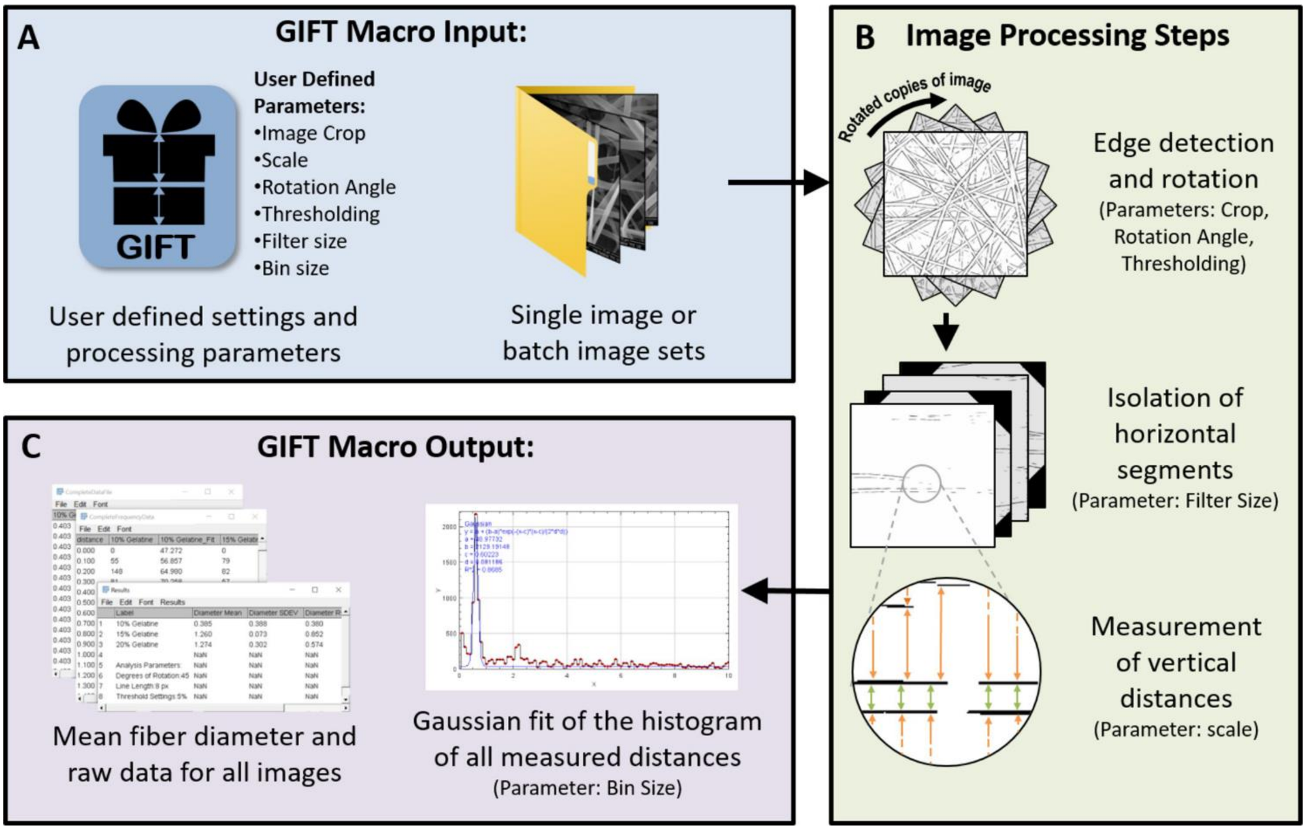

Abb. 5: Wesentliche Elemente der Bild- und Datenverarbeitung aufbereitet für englischsprachige Anwender, A: Festlegung der Prozessparameter auf einer interaktiven Benutzeroberfläche, B: automatische Bildverarbeitung, C: Datenverarbeitung und Ausgabe der Ergebnisse in Grafiken und Tabellen.

2.4. GIFT - Vergleich mit etablierter Software und Validierung

GIFT wurde vergleichend mit der etablierten Software „DiameterJ“ getestet [25], die speziell für die Messung von Faserdurchmessern in REM-Bildern entwickelt und validiert wurde. Auch bei augenscheinlich guten kontrastreichen REM-Bildern liefert DiameterJ oft unzuverlässige Ergebnisse, was ursprünglich als eine wesentliche Motivation für die Entwicklung von GIFT gewirkt hat. Anhand einer vergleichenden Auswertung von einem Testbild und drei alltäglichen REM-Bildern werden die Unterschiede in Abb. 6 veranschaulicht. Die manuelle Messung wird hier als Referenz herangezogen.

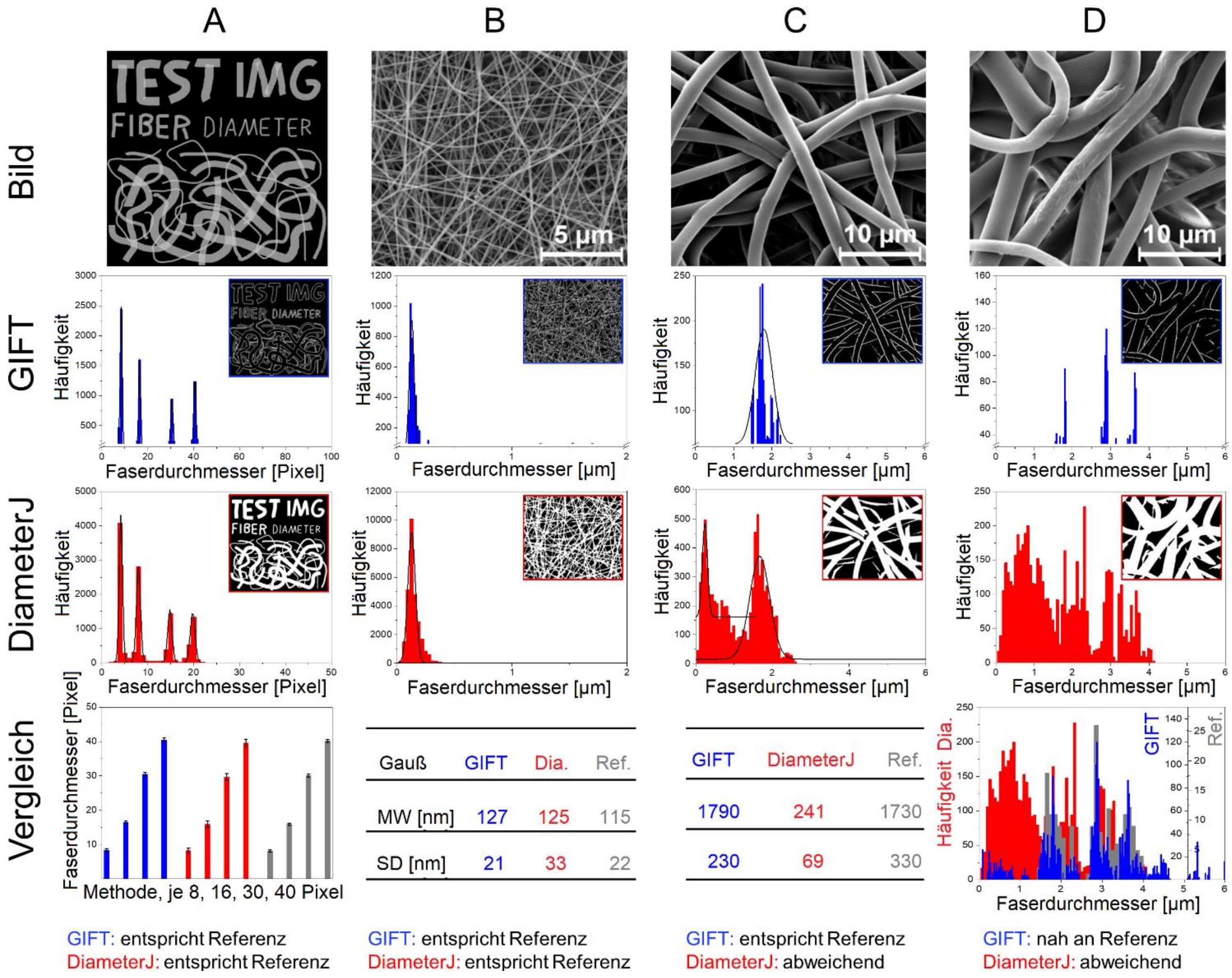

Gauß	GIFT	Dia.	Ref.
MW [nm]	127	125	115
SD [nm]	21	33	22

GIFT	DiameterJ	Ref.
1790	241	1730
230	69	330

GIFT: entspricht Referenz
DiameterJ: entspricht Referenz

GIFT: entspricht Referenz
DiameterJ: entspricht Referenz

GIFT: entspricht Referenz
DiameterJ: abweichend

GIFT: nah an Referenz
DiameterJ: abweichend

Abb. 6: Methodenvergleich GIFT mit DiameterJ und manueller Messung als Referenz an verschiedenen Bildern. Die Bilder sind in der ersten Reihe dargestellt. Die zweite Reihe zeigt die Ergebnisse von GIFT, wobei das statistische Rauschen entfernt wurde. Als Einschub sind die segmentierten Faserkanten dargestellt. Die Ergebnisse von DiameterJ (Dia.) sind in der dritten Reihe mit dem segmentierten Bild als Einschub dargestellt. Die untere Reihe zeigt die Ergebnisse in verschiedenen Formen für die unterschiedlichen Bilder, um die Unterschiede zwischen den Ergebnissen am deutlichsten hervorzuheben. Die drei Messmethoden sind durchweg in der gleichen Farbe dargestellt. A: Testbild mit genau vier Faserdurchmessern in buchstabenförmigen und zufällig orientierten Fasern, B: dünne Fasern, C: mittlere Fasern, fehlerhaftes Messergebnis von DiameterJ, mit Mittelwert (MW) und Standardabweichung (SD), D: dicke Fasern, kein Ergebnis von DiameterJ, ähnliche Peak-Verteilung von GIFT und Referenz, Ergebnis ist als Überlagerungsdiagramm gezeigt.

In zahlreichen Versuchen haben sich bestimmte Parameter für die Auswertung alltäglicher REM-Bilder als geeignet erwiesen. Für die Binarisierung bei kontrastreichen Bildern sind Schwellwerte um 200 geeignet. Bei 8 Bit Farbtiefe umfasst das Bild 256 Grauwerte (0 ≙ Schwarz, 255 ≙ Weiß), ein Wert von 200 entspricht einem hellen Grau. Die Länge der horizontalen Linie für den morphologischen Filter von acht Pixeln zeigte sich als sinnvoll. Für die Wiederholungsmessung haben sich vier Rotationsschritte in Winkeln von 0, 45, 90 und 135 Grad als ausreichend für die meisten Bilder erwiesen. Diese Werte wurden als Standardeinstellungen in das GIFT-Makro übernommen, wobei der Schwellwert statt des Grauwertes 200 auf 5% der Bildfläche geändert wurde. Aufgrund der 45-Grad-Schritte könnte es Faseranteile zwischen diesen Winkeln geben, die von der Messung nicht erfasst werden. Hierfür wurden ein REM-Bild und das Testbild in 6-Grad-Schritten zwischen 0 und 45 Grad gedreht und jeweils als initiale Bilder verwendet, damit jeweils ein anderer Anteil der Fasern „übersehen" wird. Im Ergebnis fällt der Einfluss der eventuell entgangenen Fasern nicht ins Gewicht. Die Messung am Testbild bestätigt des Weitern, dass die Faserdurchmesser zuverlässig erkannt werden. Selbst bei kontrastarmen REM-Bildern oder nicht ideal gewählten Parametern liefert GIFT zuverlässige Ergebnisse, an dieser Stelle sei auf die eigene Publikationen 1 verwiesen [Pub 1].

Zur Beurteilung der Zuverlässigkeit wurde das GIFT-Makro zur Stapelverarbeitung mittels einer Reihe von synthetischen Testbildern sowie realen REM-Bildern mit den Programmen „DiameterJ“ [25] und „SIMPoly“ [55] verglichen, siehe dazu Abb. 7. GIFT schneidet bei der Durchmesserbestimmung ungeordneter Fasern, die der typischen Struktur von elektrogesponnenen Fasern entsprechen, ähnlich oder besser ab als DiameterJ und SIMPoly. Das GIFT-Makro hat mit den Standardeinstellungen zuverlässige Ergebnisse geliefert. Auch hat sich GIFT deutlich robust gegen die Variation der eingestellten Parameter erwiesen, was Bedienfehler verzeiht.

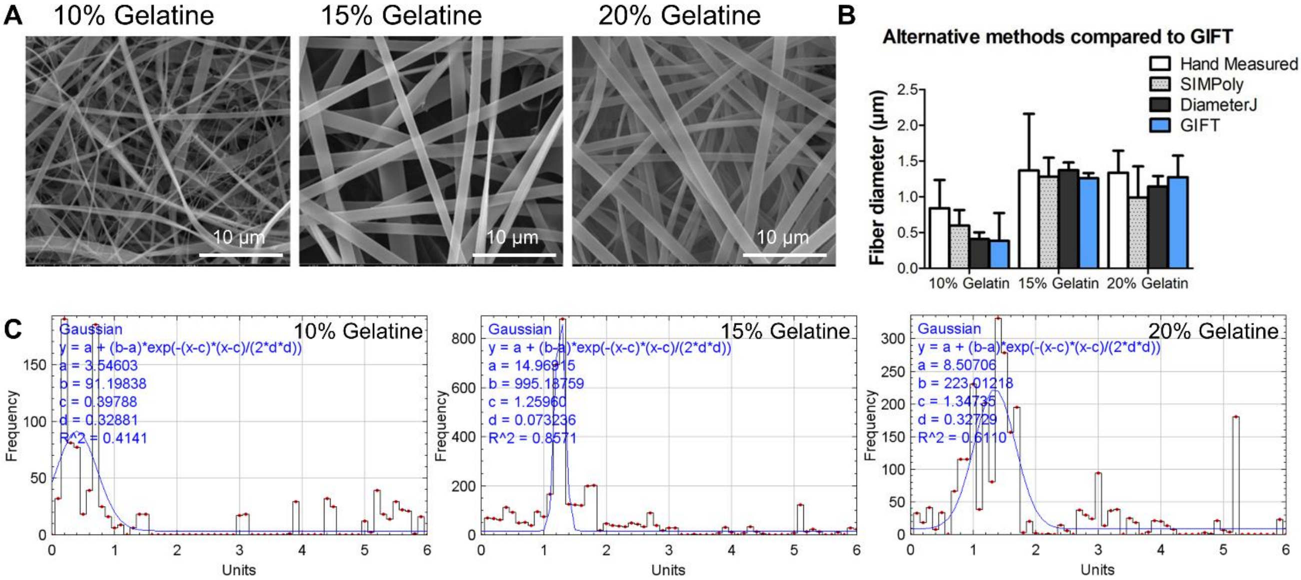

Abb. 7: Methodenvergleich, A: REM-Bilder von elektrogesponnenen Gelatinelösungen unterschiedlicher Konzentration, B: Vergleich der Ergebnisse von manueller Messung (n = 10 pro Bild), SIMPoly, DiameterJ und GIFT mit Standardeinstellungen, C: Histogramme des GIFT-Makros für jedes Bild, die Einheiten auf der Abszisse entsprechen Mikrometern, die blaue Kurve repräsentiert die angepasste Gaußfunktion, die ausgegeben Zahlenwerte sind in die Grafik eingeblendet.

DiameterJ erfordert die subjektive Auswahl eines segmentierten Bildes und ist somit von der Intuition des Benutzers abhängig. Mit neueren Versionen von ImageJ ist DiameterJ nicht kompatibel. SIMPoly ist wenig flexibel bezüglich Parametereinstellungen über Benutzereingaben. Die Nutzung ist an die nicht frei verfügbare Software „Matlab“ gebunden. Kommerzielle Software wie beispielsweise „Phenom FiberMetric“ (Thermo Fisher Scientific Inc, USA) ist an den Betrieb zusammen mit Elektronenmikroskopen gebunden [29]. Somit stellt das GIFT-Makro eine Alternative zu bestehender Software dar.

3. Detektion von Nanofaserversagen bei elektrogesponnenen Vliesen unter Zugbelastung

3.1. Methodische Fragestellung auf werkstofflicher Mikroebene

Neben der morphologischen Beschaffenheit eines Nanofaservlieses bildet die Bestimmung mechanischer Kennwerte eine wichtige Säule der Materialcharakterisierung. Ein Standardverfahren ist der uniaxiale Zugversuch, bei dem die Zugprobe mit konstanter Geschwindigkeit bei gleichzeitiger Aufzeichnung von Kraft und Weg in die Länge gezogen wird. Üblicherweise werden die Versuche bis zum Bruch der Probe geführt. Im Spannungs-Dehnungs-Diagramm veranschaulicht die Zugkurve das Versagensverhalten und liefert spezifische Materialkennwerte. Die Spannung wird gewöhnlich nominell und die Dehnung prozentual angegeben und dabei bezogen auf den Ausgangsquerschnitt und die Ausgangslänge der Probe. Der typische Verlauf der Zugkurve eines Nanofaservlieses ist in Abb. 8 dargestellt. Das Spannungs-Dehnungs-Diagramm liefert makroskopische Informationen über die gesamte Zugprobe, es sind keine Informationen über das Materialversagen auf mikroskopischer Ebene ableitbar.

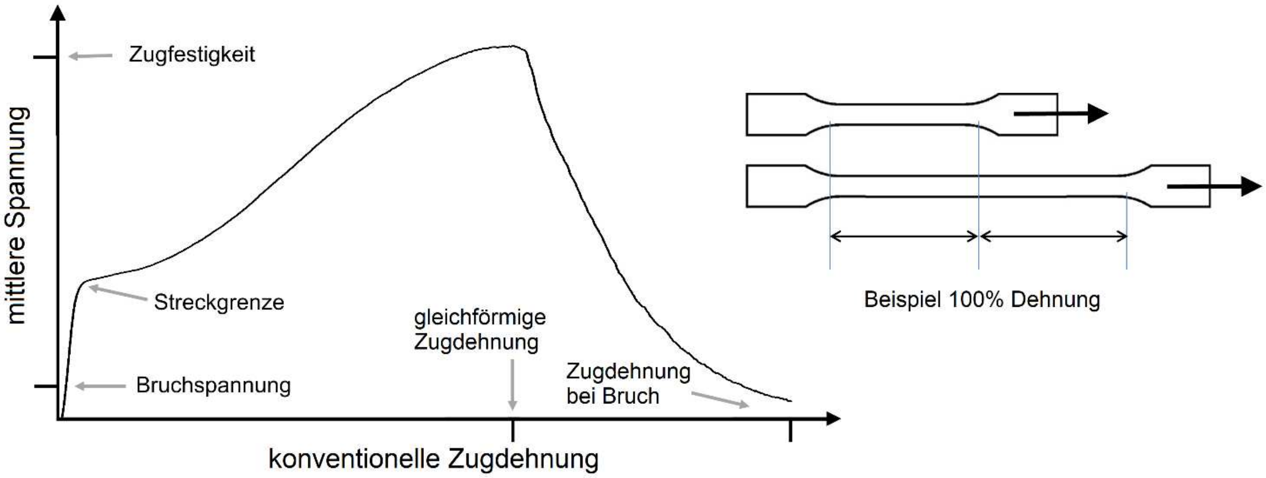

Abb. 8: Repräsentatives Spannungs-Dehnungs-Diagramm eines Nanofaservlieses (eigene Daten), wichtige Kennwerte entsprechend DIN EN ISO 9073-3 [65], Illustration der prozentualen Dehnung an einer typischen Zugprobe in Anlehnung an DIN EN ISO 527-2 [66] (Längenzuwachs bezogen auf Anfangslänge).

Die Vlies-Zugprobe besteht aus einer Vielzahl von Einzelfasern, die im Normalfall ungeordnet aufeinanderliegen, mehr oder weniger untereinander verbunden sind und zudem große Zwischenräume bilden (Porosität typisch um 80% Luft, nach eigenen Messungen). Eine unkomplizierte Methode wurde als Zielstellung definiert, die Informationen zu den Vorgängen auf mikroskopischen Skalen liefert. Die komplexen Vorgänge und Wechselwirkungen, wie beispielsweise Geradestreckung von Krümmungen, Umlagerung, Lösen von Verbindungen, Gleiten (Reibung), Faserverjüngung, oder Reißen, können sicher nicht durch eine einzelne Methode aufgeklärt werden. Die Entwicklung einer Methode ist auch stets vor dem Hintergrund der Integration in die alltäglichen Arbeitsabläufe im Labor zu sehen, um praktisch nutzbar zu sein.

Die Nanofaserdurchmesser liegen in der Größenordnung von Lichtwellenlängen oder deutlich darunter, und sind damit zu dünn für erschöpfende optische Analysen. Mit guten optischen Mikroskopen lassen sich die Fasern zwar darstellen, aber keine Detailaussagen gewinnen. Die Nutzung der Lichtbeugung an einzelnen dünnen Strukturen ist zwar grundsätzlich geeignet, um Durchmesser oder Faserausrichtungen zu bestimmen, setzt aber mehrere definierte Bedingungen und voraus [67]. Die schiere Vielzahl dicht übereinanderliegender Fasern und deren unbekannte räumliche Anordnung erzeugt zu viele unberechenbare Variablen. Daher wären nur optische Verfahren denkbar, die statistische Aussagen liefern. Zudem müsste die zeitliche Abtastrate der optischen Methode sehr hoch sein, um schnelle Vorgänge, z.B. Reißen, nachweisen zu können. Für die Elektronenmikroskopie sind mikromechanische Prüfmaschinen „on stage“ verfügbar [68,69], aber die Bildgebung ist zu langsam, um schnelle Faserveränderungen zu dokumentieren, außerdem sind viele Polymermaterialien nur begrenzt elektronenstrahlstabil. Einzelfasern sind für spezielle Untersuchungen aus dem Vliesverbund nicht gezielt isolierbar, da keine geeigneten feinmechanischen Werkzeuge für diese Größenordnung zur Verfügung stehen. Selbst wenn es gelänge, Einzelfasern zu isolieren, wäre weder die geringe Reißkraft messbar, noch eine gravimetrische Analyse der Bruchstücke möglich, da gängige Kraftsensoren oder Feinwaagen diesen Bereich nicht abdecken. Vlies-Zugproben von wenigen Millimetern Größe (z.B. 1BB Normproben nach DIN EN ISO 527-2 [66]) reagieren empfindlich auf schwache Luftbewegungen und elektrostatische Aufladung, erfordern Fingerspitzengefühl im Umgang und sind zu filigran für das Anbringen von kleinen Sensoren jeder Art. Daher können beim Zugversuch nur berührungslose Untersuchungsverfahren zum Einsatz kommen. Aus der Distanz ist während der Zugprüfung eine lautlose Streckung und Verjüngung der Zugprobe beobachtbar, Aussagen zu den Vorgängen auf Faserebene scheinen unter diesen Voraussetzungen schwer möglich.

3.2. Darstellung des Lösungsansatzes

In der Werkstoffprüfung sind Zugversuche in Kombination mit der AE-Detektion bei Festkörpern und Faserverbundwerkstoffen seit Jahrzehnten etabliert [70–72]. Zur Untersuchung nichteingebetteter Nanofaservliese hingegen ist diese Technik nicht geeignet. Signale von beispielsweise reißenden Nanofasern würden aufgrund unzähliger instabiler Kontaktstellen schon innerhalb der Zugprobe erheblich gedämpft und zeitlich verzerrt. Daher ist die direkte Detektion mittels Körperschalltechnik oder Kraftmessdose weder möglich noch sinnvoll.

Die entscheidende Idee brachte ein historischer Sinnspruch aus dem Bergbau: „Die Fichte spricht, bevor sie bricht.“ Stollen wurden früher mit Holzkonstruktionen abgestützt, an kritischen Stellen wurden Warnhölzer (z.B. Fichte) verwendet, die bei Bewegungen im Berg durch hörbares Knistern mit ausreichend Vorwarnzeit das baldige Zusammenbrechen des Stollens ankündigten [73,74]. Das Reißen der dünnen Holzfasern setzt genügend Energie frei, um ein hörbares Signal zu erzeugen. Das Reißen einer Nanofaser setzt ebenso schlagartig Energie frei, aber deutlich weniger als eine Holzfaser. Der Grundgedanke ist: falls akustische Emissionen entstehen, dann haben diese erstens eine sehr geringe Intensität. Zweitens liegen die Signale außerhalb des hörbaren Frequenzbereichs. Drittens liegen sie aufgrund der mikroskopischen Dimensionen und der daraus folgend schnellen Faserbewegungen im Ultraschallbereich. Viertens lassen sich diese Signale nur auf dem Luftweg detektieren. Zum Wesen dieser AE gibt es keine Beispiele oder Anhaltspunkte, da in der wissenschaftlichen Literatur keine vergleichbaren Studien gefunden werden konnten. Daher ist ein Mithören und Bewerten der AE in Echtzeit notwendig. Hierbei wird ein Signal erwartet, das einem reißenden Stück Textilstoff ähnelt. Eine praktische Umsetzung der Idee erfordert bestimmte Annahmen und Überlegungen, die in Tab. 2 aufgeführt sind.

Tab. 2: Annahmen und Überlegungen zur Entwicklung einer AE-Detektionsmethode für Nanofaserrisse in Luft.

Überlegung	**Erläuterung**
1 Signalstärke	Die größte Herausforderung ist die geringe Energiefreisetzung einer reißenden Nanofaser, die zu einem schwachen Signal führt und einen hochempfindlichen Sensor sowie eine Abschirmung gegen Störungen erfordert.
2 Eigenresonanz ausnutzen	Die Eigenresonanz einer schwingfähigen Sensormembran kann mit geringen Energiemengen angeregt werden. Das Schallsignal muss dazu Frequenzanteile der Resonanzfrequenz der Sensormembran enthalten. Somit gelingt der Nachweis eines verursachenden Schallsignals.
3 Störgeräusche und Rückkopplungen vermeiden	Hintergrundgeräusche und Störquellen müssen unterdrückt werden. Akustische Rückkopplungen des verstärkten Signals sind zu vermeiden.
4 obere Abschätzung Frequenzbereich	Ohne Einbettung in ein hartes Material (Faserverbundwerkstoffe) werden AE von reißenden Vliesproben in einem Frequenzbereich unter 100 kHz erwartet, da die mechanische Kopplung in die Luft geringer und deren Schallgeschwindigkeit niedriger ist.
5 untere Abschätzung Frequenzbereich	Aufgrund der praktisch unhörbaren Geräusche von reißenden Vliesen, der kleinen Faserdurchmesser und einer geringen Massenträgheit sind AE in einem Frequenzbereich zu erwarten, der oberhalb des hörbaren Spektrums liegt.
6 erwarteter Frequenzbereich	In Anlehnung an die Punkte 4 und 5 werden AE beim Reißen von Nanofaservliesen im Ultraschallbereich von einigen zehn Kilohertz erwartet. Unter Annahme der Theorie zur Saitenschwingung [75] kann dieser Frequenzbereich bestätigt werden.
7 erwartetes Signal	Die schwache Ultraschall AE von reißenden Nanofasern wird als Pop-Signal in einem breiten Frequenzband erwartet. FFT-Spektren von Faserbruchsignalen decken ein breites Frequenzband ab [76].
8 erfassbarer Signalanteil	Unter Berücksichtigung der Punkte 6 und 7 kann ein Teil des AE-Signals mit einem Schmalband-Ultraschallsensor mit einem Empfindlichkeitsmaximum bei einigen zehn Kilohertz erfasst werden.
9 Qualität der Aussage	Das Hauptaugenmerk dieser Arbeit liegt auf qualitativen Aussagen, weniger auf quantitativen Messungen, da Energiebewertungen nicht unbedingt einen Vorteil gegenüber Zähltechniken haben [77].
10 berührungslose Methode	Um eine Beeinflussung der Mechanik des Zugversuchs zu vermeiden, wird eine berührungslose Methode gewählt. Daher wird der Sensor einige Millimeter hinter der Zugprobe ohne direkten Kontakt positioniert.
11 Begründung für Mithören in Echtzeit	Aufgrund nicht verfügbarer Vergleiche zur Literatur ist es sehr schwierig, die aufgezeichneten Daten richtig zu interpretieren und zwischen einem echten Signal, einem Störsignal und Hintergrundrauschen zu unterscheiden. Eine Ausgabe im Hörbereich in Echtzeit ermöglicht die direkte Beurteilbarkeit und erlaubt eine Plausibilitätsprüfung.
12 Begründung für Heruntermischen auf Sensor-Resonanzfrequenz	Unter Berücksichtigung von Punkt 11 wird in dieser Arbeit eine Signaltransformation gewählt, mit der das Signal ohne großen Informationsverlust hörbar gemacht werden kann. Um das Ultraschallsignal in ein hörbares Schallsignal umzuwandeln, wird das hochfrequente Schallsignal mit

	einem Oszillatorsignal gemischt, das auf das Empfindlichkeitsmaximum des Sensors abgestimmt wird. Das heruntergemischte Differenzfrequenzsignal (synthetisches Audiosignal) wird zur Aufzeichnung und hörbaren Ausgabe weiter verstärkt.
13 mehrere Vorteile der Methode, erkauft durch Schmalbandigkeit	Aus den Punkten 8 und 12 ergeben sich die Vorteile, dass die meisten Hintergrundgeräusche aufgrund der Schmalbandigkeit eliminiert sowie mögliche akustische Rückkopplungen verhindert werden. Somit ist ein Mithören in Echtzeit möglich, ohne das ursprüngliche Ultraschallsignal zu stören.

3.3.Technische Umsetzung

Die technische Umsetzung zur Detektion von AE aus zugbelasteten Nanofaservliesen ist in Abb. 9 gezeigt. Die Zugprüfmaschine bleibt dabei von der AE-Detektion unbeeinflusst, die Signale der Kraftmessdose werden digitalisiert und zusammen mit Weg-Daten aus der Antriebseinheit aufgezeichnet. Zur AE-Detektion wurde ein kompaktes Device gefertigt, das auf die räumlichen Verhältnisse der Zugprüfmaschine angepasst ist und den Sensor etwa 10 mm hinter der Zugprobe positioniert. Das Device enthält den Sensor, die analoge Elektronik, eine Batterie, und es ist elektromagnetisch abgeschirmt. Als Detektor findet der piezoelektrische Ultraschallsensor MA40S4R (Murata Manufacturing Co. Ldt., Japan) [78] mit freistehender Membran Verwendung. Zur Maximierung der Empfindlichkeit wurde dieser modifiziert. Hierzu wurden Teile des Gehäuses und eine Schutzbeschichtung auf der Membran entfernt, um mit der „nackten“ Membran hören zu können. Das Sensorsignal wird zunächst verstärkt, dann dem Frequenzmischer zusammen mit einem Oszillatorsignal zugeführt. Das heruntergemischte Signal entspricht der Differenzfrequenz beider Eingangssignale. Dieses Differenzsignal wird verstärkt und an drei externe Geräte ausgegeben. Die direkte Aufzeichnung erfolgt mittels eines Digitaloszilloskops (1) (PicoScope 2004A von Pico Technology Ltd., United Kingdom) [79]. Eine weitere Aufzeichnung erfolgt als Audiosignal am Mikrofoneingang eines Computers (2). Die hörbare Ausgabe als Tonsignal erfolgt nach einer weiteren Verstärkung per Aktivlautsprecher (3). Das bewährte Prinzip der Frequenzmischung wird beispielsweise in den meisten Radioempfängern seit Jahrzehnten verwendet, auch hier werden schwache hochfrequente Signale in den Hörbereich heruntergemischt. Die Anwendung dieses Prinzips auf die AE-Detektion bei Nanofaservliesen ist im Rahmen dieser Arbeit neu. Um das „Hörvermögen“ von Sensor und der Kombination von Sensor und Device zu bestimmen (Abb. 9), wurde für ein breitbandiges Rauschen der Frequenzgang mithilfe des Digitaloszilloskops gemessen. Die Angaben aus dem Datenblatt des Sensors konnten ergänzend bestätigt werden [78]. Zudem folgt der Frequenzgang des Devices im Wesentlichen dem Sensor, keine Teilbereiche werden auffällig verstärkt oder unterdrückt.

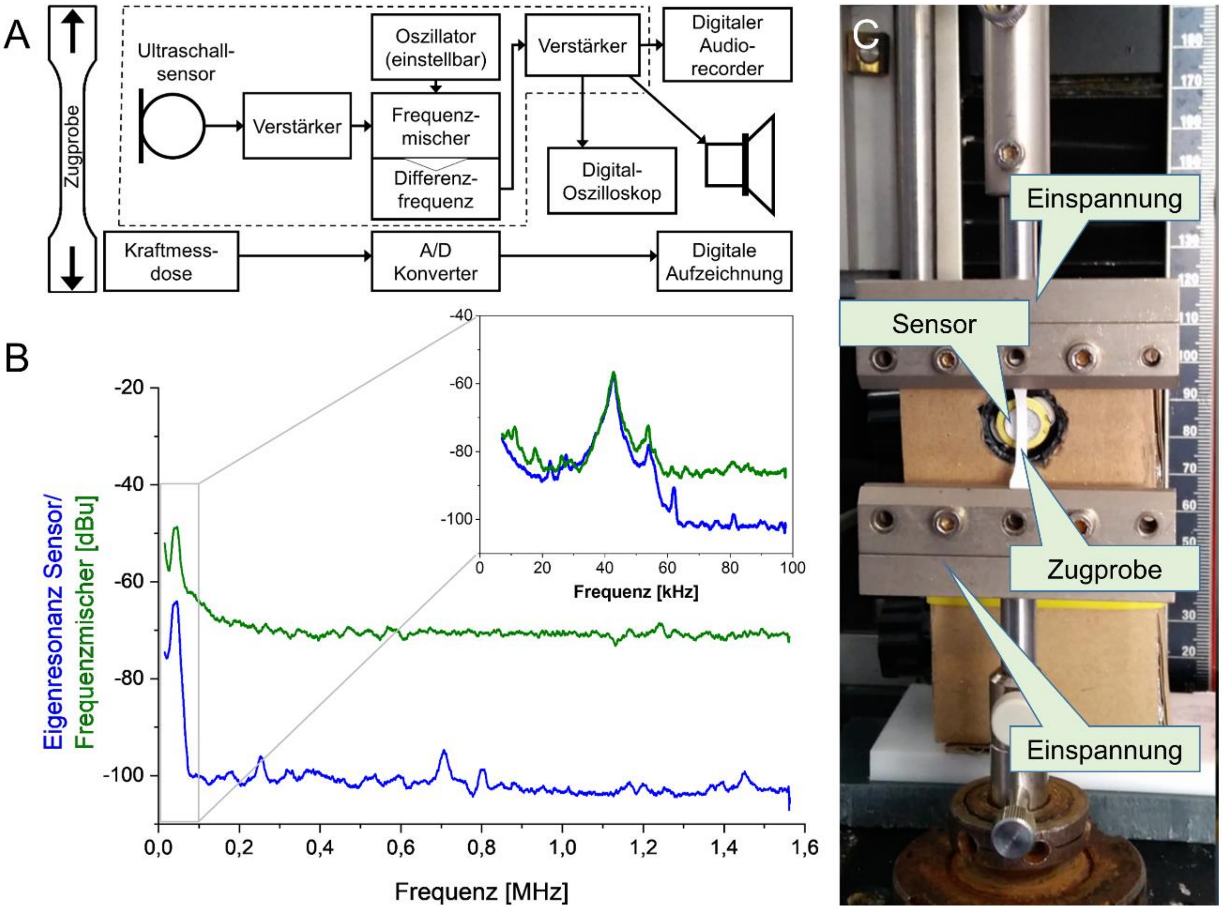

Abb. 9: AE-Detektion während des Zugversuchs, A: Im Blockschaltbild sind wesentliche Komponenten aufgeführt, die gestrichelte Umrandung kennzeichnet den Inhalt des Devices. B: Die Frequenzgänge zeigen für ein breitbandiges Rauschen die Eigenresonanz des Sensors (blau) sowie die Kombination mit dem Frequenzmischer (grün). Die Resonanz und damit maximale Empfindlichkeit liegt bei 42,7 kHz. C: Der Laboraufbau zeigt das Device hinter der eingespannten Zugprobe.

Die AE-Detektion mit dieser Methode funktioniert relativ gut für steife Fasermaterialien, während nahezu des gesamten Zugversuchs können Signale registriert werden. Bei weniger steifen, gummielastischen Fasermaterialien tritt erst Sekundenbruchteile vor Versagen der Probe ein Rauschen auf. In Analogie zur makroskopischen Größenordnung dehnt sich ein Gummiband geräuschlos und reißt dann plötzlich. Für die experimentellen Untersuchungen in der eigenen Publikation 3 [Pub 3] wurden Nanofaservliese aus PLLA mit drei verschiedenen mittleren Faserdurchmessern verwendet (Vlies S, M, und L), da PLLA ein in der Biomedizintechnik weit verbreitetes Material ist. Die aufgezeichneten Signale unterscheiden sich von Vlies zu Vlies deutlich. Ein repräsentatives Beispiel für die AE eines qualitativ nicht beanstandeten Nanofaservlieses (Vlies L) ist in Abb. 10 gezeigt. Ein schwaches Hintergrundrauschen ist bereits vor dem Start der Zugprüfmaschine vorhanden (Bereich A). Nach Überschreiten der Steckgrenze tritt ein schwaches Rauschen auf, das im mittleren Bereich nachlässt (Bereich B). Etwa 15 Sekunden vor Erreichen der maximalen Spannung treten deutlich hörbare Knacks-Signale auf, deren Häufigkeit und Stärke stetig zunehmen (Bereich C). Bis zum Spannungsmaximum verjüngt sich die Zugprobe gleichmäßig. Nach Überschreitung des Spannungsmaximums wird ein Teilbereich unter weiterer Verjüngung gestreckt, hier treten die stärksten AE auf, die sich als intensives knisterndes Rauschen äußern (Bereich D).

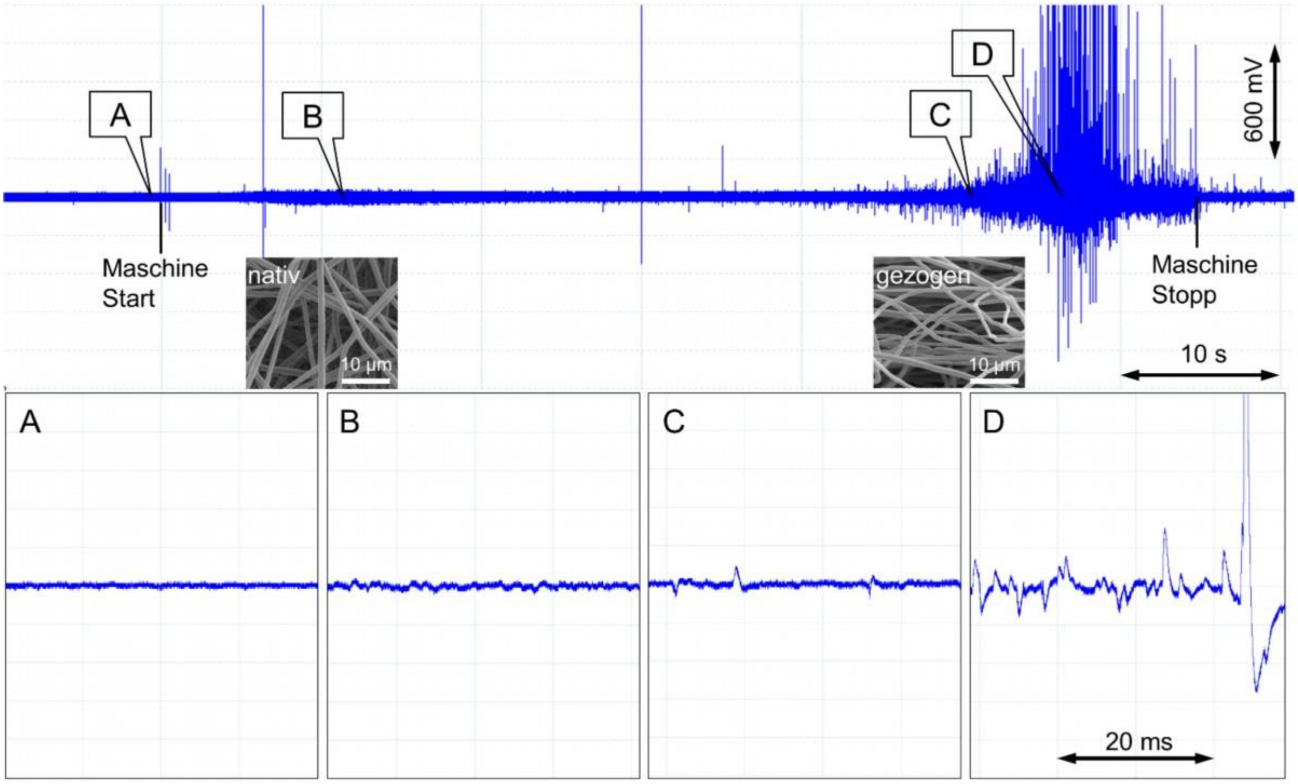

Abb. 10: Oszilloskop-Aufzeichnung des Differenzsignals eines repräsentativen PLLA Nanofaservlieses (Vlies L), oben ist der gesamte Datensatz abgebildet, unten ausgewählte Abschnitte, Geschwindigkeit 25 mm/min, A: Hintergrundrauschen vor Maschinenstart, B: schwaches Signal ohne besondere Auffälligkeiten, C: einzelne deutliche Knacks-Signale zeigen sich als Peaks, D: lautes Knistern und Rauschen während Versagen der Zugprobe, Einzelereignisse sind aufgrund der Überlagerung nicht zählbar. Die eingefügten REM-Bilder zeigen die Fasermorphologie vor und nach dem Zugversuch.

3.4. Signalanalyse und methodischer Nutzen als Erweiterung zum Zugversuch

Die Qualitätskontrolle von Nanofaservliesen am Institut für Biomedizinische Technik der Universitätsmedizin Rostock basiert hauptsächlich auf REM-Bildern und Zugversuchen. Sind keine Auffälligkeiten erkennbar, wird das Vlies nicht beanstandet. In Abb. 11 sind zwei nicht beanstandete Vliese verglichen, allerdings enthüllten sich Auffälligkeiten im AE-Signal des links dargestellten Vlieses (M). Im REM-Bild von Vlies M waren einseitig nur wenige dicke Fasern erkennbar, was gelegentlich vorkommt, aber nicht beanstandet wird. Auf der rechten Seite in Abb. 11 ist das unauffällige Vlies aus obigem Beispiel gezeigt (Vlies L). Beide Zugkurven zeigen einen nahezu glatten Verlauf und entsprechen im Wesentlichen den Erwartungen. Nach Überschreiten der Streckgrenze zeigt Vlies M ein schwaches Rauschen, das mit einzelnen deutlich hörbaren Knacksen überlagert ist. Nach etwa 25 s setzen plötzlich laute Einzelknackse ein, deren Häufigkeit im Verlauf bis zur Maximalspannung etwas nachlässt. Das Versagen der Zugprobe geht mit einem lauten Rauschen einher (Grafik A). Die Verläufe der kumulierten AE-Signale offenbaren deutliche Unterschiede (Grafiken C und D), bei Vlies M zeigt sich mit Einsetzen der lauten Einzelknackse ein auffälliger Kurvenknick mit fast treppenartigem weiteren Verlauf, während die Kurven von Vlies L glatt verlaufen. Bei genauer Betrachtung ist eine vage zu erahnende Krümmung der Zugkurve von Vlies M beim Einsetzen der lauten Einzelknackse erkennbar. Während des Versagens der Zugprobe oder bei Delamination offenbart sich eine weitere Eigenheit, die bei den meisten Vliesen gefunden wurde. Für das Knister/Rauschsignal ist ein Absinken der Tonhöhe und ein folgendes Wiederansteigen hörbar. Die Frequenzspektren der Audiosignale (Grafiken E und F) bestätigen dieses Phänomen, gekennzeichnet mit gestrichelten Linien (orange). Aufgrund der Frequenzsymmetrie des Differenzsignals und des hier auftretenden zeitlichen Verlaufs ist davon auszugehen, dass sich die mittlere

Frequenz des Ultraschallrauschens zunächst der Oszillatorfrequenz annähert und danach wieder entfernt. Eine plausible Erklärung liefert das Modell der schwingenden Saite, nach dem mit zunehmender Spannung der Saite deren Schwingungsfrequenz steigt [75].

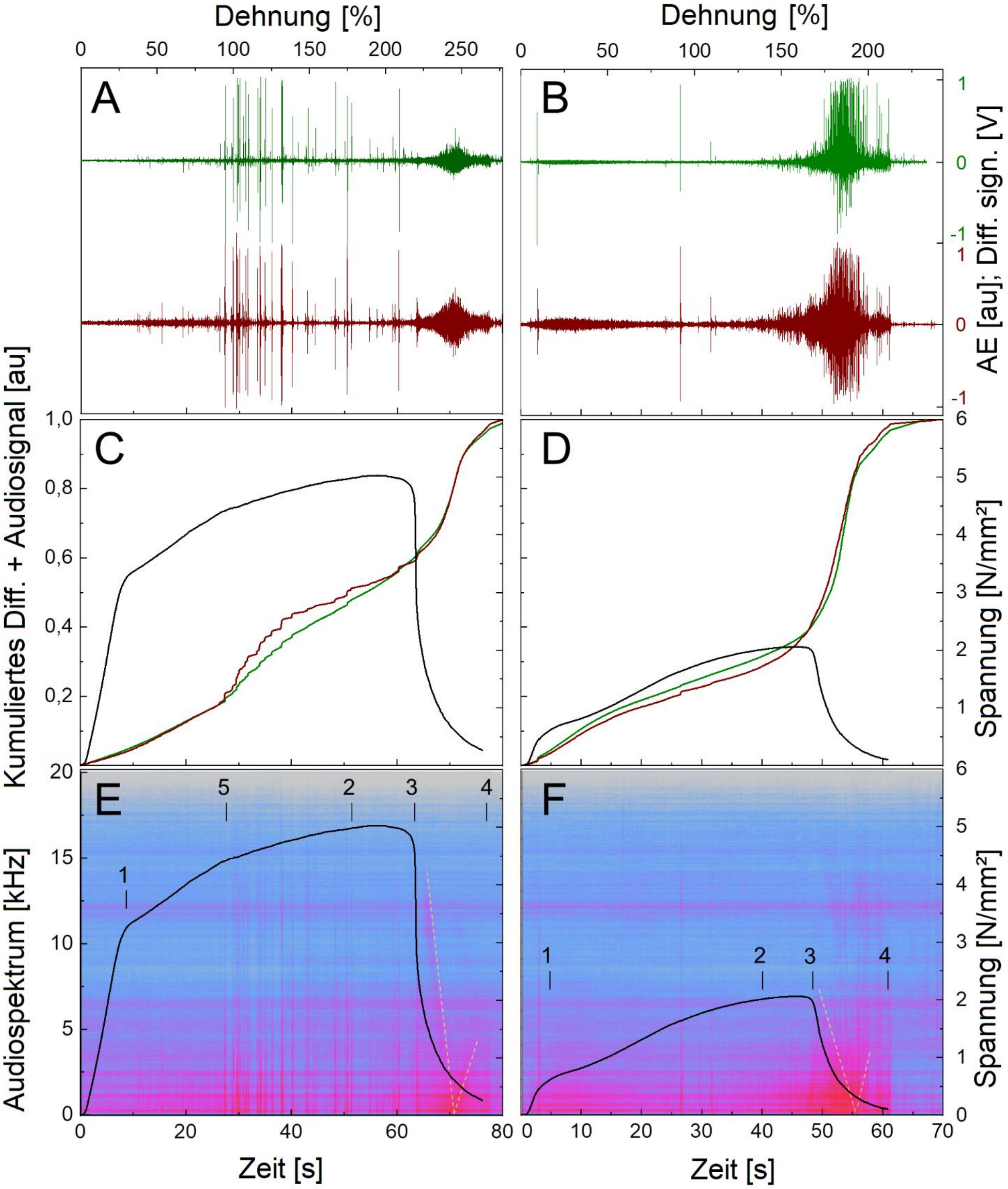

Abb. 11: AE-Signal und Zugkurven für Vlies M (links) und Vlies L (rechts) bei 25 mm/min, A und B: Differenzsignal im Bereich ±1 V (grün) und Audiosignal normiert (dunkelrot), C und D: Spannungs-Dehnungs-Diagramme (schwarz) mit kumuliertem Differenzsignal (grün) und kumuliertem Audiosignal (dunkelrot). Auffallend ist ein Knick und unruhiger AE-Kurvenverlauf für Vlies M, während Vlies L einen glatten AE-Kurvenverlauf aufweist. E und F: Spannungs-Dehnungs-Diagramme (schwarz) und Audiospektrum von 0 Hz (unten) bis 20 kHz (oben) in linearer Skalierung, charakteristische Punkte: 1: Streckgrenze, 2: Abflachen der Zugkurve vor 3: Beginn des Versagens, 4: Maschine Stopp, 5: Beginn deutlicher akustischer Aktivität. Das hörbare Absinken und Wiederansteigen der Tonhöhe des Rauschens während des Versagens der Zugprobe ist durch gestrichelte Linien gekennzeichnet (orange).

Während des Versagens der Probe reißt ein großer Teil der Nanofasern, ein weiterer Teil wird durch Auseinanderziehen voneinander getrennt. In der Konsequenz müssen immer weniger verbliebene Fasern immer höheren Spannungen standhalten, d.h. deren Schwingungsfrequenz steigt kontinuierlich. Die Anregung der Schwingungen erfolgt dabei wahrscheinlich durch Impulsübertragung nach dem Reißen benachbarter Fasern. Somit ist ein fortschreitender Anstieg der mittleren Frequenz des Ultraschallrauschens erklärbar, das unterhalb der Oszillatorfrequenz beginnt (Differenzfrequenz groß), die Oszillatorfrequenz durchläuft (Differenzfrequenz gering) und schließlich über die Oszillatorfrequenz weiter ansteigt (Differenzfrequenz wieder groß). Dieses Phänomen liefert außerdem den indirekten Nachweis, dass die eingangs abgeschätzten Frequenzbereiche von einigen zehn Kilohertz (Punkt 6) sehr gut mit den experimentell gefundenen Effekten korrelieren. Die in allen Einzelproben nachgewiesene deutlich einsetzende akustische Aktivität von Vlies M im mittleren Bereich des Zugversuchs und der nahezu unauffälligen Zugkurve wird als „versteckter Defekt“ interpretiert. Für eine detailliertere Untersuchung ist der Zugversuch an bestimmten Punkten abgebrochen worden, siehe Abb. 12. Die teilweise gezogenen Proben wurden unter Restspannung auf der Zugprüfmaschine direkt in ringförmigen Halterungen fixiert und ohne Zeitverzug dem REM zugeführt. Somit sind morphologische Veränderungen durch die üblicherweise nachträgliche und spannungsfreie Probenaufbereitung verhindert. Nach Überschreiten der Streckgrenze erscheinen die Fasern zum Teil gespannt und weisen vereinzelte Bruchstellen auf. Im mittleren Bereich des Zugversuchs erscheinen die Fasern längsgerichtet, gestreckt und weisen mehrere Bruchstellen auf. Kurz vor dem vollständigen Reißen der Zugprobe ist noch ein Teil der Fasern gerichtet und gestreckt. Ein weiterer Teil liegt in gekräuselter Form und ungerichtet vor, dies entspricht gerissenen und/oder aus dem Verbund gelösten Faserfragmenten. Die Anteile der Zugkurven in Abb. 12 verlaufen glatt im Bereich um 25 s, und bestärken den Verdacht auf einen versteckten Defekt, zudem sind auch hier o.g. Auffälligkeiten im kumulierten Audiosignal deutlich erkennbar.

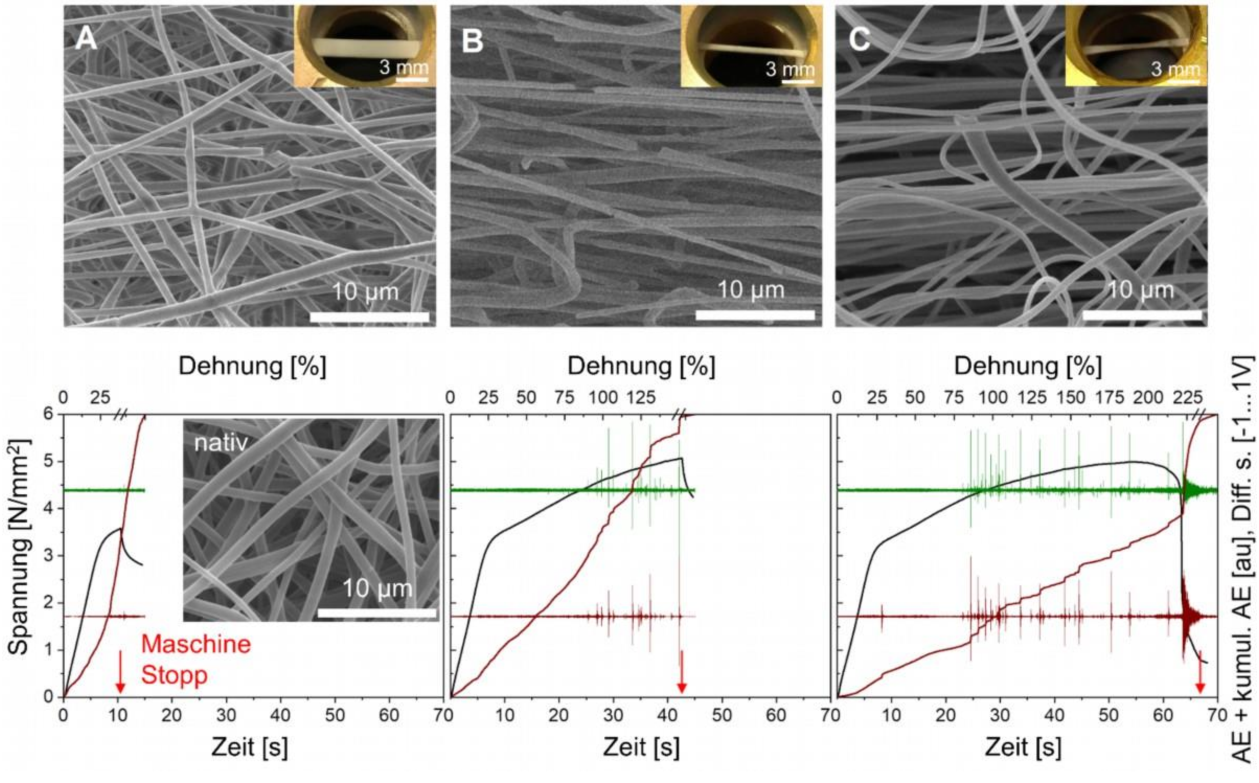

Abb. 12: Unterschiedlich gedehnte Proben von Vlies M mit 25 mm/min, der Zugversuch wurde an bestimmten Punkten abgebrochen. A: nach Überschreiten der Streckgrenze, B: nach Einsetzen starker AE-Aktivität im mittleren Bereich, C: kurz vor vollständigem Reißen der Zugprobe. Die obere Reihe zeigt repräsentative REM-Bilder und kleine Ansichten der Zugproben in den Halterungen. Die untere Reihe zeigt, neben einem REM-Bild der nativen Zugprobe, Kombinationsgrafiken aus Zugkurven (schwarz), Differenzsignalen (grün), sowie die normierten und kumulierten Audiosignale (dunkelrot). Der Zeitpunkt des Abbruchs ist jeweils durch einen roten Pfeil markiert.

Die in dieser Arbeit vorgestellte Methode zur Verarbeitung von Ultraschall-AE-Signalen nicht eingebetteter Nanofaservliese während der Zugprüfung erlaubt es, schwache Signale zu detektieren, in Echtzeit mitzuhören, akustische Rückkopplungen zu vermeiden und die meisten Hintergrundgeräusche auszuschließen, ohne das Zugexperiment zu beeinflussen. AE-Signale in direkter oder kumulativer Darstellung bieten wesentlich mehr Informationen, als die reinen Zugkurven liefern können. Die AE-Detektion kann versteckte Defekte aufspüren somit zur Qualitätskontrolle eingesetzt werden, zudem liefert die Methode indirekte Hinweise über die Stabilität des Vlies-Herstellungsprozesses.

4. Entwicklung und Prüfung nanofaserbasierter Venenklappenprothesen

4.1.Klappenprothesen zur Therapie der chronisch-venösen Insuffizienz

Das klinische Bild der chronisch-venösen Insuffizienz (CVI) ist gekennzeichnet durch Krampfadern (Varikosis), Schwellungen (Ödeme) und Hautveränderungen bis hin zu offenen Wunden (Ulcus cruris), die CVI gilt aufgrund der hohen Prävalenz als Volkskrankheit [80], siehe hierzu Abb. 13. Gängige Therapiemethoden sind nur begrenzt erfolgreich [81–84]. Es besteht ein ungedeckter klinischer Bedarf an neuen Therapiekonzepten hinsichtlich des Klappenersatzes als sog. „unmet medical need“ [85]. Am Markt ist keine Venenklappenprothese kommerziell verfügbar. Verschiedene Implantatkonzepte sind bereits in der klinischen Testphase [86–92]. Trotz des Erfordernisses nach technischer Standardisierung existiert keine allgemeingültige Richtschnur für die Entwicklung einer Venenklappenprothese [93–98]. Die Verwendung nanofaserbasierter Materialien für Venenklappenprothesen stellt hohe Anforderungen an eine definierte Qualität dieser Materialien. So spannt sich der Bogen zu Prüfungen komplett aufgebauter Implantat-Prototypen. Ein Material, dessen Performance bestimmbar und somit bekannt ist, kann zu einem sicheren Medizinprodukt weiterentwickelt werden. Als aussichtsreiche Biomaterialien für Venenklappenprothesen werden biostabile Polymere aus der Klasse der Polycarbonaturethane oder Polytetrafluorethylene [99–103], oder bioresorbierbare Polymere aus verschiedenen Stoffklassen [104–106] gesehen.

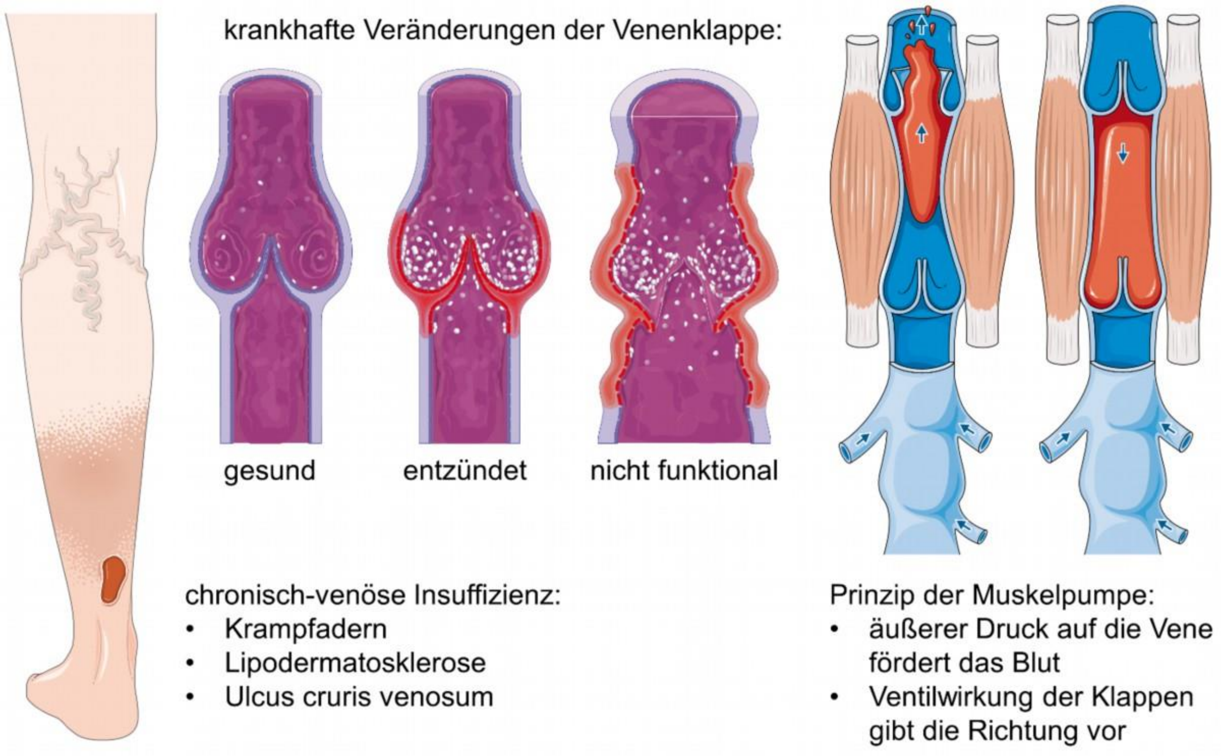

Abb. 13: Krankheitsbild der chronisch-venösen Insuffizienz, klinisches Bild, Venenklappen und Prinzip der Muskelpumpe (Bilder adaptiert von Servier Medical Art [107]).

4.2.Ausgangssituation für die eigene Implantatentwicklung

In vorangegangen Arbeiten, die nicht Bestandteil dieser Arbeit sind, wurde am Institut für Biomedizinische Technik der Universitätsmedizin Rostock eine nanofaservliesbasierte Venenklappenprothese entwickelt und bereits zum Patent angemeldet [108]. Dieses Design wird im Folgenden als „Version A“ bezeichnet. Die Klappe besteht aus einem Nitinol-Stent mit 14 mm Durchmesser, der in zwei Ringe aus rautenförmigen Zellen unterteilt ist und dazwischen die gebogenen Stützstreben für die Klappensegel trägt. Die Klappensegel bestehen aus TSPCU-Nanofaservlies, das auf speziellen Formkörpern in verschiedenen Größen elektrogesponnen wird [109,110]. Die vorliegende Arbeit befasst sich mit der Testung und Weiterentwicklung der Venenklappenprothese aus Nanofaservlies. Im Rahmen der Arbeit ist eine Neukonstruktion des Formkörpers erfolgt, der aus Aluminium gefräst werden kann und somit für den Herstellungsprozess der Nanofaservliesklappe per Elektrospinning eine wesentlich bessere Schichtabscheidung ermöglicht. Die zuvor verwendeten Formkörper wurden aus 3D-Printmaterial gefertigt und mit Gold besputtert, diese zeigten oft eine ungleichmäßige Vliesbeschichtung. Der Formkörper dient als Negativform für die Venenklappensegel und berücksichtigt eine Verlängerung, die zum Befestigen auf dem Stent benötigt wird. Des Weiteren sind mikroskopische Untersuchungen und mechanische Zugversuche von Nanofaservlies-Schweißverbindungen durchgeführt worden. In einer experimentellen Testreihe wurden die Grenzbereiche der Venenklappe Version A unter pulsatilen Bedingungen bei höheren Fluss- und Druckwerten untersucht und spezifische Defizite identifiziert. Bis zu einem Druck von 60 mmHg ist die Venenklappe Version A im Wesentlichen funktional. Bei einem Druck von 80 mmHg treten mehrere Defizite verstärkt in den Vordergrund und führen schließlich zum Versagen. In Abb. 14 sind wesentliche Defizite der Venenklappe Version A herausgestellt:

- Die Seitenflächen wölben sich bei der geschlossenen Klappe tief nach innen (in Abb. 14 A, D und G durch eine eingekreiste 1 gekennzeichnet). Bei geöffneter Klappe geht die Einwölbung nicht in die Ausgangslage zurück, sondern behält etwa die halbe Tiefe bei, was sich im rückwärtigen Kamerabild oben und unten zeigt. Die Einwölbung ist zwar nicht direkt am Öffnungsquerschnitt der Segelkanten beteiligt, ist vermutlich aber für einen Teil des Strömungswiderstands der Venenklappe Version A verantwortlich.
- Der Stent besteht aus zwei Rautenringen und den dazwischen befindlichen Stützstreben für die Klappensegel. Der Rautenring an der Stentbasis führt aufgrund wechselnder Krafteinleitung eine Schaukelbewegung aus, im Bild durch tangentiale Geraden und gekrümmte Pfeile unter Nummer 2 in Abb. 14 G und H gekennzeichnet. In Kombination mit unterschiedlich großen axialen Kräften bei geöffneter und geschlossener Klappe führt diese Schaukelbewegung zu einer Migration und einem langsamen Herauswandern der Klappe aus der Halterung. Auch ein zusätzlich eingebrachter Stützring hinter der Stentbasis (O-Ring, der 1 mm nach innen ragt) konnte das Herauswandern nicht verhindern (Abb. 14, I und J). Durch die Beweglichkeit des Rautenrings ist auch die Abdichtung zur Gefäßwand beeinträchtigt.
- Die Vorderkanten der Rauten werden zyklisch gegen die eingewölbten Seitenflächen gedrückt, im Bild durch kleine Kreise unter Nummer 3 (Abb. 14, G und H) gekennzeichnet. Die punktuelle Belastung würde über längere Zeit zur Abrasion, folglich Löchern und somit zum Ausfall der Klappe führen.
- Die Segel sind auf den Stützstreben nicht befestigt und rutschen bei jedem Schließvorgang etwas nach distal, besonders bei höheren Drücken. Beim Öffnungsvorgang werden die Segel wieder etwas nach proximal geschoben. Nach längerer Zeit überwiegt aber das Zurückrutschen, was nach Überschreiten etwa der mittleren Höhe unumkehrbar wird und zum Versagen der Venenklappe Version A führt (Abb. 14, I).

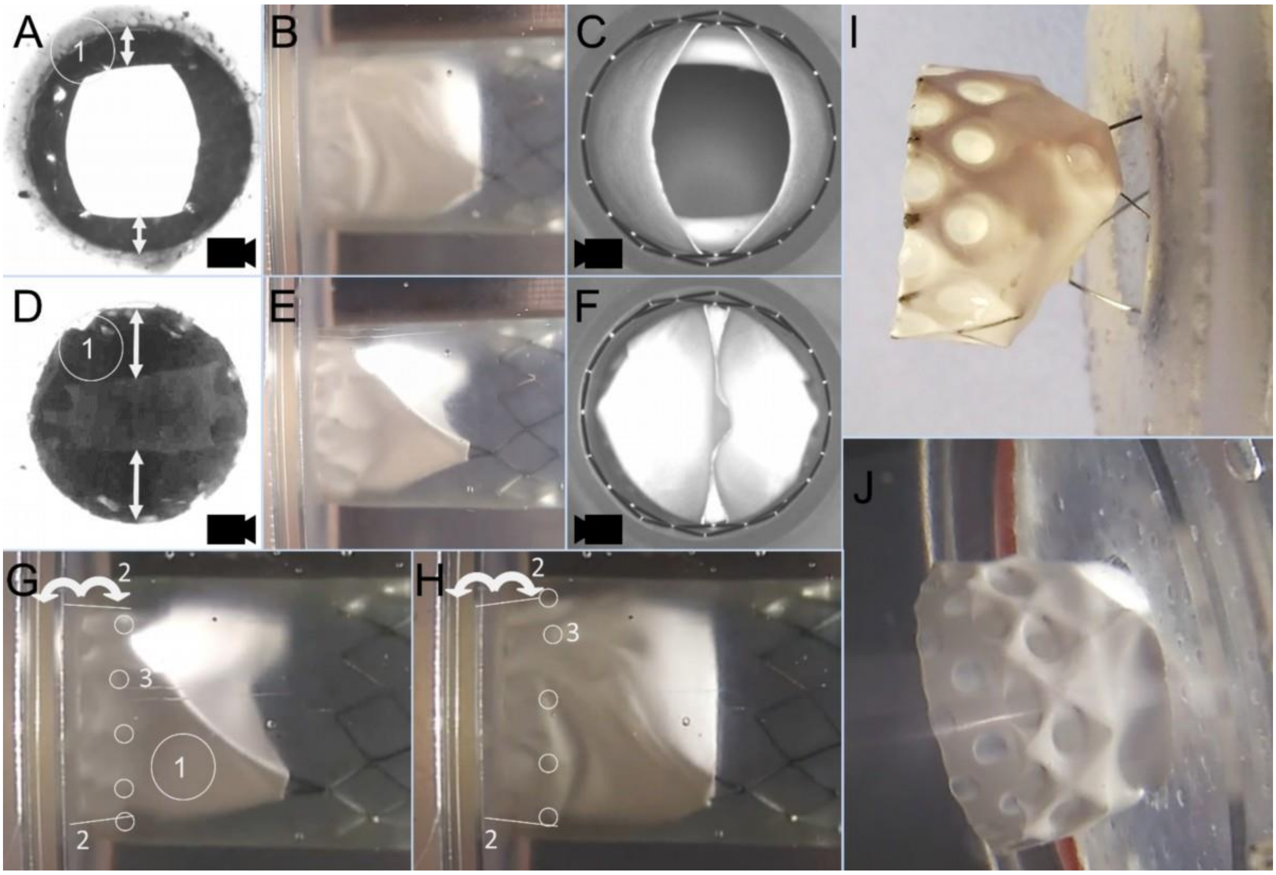

Abb. 14: Defizite der Venenklappe Version A unter pulsatiler Belastung bei 80 mmHg und 1,6 L/min, A, B und C: geöffnete Klappe aus rückwärtiger, seitlicher und vorderer Ansicht, Nummer 1 und die Pfeile kennzeichnen die Einwölbung der Seitenflächen, D, E und F: geschlossene Klappe aus rückwärtiger, seitlicher und vorderer Ansicht, Nummer 1 und die Pfeile kennzeichnen die Einwölbung der Seitenflächen, G und H: Kennzeichnung von Defiziten an geschlossener und geöffneter Klappe: 1 – Einwölbung der Seitenflächen, 2 – Tangenten an Rautenring und Pfeile zur Verdeutlichung der Schaukelbewegung, 3 – kreisförmige Markierung von punktuellen Belastungen an den Vorderkanten der Rauten, I: Klappe über zusätzlich eingebauten Stützring aus der Halterung gewandert mit dislozierten Segeln, J: aus Halterung migrierte Klappe in situ.

Die oben beschriebenen Defizite sind nicht in die ursprüngliche Designentwicklung eingeflossen, da diese zum Zeitpunkt nicht bekannt waren, oder deren Einfluss unterschätzt wurde. Dies unterstreicht die Bedeutung experimenteller Untersuchungen, die theoretische Erwartungen bestätigen, oder die Einflüsse bisher nicht berücksichtigter Aspekte aufdecken. Im beabsichtigten Implantationsgebiet im Bereich Becken-Oberschenkel werden bei einer stehenden Person venöse Druckwerte bis etwa 50 mmHg (in Kniehöhe etwa 60 mmHg) erwartet, die sich schwerkraftbedingt unterhalb der Herzhöhe einstellen. Die Klappe der Version A ist hier funktional, aber nah am Grenzbereich. Einer Anwendung von Version A als Implantat stehen die gefundenen Defizite im Wege. Deshalb sind in dieser Arbeit unter Berücksichtigung der Defizite Änderungen des Designs von Stent und Segel vorgenommen worden. Die modifizierte Variante wird im Folgenden als „Version B“ bezeichnet. Die in Version B umgesetzten Modifikationen basieren auf theoretischen Überlegungen. Ob die erwarteten Verbesserungen erreicht werden, kann nur in experimentellen Laboruntersuchungen aufgeklärt werden. Klappen von Versionen A und B sind unter stationären und pulsatilen Bedingungen charakterisiert worden, womit sich die eigene Publikation 4 befasst [Pub 4].

4.3. Umsetzung von Designmodifikationen

Basierend auf den experimentell ermittelten und oben ausgeführten Defiziten von Version A wurde nach Designanpassungen gesucht. Im Rahmen dieser Arbeit wurde die modifizierte Version B entwickelt, welche sich durch folgende Überlegungen und Modifikationen auszeichnet:

- Die Rautenringe bestehen aus jeweils drei Rautenreihen statt einer. Hintergrund der Überlegung ist das Verhindern der Schaukelbewegung. Drei Reihen werden hierfür als Mindestzahl gesehen, mit mehr als fünf Rautenreihen wäre das Implantat zu lang.
- Die Seitenflächen sind aus drei Gründen mit Rauten gefüllt:
    1. Das Einwölben der Seitenflächen wird verhindert.
    2. Die Segel werden durch Schweißpunkte an ihrer Position gehalten und können nicht dislozieren.
    3. Die Abdichtung zur Gefäßwand wird verbessert.
- Bei Version A laufen die Stützstreben beidseits zu je einer Spitze mit je einem Verbindungspunkt zum oberen Rautenring. Bei einer Längsbiegung des Implantats oder unsymmetrischen Lastverteilung auf den Stützstreben werden diese Verbindungspunkte zu Drehpunkten, bzw. die Stützstreben werden ungleichmäßig verbogen, das Implantat kann dadurch verkippen. Im stationären Test ist Version A zwischen 60 und 80 mmHg verkippt. In Version B werden daher gerade Doppelstege eingesetzt, der Stent erhält dadurch mehr Stabilität, ein Verkippen wird wirksam verhindert. Zudem werden die Segel in Neutralstellung in einer leicht geöffneten Position gehalten.
- Die Segel von Version B bilden im maximal geöffneten Zustand eine zylindrische Form mit dem Durchmesser des Stents bzw. Gefäßes. Dies bietet drei Vorteile:
    1. Die theoretisch maximale Öffnungsfläche entspricht dem vollen Querschnitt des Stents und stellt somit den geringstmöglichen Strömungswiderstand dar.
    2. Zur Herstellung der Klappe/Segel aus Nanofaservlies wird weder ein spezieller Formkörper benötigt, noch sind diffizile Arbeitsschritte zu dessen Übertragung auf den Stent erforderlich. Die Klappe kann direkt auf den Stent elektrogesponnen werden.
    3. Schlauchförmige Klappen passenden Durchmessers aus anderen Quellen, die nicht direkt auf den Stent elektrogesponnen werden (z.B. biogenes Gewebe oder extrahiertes Material, Folienmaterial, Gewebe od. Gestricke aus künstlichen Materialen, etc.), lassen sich auf den Stent der Version B aufziehen und befestigen.

Die beiden Klappenversionen sind vergleichend in Abb. 15 dargestellt. Die Stents werden per Femtosekunden-Laser (StarCut Tube system, Coherent Corp., USA) aus Nitinolrohr von 5 mm Durchmesser geschnitten (Euroflex GmbH, Deutschland), in einem mehrstufigen Glühprozess aufgeweitet, und von einem externen Partner (CORTRONIK GmbH, Deutschland) poliert. Nitinol ist eine spezielle Legierung, die ein temperaturabhängiges Formgedächtnis (Memory Effekt) und Superelastizität aufweist [111]. Die hier verwendete Legierung hat eine Transformationstemperatur bei etwa Zimmertemperatur, darunter ist das Material plastisch verformbar, darüber wird die im Glühprozess eingeprägte Form angenommen. Für Version A werden Formkörper aus Aluminium gefräst und elektrobesponnen, das so erzeugte Cover aus Nanofaservlies abgenommen, auf den Stent übertragen und anschließend thermisch verschweißt [112]. Das Nanofaservlies wird bei Version B direkt auf dem Stent per Elektrospinning erzeugt und im Nachgang ebenso thermisch verschweißt. Die in Wasser gelagerten (vorkonditionierten) Klappen werden in 0 °C Eiswasser von Hand gecrimpt, in 3D-gedruckte Halterungen implantiert und in experimentellen Testreihen untersucht. In gleicher Weise erfolgt der Wechsel einer Klappe zwischen verschiedenen Halterungen auch unter Eiswasser.

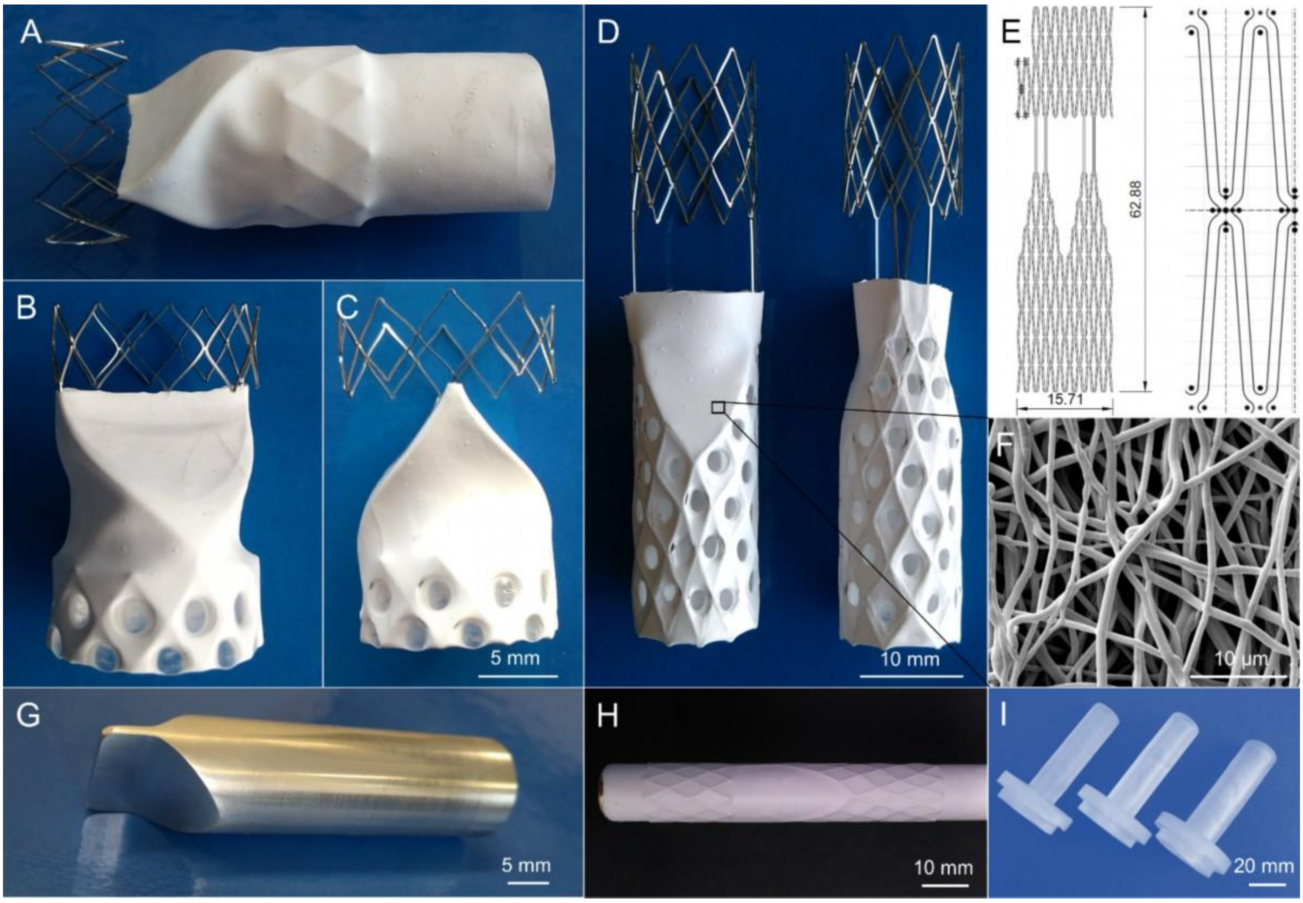

Abb. 15: Klappenversionen, A: Version A Stent mit übergezogener elektrogesponnener Hülle (Cover), der überstehende Anteil wird zur Befestigung nach innen gestülpt. B und C: fertig aufgebaute Klappe von Version A in Vorder- und Seitenansicht, D: fertig aufgebaute Klappe von Version B in Vorder- und Seitenansicht, E: Stent von Version B in Gesamtansicht als Abwicklung und ein Basiselement in Detailansicht, F: REM-Bild des TSPCU-Nanofaservlieses, G: Formkörper zum Elektrospinning für Version A aus Aluminium, H: elektrogesponnenes Nanofaservlies auf einem Stent von Version B, der auf einem Metallzylinder steckt, I: 3D-gedruckte Halterungen.

4.4. Hydromechanische Untersuchung unter stationären und pulsatilen Bedingungen

Für die akuten experimentellen Untersuchungen sind Klappen beider Versionen in verschiedenen Größen von Halterungen kombiniert worden, wobei sich die Gefäßdurchmesser an Literatur orientieren [113–117], einen Überblick über die getesteten Konstellationen bietet Tab. 3.

Tab. 3: Testkonstellationen, Kürzel bezeichnen die Klappenversion, den Stentdurchmesser und das Übermaß (Oversizing) in Millimetern hinter dem Bindestrich, das prozentuale Übermaß ist in Klammern angegeben.

Klappen-version	**Stent Durchmesser**	**Kürzel mit Stentdurchmesser und Oversizing (O.S) bezogen auf den Durchmesser der Halterung ($Ø_{Halterung}$)**					
		Ø10 mm	O.S	**Ø11 mm**	O.S	**Ø12 mm**	O.S
A	Ø14 mm	X		X		**A14-17**	2 (17%)
B	Ø12 mm	**B12-20**	2 (20%)	**B12-9**	1 (9%)	X	
B	Ø13 mm	X		**B13-18**	2 (18%)	**B13-8**	1 (8%)

Die Eigenschaften der Klappen sind unter akuten stationären und pulsatilen Bedingungen untersucht worden, siehe hierzu Abb. 16. Die stationären Tests sollen modellhaft die Bedingungen für eine aufrechtstehende bzw. liegende Person nachempfinden. Der physiologische Schweredruck auf eine geschlossene Venenklappe im Bereich Becken-Oberschenkel wird mit 30 – 50 mmHg angenommen, falls keine kompetente Klappe weiter proximal existiert. In diesem Druckbereich müssen die Klappen mit einer gewissen Sicherheitsreserve für diese Implantationsorte funktional sein. Kurzzeitig können zwar höhere Druckwerte auftreten, beispielsweise beim Hüpfen, Husten oder Niesen, diese spielen aber für die eigentliche Klappenfunktion eine untergeordnete Rolle [118–121]. Bei einer liegenden Person befinden sich die Klappen etwa auf Herzhöhe, ein Rückfluss kommt nicht vor. Die Klappen müssen in diesem Betriebszustand leicht zu öffnen sein, um dem Vorwärtsfluss nur einen geringen Widerstand entgegen zu setzen [93,122,123].

Die pulsatilen Tests sollen modellhaft die Bedingungen für eine gehende Person bei Aktivität der Muskelpumpe nachbilden. Hierzu wurden, basierend auf Literaturdaten, drei Szenarien zum Nachstellen verschiedener körperlicher Belastung entworfen [113,123–129]: langsames Gehen/geringe Belastung (0.5 L/min mit 40 bpm), zügiges Gehen/moderate Belastung (1 L/min mit 60 bpm), und Eile oder Treppensteigen/hohe Belastung (2 L/min mit 80 bpm).

Für stationäre Messungen wird der Schweredruck verschiedener Wassersäulen genutzt. Die pulsatile Druckerzeugung erfolgt über die gesteuerte Bewegung einer Kolbenpumpe und einen einstellbaren Flusswiderstand. Um eventuelle Trends in den Eigenschaften oder Schwächen der Klappen zu entdecken, wird in beiden Verfahren mit 140 mmHg bis weit über den normalen Betriebsdruck von 50 mmHg getestet (Abb. 16).

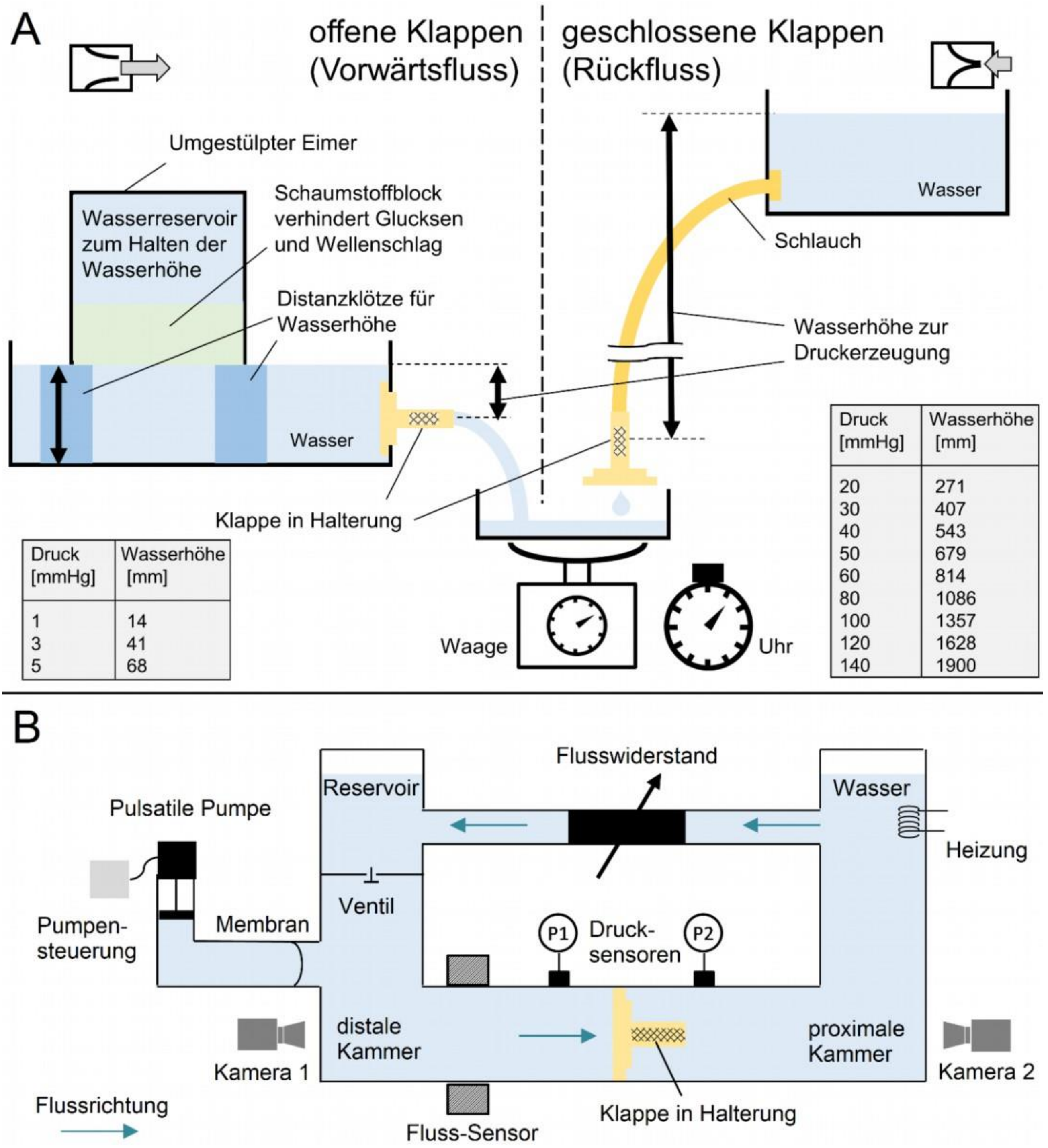

Druck [mmHg]	Wasserhöhe [mm]
1	14
3	41
5	68

Druck [mmHg]	Wasserhöhe [mm]
20	271
30	407
40	543
50	679
60	814
80	1086
100	1357
120	1628
140	1900

Abb. 16: Experimenteller Laboraufbau schematisch, A: Stationäre Messung, Bestimmung der Wassermasse pro Zeit, Wasserdruck wird per Schwerkraft erzeugt, die verwendeten Druckwerte und Wasserhöhen sind im Bild angegeben. B: Pulsatile Messung, Bestimmung von Druck- und Flusswerten in Abhängigkeit der Zeit, zusätzliche Aufzeichnung von Videosequenzen.

Vergleichende stationäre Testreihen haben ein differenziertes Bild ergeben, siehe hierzu Abb. 17. Im Vorwärtsfluss wurden die leeren Halterungen ohne Klappen mituntersucht (im Bild schwarz und grau gekennzeichnet). Die Konstellation A14-17 erlaubt knapp ein Drittel des maximalen Durchflusses, während die B-Klappen etwa zwei Drittel des maximal möglichen Durchflusses erreichen. Die Vorwärtsflüsse von Version A sind etwa halb so groß wie bei den Versionen B. Die Versuche zeigen auch, dass der Vorwärtsfluss mit abnehmendem Übermaß für die gleiche Klappe zunimmt, was durch die größere Öffnungsfläche erklärbar ist.

Klappen sollen einen Öffnungsdruck unter 5 mmHg aufweisen [123], bei diesem Druck erreicht selbst A14-17 fast 2 L/min. In Rückflussrichtung ist A14-17 zwischen 60 und 80 mmHg verkippt, was auch in pulsatilen Vorstudien in anderen Halterungen aufgetreten ist. Bis 60 bzw. 80 mmHg zeigen die B-Versionen (außer B13-8) einen etwa konstanten Rückfluss und bei höheren Drücken einen druckproportionalen Anstieg der Rückflussrate. B13-8 zeigt einen etwa linearen Anstieg zum Druck, was vermutlich aufgrund unzureichender Abdichtung die untere Grenze des Übermaßes darstellt. Im pulsatilen Betrieb hat B13-8 erhöhte Leckvolumina gezeigt, die diese Vermutung stützen. Prinzipiell sind die getesteten Konstellationen (außer B13-8) im stationären Betrieb bis mindestens 60 mmHg funktional und bieten somit eine gewisse Sicherheitsreserve.

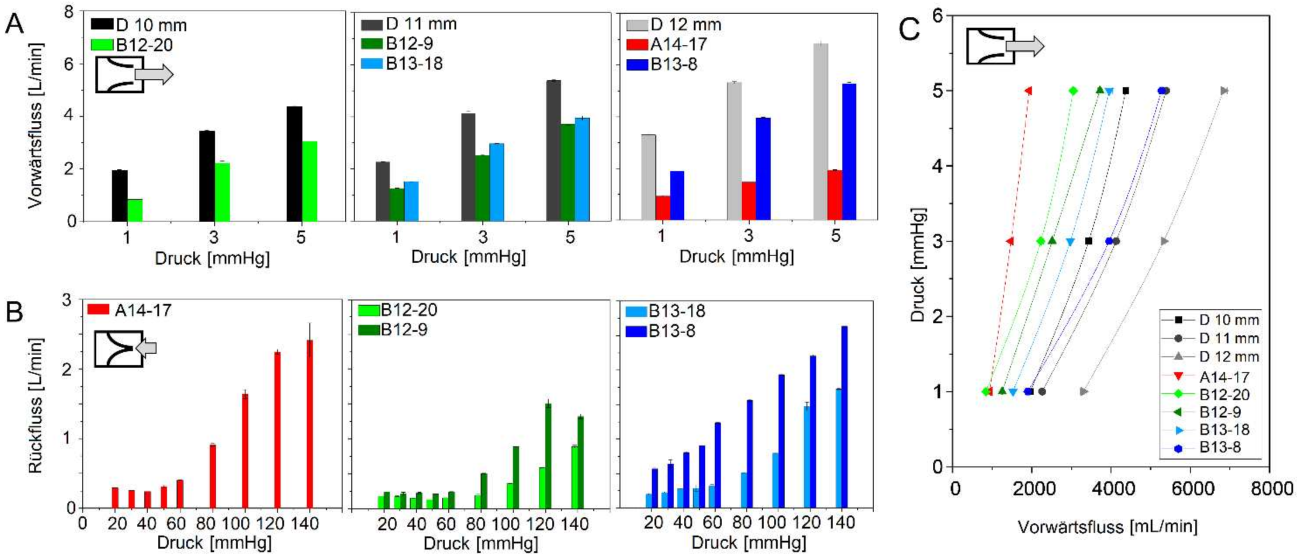

Abb. 17: Ergebnisse stationärer Tests, A: geöffnete Klappen im Vorwärtsfluss in Halterungen mit Innendurchmessern von 10 mm (links), 11 mm (Mitte) und 12 mm (rechts), in den Farben: schwarz/grau: leere Halterung ohne Klappe, rot: Version A 14 mm Stentdurchmesser, grün: Version B 12 mm Stentdurchmesser, blau: Version B 13 mm Stentdurchmesser. B: geschlossene Klappen in Rückflussrichtung, Version A 14 mm Stentdurchmesser (links), die Klappe ist zwischen 60 und 80 mmHg verkippt (Fotos als Einschub), Version B 12 mm Stentdurchmesser (Mitte), Version B 13 mm Stentdurchmesser (rechts). C: Druck-Fluss-Charakteristiken aller getesteten Konstellationen im Vergleich, alle Grafiken: jeweils n = 3 Messungen.

In Abb. 18 sind repräsentative Ergebnisse für A14-17 (A) und B12-9 (B) bei simulierter moderater Belastung gezeigt, sowie ausgewählte Ergebnisse aller Konstellationen im Vergleich (C – E). Die Druck- und Flusskurven präsentieren den zeitlichen Verlauf während eines Zyklus, die Fotos zeigen den Zustand der Klappensegel zu ausgewählten Zeitpunkten. Die gestrichelten senkrechten Linien (Cursor) markieren spezifische Punkte im Zyklus, wie im Bild bezeichnet.

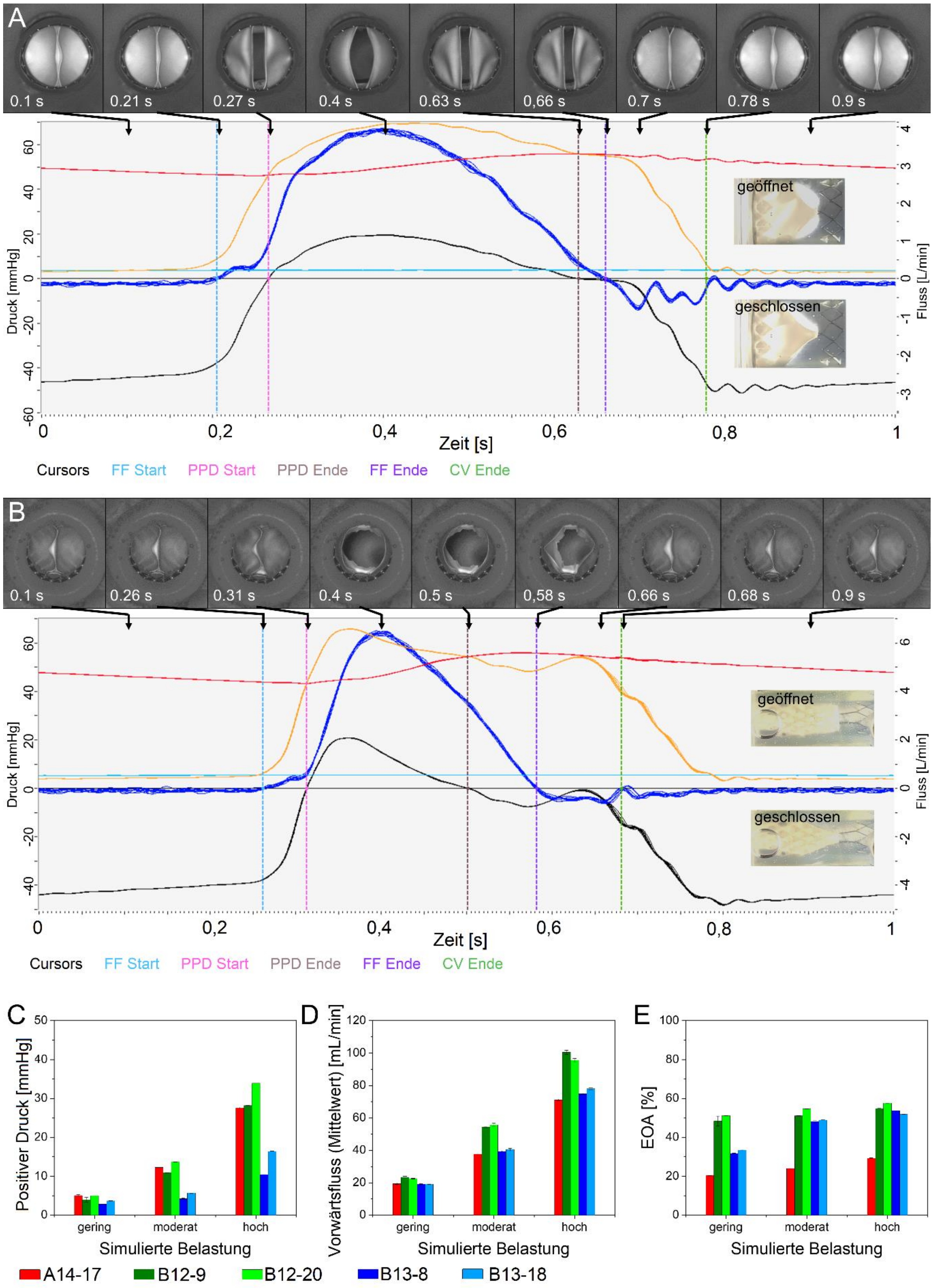

Abb. 18: Ergebnisse pulsatiler Tests, A: A14-17 bei simulierter moderater Belastung, Kurven (n = 10): Rot - Druck hinter der Klappe, Gelb - Druck vor der Klappe, Schwarz - Differenzdruck, Dunkelblau - Fluss, Hellblau - Vordruck am Wasserreservoir, Cursors: FF – Start bzw. Ende Vorwärtsfluss, PPD - Start bzw. Ende positive Druckdifferenz, CV – Ende Schließvolumen, Bilder: von der vorderen Inline-Kamera zu den angegebenen Zeitpunkten und Fotos in Seitenansicht im offenen und geschlossenen Zustand, B: B12-9 analog zu A, C: mittlerer positiver Druck für alle getesteten Konstellationen und simulierten Belastungen, D: mittlerer Vorwärtsfluss für alle getesteten Konstellationen und simulierten Belastungen, E: effektive Öffnungsflächen für alle getesteten Konstellationen und simulierten Belastungen, normiert auf die Querschnitte der Halterungen.

Die Klappe A14-17 öffnet nach 0,21 s, erreicht den maximalen Vorwärtsfluss von etwa 3,5 L/min nach 0,4 s, schließt bei 0,7 s und zeigt ein Nachschwingen bis etwa 0,8 s. Die EOA wird mit 24 % angegeben. B12-9 öffnet nach 0,26 s, erreicht den maximalen Vorwärtsfluss von etwa 6,5 L/min nach ebenfalls 0,4 s und schließt bei 0,66 s, ein Nachschwingen ist nicht beobachtbar. Die EOA wird mit 51 % angegeben. Der Vorwärtsfluss benötigt 0,32 s bei B12-9, wohingegen diese Phase bei A14-17 mit 0,45 s etwa 40% länger andauert, was sich mit der geringeren EOA erklären lässt. Da bei etwa gleicher Wassermenge und halber EOA die Vorwärtsflussphase aber nicht die doppelte Zeit dauert, muss bei A14-17 die mittlere Strömungsgeschwindigkeit höher sein.

Bei A14 und B13 wurde ein ähnlicher mittlerer Vorwärtsfluss beobachtet, allerdings mit dem halben Differenzdruck (PPD) für B13, d.h. B13 hat einen geringeren Flusswiderstand. Der mittlere Vorwärtsfluss von B12 ist erkennbar höher als von A14 und B13, die etwa gleiche Werte zeigen. Aufgrund ähnlicher Differenzdrücke (PPD) von A14 und B12 deutet der höhere Vorwärtsfluss auf einen geringeren Flusswiderstand von B12 hin. Die Erklärung für diese Beobachtungen ist in der EOA zu finden, die bei A14 am niedrigsten ist (20 - 30 %). Bei B12 lag die EOA bei 50 - 60 % und stieg mit der simulierten Belastung leicht an. Die EOA der Version A ist etwa die Hälfte von Version B12 und B13 bei moderater und hoher simulierter Belastung. Bei geringer Belastung öffnet B13 nur zum Teil, was einer Öffnungsreserve für höhere Belastungen gleichkommt. Wird die Norm für Herzklappen (DIN EN ISO 5840) [130] als Richtschnur betrachtet, gelten im pulsatilen Betrieb Rückflussraten von 20 % als akzeptabel. Bei stimulierter moderater Belastung und 50 mmHg zeigt A14-17 einen Rückfluss von 10,2%, und B12-9 einen Rückfluss von 9,7% des Vorwärtsflusses. Im Vergleich der stationären zu den pulsatilen Tests bei 50 mmHg hat A14-17 etwa den dreifachen Rückfluss und B12-9 den doppelten Rückfluss gezeigt. Der Öffnungsdruck wurde für beide mit 0,2 mmHg quantifiziert und liegt deutlich unter den in der Literatur genannten 5 mmHg [123]. Die Schließdrücke sind mit -4,9 mmHg für A14-17 und -4,7 mmHg für B12-9 ähnlich, die Klappen beider Versionen öffnen und schließen unterhalb von 5 mmHg. Ohne Druck sind die Klappen beider Versionen leicht geöffnet und ermöglichen einen langsamen Fluss ohne nennenswerten Widerstand, beispielsweise bei einer horizontal liegenden Person. Beide Klappenversionen scheinen unter physiologischen Bedingungen anwendbar zu sein, wobei aber Version A bereits nahe an den Grenzen arbeitet (Flusswiderstand, EOA, Stabilität) und aufgrund der oben beschriebenen Defizite als Implantat ausscheidet. Version B bietet noch Reserven (Flusswiderstand, EOA), hat keine strukturellen oder dynamischen Schwachpunkte (z.B. Verkippen, Schaukelbewegungen) aufgewiesen und hat pulsatil ein nahezu konstantes Betriebsverhalten im gesamten getesteten Druckbereich bis 140 mmHg offenbart (siehe dazu die Supporting Information der eigenen Publikation 4 [Pub 4]).

5. Zusammenfassung und Ausblick

Das Ziel dieser Arbeit ist die Weiterentwicklung eines Venenklappenimplantats über die Etablierung neuer Charakterisierungsmethoden der Eigenschaften von Nanofaservliesmaterialien auf verschiedenen Größenskalen, insbesondere der Erweiterung des wissenschaftlichen Methodenspektrums auf Nano- und Mikro-Skala, bis hin zur Modifikation und Testung einer innovativen Implantat-Plattform auf Makro-Skala. Die in dieser Arbeit vorgestellten Charakterisierungsmethoden für Nanofaservliesmaterialien sind dabei nicht zwingend auf den Bereich der Medizintechnik beschränkt und können für ähnliche Fragestellungen auf andere technisch-wissenschaftliche Gebiete erweitert werden.

In dieser Arbeit wird ein Verfahren (GIFT) zur computergestützten Bestimmung des Nanofaserdurchmessers in REM-Bildern vorgestellt, welches eigenständig und vollkommen neu entwickelt wurde und jetzt als fertige, weltweit frei verfügbare Software zur Verfügung steht. GIFT zeigt sich etablierter Software vergleichbar leistungsfähig und teilweise überlegen.
GIFT kann nicht nur für die Bestimmung von Faserdurchmessern in REM-Bildern verwendet werden. Weitere Anwendungsgebiete werden in der eigenen Publikation 1 erwähnt [Pub 1], hierzu sind ggf. Anpassungen der Bildvorverarbeitung notwendig [131–145]. Auch für eigene Studien im Bereich der Medizintechnik kann GIFT für andere Anwendungen weiterentwickelt werden. GIFT kann beispielsweise als indirekte Methode zur Bestimmung von Beschichtungsdicken genutzt werden, indem Bilder von Mikrostrukturen vor und nach der Beschichtung verglichen werden (z.B. Fasern werden durch den Schichtauftrag dicker, od. Öffnungen kleiner).

Bisher standen kaum Verfahren zur Verfügung, Informationen zum mechanischen Versagensverhalten von Nanofaservliesen auf Faserebene zu gewinnen. In dieser Arbeit wird ein Weg eröffnet, die akustische Emission (AE) bei Zugbelastung zu detektieren, in Echtzeit mitzuhören, und Analysen der aufgezeichneten Signale vorzunehmen. Dem Nanofaservlies inhärente Material- bzw. Herstellungsfehler, die üblichen Untersuchungsmethoden verborgen bleiben, können hiermit nachgewiesen werden. Die Untersuchung von Interaktionen im Faserverbund unter mechanischer Belastung bildet die Brücke hin zur Anwendung eines makroskopischen Nanofaservlieses als Implantat.
Eine Weiterentwicklung der Methode könnte durch Verwendung von breitbandigen Mikrofonen realisiert werden, wobei dann verstärkt auf die Abschirmung von Umgebungsgeräuschen zu achten ist. Je nach Frequenzband ist folglich ein Mithören in Echtzeit aufgrund von Rückkopplungseffekten eventuell nicht möglich. Weiteres Potential bietet die Verwendung von zwei oder mehr Sensoren, aus Unterschieden in Laufzeit und Intensität lässt sich die Richtung und Entfernung einer Schallquelle bestimmen. Möglicherweise lassen sich kommerzielle Schallkameras für den Einsatz an Zugprüfmaschinen adaptieren oder speziell auf die Anforderungen von Nanofasermaterialen designen [146]. Eine AE-Detektion unter Wasser ist ebenfalls interessant für im Körper mechanisch beanspruchte Implantate. Beispielsweise beim Aufweiten eines mit Nanofaservlies umhüllten Stents (Covered Stent) sind AE zu erwarten, die sich aus der Verformung des Stents und den oben beschriebenen AE (Rauschen, Knistern) aus dem Nanofaservlies zusammensetzen. Hierzu wurden keine wissenschaftlichen Studien gefunden. AE Signale sind komplex hinsichtlich Herkunft, Ausbreitung, Dämpfung und Dispersion [147], eine Signalanalyse mit KI-Hilfe sollte bei zukünftigen Entwicklungen berücksichtigt werden. Mechanisch versagende Materialien (auch Nanofaservliese) erzeugen neben AE auch elektromagnetische Emissionen (EME) [148], es wurden initiale Experimente zu deren Nachweis durchgeführt, aber vorerst nicht weiterverfolgt.

Die Anwendung von Nanofaservliesen als Segelmaterial für Venenklappenimplantate, die im Patienten komplexen Einsatzbedingungen unterliegen, erfordert umfängliche Testreihen, um das Zusammenspiel von Nanofaservlies, Stent und Gefäß zu untersuchen. Die durchgeführten experimentellen Untersuchungen

helfen, Schwachpunkte zu identifizieren und entsprechende Designmodifikationen vorzunehmen. In dieser Arbeit werden Designmodifikationen an einer Venenklappenprothese vorgestellt, die sich auf experimentell gefundenen Defiziten eines bereits vorhanden gewesenen Vorgängermodells begründen. Am modifizierten Design sind die genannten Defizite nicht beobachtet worden.
Die Ergebnisse der akuten stationären und pulsatilen Testreihen bestätigen Auswirkungen der Designmodifikationen auf die Performance von Version B. Weiterführende Studien sollten zum einen die Langzeitstabilität bzw. Dauerhaltbarkeit sowie Crimpbarkeit und zum anderen verschiedene Materialstudien (z.B. Polymere, Kombimaterialien, Segeldicke, Vliese, Folien) ins Auge fassen. Erfolgversprechende Kombinationen können dann in Kooperation mit klinischen Partnern für einen Tierversuch vorgesehen werden.

Die Neuentwicklung von Untersuchungsmethoden, von der Charakterisierung einzelner Nanofasern, über die Beschreibung des Versagensverhaltens im Nanofaserverbund bis hin zu Designmodifikationen und experimentellen Testreihen an nanofaserbasierten Materialien und Prototypen bilden einen methodischen Rahmen mit hoher Relevanz für biomedizinische Implantatanwendungen und darüber hinaus auch für den Einsatz von Nanofasertechnologien außerhalb der Medizintechnik.

Literaturverzeichnis

[Pub 1] A. Götz, V. Senz, W. Schmidt, J. Huling, N. Grabow, S. Illner, General image fiber tool: A concept for automated evaluation of fiber diameters in SEM images, Measurement 177 (2021) 109265. https://doi.org/10.1016/j.measurement.2021.109265.

[Pub 2] J. Huling, A. Götz, N. Grabow, S. Illner, GIFT: An ImageJ macro for automated fiber diameter quantification, PLOS ONE 17 (2022) e0275528. https://doi.org/10.1371/journal.pone.0275528.

[Pub 3] A. Götz, V. Senz, W. Schmidt, D. Koper, N. Grabow, S. Illner, Detection of acoustic emission from nanofiber nonwovens under tensile strain – An ultrasonic test setup for critical medical device components, Journal of the Mechanical Behavior of Biomedical Materials 140 (2023) 105720. https://doi.org/10.1016/j.jmbbm.2023.105720.

[Pub 4] A. Götz, S. Illner, N. Fiedler, J. Schubert, J. Oldenburg, H. Müller, W. Schmidt, K.-P. Schmitz, N. Grabow, K. Lebahn, Transcatheter bicuspid venous valve prostheses: fluid mechanical performance testing of artificial nonwoven leaflets, Biomed. Eng. Online 23 (2024) 124. https://doi.org/10.1186/s12938-024-01316-x.

[1] L.É. Uhljar, R. Ambrus, Electrospinning of Potential Medical Devices (Wound Dressings, Tissue Engineering Scaffolds, Face Masks) and Their Regulatory Approach, Pharmaceutics 15 (2023). https://doi.org/10.3390/pharmaceutics15020417.

[2] S. Omer, L. Forgách, R. Zelkó, I. Sebe, Scale-up of Electrospinning: Market Overview of Products and Devices for Pharmaceutical and Biomedical Purposes, Pharmaceutics 13 (2021). https://doi.org/10.3390/pharmaceutics13020286.

[3] D.I. Braghirolli, D. Steffens, P. Pranke, Electrospinning for regenerative medicine: a review of the main topics, Drug Discovery Today 19 (2014) 743–753. https://doi.org/10.1016/j.drudis.2014.03.024.

[4] J.R. Dias, P.L. Granja, P.J. Bártolo, Advances in electrospun skin substitutes, Progress in Materials Science 84 (2016) 314–334. https://doi.org/10.1016/j.pmatsci.2016.09.006.

[5] J. Fernández-Pérez, K.E. Kador, A.P. Lynch, M. Ahearne, Characterization of extracellular matrix modified poly(ε-caprolactone) electrospun scaffolds with differing fiber orientations for corneal stroma regeneration, Mater. Sci. Eng. C Mater. Biol. Appl. 108 (2020) 110415. https://doi.org/10.1016/j.msec.2019.110415.

[6] A.J. Hassiba, M.E. El Zowalaty, G.K. Nasrallah, T.J. Webster, A.S. Luyt, A.M. Abdullah, A.A. Elzatahry, Review of recent research on biomedical applications of electrospun polymer nanofibers for improved wound healing, Nanomedicine (Lond) 11 (2016) 715–737. https://doi.org/10.2217/nnm.15.211.

[7] N.H.A. Ngadiman, M.Y. Noordin, A. Idris, D. Kurniawan, A review of evolution of electrospun tissue engineering scaffold: From two dimensions to three dimensions, Proc. Inst. Mech. Eng. H 231 (2017) 597–616. https://doi.org/10.1177/0954411917699021.

[8] F. Topuz, T. Uyar, Electrospinning of gelatin with tunable fiber morphology from round to flat/ribbon, Mater. Sci. Eng. C Mater. Biol. Appl. 80 (2017) 371–378. https://doi.org/10.1016/j.msec.2017.06.001.

[9] J. Xue, T. Wu, Y. Dai, Y. Xia, Electrospinning and Electrospun Nanofibers: Methods, Materials, and Applications, Chem. Rev. 119 (2019) 5298–5415. https://doi.org/10.1021/acs.chemrev.8b00593.

[10] Y. Li, J. Zhu, H. Cheng, G. Li, H. Cho, M. Jiang, Q. Gao, X. Zhang, 2021. Developments of Advanced Electrospinning Techniques: A Critical Review. Adv Materials Technologies 6, 2100410. https://doi.org/10.1002/admt.202100410.

[11] A. Luraghi, F. Peri, L. Moroni, Electrospinning for drug delivery applications: A review, J. Control. Release 334 (2021) 463–484. https://doi.org/10.1016/j.jconrel.2021.03.033.

[12] V.S. Naragund, P.K. Panda, Electrospun nanofiber-based respiratory face masks-a review, emergent mater. 5 (2022) 261–278. https://doi.org/10.1007/s42247-022-00350-6.

[13] A.S. Badami, M.R. Kreke, M.S. Thompson, J.S. Riffle, A.S. Goldstein, Effect of fiber diameter on spreading, proliferation, and differentiation of osteoblastic cells on electrospun poly(lactic acid) substrates, Biomaterials 27 (2006) 596–606. https://doi.org/10.1016/j.biomaterials.2005.05.084.

[14] T. Okuda, K. Tominaga, S. Kidoaki, Time-programmed dual release formulation by multilayered drug-loaded nanofiber meshes, J. Control. Release 143 (2010) 258–264. https://doi.org/10.1016/j.jconrel.2009.12.029.

[15] N. Narayanan, C. Jiang, C. Wang, G. Uzunalli, N. Whittern, Da Chen, O.G. Jones, S. Kuang, M. Deng, Harnessing Fiber Diameter-Dependent Effects of Myoblasts Toward Biomimetic Scaffold-Based Skeletal Muscle Regeneration, Front. Bioeng. Biotechnol. 8 (2020) 203. https://doi.org/10.3389/fbioe.2020.00203.

[16] G.T. Christopherson, H. Song, H.-Q. Mao, The influence of fiber diameter of electrospun substrates on neural stem cell differentiation and proliferation, Biomaterials 30 (2009) 556–564. https://doi.org/10.1016/j.biomaterials.2008.10.004.

[17] A.L. Yarin, S. Koombhongse, D.H. Reneker, Taylor cone and jetting from liquid droplets in electrospinning of nanofibers, J. Appl. Phys. 90 (2001) 4836–4846. https://doi.org/10.1063/1.1408260.

[18] K. Lin, K.-N. Chua, G.T. Christopherson, S. Lim, H.-Q. Mao, Reducing electrospun nanofiber diameter and variability using cationic amphiphiles, Polymer 48 (2007) 6384–6394. https://doi.org/10.1016/j.polymer.2007.08.056.

[19] X. Yan, M. Gevelber, Investigation of electrospun fiber diameter distribution and process variations, Journal of Electrostatics 68 (2010) 458–464. https://doi.org/10.1016/j.elstat.2010.06.009.

[20] A. Haider, S. Haider, I.-K. Kang, A comprehensive review summarizing the effect of electrospinning parameters and potential applications of nanofibers in biomedical and biotechnology, Arabian Journal of Chemistry 11 (2018) 1165–1188. https://doi.org/10.1016/j.arabjc.2015.11.015.

[21] R. Girwidz, Didactics of physics, 2021. https://www.didaktikonline.physik.uni-muenchen.de/programme/e_feld/E_Feld_leifi.html# (accessed 11 August 2024).

[22] S.V. Langwald, A. Ehrmann, L. Sabantina, Measuring Physical Properties of Electrospun Nanofiber Mats for Different Biomedical Applications, Membranes (Basel) 13 (2023) 488. https://doi.org/10.3390/membranes13050488.

[23] N.A. Hotaling, J. Jeon, M.B. Wade, D. Luong, X.-L. Palmer, K. Bharti, C.G. Simon, Training to Improve Precision and Accuracy in the Measurement of Fiber Morphology, PLoS ONE 11 (2016) e0167664. https://doi.org/10.1371/journal.pone.0167664.

[24] N.A. Hotaling, K. Bharti, H. Kriel, C.G. Simon, Dataset for the validation and use of DiameterJ an open source nanofiber diameter measurement tool, Data Brief 5 (2015) 13–22. https://doi.org/10.1016/j.dib.2015.07.012.

[25] N.A. Hotaling, K. Bharti, H. Kriel, C.G. Simon, DiameterJ: A validated open source nanofiber diameter measurement tool, in: pp. 327–338.

[26] L. Garcia, S. Soliman, M.P. Francis, M.J. Yaszemski, J. Doshi, C.G. Simon, R. Robinson-Zeigler, Workshop on the characterization of fiber-based scaffolds: Challenges, progress, and future directions, J. Biomed. Mater. Res. Part B Appl. Biomater. 108 (2020) 2063–2072. https://doi.org/10.1002/jbm.b.34545.

[27] Radical Scientific Equipments Pvt. Ltd., Fiber Pro, 2021. https://www.radicalindia.com/material-fiber.php (accessed 18 January 2021).

[28] Media Cybernetics, Fiber Thickness App, 2021. https://www.mediacy.com/support/imagepro/appcenter/fiber-thickness-detail (accessed 18 January 2021).

[29] Thermo Fisher Scientific Inc, Phenom FiberMetric Software: Better, faster fiber analysis. PRODUCT SPECIFICATIONS, 2019. https://www.thermofisher.com/de/de/home/electron-microscopy/products/software-em-3d-vis/fibermetric-software.html (accessed 7 August 2024).

[30] Sympatec GmbH, PAQXOS, 2021. https://www.sympatec.com/en/particle-measurement/application-software/paqxos/ (accessed 18 January 2021).

[31] S. Baheti, M. Tunak, Characterization of fiber diameter using image analysis, IOP Conf. Ser.: Mater. Sci. Eng. 254 (2017) 142002. https://doi.org/10.1088/1757-899X/254/14/142002.

[32] B. Pourdeyhimi, R. Dent, Measuring Fiber Diameter Distribution in Nonwovens, Textile Research Journal 69 (1999) 233–236. https://doi.org/10.1177/004051759906900401.

[33] M. Ziabari, V. Mottaghitalab, A.K. Haghi, Application of direct tracking method for measuring electrospun nanofiber diameter, Braz. J. Chem. Eng. 26 (2009) 53–62. https://doi.org/10.1590/S0104-66322009000100006.

[34] M. Ziabari, V. Mottaghitalab, A.K. Haghi, Distance transform algorithm for measuring nanofiber diameter, Korean J. Chem. Eng. 25 (2008) 905–918. https://doi.org/10.1007/s11814-008-0149-4.

[35] M. Ziabari, V. Mottaghitalab, S.T. McGovern, A.K. Haghi, A New Image Analysis Based Method for Measuring Electrospun Nanofiber Diameter, Nanoscale Res Lett 2 (2007) 597–600. https://doi.org/10.1007/s11671-007-9093-1.

[36] E. Tomba, P. Facco, M. Roso, M. Modesti, F. Bezzo, M. Barolo, Artificial Vision System for the Automatic Measurement of Interfiber Pore Characteristics and Fiber Diameter Distribution in Nanofiber Assemblies, Ind. Eng. Chem. Res. 49 (2010) 2957–2968. https://doi.org/10.1021/ie901179m.

[37] L. Zhang, W. Yu, Orientation image analysis of electrospun submicro-fibers based on Hough transform and Regionprops function, Textile Research Journal 87 (2017) 2263–2274. https://doi.org/10.1177/0040517516669070.

[38] A. Götz, V. Senz, S. Illner, N. Grabow, Computed fiber evaluation of SEM images using DiameterJ: Capabilities and limitations, Current Directions in Biomedical Engineering 6 (2020). https://doi.org/10.1515/cdbme-2020-3113.

[39] J.J. Stanger, N. Tucker, N. Buunk, Y.B. Truong, A comparison of automated and manual techniques for measurement of electrospun fibre diameter, Polymer Testing 40 (2014) 4–12. https://doi.org/10.1016/j.polymertesting.2014.08.002.

[40] X.M. Zhang, R.W. Wang, H.B. Wu, B. Xu, Automated measurements of fiber diameters in melt-blown nonwovens, Journal of Industrial Textiles 43 (2014) 593–605. https://doi.org/10.1177/1528083712471696.

[41] N.J. Schaub, S.J. Kirkpatrick, R.J. Gilbert, Automated Methods to Determine Electrospun Fiber Alignment and Diameter Using the Radon Transform, BioNanoSci. 3 (2013) 329–342. https://doi.org/10.1007/s12668-013-0100-y.

[42] E. Öznergiz, Y.E. Kiyak, M.E. Kamasak, I. Yildirim, Automated Nanofiber Diameter Measurement in SEM Images Using a Robust Image Analysis Method, Journal of Nanomaterials 2014 (2014) 1–6. https://doi.org/10.1155/2014/738490.

[43] D. RanjanNayak, S. Kumar Sahu, J. Mohammed, A Cellular Automata based Optimal Edge Detection Technique using Twenty-Five Neighborhood Model, IJCA 84 (2013) 27–33. https://doi.org/10.5120/14614-2869.

[44] M. Hasanzadeh Mofrad, S. Sadeghi, A. Rezvanian, M.R. Meybodi, Cellular edge detection: Combining cellular automata and cellular learning automata, AEU - International Journal of Electronics and Communications 69 (2015) 1282–1290. https://doi.org/10.1016/j.aeue.2015.05.010.

[45] I. Usov, R. Mezzenga, FiberApp: An Open-Source Software for Tracking and Analyzing Polymers, Filaments, Biomacromolecules, and Fibrous Objects, Macromolecules 48 (2015) 1269–1280. https://doi.org/10.1021/ma502264c.

[46] A. Boudaoud, A. Burian, D. Borowska-Wykręt, M. Uyttewaal, R. Wrzalik, D. Kwiatkowska, O. Hamant, FibrilTool, an ImageJ plug-in to quantify fibrillar structures in raw microscopy images, Nat. Protoc. 9 (2014) 457–463. https://doi.org/10.1038/nprot.2014.024.

[47] F.e.V. SKZ, FiVer, 2021. https://www.skz.de/de/forschung/geschaeftsfelder/spritzgiessen-neu/dienstleistungen/7313.Faserlaengenverteilung.html (accessed 18 January 2021).

[48] E.E. Morrill, A.N. Tulepbergenov, C.J. Stender, R. Lamichhane, R.J. Brown, T.J. Lujan, A validated software application to measure fiber organization in soft tissue, Biomech. Model. Mechanobiol. 15 (2016) 1467–1478. https://doi.org/10.1007/s10237-016-0776-3.

[49] E.H. Shin, K.S. Cho, M.H. Seo, H. Kim, Determination of electrospun fiber diameter distributions using image analysis processing, Macromol. Res. 16 (2008) 314–319. https://doi.org/10.1007/BF03218523.

[50] P.C. Reyes-Fernandez, B. Periou, X. Decrouy, F. Relaix, F.J. Authier, Automated image-analysis method for the quantification of fiber morphometry and fiber type population in human skeletal muscle, Skelet. Muscle 9 (2019) 15. https://doi.org/10.1186/s13395-019-0200-7.

[51] J.P. Chiverton, A. Kao, M. Roldo, G. Tozzi, Automatic diameter and orientation distribution determination of fibrous materials in micro X-ray CT imaging data, J. Microsc. 272 (2018) 180–195. https://doi.org/10.1111/jmi.12719.

[52] J.D. Eekhoff, S.P. Lake, Three-dimensional computation of fibre orientation, diameter and branching in segmented image stacks of fibrous networks, J. R. Soc. Interface 17 (2020) 20200371. https://doi.org/10.1098/rsif.2020.0371.

[53] A. Youssef, A. Hrynevich, L. Fladeland, A. Balles, J. Groll, P.D. Dalton, S. Zabler, The Impact of Melt Electrowritten Scaffold Design on Porosity Determined by X-Ray Microtomography, Tissue Eng. Part C Methods 25 (2019) 367–379. https://doi.org/10.1089/ten.TEC.2018.0373.

[54] T. Blachowicz, A. Ehrmann, Investigating surface properties of fibers and yarns by image processing and statistical analysis techniques, in: Applications of Computer Vision in Fashion and Textiles, WOODHEAD, 2017, pp. 105–121.

[55] R. Murphy, A. Turcott, L. Banuelos, E. Dowey, B. Goodwin, K.O. Cardinal, SIMPoly: A Matlab-Based Image Analysis Tool to Measure Electrospun Polymer Scaffold Fiber Diameter, Tissue Eng. Part C Methods 26 (2020) 628–636. https://doi.org/10.1089/ten.TEC.2020.0304.

[56] T. Ferreira, W. Rasband, ImageJ User Guide: ImageJ/Fiji 1.46, 2012, p. 107.

[57] K.R. Castleman, Digital image processing, Prentice Hall, Upper Saddle River, NJ, 1996.

[58] P. Karas, V. Morard, J. Bartovský, T. Grandpierre, E. Dokládalová, P. Matula, P. Dokládal, GPU implementation of linear morphological openings with arbitrary angle, J Real-Time Image Proc 10 (2015) 27–41. https://doi.org/10.1007/s11554-012-0248-7.

[59] P. Soille, E.J. Breen, R. Jones, Recursive implementation of erosions and dilations along discrete lines at arbitrary angles, IEEE Trans. Pattern Anal. Machine Intell. 18 (1996) 562–567. https://doi.org/10.1109/34.494646.

[60] P. Soille, Morphological Image Analysis, Springer Berlin Heidelberg, Berlin, Heidelberg, 1999.

[61] G. Bourier, Statistik-Übungen: Beschreibende Statistik – Wahrscheinlichkeitsrechnung – Schließende Statistik, eighth. Auflage, Springer Gabler, Wiesbaden, 2024.

[62] C.A. Schneider, W.S. Rasband, K.W. Eliceiri, NIH Image to ImageJ: 25 years of image analysis, Nat. Methods 9 (2012) 671–675. https://doi.org/10.1038/nmeth.2089.

[63] C.T. Rueden, J. Schindelin, M.C. Hiner, B.E. DeZonia, A.E. Walter, E.T. Arena, K.W. Eliceiri, ImageJ2: ImageJ for the next generation of scientific image data, BMC Bioinformatics 18 (2017) 529. https://doi.org/10.1186/s12859-017-1934-z.

[64] J. Schindelin, I. Arganda-Carreras, E. Frise, V. Kaynig, M. Longair, T. Pietzsch, S. Preibisch, C. Rueden, S. Saalfeld, B. Schmid, J.-Y. Tinevez, D.J. White, V. Hartenstein, K. Eliceiri, P. Tomancak, A. Cardona, Fiji: an open-source platform for biological-image analysis, Nat. Methods 9 (2012) 676–682. https://doi.org/10.1038/nmeth.2019.

[65] DIN Deutsches Institut für Normung e. V., DIN EN ISO 9073-3, Vliesstoffe – Prüfverfahren – Teil 3: Bestimmung der Höchstzugkraft und der Höchstzugkraftdehnung (ISO 9073-3:2023): Deutsche Fassung EN ISO 9073-3:2023, Beuth Verlag GmbH.

[66] DIN Deutsches Institut für Normung e. V., DIN EN ISO 527-2: Kunststoffe – Bestimmung der Zugeigenschaften –Teil 2: Prüfbedingungen für Form- und Extrusionsmassen (ISO 527-2:2012) Deutsche Fassung EN ISO 527-2:2012;, Beuth Verlag GmbH, 10772 Berlin ICS 83.080.01, 2012.

[67] W. Demtröder, Elektrizität und Optik, seventh., korrigierte und erweiterte Auflage, Springer, Berlin, 2017.

[68] ZwickRoell GmbH & Co. KG, ZHN/SEM - Nanoindenter für Rasterelektronenmikroskope: Produktinformation, 2022. https://www.zwickroell.com/de/produkte/haertepruefmaschinen/instrumentierte-eindringpruefung/zhn/sem/#c5701 (accessed 7 August 2024).

[69] Bruker Corporation, 40 Manning Road, Billerica, MA 01821, Nanomechanical Instruments for SEM/TEM, 2025. https://www.bruker.com/en/products-and-solutions/test-and-measurement/nanomechanical-instruments-for-sem-tem.html.

[70] Á. Carrasco, F. Méndez, F. Leaman, C. Molina Vicuña, Short Review of the Use of Acoustic Emissions for Detection and Monitoring of Cracks, Acoust Aust 49 (2021) 273–280. https://doi.org/10.1007/s40857-021-00219-4.

[71] N. Ghadarah, D. Ayre, A Review on Acoustic Emission Testing for Structural Health Monitoring of Polymer-Based Composites, Sensors 23 (2023) 6945. https://doi.org/10.3390/s23156945.

[72] W. Zhou, Z. Pan, J. Wang, S. Qiao, L. Ma, J. Liu, X. Ren, Y. Liang, Review on acoustic emission source location, damage recognition and lifetime prediction of fiber-reinforced composites, J Mater Sci 58 (2023) 583–607. https://doi.org/10.1007/s10853-022-08063-1.

[73] Rupert Wimmer, Holz hören: Holzgeräusche - Was erzählen Sie uns?, Zuschnitt Zeitschrift über Holz als Werkstoff und Werke in Holz proHolz Austria, Jahrgang 14, 2014. https://www.proholz.at/publikationen/zuschnitt-56 (accessed 19 December 2024).

[74] Günter Meier, Holz im Altbergbau: 6. Altbergbau-Kolloquium, 09. bis 11. November 2006, Aachen/Alsdorf, VGE Verl. Glückauf, Essen, 2006.

[75] K. Tsuji, S.C. Müller, Physics and music: Essential connections and illuminating excursions, Corrected publication, Springer, Cham, Switzerland, 2022.

[76] M.R. Gorman, Modal AE analysis of fracture and failure in composite materials, and the quality and life of high pressure composite pressure vessels, Journal of Acoustic Emission 29 (2011).

[77] D.O. Harris, R.L. Bell, The measurement and significance of energy in acoustic-emission testing, Experimental Mechanics 17 (1977) 347–353. https://doi.org/10.1007/BF02326321.

[78] Murata Manufacturing Co., Ltd., MA40S4R, 2024. https://www.murata.com/en-eu/api/pdfdownloadapi?cate=cgsubUltrasonicSensors&partno=MA40S4R.

[79] Pico Technology Ltd., PicoScope 2204A. https://www.picotech.com/oscilloscope/2000/picoscope-2000-overview (accessed 12 December 2024).

[80] J.L. Beebe-Dimmer, J.R. Pfeifer, J.S. Engle, D. Schottenfeld, The Epidemiology of Chronic Venous Insufficiency and Varicose Veins, Annals of Epidemiology 15 (2005) 175–184. https://doi.org/10.1016/j.annepidem.2004.05.015.

[81] J. Azar, A. Rao, A. Oropallo, Chronic venous insufficiency: a comprehensive review of management, Journal of Wound Care (2022). https://doi.org/10.12968/jowc.2022.31.6.510.

[82] K. Gujja, T. Kayiti, C. Sanina, J.M. Wiley, Chronic Venous Insufficiency, in: G.D. Dangas, C. Di Mario, H. Thiele, P. Barlis (Eds.), Interventional Cardiology: Principles and Practice, thirdrd ed., John Wiley & Sons Incorporated, Newark, 2022, pp. 835–843.

[83] C. Recek, The hemodynamic paradox as a phenomenon triggering recurrent reflux in varicose vein disease, Int. J. Angiol. 21 (2012) 181–186. https://doi.org/10.1055/s-0032-1325168.

[84] C. Recek, Calf pump activity influencing venous hemodynamics in the lower extremity, Int. J. Angiol. 22 (2013) 23–30. https://doi.org/10.1055/s-0033-1334092.

[85] K. Zhang, G. Kumar, C. Skedgel, Towards a New Understanding of Unmet Medical Need, Appl. Health Econ. Health Policy 19 (2021) 785–788. https://doi.org/10.1007/s40258-021-00655-3.

[86] S. Cifuentes, J.H. Ulloa, T.E. Rasmussen, An Implantable Bioprosthetic Venous Valve to Establish Deep Vein Competence for Post-Thrombotic Syndrome, JAMA Surg 158 (2023) 316–317. https://doi.org/10.1001/jamasurg.2022.6362.

[87] J. Ulloa, S. Cifuentes, M. Glickman, E. Nieves, J. Velez, A New Transcatheter Device for Treatment of Venous Reflux in the Deep Venous System: Early Results of First-in-human Study, Journal of Vascular Surgery: Venous and Lymphatic Disorders 11 (2023) 469. https://doi.org/10.1016/j.jvsv.2022.12.060.

[88] J.H. Ulloa, S. Cifuentes, V. Figueroa, M. Glickman, Two-Year Results of a First-In-Human Study in Patients Surgically Implanted With a Bioprosthetic Venous Valve, the VenoValve in Patients With Severe Chronic Venous Insufficiency, Vasc. Endovascular Surg. 57 (2023) 547–554. https://doi.org/10.1177/15385744231155327.

[89] J.H. Ulloa, M. Glickman, One-Year First-in-Human Success for VenoValve in Treating Patients With Severe Deep Venous Insufficiency, Vasc. Endovascular Surg. 56 (2022) 277–283. https://doi.org/10.1177/15385744211073730.

[90] enVVeno Medical Corporation, Irvine, CA (2022) US20230363900A1, 2023.

[91] Innovein, Inc., San Carlos, CA US 2017/0056175 A1, 2016.

[92] Innovein, Inc., San Carlos, CA, SBIR Phase II: Venous Valve Prosthesis as a Cure for Chronic Venous Insufficiency, 2024. https://www.sbir.gov/sbirsearch/detail/1644629.

[93] J. D'Addario, M.R. Smeds, C. Wittgen, Surgical treatment of deep venous insufficiency and requirements for novel interventions, JVS-Vascular Insights 1 (2023) 100011. https://doi.org/10.1016/j.jvsvi.2023.100011.

[94] C. Zervides, A.D. Giannoukas, Historical overview of venous valve prostheses for the treatment of deep venous valve insufficiency, J. Endovasc. Ther. 19 (2012) 281–290. https://doi.org/10.1583/11-3594MR.1.

[95] C. Zervides, H. Mahdi, R.A. Staub, H. Jouni, Prosthetic venous valves: Short history and advancements from 2012 to 2020, Phlebology (2021). https://doi.org/10.1177/0268355520962451.

[96] N.M. Wilson, D.L. Rutt, N.L. Browse, Repair and replacement of deep vein valves in the treatment of venous insufficiency, Br. J. Surg. 78 (1991) 388–394. https://doi.org/10.1002/bjs.1800780404.

[97] G.J.d. Borst, F.L. Moll, Percutaneous Venous Valve Designs for Treatment of Deep Venous Insufficiency, Journal of Endovascular Therapy 19 (2012) 291–302. https://doi.org/10.1583/11-3766R.1.

[98] D. Boersma, A. Vink, F.L. Moll, G.J. de Borst, Proof-of-Concept Evaluation of the SailValve Self-Expanding Deep Venous Valve System in a Porcine Model, J. Endovasc. Ther. 24 (2017) 440–446. https://doi.org/10.1177/1526602817700120.

[99] Z. Liu, B. Liu, C. Li, Y. Xiao, H. Wei, J. Zhou, Z. Feng, Zwitterionic modification: A strategy to enhance the mechanical properties, lubricity and hemo- and biocompatibility of silicone poly(carbonate urethane urea), Reactive and Functional Polymers 203 (2024) 106007. https://doi.org/10.1016/j.reactfunctpolym.2024.106007.

[100] S. Wei, J. Wu, X. Gu, S. Shen, M. Ma, Y. Shi, H. He, Y. Zhu, S. Chen, X. Wang, Low protein adsorption and high cellular activity of PEG-based silicone polyurethane for artificial heart valves, Materials Today Communications 39 (2024) 109357. https://doi.org/10.1016/j.mtcomm.2024.109357.

[101] Y. Wang, Y. Fu, Q. Wang, D. Kong, Z. Wang, J. Liu, Recent advancements in polymeric heart valves: From basic research to clinical trials, Materials Today Bio 28 (2024) 101194. https://doi.org/10.1016/j.mtbio.2024.101194.

[102] D.K. Dempsey, C. Carranza, C.P. Chawla, P. Gray, J.H. Eoh, S. Stacy Cereceres, E.M. Cosgriff-Hernandez, Comparative analysis of in vitro oxidative degradation of poly(carbonate urethanes) for biostability screening, Journal of Biomedical Materials Research Part A 102 (2014) 3649–3665. https://doi.org/10.1002/jbm.a.35037.

[103] E.O. Bachtiar, O. Erol, M. Millrod, R. Tao, D.H. Gracias, L.H. Romer, S.H. Kang, 3D printing and characterization of a soft and biostable elastomer with high flexibility and strength for biomedical applications, J. Mech. Behav. Biomed. Mater. 104 (2020) 103649. https://doi.org/10.1016/j.jmbbm.2020.103649.

[104] Q. Zong, J. Liu, Y. Chen, Y. Kong, Y. Dang, Z. Wang, Prosthetic venous valves for chronic venous insufficiency: Advancements and future design directions, Medicine in Novel Technology and Devices 21 (2024) 100288. https://doi.org/10.1016/j.medntd.2024.100288.

[105] R.Y. Kannan, H.J. Salacinski, J. de Groot, I. Clatworthy, L. Bozec, M. Horton, P.E. Butler, A.M. Seifalian, The antithrombogenic potential of a polyhedral oligomeric silsesquioxane (POSS) nanocomposite, Biomacromolecules 7 (2006) 215–223. https://doi.org/10.1021/bm050590z.

[106] A.G. Kidane, G. Burriesci, M. Edirisinghe, H. Ghanbari, P. Bonhoeffer, A.M. Seifalian, A novel nanocomposite polymer for development of synthetic heart valve leaflets, Acta Biomaterialia 5 (2009) 2409–2417. https://doi.org/10.1016/j.actbio.2009.02.025.

[107] Servier Medical Art, Servier Medical Art: CC BY 4.0 licence, https://smart.servier.com/.

[108] M. Stiehm, W. Schmidt, N. Grabow, J. Keiler, M. Reumann, A. Wree, A. Hof, H. Müller, C. Momma, K.-P. Schmitz, C. Koop, J. Schubert, K. Lebahn, S. Illner, S. Kischkel, J. Ortelt (CORTRONIK GMBH, DE) US020230372103A1, 2021.

[109] J. Schubert, D. Arbeiter, A. Götz, K. Lebahn, W. Schmidt, N. Grabow, S. Illner, Investigations on physico-chemical properties of TSPCU nonwoven for application as prosthetic venous valve, CDBME 7 (2021) 613–616. https://doi.org/10.1515/cdbme-2021-2156.

[110] J. Schubert, K. Schümann, S. Kischkel, W. Schmidt, N. Grabow, M. Stiehm, S. Pfensig, K.-P. Schmitz, J. Keiler, A. Wree, Numerical simulation of the functionality of a stent structure for venous valve prostheses, CDBME 5 (2019) 477–479. https://doi.org/10.1515/cdbme-2019-0120.

[111] A. Wadood, Brief Overview on Nitinol as Biomaterial, Advances in Materials Science and Engineering 2016 (2016) 1–9. https://doi.org/10.1155/2016/4173138.

[112] C. Tautorat, K. Lebahn, S. Oschatz, D. Arbeiter, K.-P. Schmitz, N. Grabow, W. Schmidt, Thermal welding of polymeric biomaterials: Development of a novel device for temperature controlled local application, CDBME 7 (2021) 660–663. https://doi.org/10.1515/cdbme-2021-2168.

[113] S.E. Rittgers, M.T. Oberdier, S. Pottala, Physiologically-based testing system for the mechanical characterization of prosthetic vein valves, BioMed Eng OnLine 6 (2007) 1–12. https://doi.org/10.1186/1475-925X-6-29.

[114] A. Fronek, M.H. Criqui, J. Denenberg, R.D. Langer, Common femoral vein dimensions and hemodynamics including Valsalva response as a function of sex, age, and ethnicity in a population study, J. Vasc. Surg. 33 (2001) 1050–1056. https://doi.org/10.1067/mva.2001.113496.

[115] J. Keiler, R. Seidel, A. Wree, The femoral vein diameter and its correlation with sex, age and body mass index - An anatomical parameter with clinical relevance, Phlebology 34 (2019) 58–69. https://doi.org/10.1177/0268355518772746.

[116] J. Keiler, M. Schulze, H. Claassen, A. Wree, Human Femoral Vein Diameter and Topography of Valves and Tributaries: A Post Mortem Analysis, Clin. Anat. 31 (2018) 1065–1076. https://doi.org/10.1002/ca.23224.

[117] S.X. Salles-Cunha, S. Shuman, H.G. Beebe, Planning endovascular vein valve implantation: significance of vein size variability, J. Vasc. Surg. 37 (2003) 984–990. https://doi.org/10.1067/mva.2003.245.

[118] A. Iqbal, M. Haider, R.J. Stadlhuber, A. Karu, S. Corkill, C.J. Filipi, A study of intragastric and intravesicular pressure changes during rest, coughing, weight lifting, retching, and vomiting, Surg Endosc 22 (2008) 2571–2575. https://doi.org/10.1007/s00464-008-0080-0.

[119] W.S. Cobb, J.M. Burns, K.W. Kercher, B.D. Matthews, H. James Norton, B. Todd Heniford, Normal Intraabdominal Pressure in Healthy Adults, Journal of Surgical Research 129 (2005) 231–235. https://doi.org/10.1016/j.jss.2005.06.015.

[120] A. Schattner, The Wide-Ranging Spectrum of Cough-Induced Complications and Patient Harm, The American Journal of Medicine 133 (2020) 544–551. https://doi.org/10.1016/j.amjmed.2019.12.044.

[121] J.A. Smith, A. Aliverti, M. Quaranta, K. McGuinness, A. Kelsall, J. Earis, P.M. Calverley, Chest wall dynamics during voluntary and induced cough in healthy volunteers, J Physiol 590 (2012) 563–574. https://doi.org/10.1113/jphysiol.2011.213157.

[122] A. Fernández-Colino, S. Jockenhoevel, Advances in Engineering Venous Valves: The Pursuit of a Definite Solution for Chronic Venous Disease, Tissue Eng. Part B Rev. 27 (2021) 253–265. https://doi.org/10.1089/ten.TEB.2020.0131.

[123] R.D. Sathe, D.N. Ku, Flexible Prosthetic Vein Valve, Journal of Medical Devices 1 (2007) 105–112. https://doi.org/10.1115/1.2736393.

[124] P.B. Rudolphi, A. Recke, E.A. Langan, P. Hunold, B.K. Kahle, Are Sonographically Measured Vascular Haemodynamic Parameters Reproducible Using Magnetic Resonance Imaging?, Eur. J. Vasc. Endovasc. Surg. 52 (2016) 665–672. https://doi.org/10.1016/j.ejvs.2016.08.004.

[125] L. Jorfeldt, J. Wahren, Leg blood flow during exercise in man, Clin. Sci. 41 (1971) 459–473. https://doi.org/10.1042/cs0410459.

[126] M.E. Tschakovsky, N.R. Saunders, K.A. Webb, D.E. O'Donnell, Muscle blood-flow dynamics at exercise onset: do the limbs differ?, Med. Sci. Sports Exerc. 38 (2006) 1811–1818. https://doi.org/10.1249/01.mss.0000230341.86870.4f.

[127] M.J. MacDonald, J.K. Shoemaker, M.E. Tschakovsky, R.L. Hughson, Alveolar oxygen uptake and femoral artery blood flow dynamics in upright and supine leg exercise in humans, Journal of Applied Physiology. https://doi.org/10.1152/jappl.1998.85.5.1622.

[128] D.W. Koch, S.C. Newcomer, D.N. Proctor, Blood flow to exercising limbs varies with age, gender, and training status, Canadian journal of applied physiology = Revue canadienne de physiologie appliquee 30 (2005). https://doi.org/10.1139/h05-141.

[129] J.D. Posner, K.M. Gorman, H.S. Klein, A. Woldow, Exercise capacity in the elderly, The American Journal of Cardiology 57 (1986) C52-C58. https://doi.org/10.1016/0002-9149(86)91027-1.

[130] DIN EN ISO 5840, DIN EN ISO 5840: 2021-05, Herz- und Gefäßimplantate- Herzklappenprothesen- Teil 1, 2, 3, Beuth Verlag GmbH, Berlin, 2021.

[131] N. Narisetti, M. Henke, C. Seiler, R. Shi, A. Junker, T. Altmann, E. Gladilin, Semi-automated Root Image Analysis (saRIA), Sci. Rep. 9 (2019) 19674. https://doi.org/10.1038/s41598-019-55876-3.

[132] Z. Fan, J. Lu, C. Wei, H. Huang, X. Cai, X. Chen, A Hierarchical Image Matting Model for Blood Vessel Segmentation in Fundus Images, IEEE Trans. Image Process. (2018) 2367–2377. https://doi.org/10.1109/TIP.2018.2885495.

[133] C. Oettmeier, H.-G. Döbereiner, A lumped parameter model of endoplasm flow in Physarum polycephalum explains migration and polarization-induced asymmetry during the onset of locomotion, PLoS ONE 14 (2019) e0215622. https://doi.org/10.1371/journal.pone.0215622.

[134] A.E. Hall, L. Vitale, M.J. Kingsford, Planktonic larval duration, early growth, and the influence of dietary input on the otolith microstructure of Scolopsis bilineatus (Nemipteridae), Environ Biol Fish 102 (2019) 541–552. https://doi.org/10.1007/s10641-019-00852-z.

[135] S. Lechthaler, P. Colangeli, M. Gazzabin, T. Anfodillo, Axial anatomy of the leaf midrib provides new insights into the hydraulic architecture and cavitation patterns of Acer pseudoplatanus leaves, J. Exp. Bot. 70 (2019) 6195–6201. https://doi.org/10.1093/jxb/erz347.

[136] Z. Sun, T. Cui, Y. Zhu, W. Zhang, S. Shi, S. Tang, Z. Du, C. Liu, R. Cui, H. Chen, X. Guo, The mechanical principles behind the golden ratio distribution of veins in plant leaves, Sci. Rep. 8 (2018) 13859. https://doi.org/10.1038/s41598-018-31763-1.

[137] G. Bueno, O. Deniz, A. Pedraza, J. Ruiz-Santaquiteria, J. Salido, G. Cristóbal, M. Borrego-Ramos, S. Blanco, Automated Diatom Classification (Part A): Handcrafted Feature Approaches, Applied Sciences 7 (2017) 753. https://doi.org/10.3390/app7080753.

[138] S.J. Newman, B.C. Jayne, Crawling without wiggling: muscular mechanisms and kinematics of rectilinear locomotion in boa constrictors, J. Exp. Biol. 221 (2018). https://doi.org/10.1242/jeb.166199.

[139] E.J. Leonard, R.T. Pappalardo, A. Yin, Analysis of very-high-resolution Galileo images and implications for resurfacing mechanisms on Europa, Icarus 312 (2018) 100–120. https://doi.org/10.1016/j.icarus.2018.04.016.

[140] A. Mohan, S. Poobal, Crack detection using image processing: A critical review and analysis, Alexandria Engineering Journal 57 (2018) 787–798. https://doi.org/10.1016/j.aej.2017.01.020.

[141] V. Martínez-Martínez, M. del Alamo-Sanza, M. Menéndez-Miguélez, I. Nevares, Method to estimate the medullar rays angle in pieces of wood based on tree-ring structure: application to planks of Quercus petraea, Wood Sci Technol 52 (2018) 519–539. https://doi.org/10.1007/s00226-017-0979-5.

[142] C. McKenna Neuman, o. Bédard, A wind tunnel investigation of particle segregation, ripple formation and armouring within sand beds of systematically varied texture, Earth Surf. Process. Landforms 42 (2017) 749–762. https://doi.org/10.1002/esp.4019.

[143] M.G.A. Lapotre, R.C. Ewing, C.M. Weitz, K.W. Lewis, M.P. Lamb, B.L. Ehlmann, D.M. Rubin, Morphologic Diversity of Martian Ripples: Implications for Large-Ripple Formation, Geophys. Res. Lett. 45 (2018) 10,229-10,239. https://doi.org/10.1029/2018GL079029.

[144] N. Wang, W. Jiang, Y. Zhang, Misalignment measurement with dual-frequency moiré fringe in nanoimprint lithography, Opt. Express 28 (2020) 6755–6765. https://doi.org/10.1364/OE.382413.

[145] P. Drotár, J. Mekyska, I. Rektorová, L. Masarová, Z. Smékal, M. Faundez-Zanuy, Decision support framework for Parkinson's disease based on novel handwriting markers, IEEE Trans. Neural Syst. Rehabil. Eng. 23 (2015) 508–516. https://doi.org/10.1109/TNSRE.2014.2359997.

[146] Fluke Corporation, Präzisions-Schallkamera Fluke ii910, 2024. https://www.fluke.com/de-de/produkt/thermografie-in-der-industrie/prazisions-schallkamera-ii910 (accessed 18 August 2024).

[147] W. Demtröder, Mechanics and Thermodynamics, Springer, Cham, 2017.

[148] S.K. Sharma, V.S. Chauhan, M. Sinapius, A review on deformation-induced electromagnetic radiation detection: history and current status of the technique, J Mater Sci 56 (2021) 4500–4551. https://doi.org/10.1007/s10853-020-05538-x.

Abbildungsverzeichnis

Tabellenverzeichnis

Selbstständigkeitserklärung

Ich erkläre, dass ich die eingereichte Dissertation selbstständig und ohne fremde Hilfe verfasst, andere als die von mir angegebenen Quellen und Hilfsmittel nicht benutzt und die den benutzten Werken wörtlich oder inhaltlich entnommenen Stellen als solche kenntlich gemacht habe.

Des Weiteren erkläre ich, dass ich mich bisher noch keinem Promotionsverfahren unterzogen oder um eine Zulassung zu solchem beworben habe. Die eingereichte Schrift wurde an keiner anderen Hochschule vorgelegt.

Rostock, 3. Januar 2025

Andreas Götz

Verwendete Originalarbeiten zur kumulativen Dissertation und Erklärung über eigene Anteile an den Publikationen

Publikation 1

[Pub 1] **Andreas Götz**, Volkmar Senz, Wolfram Schmidt, Jennifer Huling, Niels Grabow, Sabine Illner
General image fiber tool: A concept for automated evaluation of fiber diameters in SEM images
Measurement 177 (2021) 109265
doi.org/10.1016/j.measurement.2021.109265
Eingereicht: 27. Oktober 2020
Veröffentlichung: 14. März 2021
IF = 5,131*

Eigene Anteile an der Publikation:

- Entwicklung der prinzipiellen Idee, Konzept für Realisierung per EDV,
- schrittweise Umsetzung mit Methoden der Bildverarbeitung und Datenanalyse,
- Verknüpfung der Einzelschritte zu automatisch ablaufenden Algorithmen,
- Validierung an speziell entwickelten Testbildern und Bildserien sowie „herausfordernden" REM-Bildern,
- Anwendung/Funktionstest an einer Vielzahl alltäglicher REM-Bilder und anderen Nicht-Faser-Bildern incl. begleitender Experimente und Bildvorverarbeitung,
- Ausführung von Messungen mit etablierter Software, Parameterstudien zur Analyse,
- Ergebnisvergleiche von GIFT mit etablierter Software,
- Recherche in der wissenschaftlichen Literatur,
- Manuskripterstellung,
- Erstellung von Grafiken und Bildern

Publikation 2

[Pub 2] Jennifer Huling, **Andreas Götz**, Niels Grabow, Sabine Illner
GIFT: An ImageJ macro for automated fiber diameter quantification
PLoS ONE 17(10)
doi.org/10.1371/journal.pone.0275528
Eingereicht: 21. Juli 2022
Veröffentlichung: 3. Oktober 2022
IF = 3,7*

Eigene Anteile an der Publikation:

- Entwicklung des Konzepts einer benutzerfreundlichen Software,
- Entwicklung von Teilkomponenten der Macros,
- umfangreiche Funktionstests an REM- und Testbildern,
- Manuskripterstellung

Publikation 3

[Pub 3] **Andreas Götz**, Volkmar Senz, Wolfram Schmidt, Daniela Koper, Niels Grabow, Sabine Illner
Detection of acoustic emission from nanofiber nonwovens under tensile strain – An ultrasonic test setup for critical medical device components
Journal of the mechanical behavior of biomedical materials 140 (2023) 105720
doi.org/10.1016/j.jmbbm.2023.105720
Eingereicht: 15. Juli 2022
Veröffentlichung: 9. Februar 2023
IF =3,3*

Eigene Anteile an der Publikation:

- Entwicklung der Idee zur Detektion eines schwachen nicht hörbaren Signals und dessen Umwandlung in ein hörbares Signal,
- Suche nach empfindlichem Sensor und dessen technische Modifikation,
- Experimentelle Vorarbeiten,
- Anfertigung eines kompakten Devices zur Platzierung auf der Zugprüfmaschine,
- Vorbereitung und Durchführung der Messungen,
- Aufbereitung und Analyse der Daten,
- Recherche in der wissenschaftlichen Literatur,
- Manuskripterstellung,
- Erstellung von Grafiken und Bildern

Publikation 4

[Pub 4] **Andreas Götz**, Sabine Illner, Nicklas Fiedler, Julia Schubert, Jan Oldenburg, Heinz Müller, Wolfram Schmidt, Klaus-Peter Schmitz, Niels Grabow, Kerstin Lebahn
Transcatheter bicuspid venous valve prostheses: fluid mechanical performance testing of artificial nonwoven leaflets
BioMedical Engineering OnLine (2024) 23:124
doi.org/10.1186/s12938-024-01316-x
Eingereicht: 12. Juli 2024
Veröffentlichung: 29. November 2024
IF = 2,9*

Eigene Anteile an der Publikation:

- Aufbau auf am IBMT bereits vorhandenem Venenklappenprototyp in Version A,
- Neukonstruktion Formkörper für E-Spinning,
- pulsatile Tests an Version A,
- Modifikation und Neukonstruktion des Stentdesigns zu Version B unter Berücksichtigung der Testergebnisse an Version A,
- Konstruktion von Halterungen für 3D-Druck,
- Anwendung vorhandener Fügetechnik zur Montage der Vliesklappen auf den Stents beider Versionen,
- Erstellen von Testparametern und -programmen,
- Durchführung stationärer und pulsatiler Messreihen beider Versionen,

- Aufbereitung und Analyse der Daten,
- Recherche in der wissenschaftlichen Literatur,
- Manuskripterstellung,
- Erstellung von Grafiken und Bildern

* Die angegebenen Impact-Faktoren entsprechen den in den Journal Citation Reports (JCR, Clarivate) der jeweiligen Fachzeitschrift für das Erscheinungsjahr der einzelnen Publikationen zugeordneten Impact-Faktoren. Für das Erscheinungsjahr 2024 wurden die für das Jahr 2023 angegebenen Impact-Faktoren verwendet.

Measurement 177 (2021) 109265

Contents lists available at ScienceDirect

Measurement

journal homepage: www.elsevier.com/locate/measurement

General image fiber tool: A concept for automated evaluation of fiber diameters in SEM images

Andreas Götz *, Volkmar Senz, Wolfram Schmidt, Jennifer Huling, Niels Grabow, Sabine Illner

Institute for Biomedical Engineering, Rostock University Medical Center, Friedrich-Barnewitz-Strasse 4, D-18119 Rostock, Germany

ARTICLE INFO

Keywords:
Image processing
Microfiber
Structure analysis
Automatic measurement
Fiber fabric product
Characterization

ABSTRACT

Fiber imaging is becoming increasingly important in various fields. The current standard method of quality assurance is the manual quantification of fiber diameters in Scanning Electron Microscope (SEM) images, which is time consuming and introduces bias. However, due to partly insufficient reliability of automated software, improved concepts are required. We introduce an innovative routine for computerized evaluation of fiber diameters in SEM images with improved accuracy. This **G**eneral **I**mage **F**iber **T**ool (GIFT) automatically calculates the average fiber diameter and standard deviation by statistical analysis. In a comparative study, GIFT was benchmarked to an existing popular fiber analysis tool, DiameterJ, and manual quantification. GIFT has detected fiber diameters with improved accuracy in numerous SEM images, and has been shown to be a remarkably sound method when challenged with difficult image types. The work presented here validates the GIFT concept and demonstrates its potential for applications in biomedicine and various other fields.

1. Introduction

In biomedical research, industry and other fields, fiber materials, in particular electrospun fibers, are a focus of current research due to their wide-ranging capabilities [1–5]. Electrospinning is a promising approach to imitate hierarchically structured biological models by designing biomimetic synthetic fiber composites or layered structures of mixed fibers with inherently different properties [6]. The development and application of fiber-based medical devices or implants necessitates a controlled and consistent manufacturing process. Fiber diameter is a critical parameter of electrospun biomaterials and has been shown to influence cell proliferation, differentiation and function [7–12]. Therefore, quality control of fiber-based products is of particular importance. The fiber production technology of electrospinning uses the force of a strong electric field to stretch and deposit a small jet of polymer solution resulting in nonwoven fabric products with fiber diameters in the micro or nano range. Many parameters influence the electrospinning process, and consequently the fiber diameters [13–15]. Additionally, the cross-sectional morphology of nanofibers provides further information [16]. To monitor fiber consistency, some researchers describe that the fiber diameter can be directly measured by laser diffraction [17] or by different optical and mechanical measurement methods [18].

Despite efforts to automate the process, the state of the art for evaluating fiber morphology is still manual analysis of scanning electron microscope (SEM) images utilizing the widely-used software ImageJ [19,20]. The equally used Fiji project is a software upgrade supporting more complex plugins [21] and ImageJ2 provides additional functionality to ImageJ [22]. However, subjective selection of data by a human operator can possibly influence the result. Three detriments of these manual analysis methods are worth mentioning: (i) individual experience and consistency of the human operator influences the result, (ii) the relatively low number of measurement points, and (iii) the process is inherently time consuming.

Replacing manual measurement with software tools can provide significant advantages and is a very promising means to achieve automated quality assurance. Software does not decide subjectively and generates reproducible results, which are independent of the respective user. On one hand, automatic methods are currently less accurate than manual measurements. On the other hand, the processing speed of computers is a clear advantage. Many automated image analysis methods rely on some combination of common image processing steps, such as preprocessing, segmentation, registration, object detection, tracing, tracking, feature selection, and classification, partially combined with machine learning [23]. Attempts have been made to develop improved computer-aided methods and an overview of important methodologies is presented in Table 1.

---

* Corresponding author.
E-mail address: andreas.goetz@uni-rostock.de (A. Götz).

https://doi.org/10.1016/j.measurement.2021.109265
Received 27 October 2020; Received in revised form 18 February 2021; Accepted 7 March 2021

Table 1

Overview of different fiber analysis methods and approaches, grouped by technique type. Key characteristics and limitations are summarized and the availability as standalone software is indicated.

Methods or approaches	Key characteristics and processing steps	Availability	Ref.
Focus on grayscale values			
DiameterJ	• Freeware, plugin for ImageJ • Validated for the quantification of fiber diameters and pores • Fiber diameter range: 10 pixels up to 10% of the image size • Requires subjective user input	yes	[24–27]
Fiber Pro	• Semi-automatic software provided by Radical Scientific Equipments Pvt. Ltd., India	yes	[28]
Fiber Thickness App	• App for Image-Pro provided by Media Cybernetics, USA • Automatic or manual mode	yes	[29]
Phenom FiberMetric Software	• Software (device-bound package) provided by Thermo Fisher Scientific Inc, USA • Automatic or manual mode • Measurement points per image: up to 1000 • Fiber diameter range: 100 nm to 40 μm • Image size: up to 1024 × 1024 pixels	yes	[30]
PAQXOS	• Image analysis system (device-bound package) provided by Sympatec GmbH, Clausthal-Zellerfeld, Germany • Fiber and particle quantification	yes	[31]
Euclidean distance approach	• Distance transform and/or direct tracking, additional local thresholding, segmentation & skeletonization steps • Thresholding affects the results dramatically • Different accuracy and limitations on fiber bending, crossovers and overlapping	no	[32–36]
Artificial Vision System	• Multivariate image analysis procedure • Sub-images, fiber linearization	no	[37]
Hough transform approach	• Image analysis technique contained in MATLAB toolbox • Less influence of punctate noise & curled fiber segments • Higher accuracy compared to regionprops function	no	[38]
Regionprops function approach	• Image analysis method contained in MATLAB toolbox • Multiple image pre-processing steps required, e.g. grayscale adjustment and binarization • Highly sensitive to the binarization threshold	no	[38]
Focus on edges			
SEMAnalyser™	• Software provided by Electrospinz, Blenheim, New Zealand • Main steps not announced	yes	[39]
Pairing line segments strategy	• Automated measurements of microfiber diameters • Boundary detection, fitting of rectangles, segment merging	no	[40]
Radon transform approach	• MATLAB code for aligned fibers • Slope patterns, Fast Fourier transform (FFT), statistics • Canny edge detection on random fibers, normalized Radon transform	partly	[41,42]
Cellular automata approach	• Twenty-Five Neighborhood model • Cellular edge detection, learning automata • Optimized edge detection, not yet applied to fiber images	no	[43,44]
Miscellaneous or unknown focus			
FiberApp	• Open source software for fibrous structures • High length-to-width aspect ratio is required	yes	[45]
FibrilTool	• Plugin for ImageJ • Tensor based method • Quantitative description of the anisotropy of fiber arrays and their average orientation in cells • Not suitable for fiber diameters	yes	[46]
FiVer	• Software provided by SKZ, FSKZ e. V., Würzburg, Germany • Quality assurance or process analysis • Focused on fiber length of crossed and bent fibers • Not suitable for fiber diameters	yes	[47]
FiberFit Software™	• Freeware for analysis of fiber organization • Fast Fourier transform (FFT) based method • Not suitable for fiber diameters	yes	[48]
FibreQuant™	• Software provided by nanoScaffold Technologies LLC, USA • Main steps not announced	yes	[39]
Fusion method	• Combination of edges & grayscale value • Canny edge detection and thresholding • Fiber measurement on merged image	no	[49]
Histomorphometry Macro	• New automated macro script for FIJI-ImageJ • Developed in collaboration with IMRB image platform, Creteil, France • Color based segmentation • Measurement on fiber cross-sections in digital images	yes	[50]
3D-Analysis method	• Datasets of e.g. Micro X-Ray CT are required • Binarization, Volume rendering, Gaussian smoothing, Point Spread Function • Fiber diameter and volume porosity in melt-electrowritten scaffolds obtained from x-ray phase contrast images • CT spatial resolution insufficient for nano-sized fibers	no	[51–53]
Hurst exponent approach	• Random-walk method • Hurst exponent distribution, statistics	no	[54]
SIMPoly	• Matlab based image analysis tool • Histogram equalization, edge detection, morphological closing, skeleton overlay • Limited to unimodal fiber diameter distribution in the range of 10 to 100 pixel	yes	[55]

Various methodologies with proven functionality have been developed, but not all have been converted to standalone programs, which reduces the number of easily accessible software tools. The methods summarized here generate reliable results under ideal conditions. However, most methods are limited in applicability due to special image requirements, such as straight fibers, fiber alignment or image contrast, or restricted access to proprietary software. According to manufacturer data and product information, most software tools focus on grayscale values, similar to DiameterJ. According to performance specifications of DiameterJ, fibers must be at least 10 pixels in diameter, and maximally 10 percent of the smallest dimension of the image. However, as presented in this work, when applied to challenging images, DiameterJ may generate inaccurate data due to low image contrast or wide-ranging grayscale values.

To date, there is no universally suitable software with which the majority of images can be processed. The shortage of appropriate and accessible software tools and their potential susceptibility to errors have motivated the conception of a new universal method. In this work, we aim at developing a new comprehensive approach which generates reliable results comparable or superior to current established standards.

Challenges, such as a wide range of fiber diameters, different grayscale values, different contrast, grayscale gradients, fiber bending, different orientation, crossing fibers, overlapping fibers, and different SEM image types must not influence the result. The General Image Fiber Tool (GIFT) is designed to avoid many of the sources of error that hamper the previously mentioned edge focused and grayscale focused methods. While relying on the existing methods of Sobel based edge detection and morphologic filtering to perform the initial segmentation, GIFT applies an original strategy for the quantification of fiber diameters in these segmented images. Rather than attempting to identify every individual fiber or fiber edge with complete accuracy, the method instead isolates and measures distances between all parallel elements in an image. Repetitive structures, like fiber edges, will appear the most often and therefor fiber diameters will emerge with a prominent frequency. This is the first method, to the best of our knowledge, which statistically evaluates parallel fiber edges in an image to determine fiber diameter. In validation tests, GIFT worked as well as or better than our benchmarks of the established software tool DiameterJ and manual quantification. As demonstrated below, in addition to accurately measuring fiber diameters, it is potentially applicable in numerous other fields outside of electrospinning. The presented work establishes the utility of the GIFT method and supports its continued development into a multi-functional, fully automated and easily accessible fiber analysis tool.

2. Materials and methods

2.1. Choice of images

SEM images of routine electrospun nonwovens, containing fibers of different diameters and image characteristics, were used for image processing. To test and compare GIFT against DiameterJ and manual quantification under idealized conditions, a synthetic phantom image was created, which contains exactly four “fiber” types of a defined thickness without any variation (8, 16, 30, and 40 pixels). In that image, a part of the “fibers” appears in the shape of letters, another part represents randomly distributed and overlapping fibers in all directions. The total length of each type of “fiber” is unequally distributed. The images used in this study are displayed in Table 2, parameters for image processing are explained below.

2.2. Software tools

The computation and measurements of GIFT as well as manual quantification were achieved using the software tools ImageJ version 1.52a (National Institutes of Health, USA) and OriginPro 2016G version b9.3.226 (OriginLab Corporation, USA). DiameterJ (National Institute of Standards & Technology, USA) was used within the software ImageJ. Certain main operations were used in ImageJ for preprocessing, including Find Edges, Brightness/Contrast, and Rotate (without interpolation). For measurement in OriginPro the main operations used were Morphological Filtering (line opening), Peak Finding, Descriptive Statistics, Plotting, and Nonlinear Fitting.

For reference, manual quantification was used to measure fiber diameter. In general, 20 representative fibers in each SEM image were selected and measured by hand by a single person using ImageJ. In the phantom image 20 measurements per fiber diameter were taken. In the SEM image containing thick fibers, 200 measurements were manually taken to create a manual data set with a number of measurements closer to the automated methods for better statistical comparison.

DiameterJ provides three different segmentation algorithms which generate eight segmented images each (Fig. S14). The user has to subjectively choose one (Table 2) and copy it into a folder called “Best Segmentation”; further processing is done on that selected image. The segmented images for further processing were selected based on visual aspects like not being too bright or dark and having good discernible fibers. Due to subjective selection of the segmented image, results can differ.

Table 2

Images and parameters for image processing. Segmentation threshold and filtered line length for GIFT, the segmentation algorithms for processed images in DiameterJ, as well as the number of measurement points for the manual method.

Parameters for image processing with different methods		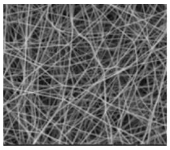	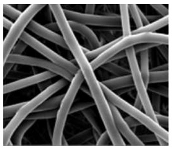	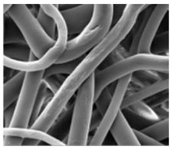	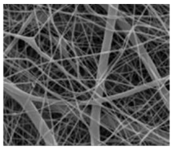	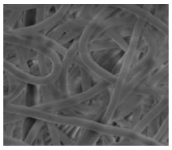
Image content	phantom image	thin fibers	midsize fibers	thick fibers	mixed fibers	low contrasted fibers
Segmentation threshold [a]	240	240	240	200	240	80
Line opening filter length (pixels) [a]	8	8	8	10	5	7
Segmentation algorithm [b]	S1	M7	S3	S5	M7	S3
Number of measuring points [c]	4 × 20	20	20	200	20 & 15	20

a - GIFT; **b** - DiameterJ; **c** - Manual method for fiber quantification (Reference)

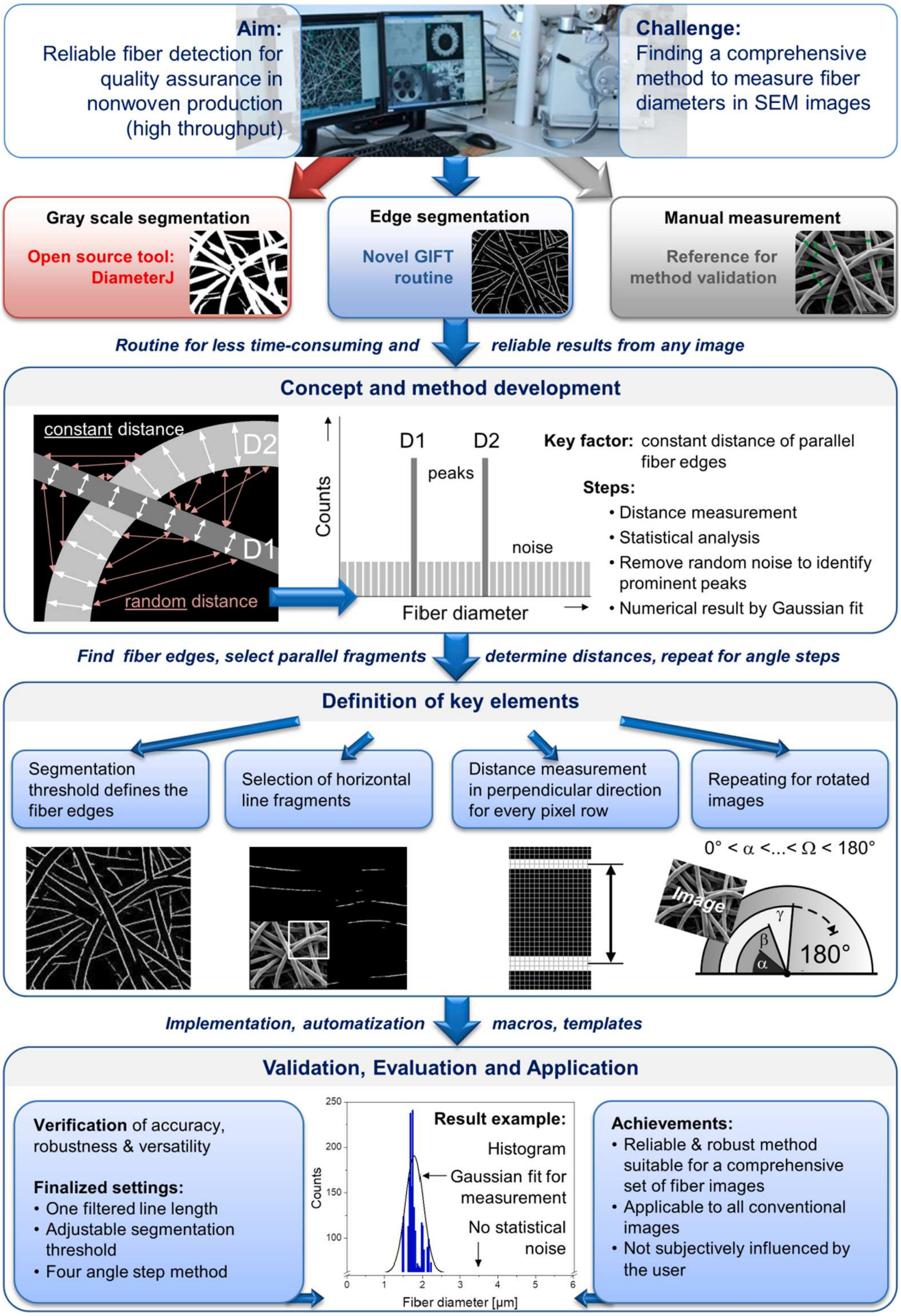

Scheme 1. Concept of GIFT. Versatile fiber measuring method for any SEM images - concept, development, validation, and application.

2.3. *Concept of GIFT*

The main process steps of GIFT are illustrated in Scheme 1 and details about the processing steps of the GIFT routine are shown in Supporting Information Fig. S1. The fundamental principle of GIFT is to count the frequency of measured distances between parallel edges in an image. While the edges of elements in the image are distributed randomly, if there is a fiber in the image the distance between its parallel edges will emerge as statistically significant. The basis for the method is the parallelism of the fiber margins on one hand and their randomly distributed location and orientation in the image on the other hand. The distance between the margins of a single fiber is constant, independent of the location and orientation in the image, thus the counts of the distance between a single fiber's edges appears with significantly higher incidence. By contrast, the distances between the margins of two different fibers are randomly distributed and are part of the statistical noise. The target of the method is the visualization of that statistical difference.

The concept was implemented by the following steps. First, SEM images, which were not already available as 8-bit black and white

Table 3

Testing capability of fiber detection, Table summarizes values and images used in the test strategy to confirm the capability of GIFT in extreme conditions.

Parameter	Validation approach	Grayscale value fiber/ background	Segmentation threshold	Fiber diameter (pixel)	Test image
Bending radius & orientation angle	• Different radii of ring shaped fibers • Contribution of every single ring	200/100	200	48	
Minimal fiber-background contrast	• Phantom image (see Table 1) • Gradation: one grayscale • Exemplified by two arbitrarily chosen grayscales	1) 101/100 2) 201/200	2	8, 16, 30, 40	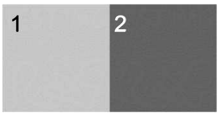
Gradient of grayscale values	• Max. extent in both directions across the fiber diameter • Min. contrast to background • White and black background	1) 253⇒0⇒253/ 255 2) 2⇒255⇒2/0	12	508	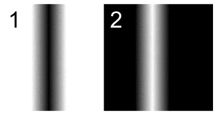
Image size	• Oversized image: 5000 × 5000 pixels • Triple size of ordinary images • Examination of two fiber diameters	177/65	200	50, 100	
Fiber diameter	• Extra-large fibers • Fiber of half image size	195/127	200	500	

images, were converted for consistency. Edge detection was performed using two combined Sobel operators of perpendicular orientation [56]. Then the images were binarized using a manually chosen segmentation threshold. High threshold values in the range of 200 help to remove most of the fiber surface, and guarantee thin remaining lines of a few pixels in thickness. A morphological opening filter separates straight line fragments of a specific length (i.e. consecutive pixels) in the horizontal direction. Line lengths between five and ten pixels were chosen. The mathematical morphology of the line opening filter is based on a two-stage algorithm, which consists of an erosion step, followed by a dilation step using a structure element [57–60]. Therein the mathematical foundation $\gamma_B(X) = \cup \{B \mid B \subseteq X\}$ is described with the opening (γ) of an image (X) using the structure element (B) [60]. A straight horizontal line of a defined length is used as a structure element. If the structure element fits completely into the set of segmented fiber edges, the corresponding pixels remain after performing the erosion step. The dilation step extends each remaining pixel to the shape of the structure element. In this way inclined fiber edges were removed. That opening step also removes the residual mottling and noise, because most artifacts are below the size cut off. In a following subroutine the pixel columns were rearranged and stacked. In the vertical (perpendicular) direction, the distances between these remaining line fragments were measured using a peak finding algorithm and subsequent calculations. These filtering and measurement steps were repeated several times on the same image as the image was rotated through equidistant angles within a semi-circular arch. All examples in this paper were measured at 0, 45, 90, and 135°. As the opposite angles are equivalent, there is no need for measuring the same data twice. Then the pixel distances were transformed into metric units based on the scale bar in the image. Next, the measured distances were plotted with respect to their frequency in a histogram. Measurements of real fiber diameters occur with a significantly higher frequency compared to statistical noise. To remove statistical noise, and to create an easily interpretable graphic showing a relatively small peak, only the highest 10% of counts were accepted for the final histogram. To quantitatively determine the average fiber diameter, a Gaussian peak fit was performed on the unfiltered histogram.

To estimate reasonable ranges for processing values, in a preliminary parameter study using ten different SEM images in a iterative procedure, the length of line opening filter was varied (2–25 pixels), and the influence of segmentation threshold was studied (10–254). The effect of the angular spacing between images for sufficient resolution to properly analyze fibers across any direction of angles was investigated (number of repeating steps 2–10), the section of accuracy verification is related to that issue.

Unless otherwise noted, images were processed using a segmentation threshold of 200, and a length for the line opening filter of eight pixels. The image containing mixed fibers was processed twice to compare the effect of the filtered line lengths of five and eight, as presented in Supporting Information (Fig. S5, Table S1).

In regard to method comparison, ideally all three methods (GIFT, DiameterJ and manual quantification) were expected to attain equivalent results, with the manual quantification serving as the reference which we considered the gold standard for comparison.

2.4. Accuracy verification

The accuracy of GIFT was assessed by comparing the generated results to known fiber thicknesses for the phantom image and to the results of the manual quantification for SEM images. Depending on the line thickness in the segmented image, the filtered line length, and the angle increment of repeated measurements there may be fibers that are not measured by GIFT. These gaps in measured image data, i.e. unconsidered lines, may influence or reduce the quality of the results. Theoretically, in the most unfavorable case, only lines angled ±7° relative to the measurement angle contribute to the data (Fig. S3). To create a data set in which every fiber edge was measured, images (SEM image and the phantom image) were rotated in steps of six degrees to create a new test set of seven slightly rotated versions of the initial image. Each image in this set of rotated variations was processed normally with GIFT and Gaussian fits on final peaks were performed for comparison. If the comparison reveals similar results for all seven rotated images, the method is not sensitive to the angle of the initial image and it is reasonable to assume that the influence of unmeasured fibers on GIFT outcomes is insignificant. In the case of aligned of fibers, remarkable changes in peak height are expected for different angles (not tested).

2.5. Robustness verification

Throughout this paper the term “robust” refers to the result’s lack of

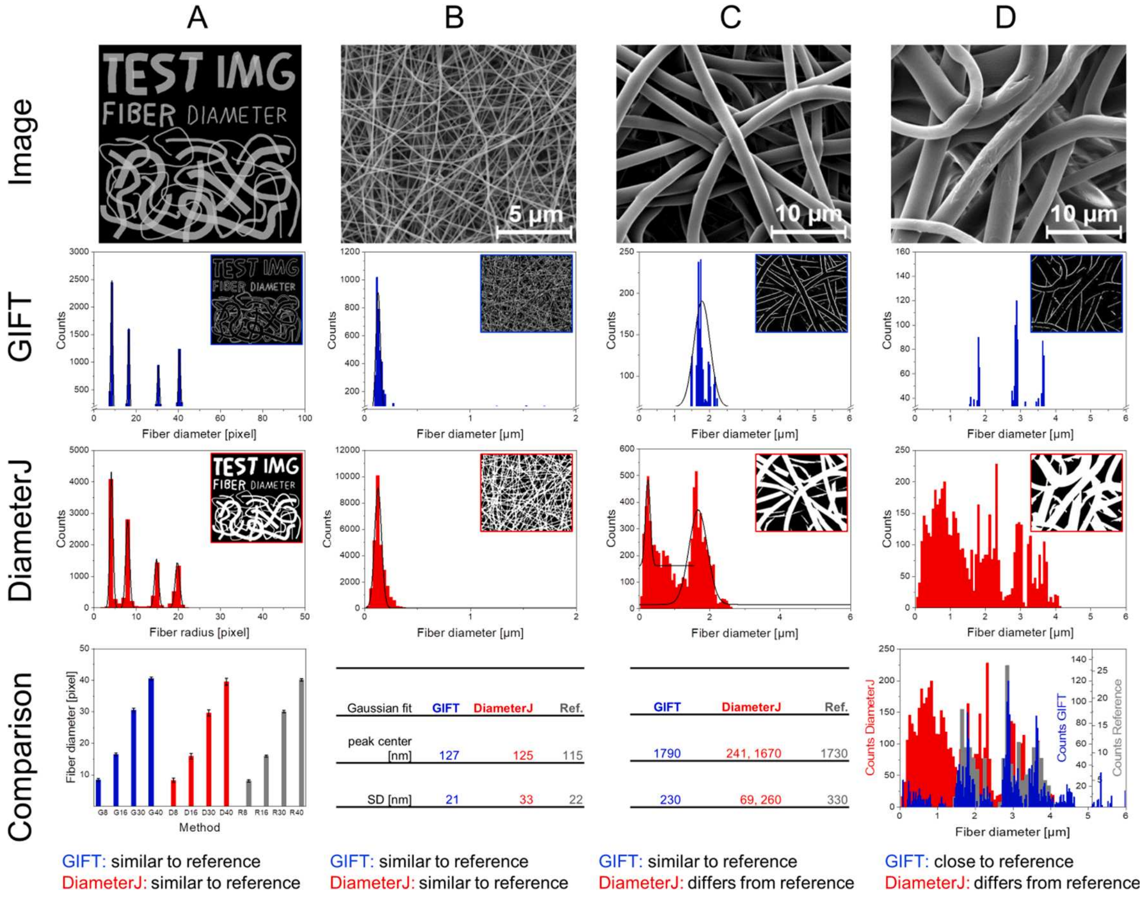

Gaussian fit	GIFT	DiameterJ	Ref.
peak center [nm]	127	125	115
SD [nm]	21	33	22

GIFT	DiameterJ	Ref.
1790	241, 1670	1730
230	69, 260	330

Fig. 1. Comparison of GIFT, DiameterJ and manual quantification (Reference) on different images. A synthetic phantom image, containing exactly four fiber diameters in letter-shaped and random orientated fibers, was completely processed (A). Additionally, SEM images containing thin fibers (B), midsize fibers (C), and thick fibers (D) were processed. The initial images are shown in the first row. The second row presents the results of GIFT with statistical noise removed. As an inset, the segmented fiber edges are displayed. The results of DiameterJ are presented in the third row with the segmented image as an inset. The bottom row provides the results in different forms for the various image types to most clearly highlight the differences between method results. The three evaluation methods consistently detected four different fiber diameters in the whole phantom image (letter shaped as well as randomly shaped fibers were measured) with low standard deviation (A). For thin and midsize fibers, peak data obtained by Gaussian fit are presented in two tables (B, C). For thick fibers, GIFT and DiameterJ generated highly different results (D). The complete datasets are presented in an overlay chart to highlight the differences between methods. Despite a low level of noise, GIFT generated three distinct peaks (blue). The reference method (200 manual measured points) found fiber diameters mainly in a range from 1.5 to 4 μm, with distinct peaks close the results of GIFT (gray). DiameterJ found fiber diameters in a wide range up to 4 μm with a tendency toward small fiber diameters (red). (For interpretation of the references to color in this figure legend, the reader is referred to the web version of this article.)

dependency on the preset parameters. The influence of the segmentation threshold and the length for the line opening filter was tested. In a test series on the SEM image containing midsize fibers the segmentation threshold was varied to 100, 150, 200, and 250. The filtered line length was varied to 5, 8, and 10 pixels. On the final histograms Gaussian fits were performed and compared to evaluations of the data after separating out the top 10% of values are shown.

2.6. *Capability of fiber detection*

GIFT was designed to be capable of processing a diverse set of SEM images and still generate reliable results. To confirm its functionality within a wide range of different image parameters, a set of test images was designed which represent extreme image cases. Fiber measurement has to be insensitive to the fiber bending radius, as well as the fiber orientation angle. Additionally, fiber detection in images of low contrast is challenging and gradients of grayscale values across the fiber diameter can cause misdetection. Conventional SEM images are of sizes less than 2000 × 2000 pixels, but fiber analysis tools should be able to handle larger images as well and large fiber diameters have to be measured correctly, independent of their dimension relative to the image size.

The main parameters of the test strategies are displayed in Table 3. Except for contrast and gradient testing strategies, the grayscale values were chosen arbitrarily to demonstrate the grayscale insensitivity of GIFT.

3. Results

3.1. *Comparative study of GIFT, DiameterJ, and manual quantification*

Ordinary images. The phantom image and three further SEM images were processed by GIFT and DiameterJ, and the results were compared to the manual measurement as a reference. The results of the evaluation are compared for the three methods in Fig. 1. The phantom image (Fig. 1, A) revealed that all methods generated an equivalent result. For thin fibers (Fig. 1, B), GIFT and DiameterJ found similar results close to the reference. In contrast, midsize fibers (Fig. 1, C) caused different results. DiameterJ generated two broad peaks of similar statistical weight. GIFT detected only fibers in the range of nearly two microns which was in good agreement with the manual quantification. Thick fibers (Fig. 1, D) also generated different results. DiameterJ generated numerous peaks of variable height in a wide range with

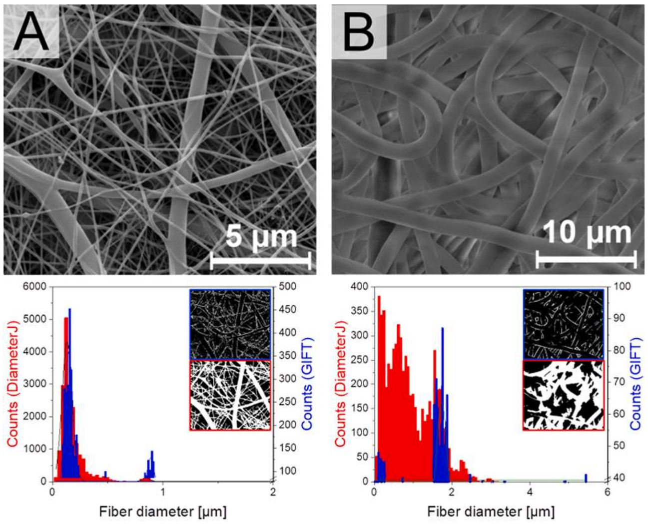

Gaussian fit	GIFT	DiameterJ	Ref.
peak center [nm]	149 & 890	132 & 847	123 & 904
SD [nm]	38 & 36	46 & 34	24 & 63

Gaussian fit	GIFT	DiameterJ	Ref.
peak center [nm]	1730	n.d.	1608
SD [nm]	160	-	111

GIFT: close to reference
DiameterJ: close to reference

GIFT: close to reference
DiameterJ: not evaluable

Fig. 2. Results of challenging images. Comparison of GIFT and DiameterJ on different SEM images: image of composite material consisting of midsize and thin fibers (A), low contrasted fiber image (B). The initial images are shown in the first row. The second row displays the histograms of diameter distribution obtained by GIFT without noise (blue) and DiameterJ (red), as insets the basic segmented images are displayed. The bottom row provides the corresponding numerical results. For the composite material (A), two peaks are analyzed corresponding to the two fiber diameters. (For interpretation of the references to color in this figure legend, the reader is referred to the web version of this article.)

remarkable statistical weight less than 2.5 µm. GIFT on the contrary, generated peaks with narrow ranges with maxima at 1.8, 2.9, and 3.6 µm. The manual measurement produced results in the range of 1.5–4 µm with three significant peaks at 1.7, 2.9, and 3.7 µm.

Challenging images. SEM images containing different fiber types are of special importance due to the increased difficulty of accurately separating and measuring the variable fiber diameters. Additionally, experiments may generate images with low contrast or mottling. It is important that any automated method is able to accurately function in these situations. The results of such challenging images are shown in Fig. 2.

For midsize fibers in combination with thin fibers (Fig. 2, A) both computing methods found both types of fibers. The height ratio (maxima of thin/thick fibers) of the corresponding peaks was different (3 for GIFT, and 45 for DiameterJ). For an image of low contrast (Fig. 2, B), GIFT generated a clear peak at 1.73 ± 0.16 µm, which was in good agreement to the manual measurement (1.61 ± 0.11 µm). A very small peak close to zero values was visible. Quite the contrary, DiameterJ generated a wide range of peaks with prominent statistical weight less than one micron.

3.2. GIFT accuracy and angular spacing

The SEM images containing midsize fibers and the synthetic phantom image were rotated stepwise to create a series of seven test images. Every image was evaluated using four angle steps (at 0, 45, 90, and 135°). As shown in Figs. 3 and S2. GIFT generated equivalent results regardless of the initial starting angle of the image. The Gaussian peak centers, as well as the peak widths, were not significantly affected.

3.3. Error analysis

Every method has limitations. GIFT has three potential sources of error from peak shift by line inclination, pixel discretization error, and missing data due to unmeasured fibers. All these sources of error did not have much influence on the final results.

Peak shift by line inclination. After performing the line opening filter, slightly inclined line fragments remain. Due to this slight slant, the angle of measurement is not exactly perpendicular to these fibers, which means that the measured fiber diameters could be overestimated by some percent. The effect depends on the segmented line thickness and the filtered line length. Thick lines and a short filtered length will increase overestimation (Figs. S3 and S4). Based on estimation the expected final overestimation is only around two percent. For more details on how this error was calculated see section SI 2 in Supporting Information.

Pixel discretization error. Computerized methods count image pixels and this can cause pixel discretization error. For the phantom image, one pixel of error means a calculated error of 12.5 percent for an eight pixel thick fiber (1/8) and 2.5 percent for a 40 pixel thick fiber (1/40). The thicker a fiber is the less pixel discretization error influences the result. A medium sized fiber usually is imaged in a range between 50 and 150 pixels and could lead to a discretization error in a range of roughly 0.7 (1/150) to 2 (1/50) percent.

Missing data due to unmeasured fibers. Some fiber parts or image corners may remain unmeasured. The influence of unmeasured fibers (missing data) is discussed separately in the accuracy Section 4.1.

Total error. The collective effect of all error sources together will result in total error. Gaussian peak fit was done for the results of the phantom image. As the phantom image contains only precisely known fiber diameters, the other natural images with unknown fiber diameters were excluded from this error comparison. To obtain relative methodical errors the standard deviation was divided by the peak center value for each peak. Due to averaging many measurements total errors indicate a range of about five percent for the eight pixels fibers, and close to one percent for the 40 pixel fiber in the phantom image. An error comparison of all three methods is presented in Fig. 4. Doubling the radius values generated by DiameterJ to achieve the diameter values, the absolute error doubles as well. However, for medium sized fibers GIFT generates diameter data with a final total error of approximately one percent.

3.4. Time requirement

Another aspect is the time consumption of computation and archiving the results. The average expenditure of time for performing different methods on a 3 GHz, six-core processor is compared in Table 4. The complete evaluation of one SEM image using GIFT needs about three minutes which is comparable to DiameterJ.

3.5. Verification of detection capability

Illustrating the capability of fiber detection and the limits of GIFT, the method was confirmed on specially designed test images. Detailed results are available for the mentioned figures in Supporting Information. GIFT detected correct diameters independent on the fiber bending radius and angular orientation in the image (Fig. S8). Fibers of a minimal contrast difference to background were correctly detected, GIFT also detected fiber edges correctly, uninfluenced by grayscale gradients within the fibers (Fig. S9). Image sizes up to at least 5000 × 5000 pixels generated correct results (Fig. S10). GIFT correctly detected fiber diameters up to at least half of image size (Fig. S11).

3.6. Robustness

In a test series, the threshold for segmentation and the length for the line opening filter were varied. Data were obtained using two methods:

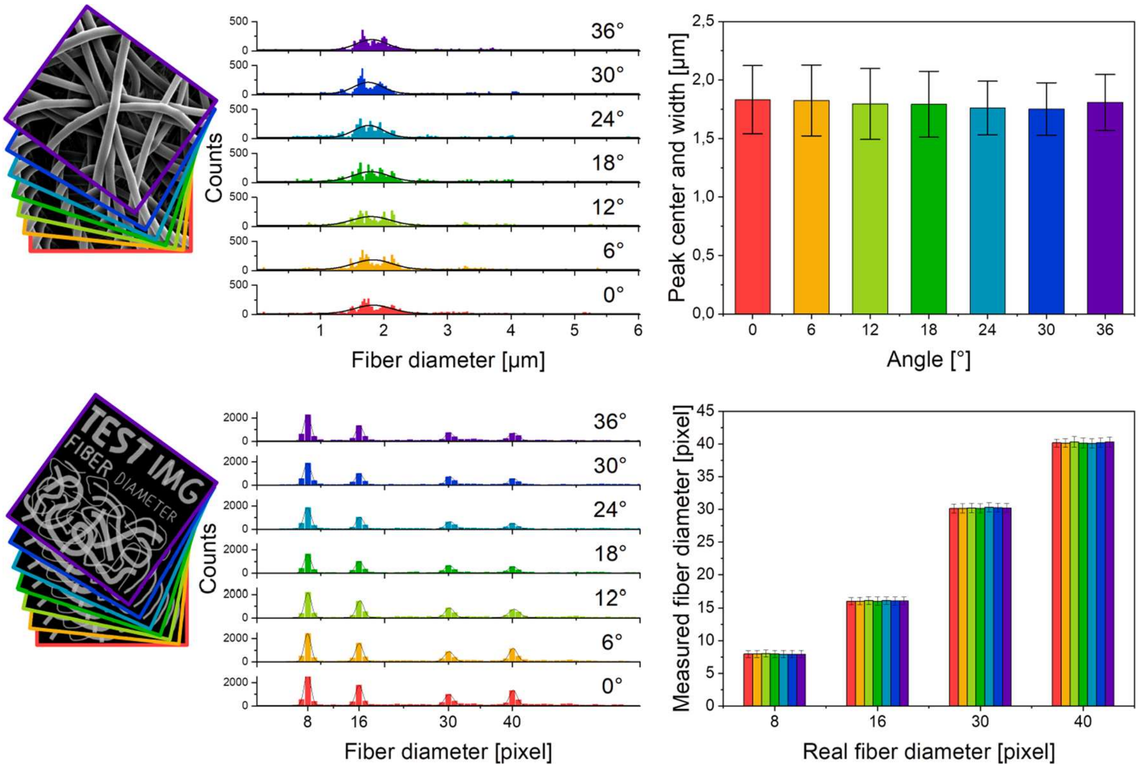

Fig. 3. Accuracy of GIFT. Evaluation of general method accuracy and influence of unmeasured fibers by comparison of rotated initial images. First row: The results of a real midsize fiber image evaluation are displayed; the histograms show the complete datasets, in which statistical noise is not hidden. Peak data in the right graphic, obtained by Gaussian fits, show equivalent results, the error bars indicate the peak width. Second row: The results of the phantom image evaluation series, the histograms display the complete datasets, statistical noise is not hidden. Diameter data, obtained by Gaussian peak fits, the error bars indicate the individual peak widths and show very uniform results.

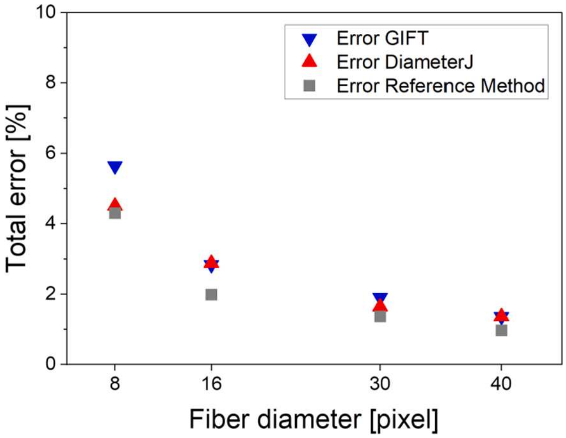

Fig. 4. Comparison of total (relative) error of fiber diameters in the phantom image. For fiber diameters of 8, 16, 30, and 40 pixels the found errors are displayed. These data refer to the evaluation which is presented in Fig. 1, A. DiameterJ generates data for fiber radii; hence the absolute error doubles for the fiber diameters. The relative errors were calculated by dividing the standard deviation of Gaussian fits by the corresponding peak center values.

Gaussian fit of the whole data set and peak analysis of the top 10% of data points. The comparison of peak data reveals similar results for peak centers and peak widths. GIFT accurately detects fiber diameters even over a range of different image processing settings. This data supports the conclusion that the same GIFT settings would reliably work on data sets containing variable SEM images. Our study showed that GIFT results are not significantly affected by processing parameters and that the top 10% of the data points accurately represent the whole data set. These results confirm the robustness of GIFT as shown in Table 5. As an empirical compromise between reliable results and usability, six segmentation threshold options (25, 60, 100, 150, 200, and 250) are given to the end user. A fixed eighth pixels filter length is used as default.

3.7. Further applications of GIFT

GIFT is not restricted to SEM images or fibers only. A great variety of imaged structures can be evaluated (images containing parallel elements, long or repetitive structures). Some examples are presented in Fig. 5 and some further examples are illustrated in Supporting Information (Figs. S12 and S13).

Roots resemble fibers and the growth of plant roots in a time step of five days is shown in Fig. 5, A. In the upper image the majority of roots were imaged in a range of roughly 21–31 pixels. For the lower image that peak slightly shifted to a range of roughly 24–33 pixels, which may correspond to root growth. Additionally a second peak in a range of 14–21 pixels appeared, which matched to the newly grown thin roots. Sand ripple are repetitive structures and after adapted preprocessing they can be investigated by GIFT. The upper image of Fig. 5, B shows airstream-formed sand ripple on a beach. The distance distribution was in the order of magnitude of 2.2 (33/15 pixel). Sand ripples formed in a small creek are shown in the lower image, here the distance distribution was in the order of magnitude of 5.3 (240/45 pixel). The strand distances in a spider web were evaluated in Fig. 5, C. The spike at 2 pixel corresponded to the diameter of strands, the strand distances were imaged in a range of 15–80 pixels. A gap at the spider's body length was prominent. Further investigation on those example images is not topic of this work, but it clarifies the potential of GIFT as broadly applicable tool.

Table 4
Time requirements for fiber diameter quantification. Comparison of average time consumption for the main processing steps of three different fiber quantification methods.

Operation	Steps	Average time	Comment
GIFT			
Preprocessing in ImageJ	Edge detection, binarization, rotation for 4 angles	less than 1 s	• Automated import in OriginPro is intended • After some images OriginPro slows down, reopening the template is useful based on experience
Transfer to OriginPro	Drag and drop	10 s	
Measurement	Line opening filter, distance measurement, statistic evaluation, graph, Gaussian fit	less than 2 s for line opening, total time: 30 to 40 s for SEM images of 1024 × 882 pixel up to 1535 × 1023 pixel	⇒Total time requirement is roughly 3 to 4 min per image
Saving	Copy or data export, archiving, additional activities	1 to 2 min	
DiameterJ			
Preprocessing	Plugin: DiameterJ Segment	10 to 20 s	• Choice of segmented image based on experience
Manual image selection	Visual inspection and subjective rating of segmented images, copying the chosen image in the folder named: Best Segmentation	1 to 2 min	⇒Total time requirement is slightly greater than for GIFT
Processing	Plugin: DiameterJ 1-018	less than 1 min	
Saving	Copy or data export, archiving, additional activities	1 to 2 min	
Manual Method (Reference)			
Measurement	Drawing lines by hand, writing numbers in a table	10 s to 15 s per point	• Operator dependent accuracy
Saving	Copy or data export, archiving, additional activities	5 to 10 min	⇒Total time depends on the number of measuring points

Table 5
Robustness of GIFT. Method robustness against altering the segmentation threshold and the length for line opening filter, achieved from SEM image of midsize fibers. The comparison of peak data, obtained by Gaussian fit and analysis of the top 10% of data points, reveals only little difference between the locations of peak centers as well as comparable peak widths.

Segmentation threshold	Line opening filter length [pixel]	Top 10% peak center [μm]	Top 10% peak width [μm]	Gaussian peak center [μm]	Gaussian peak width [μm]
100	8	1.83	0.71	1.82	0.71
150	8	1.86	0.78	1.84	0.68
200	8	1.86	0.78	1.84	0.62
250	8	1.85	0.75	1.78	0.44
200	5	1.85	0.75	1.88	0.64
200	10	1.83	0.71	1.74	0.38

4. Discussion

This paper reports a new concept for computed evaluation of fiber diameters in SEM images. The novel GIFT routine calculates the statistical distribution of the distances between fiber edges in an image to determine fiber diameters. To assess its capabilities, GIFT was compared to the ImageJ plugin DiameterJ, which is specifically designed to measure fiber diameters, and to manual quantification as a gold-standard reference. DiameterJ is an established, validated and popular tool for fiber diameter measurement, generating generally reliable results, but may generate faulty or inaccurate data in certain circumstances [61]. However, it is an adequate scale for comparison to our self-developed evaluation procedure. Numerous images representing a variety of commonly encountered fiber types were evaluated. The results revealed that both computing methods find the correct fiber diameters in ordinary SEM images. However, GIFT more accurately measured fiber diameters in challenging images and generated hardly any faulty data. GIFT is expected to be a robust method which generates reliable results.

4.1. Accuracy

Missing data due to unmeasured fibers can occur due to measuring edge distances only at specific angles in an image, as explained in Supporting Information (Fig. S3). Which fibers might be missed is dependent on the initial orientation of the image. Most fiber nonwovens will be imaged at a random orientation; hence the results of GIFT must be independent of initial image orientation. All example data presented in this paper were collected by repeated measurement of each image at four different angles (0°, 45°, 90°, and 135°), which we believe is sufficient to generate accurate data despite potentially unmeasured fibers. To support this claim, the SEM images containing midsize fibers and the synthetic phantom image were investigated in a series of seven rotated test images each. As shown in Fig. 3, GIFT generates equivalent results. The Gaussian peak centers, as well as the peak widths are not significantly affected, indicating that the resulting fiber diameter measurements are independent from initial image orientation. This result indicates that four repeated measures are a reasonable compromise between calculative effort and the trustworthiness of the result. Certainly, it would be possible to process more steps over smaller angle increments, but that would increase the computational effort while achieving an equivalent final result (Fig. S2). It is worth mentioning that parts of the image corners get lost by image rotation. However, this does not significantly affect the generation of accurate results as displayed in Fig. 3. Certainly, it would be possible to process larger matrices containing the complete image corners, but that would increase the computational effort while achieving an equivalent final result as well.

4.2. Challenges

Depending on the SEM facility, imaging technique and SEM settings, the image contrast, and brightness may differ especially for complex fiber structures. A good SEM image is characterized by clearly visible fibers, sharp edges, discernible clear background and a plastic appearance. Due to laterally positioned electron detectors and various electron-surface-interactions most fibers are imaged with a gradient of grayscale values, as the example SEM images of midsize and thick fibers in Fig. 1 show. A grayscale value focused method like DiameterJ may generate incorrectly located skeleton lines due to faulty segmentation of some fiber parts. The inaccurate measurements generated by DiameterJ mainly result from incompletely segmented fiber fragments. That issue, which is visualized using the SEM image containing midsize fibers in Figs. 6 and S7, can cause data misinterpretation.

Another example is the SEM image containing thick fibers. The broad range of peaks less than 1.5 μm generated by DiameterJ does not have a fiber equivalent in the image, hence these data are inaccurate and the histogram is unserviceable for diameter determination. For the same SEM image, GIFT and the manual method found three distinct peak

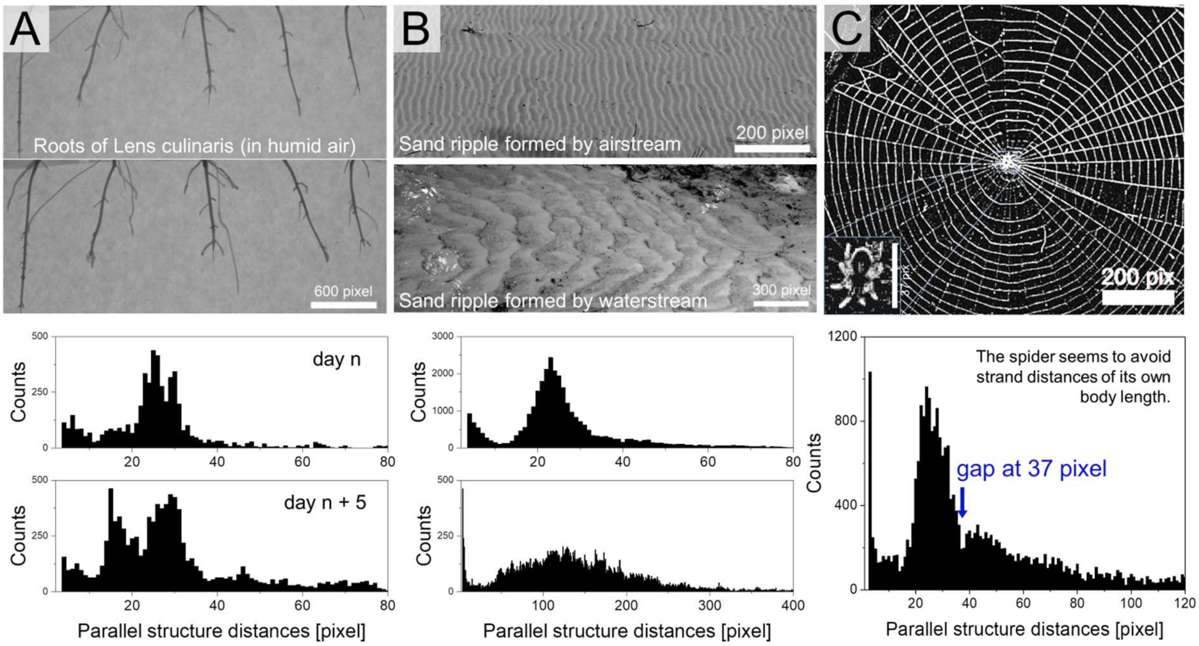

Fig. 5. Potential applications for GIFT. GIFT is useful for various applications other than fibers. The growth of roots can be investigated in regard to diameter (peak position) and length (relative peak height) (A). Information about particle properties or stream dynamics can be obtained from sand ripples (e.g. particle studies, fixed cameras at underwater groundings, streaming in creeks) (B). The distribution of line distances e.g. strands in a spider web can be measured (C).

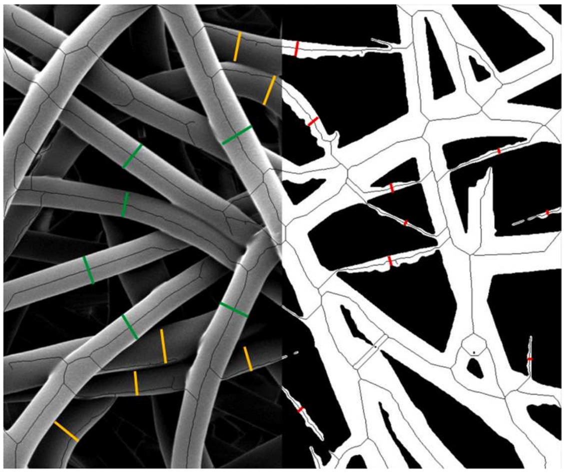

Fig. 6. Segmentation of DiameterJ. Flawed segmentation causes underestimated fiber diameters. The segmentation was performed using DiameterJ. Left part: skeleton lines in overlay on SEM image, and right part: skeleton lines in overlay on the segmented image. On homogenous gray fibers the skeleton line corresponds to the fiber center line (green). Fibers imaged with a gradient of grayscale value across the diameter (orange) may cause incomplete segmentation. Hence fiber diameters are underestimated (red). Such faulty small fibers appear as a peak in the final histogram. (For interpretation of the references to color in this figure legend, the reader is referred to the web version of this article.)

maxima at similar locations, hence the result of GIFT is much closer to manual measurement than DiameterJ (Fig. 1).

Complex fiber structures such as mixed fibers require a particularly reliable method to be measured accurately (Fig. 2). In cases where a wrong peak is generated in addition to a real peak, the user cannot distinguish between authentic fibers and false data. The fewer thin fibers in a SEM image of mixed fibers, the more the inaccuracy will reduce the reliability of the result. The peak maxima ratio of thin and thick fibers can be seen as an indication for the amount of inaccurate data and further studies may focus on that issue. As the example of the SEM image of mixed fibers shows, discrimination between real and faulty data is impossible. The fiber diameters can be measured using GIFT or DiameterJ, but due to very different peak maxima ratios (3 and 45) there is no reliable information about fiber amounts.

The results of GIFT are better compared to DiameterJ considering low contrasted fiber images with the difference between a clear peak and inaccurate data shown in Fig. 2. When processing fibers in such images, grayscale value focused methods seem to be limited by the method's inherent principles. Local thresholding, if additionally performed, may improve the result, but cannot completely prevent flawed segmentation. Furthermore, on the lowest possible contrasted image (Fig. S9), GIFT is still capable of detecting fiber edges and generates reliable results where even the best eye fails (manual measurement).

DiameterJ ideally needs fibers of similar brightness without any gradient in grayscale values within individual fibers and the whole image. That leads to a narrow range of useable images on one hand, and high requirements for SEM-imaging on the other hand.

GIFT is a non-gradient-sensitive and non-contrast-dependent method, these error sources are irrelevant. Aside from that, GIFT is independent of gray value inversion and does not fail on images of dark fibers on a bright background. Depending on image quality, GIFT generates statistical noise with values in the range of 10–30% relative to the maximum value of the histogram. To remove this noise and create easier to interpret data, in final histograms the highest 10% of bars are displayed. That top 10%-presentation also shows a similar peak width as the corresponding Gaussian fit (Table 5).

4.3. Empirical results and limitations of GIFT

GIFT generates graphical data output including numerical results about average fiber diameter and standard deviation by Gaussian fit. Substantial accuracy and robustness of the method is shown, even with non-ideal image characteristics. Evaluating numerous images, GIFT has accurately detected fiber diameters in good agreement to the manual measurement. The contrast or grayscale gradients, the crossing and overlapping of fibers, as well as all other error sources such as peak shift, missing data, and pixel discretization error did not show discernible influence on the final fiber diameter result within all processed images.

The method is limited by blurred SEM images or an extremely mottled or textured fiber surface, which could cause difficulties in edge detection. Such images were not available, and thus they are not considered here. When examining very different fiber diameters in the same image, automatic measurement per Gaussian fit was not always possible. In the case of mixed fibers the detection of thick fibers can be reduced by numerous thin fibers which overlap the thick fiber margin, hence less straight fragments remain. Like for all methods, overlapping parallel oriented fibers which hide each other are problematic. A hidden fiber edge cannot be measured, even by a human operator. For such images GIFT is expected to generate data of overlapping distances.

GIFT is not sensitive to numerous image parameters and is capable of processing most conventional images. Statistical certainty is reached based on thousands of measurements per image; some missing data do not impair the result. GIFT is able to process any data format which ImageJ accepts, and it is tested and proven successful for image sizes up to 5000 pixels. Every fiber diameter within the image size can be measured due to a pixel counting algorithm. Edge detection is independent of the average grayscale value; fibers of any grayscale can be measured. Images of any contrast are evaluable by adapting the segmentation threshold. A gradient of grayscale value across the fiber does not influence the result. The bending radius of a fiber does not have any influence as well. GIFT is not sensitive to the orientation angle of a fiber (Figs. S8–S11). Crossing and overlapping of fibers does not influence the result, due to any visible fiber margin contributing to the measured data, independent of discontinuity.

Based on practical knowledge, for processing the majority of ordinary SEM images, a segmentation threshold between 100 and 200 and a length for the line opening filter of eight pixels generate reliable results. To execute GIFT effortlessly only one parameter needs to be adjustable by the end user based on image contrast (six options for segmentation threshold), the filtered line length (8 pixels) as well as the number of measurement angle steps (4 steps) can stay fixed. These parameters were optimized in preliminary studies. The end user can thus easily process a comprehensive set of fiber images. As a matter of course, if necessary, the parameters can be adapted to special requirements.

Under challenging image conditions it may prove useful to adapt these parameters. If fibers are thin and highly bent (small radius), a reduced filtered line length might improve results. A higher value for the line opening filter may be useful in cases when only straight fibers are in the image. If fibers show preferred orientation, alignment or a higher precision of the result is needed, the number of angular steps should be increased. For images with difficult to detect fiber edges or a narrow contrast range, the value of the segmentation threshold should be well adapted. For other image types and applications (other than fibers) the preprocessing as well as the measurement parameters may require different values. GIFT has shown substantial accuracy and robustness. For a wide range of image parameters, GIFT demonstrates outstanding advantages and is revealed as a superior analysis tool.

4.4. Potential further applications for GIFT

In addition to fiber radii, DiameterJ generates data about pores and fiber orientation. Using GIFT at the current state of development, only data about fiber diameters is generated. The intermediate data collected during GIFT processing contains information about the orientation of fibers and could be utilized in a future upgrade to the method.

In fiber production for industrial applications huge amounts of SEM images have to be evaluated for quality assurance. Human operators are limited in terms of work load, labor force, ability to concentrate on monotonous tasks, and working time. Machines are better suited for completing such monotonous tasks and can operate nonstop. When designing a computation tool to automate the process of fiber diameter quantification, two aspects have to be considered. On one hand, the application has to be flexible enough to cope with very different input images. On the other hand, the application has to be robust and stable, and the results need to be highly reliable. A software application which frequently generates flawed results cannot be used, because verifying and correcting the results of an automated evaluation by a human operator is disadvantageous. GIFT is expected to fulfill these requirements, only monitoring by random samples is advisable.

SEM imaging continues to increase its importance in many fields, entailing applicability for GIFT. Current research trends explore different imaging technologies as well as three-dimensional imaged data sets, generating interest for automated image stack or volume processing techniques. A growing variety of fiber materials, fiber reinforced composites or tubular and hollow materials (negative fibers) will need to be imaged, mapped, and investigated in the future. There will be a demand for robust and reliable image processing methods, which are adaptable and implementable for different purposes. GIFT enlarges the pool of methods and may supplant existing techniques.

GIFT is not restricted to SEM images only. Any images containing parallel elements, long or repetitive structures could provide additional interesting applications for GIFT. Selected examples are shown in Fig. 5 and some further illustrations are presented in Figs. S12 and S13.

Potential broad examples include automatic classification and structural analysis in biology, geology, astronomy, remote sensing, natural sciences, dendrochronology, fiber industry and others. More specific examples include using images of the same object evaluated at different times for investigation of growth or periodic processes in geological or biological structures like cracks, rivers, roots [62], blood vessels [63], Physarum polycephalum [64], otoliths [65] or leaf veins [66,67]. The shapes of histograms or Gaussian curves based on GIFT-generated data contain a wealth of information. Diatoms can be classified by comparing characteristic repetitive microstructures [68]. Satellite images of river deltas contain information about water content in creek diameters. For activity studies the distance distribution of contracted and relaxed segments of worms or leeches, as well as studies on ventral scales of snakes in rectilinear locomotion can be performed [69]. The width distribution of ice cracks of earth Polar Regions or other planetary surfaces can be used for dynamic studies of glacial activity or investigations on climate change [70]. GIFT is a helpful tool for any crack measurement on images of buildings or micrographs [71]. The distance distribution of tree rings contains information about growth history over decades [72]. In the field of fluid dynamics the distance distribution of sand ripples can be measured, e.g. for studies on fluid-particle-interactions, oceanography or monitoring the stream [73,74]. Complex interference patterns or misalignment measurement by moiré patterns can be evaluated [75]. Hand written letters contain information about the author in characteristic line distances; it may be useful for author identification or early detection examinations for brain diseases like Parkinson [76]. There is a lot more to discover.

5. Conclusions and outlook

GIFT is a new method originally designed for computerized measurement of fiber diameters in SEM images. We demonstrate that the novel method performs as well as or better than existing methodologies, especially in situations with highly varied fiber diameters, inconstant grayscale values or when analyzing low contrast images.

The fiber evaluation tool counts the frequency of parallel fiber edges in the image, and displays a final histogram of frequency distribution of fiber diameters, including a numerical measurement determined by Gaussian fit. GIFT has been benchmarked to the validated fiber quantification software DiameterJ as a standard of comparison, and to manual evaluation as a reference. On a synthetic phantom image, as well as on real SEM images, GIFT has demonstrated substantial accuracy and robustness. Advantages over DiameterJ are demonstrated under challenging conditions. The results of GIFT provide statistical certainty by generating thousands of measurements per image and they are not affected by the absolute fiber diameter, a gradient of the grayscale value on a fiber surface, the average grayscale value in general, fiber bending, fiber direction, the image contrast, or overlapping and crossing fibers. GIFT processes all conventional image sizes and data formats that ImageJ accepts. Thus, GIFT has the potential to supersede conventional software tools in the broad field of image processing.

GIFT has the potential to be programmed as independent software or implemented as a module in commercial software packages. Upgrades regarding measuring fiber orientation or computing of three dimensional image stacks are intended for future iterations of the program. Currently, image processing functions in two software programs, ImageJ and OriginPro, are needed for analysis and therefore GIFT has not yet been developed into a standalone program or single ImageJ plugin. Based on the promising results generated by GIFT so far we plan to continue work on the program, which includes adding further functionality to the method and developing GIFT into a freely available standalone application.

In the biomedical and material engineering field, the importance of quality assurance in the growing area of fiber materials continues to increase and GIFT provides the reliable results the field requires. Not being limited to SEM as the only imaging method, GIFT offers promising applications in a wide range of further fields involving images of structures with repetitive or parallel edges.

Data availability

The raw/processed data required to reproduce these findings are available at https://doi.org/10.17632/8zzn96yd54.1 [77].

Impact statement

Nonwoven fiber materials, in particular electrospun fibers, have wide-ranging applications in biosciences, industry, research and medicine. Safe and effective application strongly depends on stable parameters, including the fiber diameter. Computer-supported evaluation of fiber diameters can provide significant advantages over manual quantification methods and is a very promising means to achieve automated quality assurance.

Funding

Partial financial support by the Federal Ministry of Education and Research (BMBF) within RESPONSE “Partnership for Innovation in Implant Technology” and by the European Social Fund (ESF) within the excellence research program of the state Mecklenburg-Vorpommern Card-ii-Omics is gratefully acknowledged. Conflict of interest: Authors state no conflict of interest. Informed consent: Informed consent is not applicable. Ethical approval: The conducted research is not related to either human or animal use.

CRediT authorship contribution statement

Andreas Götz: Conceptualization, Methodology, Software, Validation, Investigation, Data curation, Formal analysis, Writing - original draft, Visualization. **Volkmar Senz:** Resources, Investigation, Writing - review & editing. **Wolfram Schmidt:** Conceptualization, Writing - review & editing. **Jennifer Huling:** Writing - review & editing. **Niels Grabow:** Conceptualization, Project administration, Funding acquisition. **Sabine Illner:** Conceptualization, Resources, Writing - review & editing, Visualization.

Declaration of Competing Interest

The authors declare that they have no known competing financial interests or personal relationships that could have appeared to influence the work reported in this paper.

Acknowledgements

The authors would like to thank Jonathan Ortelt, Manfred Strotmeier, Babette Hummel and Katja Hahn for their skillful work.

Appendix A. Supplementary data

Supplementary data to this article can be found online at https://doi.org/10.1016/j.measurement.2021.109265.

References

[1] N.H.A. Ngadiman, M.Y. Noordin, A. Idris, D. Kurniawan, A review of evolution of electrospun tissue engineering scaffold: From two dimensions to three dimensions, Proc. Inst. Mech. Eng. H 231 (2017) 597–616, https://doi.org/10.1177/0954411917699021.

[2] A.J. Hassiba, M.E. El Zowalaty, G.K. Nasrallah, T.J. Webster, A.S. Luyt, A. M. Abdullah, A.A. Elzatahry, Review of recent research on biomedical applications of electrospun polymer nanofibers for improved wound healing, Nanomedicine (Lond.) 11 (2016) 715–737, https://doi.org/10.2217/nnm.15.211.

[3] J.R. Dias, P.L. Granja, P.J. Bártolo, Advances in electrospun skin substitutes, Prog. Mater Sci. 84 (2016) 314–334, https://doi.org/10.1016/j.pmatsci.2016.09.006.

[4] F. Topuz, T. Uyar, Electrospinning of gelatin with tunable fiber morphology from round to flat/ribbon, Mater. Sci. Eng. C Mater. Biol. Appl. 80 (2017) 371–378, https://doi.org/10.1016/j.msec.2017.06.001.

[5] J. Fernández-Pérez, K.E. Kador, A.P. Lynch, M. Ahearne, Characterization of extracellular matrix modified poly(ε-caprolactone) electrospun scaffolds with differing fiber orientations for corneal stroma regeneration, Mater. Sci. Eng. C Mater. Biol. Appl. 108 (2020), 110415, https://doi.org/10.1016/j.msec.2019.110415.

[6] W. Zheng, W. Zhang, X. Jiang, Biomimetic Collagen Nanofibrous Materials for Bone Tissue Engineering, Adv. Eng. Mater. 12 (2010) B451–B466, https://doi.org/10.1002/adem.200980087.

[7] A. Denchai, D. Tartarini, E. Mele, Cellular Response to Surface Morphology: Electrospinning and Computational Modeling, Front. Bioeng. Biotechnol. 6 (2018) 155, https://doi.org/10.3389/fbioe.2018.00155.

[8] H.P. Felgueiras, J.C. Antunes, M.C.L. Martins, M.A. Barbosa, Fundamentals of protein and cell interactions in biomaterials, in: M.A. Barbosa, M.C.L. Martins (Eds.), Peptides and proteins as biomaterials for tissue regeneration and repair, Woodhead publishing an imprint of Elsevier, Duxford, Cambridge, MA, Kidlington, 2018, pp. 1–27.

[9] A.S. Badami, M.R. Kreke, M.S. Thompson, J.S. Riffle, A.S. Goldstein, Effect of fiber diameter on spreading, proliferation, and differentiation of osteoblastic cells on electrospun poly(lactic acid) substrates, Biomaterials 27 (2006) 596–606, https://doi.org/10.1016/j.biomaterials.2005.05.084.

[10] N. Narayanan, C. Jiang, C. Wang, G. Uzunalli, N. Whittern, D. Chen, O.G. Jones, S. Kuang, M. Deng, Harnessing Fiber Diameter-Dependent Effects of Myoblasts Toward Biomimetic Scaffold-Based Skeletal Muscle Regeneration, Front. Bioeng. Biotechnol. 8 (2020) 203, https://doi.org/10.3389/fbioe.2020.00203.

[11] G.T. Christopherson, H. Song, H.-Q. Mao, The influence of fiber diameter of electrospun substrates on neural stem cell differentiation and proliferation, Biomaterials 30 (2009) 556–564, https://doi.org/10.1016/j.biomaterials.2008.10.004.

[12] E. Entekhabi, M. Haghbin Nazarpak, F. Moztarzadeh, A. Sadeghi, Design and manufacture of neural tissue engineering scaffolds using hyaluronic acid and polycaprolactone nanofibers with controlled porosity, Mater. Sci. Eng. C Mater. Biol. Appl. 69 (2016) 380–387, https://doi.org/10.1016/j.msec.2016.06.078.

[13] X. Yan, M. Gevelber, Investigation of electrospun fiber diameter distribution and process variations, J. Electrostat. 68 (2010) 458–464, https://doi.org/10.1016/j.elstat.2010.06.009.

[14] K. Lin, K.-N. Chua, G.T. Christopherson, S. Lim, H.-Q. Mao, Reducing electrospun nanofiber diameter and variability using cationic amphiphiles, Polymer 48 (2007) 6384–6394, https://doi.org/10.1016/j.polymer.2007.08.056.

[15] A. Haider, S. Haider, I.-K. Kang, A comprehensive review summarizing the effect of electrospinning parameters and potential applications of nanofibers in biomedical and biotechnology, Arabian J. Chem. 11 (2018) 1165–1188, https://doi.org/10.1016/j.arabjc.2015.11.015.

[16] S.A. Hosseini Ravandi, N. Pan, Morphological Characterization of Individual Polyacrylonitrile Nanofibers, CNANO 7 (2011) 415–419, https://doi.org/10.2174/157341311795542462.

[17] C.-T. Li, J.V. Tietz, Improved accuracy of the laser diffraction technique for diameter measurement of small fibres, J. Mater. Sci. 25 (1990) 4694–4698, https://doi.org/10.1007/BF01129926.

[18] J.G.N. Baines, A.G. Hallam, K.W. Raine, N.P. Turner, Fiber diameter measurements and their calibration, J. Lightwave Technol. 8 (1990) 1259–1268, https://doi.org/10.1109/50.59149.

[19] C.A. Schneider, W.S. Rasband, K.W. Eliceiri, NIH Image to ImageJ: 25 years of image analysis, Nat. Methods 9 (2012) 671–675, https://doi.org/10.1038/nmeth.2089.

[20] F. Papadopulos, M. Spinelli, S. Valente, L. Foroni, C. Orrico, F. Alviano, G. Pasquinelli, Common tasks in microscopic and ultrastructural image analysis

using ImageJ, Ultrastruct. Pathol. 31 (2007) 401–407, https://doi.org/10.1080/01913120701719189.

[21] J. Schindelin, I. Arganda-Carreras, E. Frise, V. Kaynig, M. Longair, T. Pietzsch, S. Preibisch, C. Rueden, S. Saalfeld, B. Schmid, J.-Y. Tinevez, D.J. White, V. Hartenstein, K. Eliceiri, P. Tomancak, A. Cardona, Fiji: an open-source platform for biological-image analysis, Nat. Methods 9 (2012) 676–682, https://doi.org/10.1038/nmeth.2019.

[22] C.T. Rueden, J. Schindelin, M.C. Hiner, B.E. DeZonia, A.E. Walter, E.T. Arena, K. W. Eliceiri, Image J2: ImageJ for the next generation of scientific image data, BMC Bioinf. 18 (2017) 529, https://doi.org/10.1186/s12859-017-1934-z.

[23] A. Shariff, J. Kangas, L.P. Coelho, S. Quinn, R.F. Murphy, Automated image analysis for high-content screening and analysis, J. Biomol. Screen. 15 (2010) 726–734, https://doi.org/10.1177/1087057110370894.

[24] N.A. Hotaling, K. Bharti, H. Kriel, C.G. Simon, Dataset for the validation and use of DiameterJ an open source nanofiber diameter measurement tool, Data Brief 5 (2015) 13–22, https://doi.org/10.1016/j.dib.2015.07.012.

[25] N.A. Hotaling, K. Bharti, H. Kriel, C.G. Simon, DiameterJ: A validated open source nanofiber diameter measurement tool, pp. 327–338.

[26] N.A. Hotaling, J. Jeon, M.B. Wade, D. Luong, X.-L. Palmer, K. Bharti, C.G. Simon, Training to Improve Precision and Accuracy in the Measurement of Fiber Morphology, PLoS ONE 11 (2016), e0167664, https://doi.org/10.1371/journal.pone.0167664.

[27] L. Garcia, S. Soliman, M.P. Francis, M.J. Yaszemski, J. Doshi, C.G. Simon, R. Robinson-Zeigler, Workshop on the characterization of fiber-based scaffolds: Challenges, progress, and future directions, J. Biomed. Mater. Res. Part B Appl. Biomater. 108 (2020) 2063–2072, https://doi.org/10.1002/jbm.b.34545.

[28] Radical Scientific Equipments Pvt. Ltd., Fiber Pro, 2021. https://www.radicalindia.com/material-fiber.php (accessed 18 January 2021).

[29] Media Cybernetics, Fiber Thickness App, 2021. https://www.mediacy.com/support/imagepro/appcenter/fiber-thickness-detail (accessed 18 January 2021.

[30] Thermo Fisher Scientific, Phenom FiberMetric Software, 2021. https://www.thermofisher.com/de/de/home/electron-microscopy/products/software-em-3d-vis/fibermetric-software.html (accessed 18 January 2021).

[31] Sympatec GmbH, PAQXOS, 2021. https://www.sympatec.com/en/particle-measurement/application-software/paqxos/ (accessed 18 January 2021).

[32] S. Baheti, M. Tunak, Characterization of fiber diameter using image analysis, IOP Conf. Ser.: Mater. Sci. Eng. 254 (2017), 142002, https://doi.org/10.1088/1757-899X/254/14/142002.

[33] B. Pourdeyhimi, R. Dent, Measuring Fiber Diameter Distribution in Nonwovens, Text. Res. J. 69 (1999) 233–236, https://doi.org/10.1177/004051759906900401.

[34] M. Ziabari, V. Mottaghitalab, A.K. Haghi, Application of direct tracking method for measuring electrospun nanofiber diameter, Braz. J. Chem. Eng. 26 (2009) 53–62, https://doi.org/10.1590/S0104-66322009000100006.

[35] M. Ziabari, V. Mottaghitalab, A.K. Haghi, Distance transform algorithm for measuring nanofiber diameter, Korean J. Chem. Eng. 25 (2008) 905–918, https://doi.org/10.1007/s11814-008-0149-4.

[36] M. Ziabari, V. Mottaghitalab, S.T. McGovern, A.K. Haghi, A New Image Analysis Based Method for Measuring Electrospun Nanofiber Diameter, Nanoscale Res Lett 2 (2007) 597–600, https://doi.org/10.1007/s11671-007-9093-1.

[37] E. Tomba, P. Facco, M. Roso, M. Modesti, F. Bezzo, M. Barolo, Artificial Vision System for the Automatic Measurement of Interfiber Pore Characteristics and Fiber Diameter Distribution in Nanofiber Assemblies, Ind. Eng. Chem. Res. 49 (2010) 2957–2968, https://doi.org/10.1021/ie901179m.

[38] L. Zhang, W. Yu, Orientation image analysis of electrospun submicro-fibers based on Hough transform and Regionprops function, Text. Res. J. 87 (2017) 2263–2274, https://doi.org/10.1177/0040517516669070.

[39] J.J. Stanger, N. Tucker, N. Buunk, Y.B. Truong, A comparison of automated and manual techniques for measurement of electrospun fibre diameter, Polym. Test. 40 (2014) 4–12, https://doi.org/10.1016/j.polymertesting.2014.08.002.

[40] X.M. Zhang, R.W. Wang, H.B. Wu, B. Xu, Automated measurements of fiber diameters in melt-blown nonwovens, J. Ind. Text. 43 (2014) 593–605, https://doi.org/10.1177/1528083712471696.

[41] N.J. Schaub, S.J. Kirkpatrick, R.J. Gilbert, Automated Methods to Determine Electrospun Fiber Alignment and Diameter Using the Radon Transform, BioNanoSci. 3 (2013) 329–342, https://doi.org/10.1007/s12668-013-0100-y.

[42] E. Öznergiz, Y.E. Kiyak, M.E. Kamasak, I. Yildirim, Automated Nanofiber Diameter Measurement in SEM Images Using a Robust Image Analysis Method, J. Nanomater. 2014 (2014) 1–6, https://doi.org/10.1155/2014/738490.

[43] D. RanjanNayak, S. Kumar Sahu, J. Mohammed, A Cellular Automata based Optimal Edge Detection Technique using Twenty-Five Neighborhood Model, IJCA 84 (2013) 27–33, https://doi.org/10.5120/14614-2869.

[44] M. Hasanzadeh Mofrad, S. Sadeghi, A. Rezvanian, M.R. Meybodi, Cellular edge detection: Combining cellular automata and cellular learning automata, AEU –Int. J. Electron. Commun. 69 (2015) 1282–1290, https://doi.org/10.1016/j.aeue.2015.05.010.

[45] I. Usov, R. Mezzenga, FiberApp: An Open-Source Software for Tracking and Analyzing Polymers, Filaments, Biomacromolecules, and Fibrous Objects, Macromolecules 48 (2015) 1269–1280, https://doi.org/10.1021/ma502264c.

[46] A. Boudaoud, A. Burian, D. Borowska-Wykręt, M. Uyttewaal, R. Wrzalik, D. Kwiatkowska, O. Hamant, FibrilTool, an ImageJ plug-in to quantify fibrillar structures in raw microscopy images, Nat. Protoc. 9 (2014) 457–463, https://doi.org/10.1038/nprot.2014.024.

[47] F.e.V. SKZ, FiVer, 2021. https://www.skz.de/de/forschung/geschaeftsfelder/spritzgiessen-neu/dienstleistungen/7313.Faserlaengenverteilung.html (accessed 18 January 2021).

[48] E.E. Morrill, A.N. Tulepbergenov, C.J. Stender, R. Lamichhane, R.J. Brown, T. J. Lujan, A validated software application to measure fiber organization in soft tissue, Biomech. Model. Mechanobiol. 15 (2016) 1467–1478, https://doi.org/10.1007/s10237-016-0776-3.

[49] E.H. Shin, K.S. Cho, M.H. Seo, H. Kim, Determination of electrospun fiber diameter distributions using image analysis processing, Macromol. Res. 16 (2008) 314–319, https://doi.org/10.1007/BF03218523.

[50] P.C. Reyes-Fernandez, B. Periou, X. Decrouy, F. Relaix, F.J. Authier, Automated image-analysis method for the quantification of fiber morphometry and fiber type population in human skeletal muscle, Skelet. Muscle 9 (2019) 15, https://doi.org/10.1186/s13395-019-0200-7.

[51] J.P. Chiverton, A. Kao, M. Roldo, G. Tozzi, Automatic diameter and orientation distribution determination of fibrous materials in micro X-ray CT imaging data, J. Microsc. 272 (2018) 180–195, https://doi.org/10.1111/jmi.12719.

[52] J.D. Eekhoff, S.P. Lake, Three-dimensional computation of fibre orientation, diameter and branching in segmented image stacks of fibrous networks, J. R. Soc. Interface 17 (2020) 20200371, https://doi.org/10.1098/rsif.2020.0371.

[53] A. Youssef, A. Hrynevich, L. Fladeland, A. Balles, J. Groll, P.D. Dalton, S. Zabler, The Impact of Melt Electrowritten Scaffold Design on Porosity Determined by X-Ray Microtomography, Tissue Eng. Part C Methods 25 (2019) 367–379, https://doi.org/10.1089/ten.TEC.2018.0373.

[54] T. Blachowicz, A. Ehrmann, Investigating surface properties of fibers and yarns by image processing and statistical analysis techniques, in: Applications of Computer Vision in Fashion and Textiles, WOODHEAD, 2017, pp. 105–121.

[55] R. Murphy, A. Turcott, L. Banuelos, E. Dowey, B. Goodwin, K.O.'H. Cardinal, SIMPoly: A Matlab-Based Image Analysis Tool to Measure Electrospun Polymer Scaffold Fiber Diameter, Tissue Eng. Part C Methods 26 (2020) 628–636, https://doi.org/10.1089/ten.TEC.2020.0304.

[56] T. Ferreira, W. Rasband, ImageJ User Guide: ImageJ/Fiji 1.46, 2012, p. 107.

[57] P. Karas, V. Morard, J. Bartovský, T. Grandpierre, E. Dokládalová, P. Matula, P. Dokládal, GPU implementation of linear morphological openings with arbitrary angle, J. Real-Time Image Proc. 10 (2015) 27–41, https://doi.org/10.1007/s11554-012-0248-7.

[58] P. Soille, E.J. Breen, R. Jones, Recursive implementation of erosions and dilations along discrete lines at arbitrary angles, IEEE Trans. Pattern Anal. Machine Intell. 18 (1996) 562–567, https://doi.org/10.1109/34.494646.

[59] K.R. Castleman, Digital image processing, Prentice Hall, Upper Saddle River, NJ, 1996.

[60] P. Soille, Morphological Image Analysis, Springer, Berlin, Heidelberg, 1999.

[61] A. Götz, V. Senz, S. Illner, N. Grabow, Computed fiber evaluation of SEM images using DiameterJ: Capabilities and limitations, Curr. Direct. Biomed. Eng. 6 (2020), https://doi.org/10.1515/cdbme-2020-3113.

[62] N. Narisetti, M. Henke, C. Seiler, R. Shi, A. Junker, T. Altmann, E. Gladilin, Semi-automated Root Image Analysis (saRIA), Sci. Rep. 9 (2019) 19674, https://doi.org/10.1038/s41598-019-55876-3.

[63] Z. Fan, J. Lu, C. Wei, H. Huang, X. Cai, X. Chen, A Hierarchical Image Matting Model for Blood Vessel Segmentation in Fundus Images, IEEE Trans. Image Process. (2018) 2367–2377, https://doi.org/10.1109/TIP.2018.2885495.

[64] C. Oettmeier, H.-G. Döbereiner, A lumped parameter model of endoplasm flow in Physarum polycephalum explains migration and polarization-induced asymmetry during the onset of locomotion, PLoS ONE 14 (2019), e0215622, https://doi.org/10.1371/journal.pone.0215622.

[65] A.E. Hall, L. Vitale, M.J. Kingsford, Planktonic larval duration, early growth, and the influence of dietary input on the otolith microstructure of Scolopsis bilineatus (Nemipteridae), Environ. Biol. Fish 102 (2019) 541–552, https://doi.org/10.1007/s10641-019-00852-z.

[66] S. Lechthaler, P. Colangeli, M. Gazzabin, T. Anfodillo, Axial anatomy of the leaf midrib provides new insights into the hydraulic architecture and cavitation patterns of Acer pseudoplatanus leaves, J. Exp. Bot. 70 (2019) 6195–6201, https://doi.org/10.1093/jxb/erz347.

[67] Z. Sun, T. Cui, Y. Zhu, W. Zhang, S. Shi, S. Tang, Z. Du, C. Liu, R. Cui, H. Chen, X. Guo, The mechanical principles behind the golden ratio distribution of veins in plant leaves, Sci. Rep. 8 (2018) 13859, https://doi.org/10.1038/s41598-018-31763-1.

[68] G. Bueno, O. Deniz, A. Pedraza, J. Ruiz-Santaquiteria, J. Salido, G. Cristóbal, M. Borrego-Ramos, S. Blanco, Automated Diatom Classification (Part A): Handcrafted Feature Approaches, Appl. Sci. 7 (2017) 753, https://doi.org/10.3390/app7080753.

[69] S.J. Newman, B.C. Jayne, Crawling without wiggling: muscular mechanisms and kinematics of rectilinear locomotion in boa constrictors, J. Exp. Biol. 221 (2018), https://doi.org/10.1242/jeb.166199.

[70] E.J. Leonard, R.T. Pappalardo, A. Yin, Analysis of very-high-resolution Galileo images and implications for resurfacing mechanisms on Europa, Icarus 312 (2018) 100–120, https://doi.org/10.1016/j.icarus.2018.04.016.

[71] A. Mohan, S. Poobal, Crack detection using image processing: A critical review and analysis, Alexandria Eng. J. 57 (2018) 787–798, https://doi.org/10.1016/j.aej.2017.01.020.

[72] V. Martínez-Martínez, M. del Alamo-Sanza, M. Menéndez-Miguélez, I. Nevares, Method to estimate the medullar rays angle in pieces of wood based on tree-ring structure: application to planks of Quercus petraea, Wood Sci. Technol. 52 (2018) 519–539, https://doi.org/10.1007/s00226-017-0979-5.

[73] C. McKenna Neuman, o. Bédard, A wind tunnel investigation of particle segregation, ripple formation and armouring within sand beds of systematically varied texture, Earth Surf. Process. Landforms 42 (2017) 749–762, https://doi.org/10.1002/esp.4019.

[74] M.G.A. Lapotre, R.C. Ewing, C.M. Weitz, K.W. Lewis, M.P. Lamb, B.L. Ehlmann, D. M. Rubin, Morphologic Diversity of Martian Ripples: Implications for Large-Ripple Formation, Geophys. Res. Lett. 45 (2018) 10229–10239, https://doi.org/10.1029/2018GL079029.

[75] N. Wang, W. Jiang, Y. Zhang, Misalignment measurement with dual-frequency moiré fringe in nanoimprint lithography, Opt. Express 28 (2020) 6755–6765, https://doi.org/10.1364/OE.382413.

[76] P. Drotár, J. Mekyska, I. Rektorová, L. Masarová, Z. Smékal, M. Faundez-Zanuy, Decision support framework for Parkinson's disease based on novel handwriting markers, IEEE Trans. Neural Syst. Rehabil. Eng. 23 (2015) 508–516, https://doi.org/10.1109/TNSRE.2014.2359997.

[77] A. Götz, GIFT raw data, Mendeley, 2020.

Supporting Information

Content:

SI 1 Process steps of GIFT

The flowchart of GIFT shows the main steps of image processing from an initial SEM image to the final histogram of frequency distribution of fiber diameters

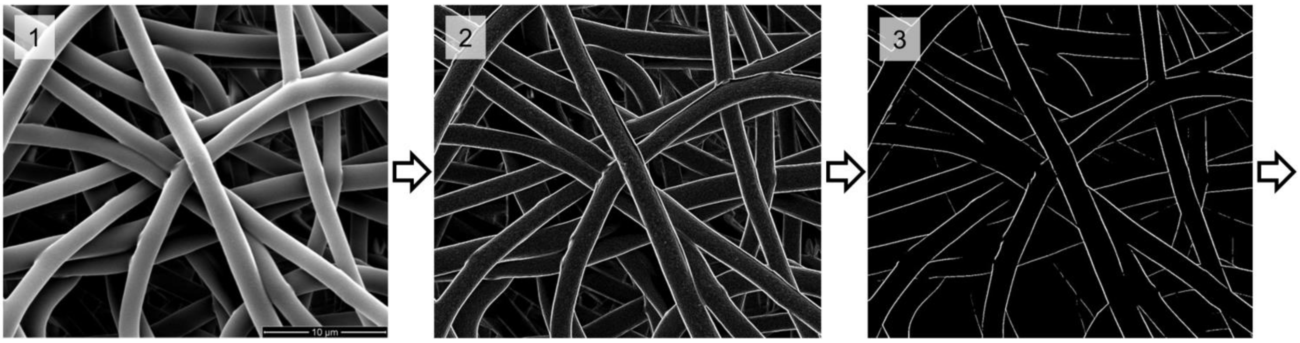

Initial SEM-image **Edge detection** **Binarization**

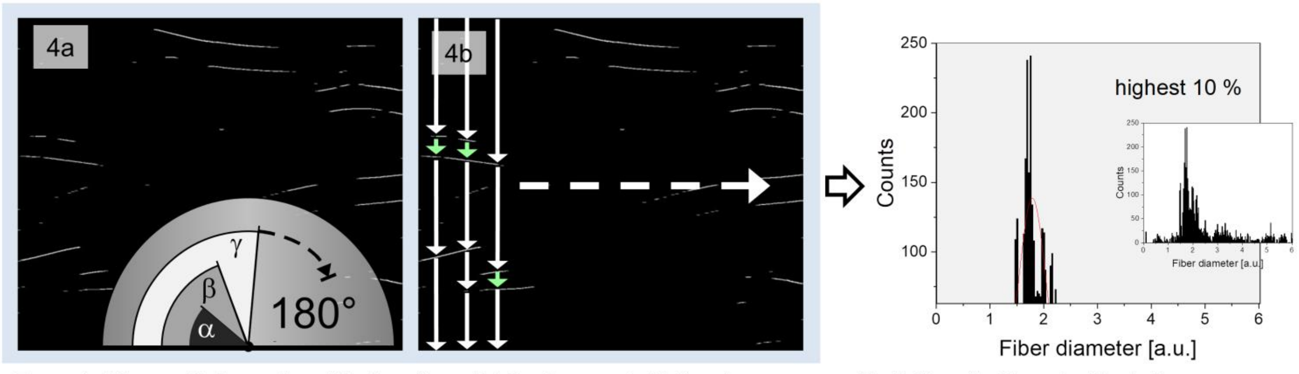

Repeated for multiple angles: Filtering of parallel line fragments (4a) and measuring of distances for every pixel column (4b)

Statistics: final bar chart including Gaussian fit, complete dataset as inset

Fig. S1. Flowchart. The flowchart of GIFT shows the main steps of image processing from an initial SEM image (1) to the final histogram of frequency distribution of fiber diameters. After edge detection (2) a binarized image of fiber edges (3) undergoes a special line opening filter which selects horizontal line fragments of a certain minimum length (4a) and an algorithm measures the distances between these remaining line fragments in the perpendicular direction for every pixel column (4b). The filtering and measurement is repeated for several angles on each image and a histogram is generated based on the distance measurements. The final histogram displays the highest 10% of counts and a Gaussian fit indicates the fiber diameter distribution.

SI 2 Peak shift by line inclination, and missing data due to unmeasured fibers

The measurement at four angle steps generates adequate results. Measurements of more angles increase the statistical certainty and the calculative effort. The four angle method achieves an adequate final result (Fig. S2).

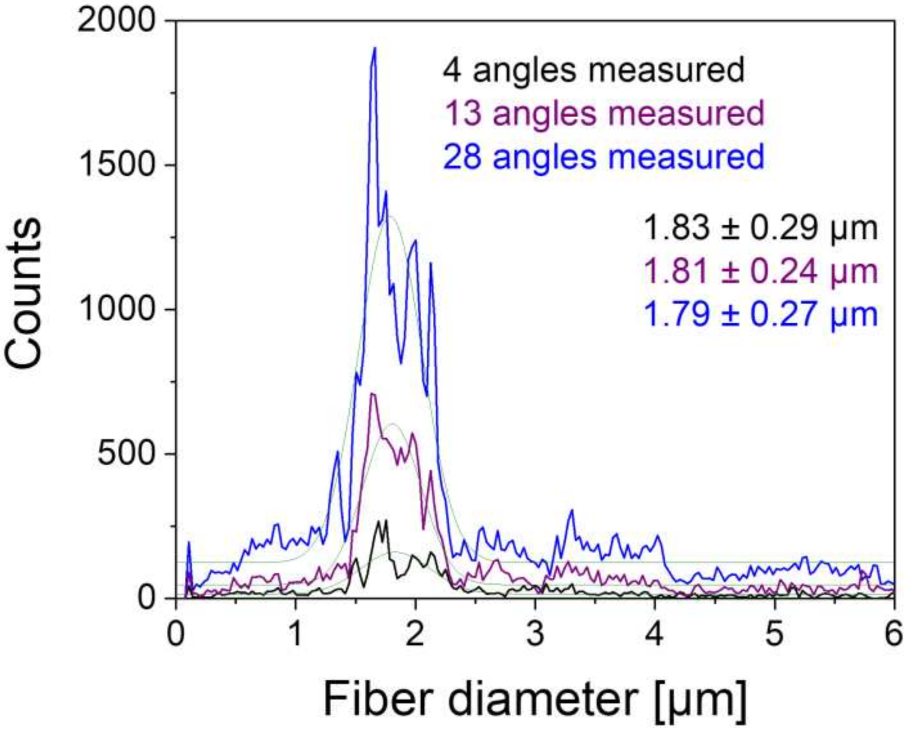

Fig. S2. Multiple measured angles vs. 4 angle method, comparison. The SEM image containing midsize fibers was measured using different numbers of angle steps. Diameter quantification based on 4 angle steps, which was the method used in the in benchmarking experiments (black), was compared to quantification using 13 (violet) and 28 (blue) rotation steps. 13 rotation steps are sufficient to analyze the full area of an image, ensuring that no fibers are missed due to their initial orientation. 28 angle steps (from the data generated in Fig. 3) represents a data set with redundant measurements, because the measured area partially overlaps from one angle step to the next. The full data sets are shown, without the noise removed. The average fiber diameter and standard deviation calculated from each data set is shown in the corresponding color and demonstrated that the number of rotation steps did not affect the results.

The majority of segmented lines appear in a thickness of one or two pixels, sometimes with sections of three pixels or more. After performing the line opening filter, only horizontal lines of at least eight pixels (by default) in length remain. They can be slightly angled, forming a stair-step pattern. The distances between slightly inclined lines are measured and contribute to the data. Due to the oblique trajectory through the parallel fiber edges the values for fiber diameter can be overestimated by a few percent. Fig. S3. gives an overview about that issue. The given numbers in the figure refer to maximum values. Additionally, the segmented line thickness depends on the segmentation threshold, as demonstrated in Fig. S4. When processing images in unfavorable conditions, assuming a line thickness of three pixels, the lines appear randomly in all angles and will be measured with the same probability. Hence, on average we expect half of the maximum value contributing to the data. That means an overestimation of fiber diameter of roughly 2.7 percent. As all thinner lines also exist in a real image and are measured, they contribute with less overestimation to the data. All in all, roughly less than two percent final overestimation seems to be a reasonable estimation. Considering every SEM image is different, and lines are segmented differently, this example is only a general estimation of scale. A rough calculation can be used to illustrate it: an example fiber diameter of around 2 µm would show a peak shift of 0.04 µm (2% of 2 µm), which is not noticeable change within the typical peak width of 0.75 µm. In actuality, that shift does not really lower the result. It also shows that if there are some small sections of thicker lines of four or more pixels, they will not significantly diminish the results, as confirmed by evaluation of numerous images.

Missing data due to unmeasured fibers are a second effect of thin lines and only measuring at four different angle steps. Under theoretically unfavorable conditions 69 percent (only a line thickness of 1 pixel), 38 percent (only a line thickness of 2 pixels), or 18 percent (only a line thickness of 3 pixels) of image data would not contribute to the result. For example, if only one pixel thick lines are segmented, data of the current measurement angle ±7 degrees contribute to the result. There could still be gaps of 31 degrees (45°-(2 x 7°)). Theoretically about half of the image could be missing. But actual segmented SEM images always contain different line thicknesses, even most lines in the segmented phantom image are two pixels thick.

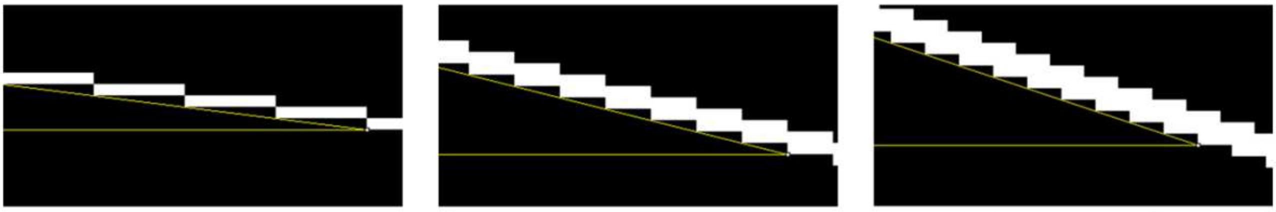

horizontal line length 8 pixel
line thickness 1 pixel
maximal angle 7.13°
maximal overestimation 0.8%

line thickness 2 pixel
maximal angle 14.04°
maximal overestimation 3.1%

line thickness 3 pixel
maximal angle 18.43°
maximal overestimation 5.4%

Fig. S3. Maximal overestimation by line inclination. Fiber margins can be segmented as lines of different thickness. After performing the line opening filter only horizontal line fragments of at least the filtered length (e.g. 8 pixels) remain. Hence, inclined fiber margins appear as stairs-like lines of a maximal possible angle, as mentioned in the image. Due to the non-perpendicular trajectory through the parallel fiber margins the distance will be overestimated (triangulation). The maximal overestimation is 0.8% for 1pixel thick lines, 3.1% for 2 pixels thick lines, and 5.4% for 3 pixels thick lines.

SI 3 Segmentation threshold

The segmentation threshold defines the grayscale value, above which the fiber edge will be segmented. Image parts of grayscale values below the threshold will remain black, as illustrated in Fig. S4.

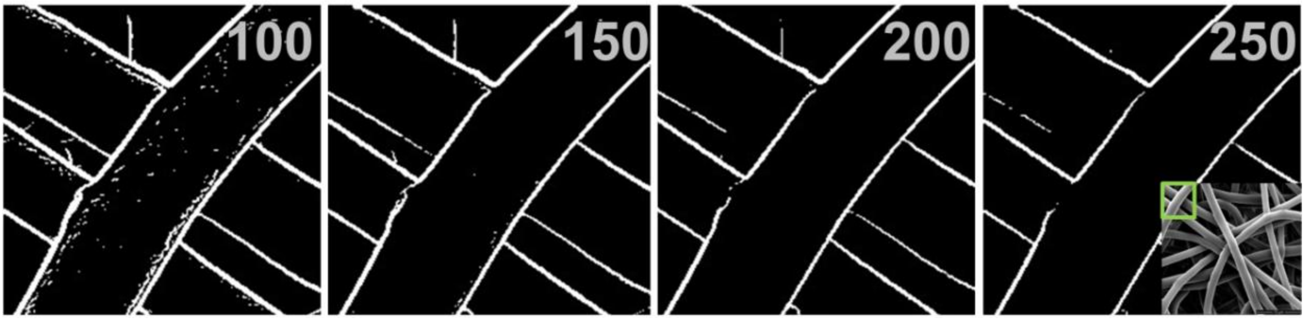

Fig. S4. Influence of segmentation threshold. The segmentation threshold influences the thickness of segmented lines, as well as the content of mottling from the fiber surface. A high value guarantees thin lines and less mottling. The numbers in the image corners specify the segmentation threshold; the small inset indicates the original image section.

SI 4 Filtered line length

For comparison the SEM image containing two different fiber types was processed twice using filtered line lengths of five and eight (segmentation threshold 240). Four peak results were generated, as presented in Fig. S5 and Table S1. The shorter filtered line length (5) results in more counts because of more data from more line fragments. For the longer filtered line length (8) the peaks appear smaller in height and partly in width because of fewer counts. But the peaks are located at the same position, in both cases, which means equivalent results.

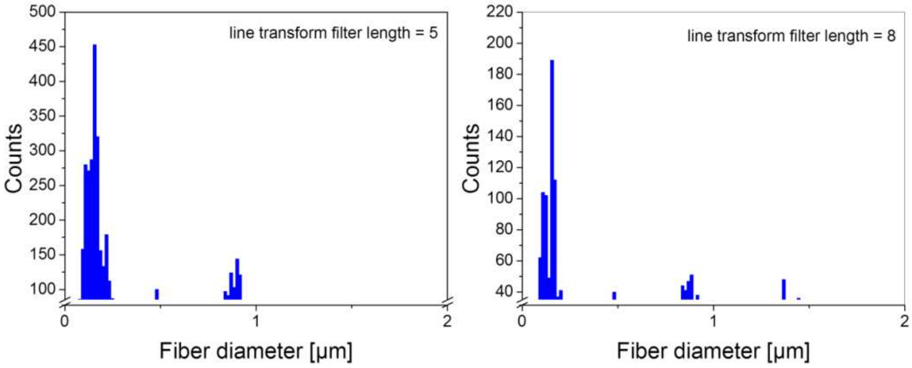

Fig. S5. Influence of line opening filter length. GIFT results for SEM image of dual fibers comparing the effect of different values (5 and 8) for the line opening filter. The fiber peaks are of different height, but are located at the same position, indicating an accurate fiber diameter measurement.

Filtered line length	Threshold for highest 10%	Peak range [µm]	Maximal counts	Maximum location [µm]
5	85	0.078 – 0.25	453	0.16
5	85	0.84 – 0.92	144	0.90
8	35	0.093 – 0.19	189	0.16
8	35	0.84 – 0.92	51	0.89

Table S1 Results of different line opening filter length. Results for SEM image of dual fibers comparing the effect of different values (5 and 8) for the line opening filter. Due to less data the fiber peaks are smaller using a filtered length of eight.

SI 5 Total error for the phantom image

Data obtained by Gaussian fit, relative errors were calculated by SD/peak center value.

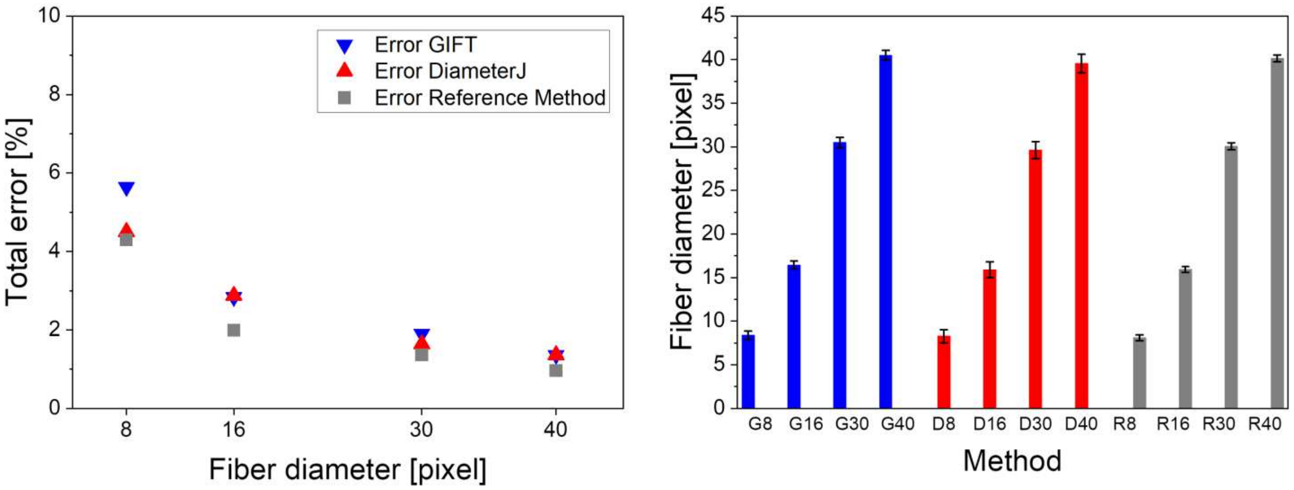

Fig. S6. **Total error graph.** Comparison of total errors of fiber diameters in the phantom image (referring to Fig. 1, A). For fiber thicknesses of 8, 16, 30, and 40 pixels the errors are displayed. DiameterJ generates data for fiber radii. The relative errors are of similar value, hence the absolute error doubles for the fiber diameters.

Fiber thickness	**Error GIFT (method) [%]**	**Error DiameterJ (method) [%]**	**Error Reference (method) [%]**
8	5.6	4.5	4.3
16	2.8	2.9	2.0
30	1.9	1.6	1.4
40	1.4	1.4	1.0

Table S2 **Total error table.** Comparison of total errors of fiber diameters in the phantom image (referring to Fig.1, A). Error calculated by Gaussian fit deviation divided by peak center. For fiber thicknesses of 8, 16, 30, and 40 pixels the errors are displayed. DiameterJ generates data for fiber radii. The relative errors are of similar value; hence the absolute error doubles for the fiber diameters.

SI 6 Potential segmentation mismatch of grayscale value focusing methods

Fiber segmentation of grayscale value focused methods like DiameterJ can result in mis-interpretation of fiber diameters. Due to fibers with a gradient of brightness, segmentation finds the brightest areas, but darker parts can get lost. Consequently such fiber segments are measured incompletely because of faulty skeletonization. As the example shows, faulty center lines of fibers (skeleton lines) lead to inaccurate and underestimated results (Fig. S7). Hence in the final histograms wide peaks in the small diameters range can lead to false interpretation of the data.

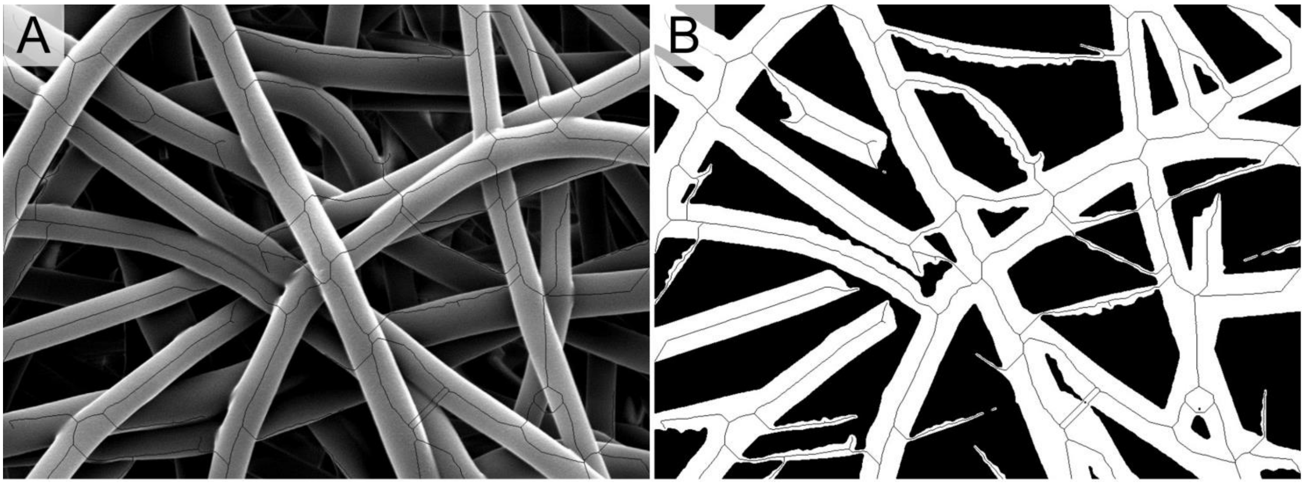

Fig. S7. Segmentation by DiameterJ. Data misinterpretation can occur when performing grayscale value focused methods. Overlay of skeleton lines on SEM image containing midsize fibers (A) and the corresponding segmented image (B). Drift of fiber center line due to a gradient of grayscale value on fiber surface is visible using DiameterJ. Incompletely segmented fiber parts appear as irregular shaped thin areas, and cause faulty peaks in final histogram due to underestimated diameters.

SI 7 Capability of fiber detection

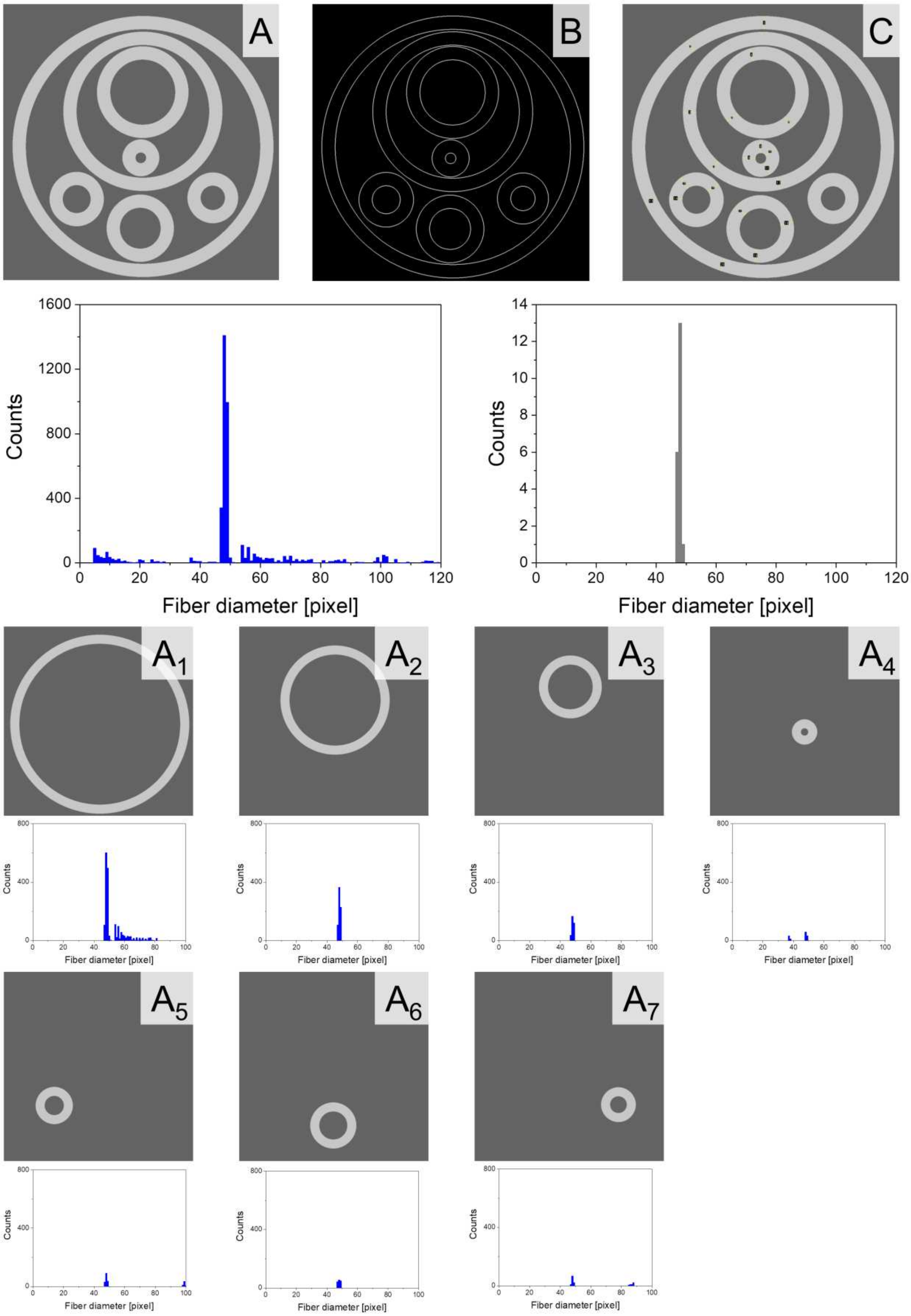

Fig. S8. Fiber bending radius and orientation. Test image with circular ring shaped fibers of different bending and angle orientation (A), segmented fiber edges by GIFT (B), reference measurement (n = 20) by manual quantification (C), upper left graph: result of GIFT for the complete test image A, upper right graph: result of reference measurement in test image C, completely processed test images of every single ring shaped fiber (A_1 to A_7).

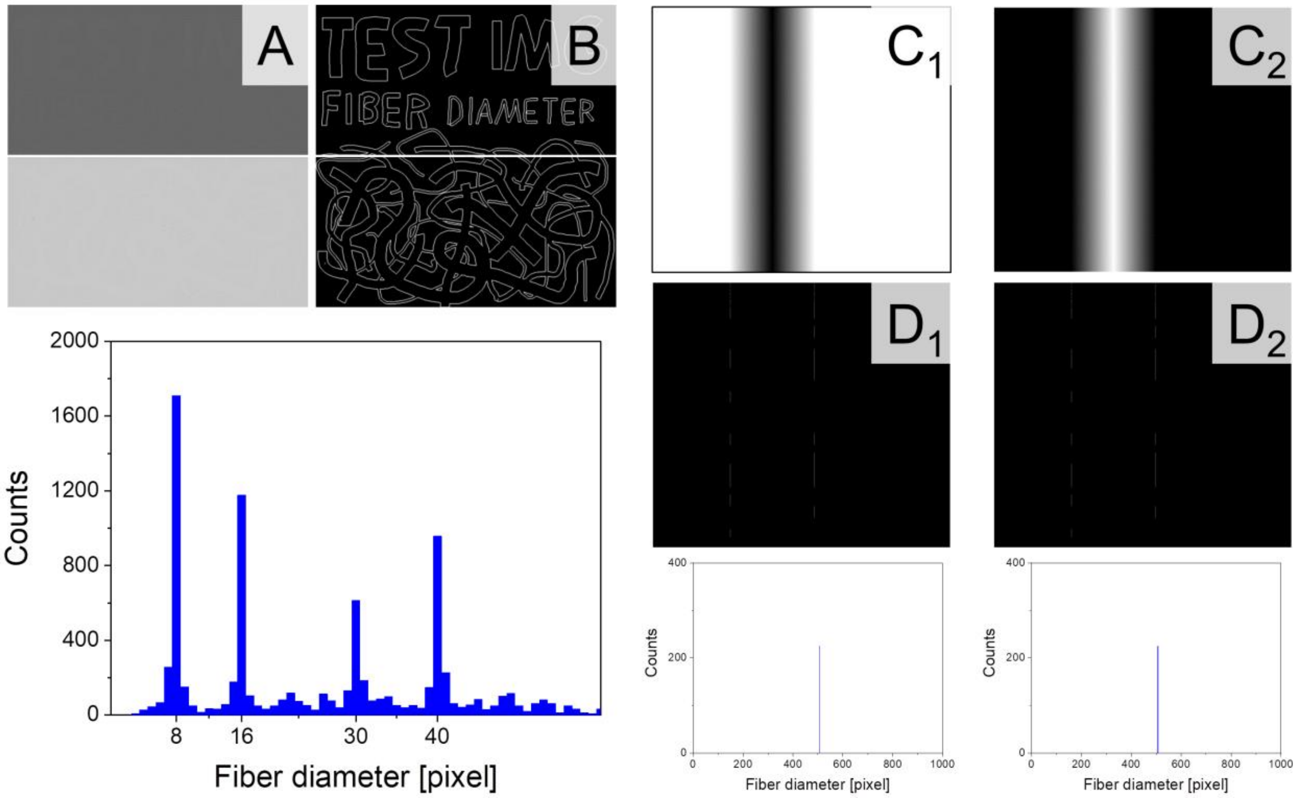

Fig. S9. **Minimal contrast, and gradient of grayscale value.** Phantom image with minimal fiber background contrast (Gradation of one grayscale), exemplified on fiber values 101 and 201 using background values of 100 and 200, respectively (A), segmented fiber edges by GIFT using a segmentation threshold of 2 (B). In each experiment the whole image (letter shaped fibers and random fibers) was processed, only half the image is displayed here (A, B). An image was processed, containing fibers of a gradient of grayscale values. Images contain a fiber with a diameter of 508 pixels, linear increasing/decreasing grayscale values 253 ⇨ 0 ⇨ 253 or 2 ⇨ 255 ⇨ 2 respectively, background is white or black (C_1, C_2).Resulting segmented fiber edges by GIFT using a segmentation threshold of 12 (D_1, D_2). Left graph: result of GIFT for the phantom image of minimal contrast. Right graphs: results of GIFT for the fiber with grayscale gradient with lowest possible contrast to background.

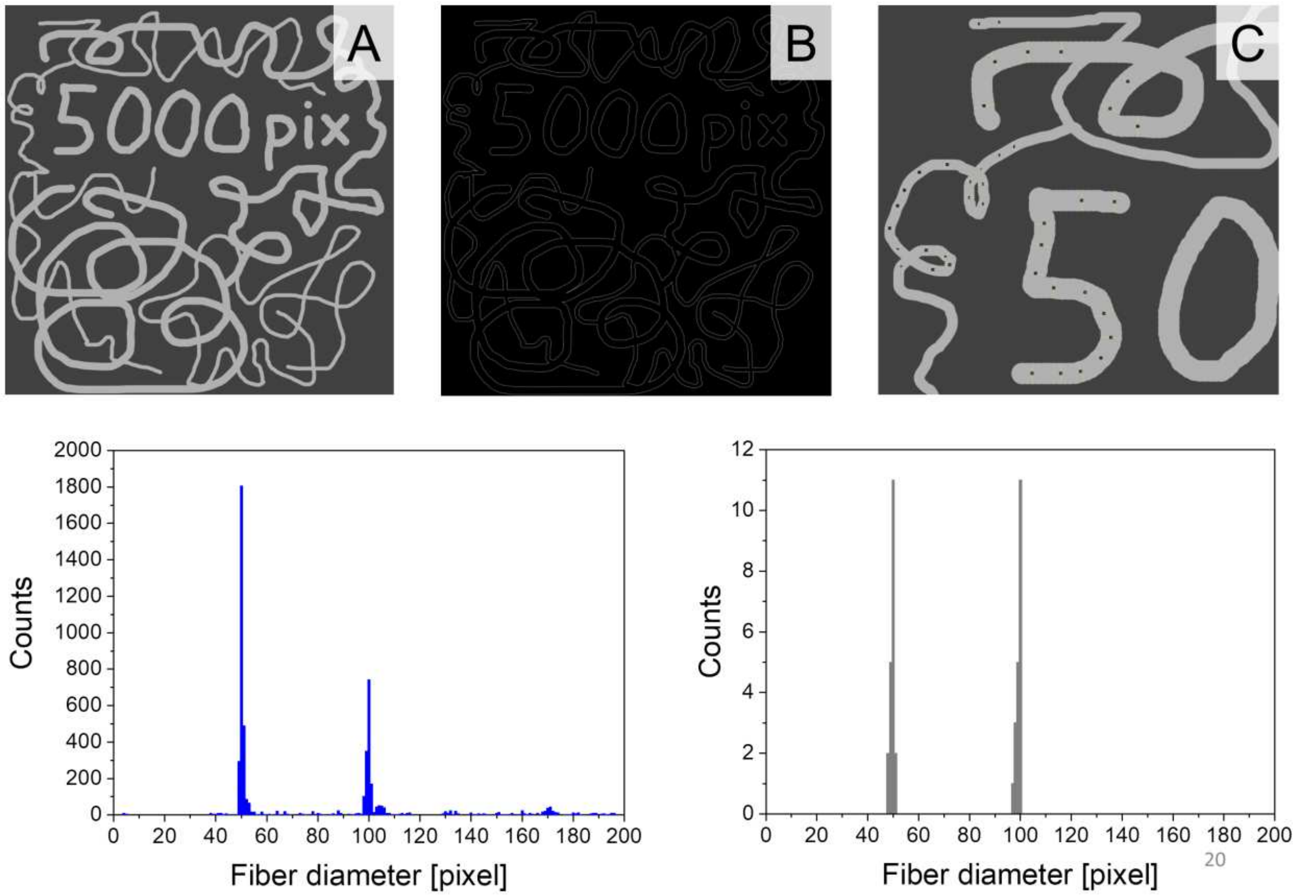

Fig. S10. Image size beyond ordinary images. Image size of 5000 pixel (A), segmented fiber edges by GIFT (B), reference measurement by manual method (C), left graph: result of GIFT, right graph: result of reference measurement.

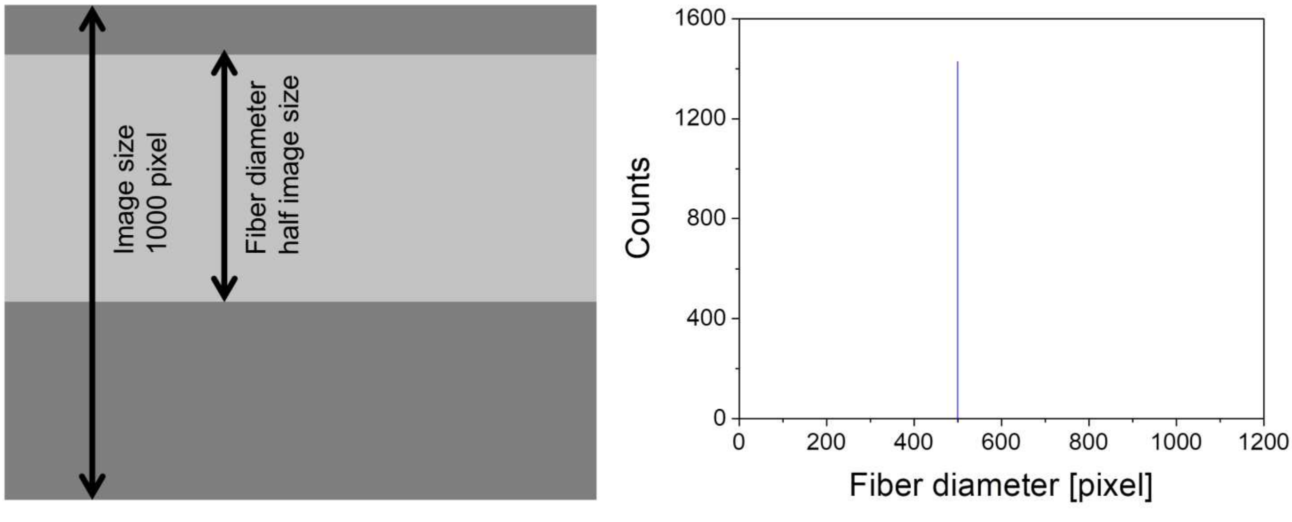

Fig. S11. Fiber diameter beyond ordinary range. Left: test image of thick fiber (bright gray) on dark background, right: result of GIFT. Fiber diameters up to half of the image size can be measured. Due to the pixel counting algorithm running over the image boundary, a single fiber of higher diameter causes a second peak of lower value (image size minus fiber diameter).

SI 8 Potential applications for GIFT in different fields

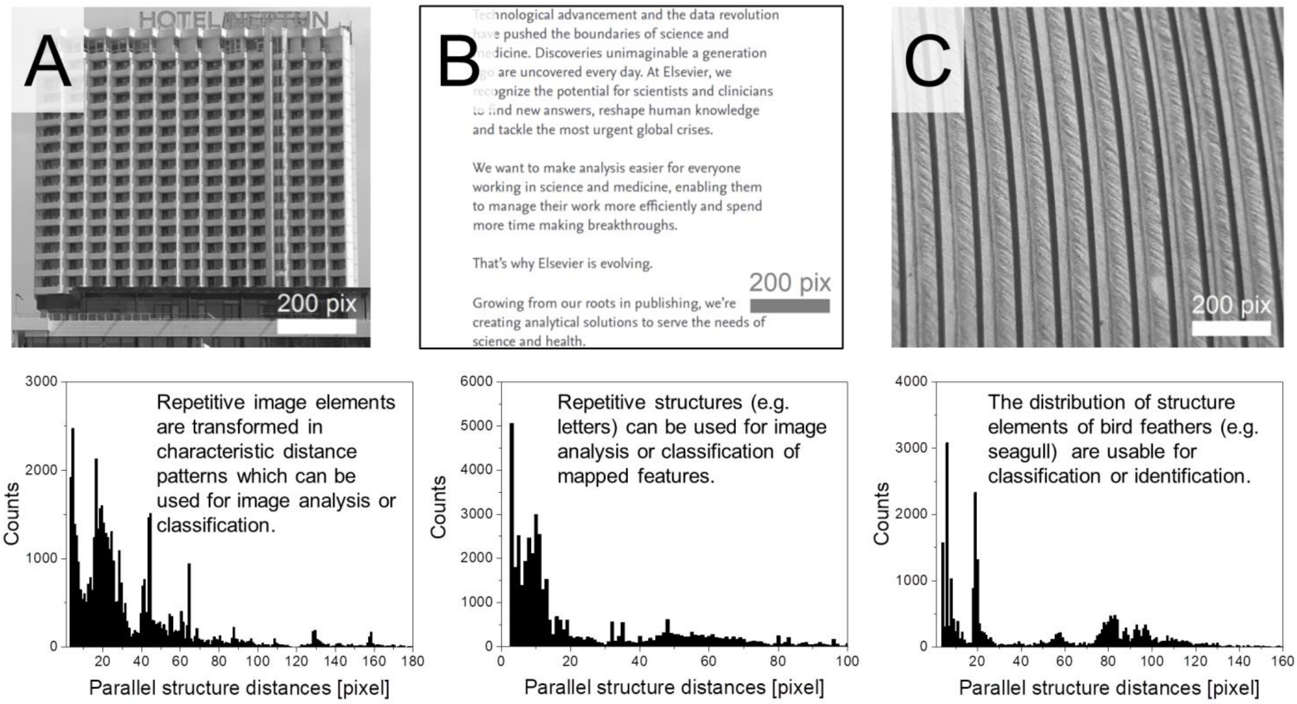

Technological advancement and the data revolution have pushed the boundaries of science and medicine. Discoveries unimaginable a generation ago are uncovered every day. At Elsevier, we recognize the potential for scientists and clinicians to find new answers, reshape human knowledge and tackle the most urgent global crises.

We want to make analysis easier for everyone working in science and medicine, enabling them to manage their work more efficiently and spend more time making breakthroughs.

That's why Elsevier is evolving.

Growing from our roots in publishing, we're creating analytical solutions to serve the needs of science and health.

Repetitive image elements are transformed in characteristic distance patterns which can be used for image analysis or classification.

Repetitive structures (e.g. letters) can be used for image analysis or classification of mapped features.

The distribution of structure elements of bird feathers (e.g. seagull) are usable for classification or identification.

Fig. S12. Further applications 1. GIFT is useful for various applications other than fiber measurement. The distribution of any repetitive structures in images can be used to analyze or classify imaged objects (A, B). Structures of biological objects like bird feathers can be investigated for classification or in situ studies e.g. altered mechanical stress (C).

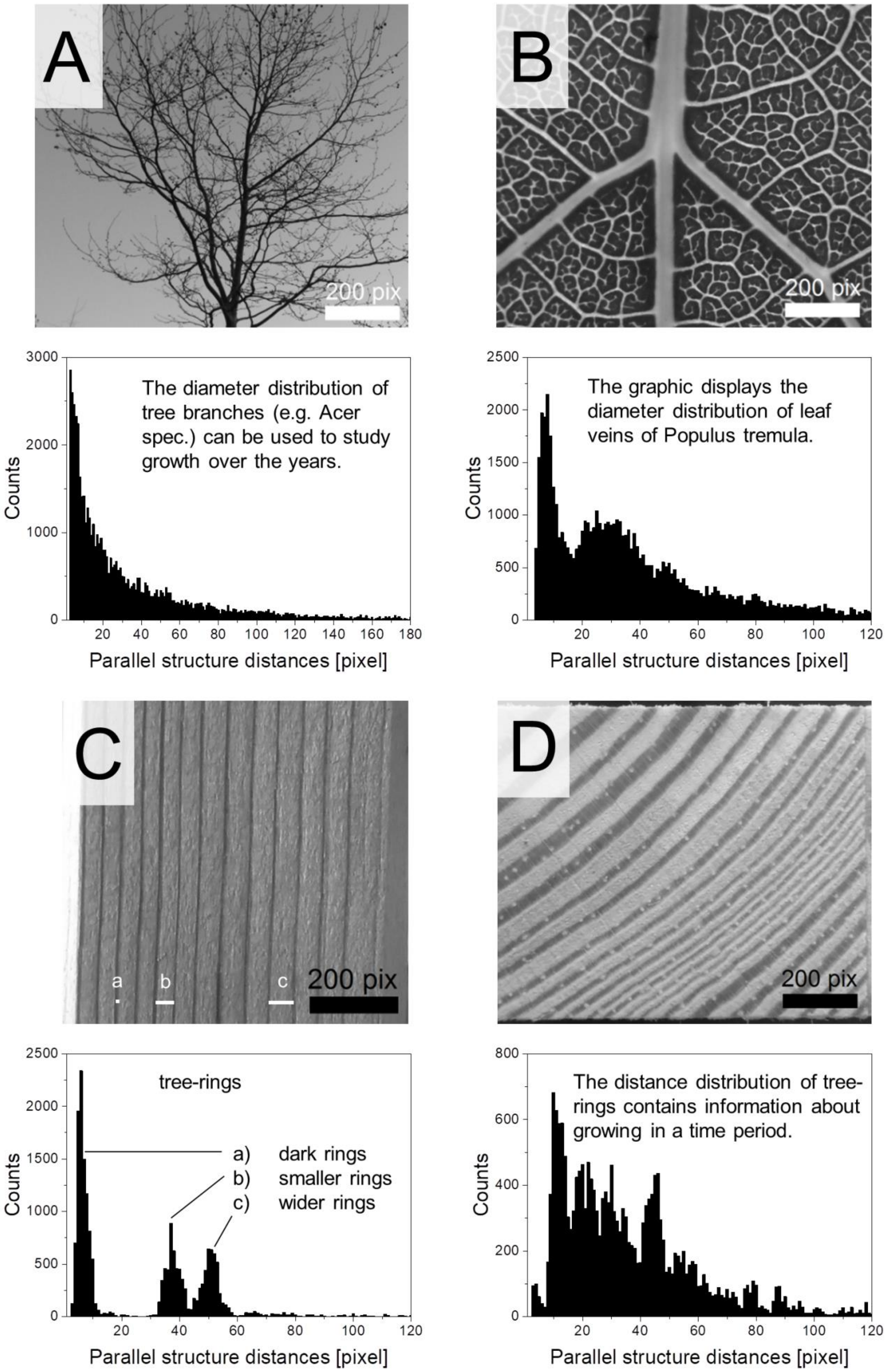

Fig. S13. **Further applications 2.** GIFT is useful for various applications other than fibers. The diameter of tree branches (or roots) can be measured for growth studies; the diameter distribution may contain information about damage or diseases (A). Leaf veins may grow differently or change diameters depending on water supply (B). The structure of wood and tree-rings contains information in their distance distribution about climate-depending growth over decades (C, D).

SI 9 Segmented images (DiameterJ)

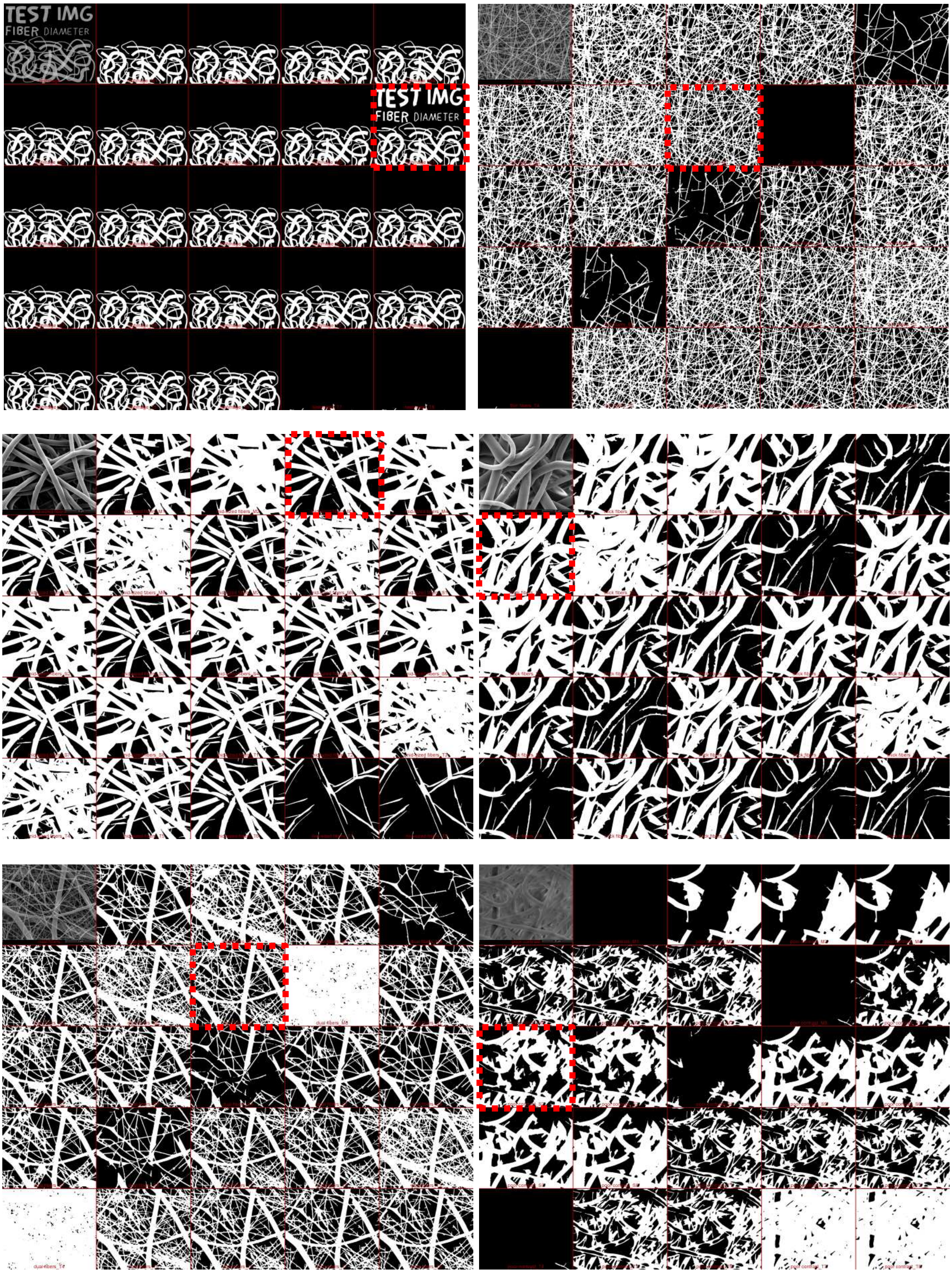

Fig. S14. Segmented images by DiameterJ (raw data). DiameterJ provides three different segmentation algorithms which generate eight segmented images each (M1 – M8, S1 – S8, T1 – T8), the user has to subjectively choose one. The red rectangles indicate the selected segmented images, which were used in this work.

RESEARCH ARTICLE

GIFT: An ImageJ macro for automated fiber diameter quantification

Jennifer Huling*☯, **Andreas Götz**☯, **Niels Grabow, Sabine Illner**

Institute for Biomedical Engineering, Rostock University Medical Center, Rostock, Germany

☯ These authors contributed equally to this work.
* Jennifer.huling@uni-rostock.de

Abstract

This paper details the development and testing of the GIFT macro, which is a freely available program for ImageJ for the automated measurement of fiber diameters in SEM images of electrospun materials. The GIFT macro applies a validated method which distinguishes fiber diameters based on distance frequencies within an image. In this work, we introduce an applied version of the GIFT method which has been designed to be user-friendly while still allowing complete control over the various parameters involved in the image processing steps. The macro quickly processes large data sets and creates results that are reproducible and accurate. The program outputs both raw data and fiber diameter averages, so that the user can quickly assess the results and has the opportunity for further analysis if desired. The GIFT macro was compared directly to other software designed for fiber diameter measurements and was found to have comparable or lower average error, especially when measuring very small fibers, and reduced processing times per image. The macro, detailed instructions for use, and sample images are freely available online (https://github.com/IBMTRostock/GIFT). We believe that the GIFT macro is a valuable new tool for researchers looking to quickly, easily and reliably assess fiber diameters in electrospun materials.

Introduction

Nonwoven fiber materials made via electrospinning have been used in a variety of applications including filters, sensors and medical products [1]. Electrospinning is a simple and fast technique that is compatible with a wide range of materials [2]. The resulting fibrous structures benefit from the high surface-to-volume ratio and can be tuned to have the desired porosity, fiber size and fiber alignment. Electrospinning is of particular interest in biomedical applications because the structure mimics the fibrous features of native tissue extracellular matrix and is known to enhance cell interactions [1]. Electrospun materials have been researched in medical applications ranging from drug delivery devices to in vitro engineering of whole tissues [3]. Several medical products have made it to commercial production including vascular stent coverings and wounds dressing [4].

In all applications, one characteristic that is critical to the function of electrospun materials is the average fiber diameter. In the case of medical face masks, reducing fibers from micro- to

OPEN ACCESS

Citation: Huling J, Götz A, Grabow N, Illner S (2022) GIFT: An ImageJ macro for automated fiber diameter quantification. PLoS ONE 17(10): e0275528. https://doi.org/10.1371/journal.pone.0275528

Editor: Wenguo Cui, Shanghai Jiao Tong University Medical School Affiliated Ruijin Hospital, CHINA

Received: July 21, 2022

Accepted: September 18, 2022

Published: October 3, 2022

Peer Review History: PLOS recognizes the benefits of transparency in the peer review process; therefore, we enable the publication of all of the content of peer review and author responses alongside final, published articles. The editorial history of this article is available here: https://doi.org/10.1371/journal.pone.0275528

Data Availability Statement: The GIFT macro, manual with instructions for installation and use, and the SEM image files used in this paper are available at https://github.com/IBMTRostock/GIFT.

All other relevant data are within the paper and its Supporting Information files.

Funding: This work was supported by the Federal Ministry of Education and Research under the project RESPONSE-"Partnership for Innovation in Implant Technology" (JH and AG). The funders had no role in study design, data collection and analysis, decision to publish, or preparation of the manuscript.

Competing interests: The authors have declared that no competing interests exist.

nano-sized in electrospun filters can reduce air resistance and increase surface area for particle capture [5]. Control of fiber diameter can also be used to tailor drug release profiles [6, 7]. Additionally, changes in fiber diameter of biocompatible materials have been shown to effect cell proliferation, differentiation and morphology [8–10]. Therefore, the ability to easily and accurately analyze fiber diameter is critical in the development and production of electrospun materials.

The most common method for the measurement of fiber diameters is via the manual measurement of fibers based on scanning electron microscopy (SEM) images using free tools like ImageJ and Fiji [11, 12]. However, measurement by hand is slow and can be influenced by the individual making the measurements [13]. A more ideal alternative is automated image analysis. Automated analysis could potentially eliminate user bias and allow for high throughput screening for the development of new electrospun materials or rapid quality control of commercial products. There have been many proposed methods and existing tools for automated fiber measurements, but all have weaknesses including limited software accessibility, high learning curve, or sensitivity to image quality or user input [14–17].

Our research group developed and published a new image analysis method for fiber diameter measurement called the General Image Fiber Tool (GIFT) [14]. The GIFT method works by measuring the distances between edges in a given image and determines which of those distances represent fiber diameter based on their frequency, therefore bypassing the need to specifically identify fibers within an image. The method proved to be accurate and faster than manual measurements or semi-automated measurements requiring user input. However, the initial version of GIFT, which was aimed at testing and validating the theory and method, was not adequately streamlined, relying on the manual transfer of data between programs and the use of proprietary software. Therefore, we felt that the positive results justified further development of GIFT into a standalone, user-friendly piece of software that could be made freely available to the research community.

In this work, we present the development of GIFT into a macro for ImageJ. The GIFT macro allows for large sets of SEM images to be processed quickly in a single step, while allowing users easy control over all of the image processing parameters. The GIFT macro is open source and freely available along with in-depth instructions for its installation, use and troubleshooting. We believe that the GIFT macro has the potential to be highly applicable in the electrospinning research community and to manufacturers requiring SEM imaging as a standard inspection method for monitoring micro and nanofiber products. Additionally, we anticipate that the new, accessible and user-friendly version of the method presented here will facilitate its application and use.

Materials and methods

Image processing and macro development

The theory behind the GIFT method was developed, tested and validated previously [14]. In the current work, we have adapted the image processing steps to function entirely within ImageJ for optimal ease of use and accessibility. A summary of the main changes and improvements is given in S1 Table in S1 File. Every image processed is first cropped as needed, then a Sobel operator is applied to the 8-bit image to identify the edges, followed by percent-based thresholding. As an improvement from the original GIFT method, the GIFT macro calculates the threshold cutoff value based on a percent of total included pixels, rather than defining the cutoff value by a single constant grayscale value. The threshold is set so that a user-provided percent of dark pixels remains after thresholding and this is calculated for each image individually during processing. Compared to setting a static grayscale value cutoff, this was found to

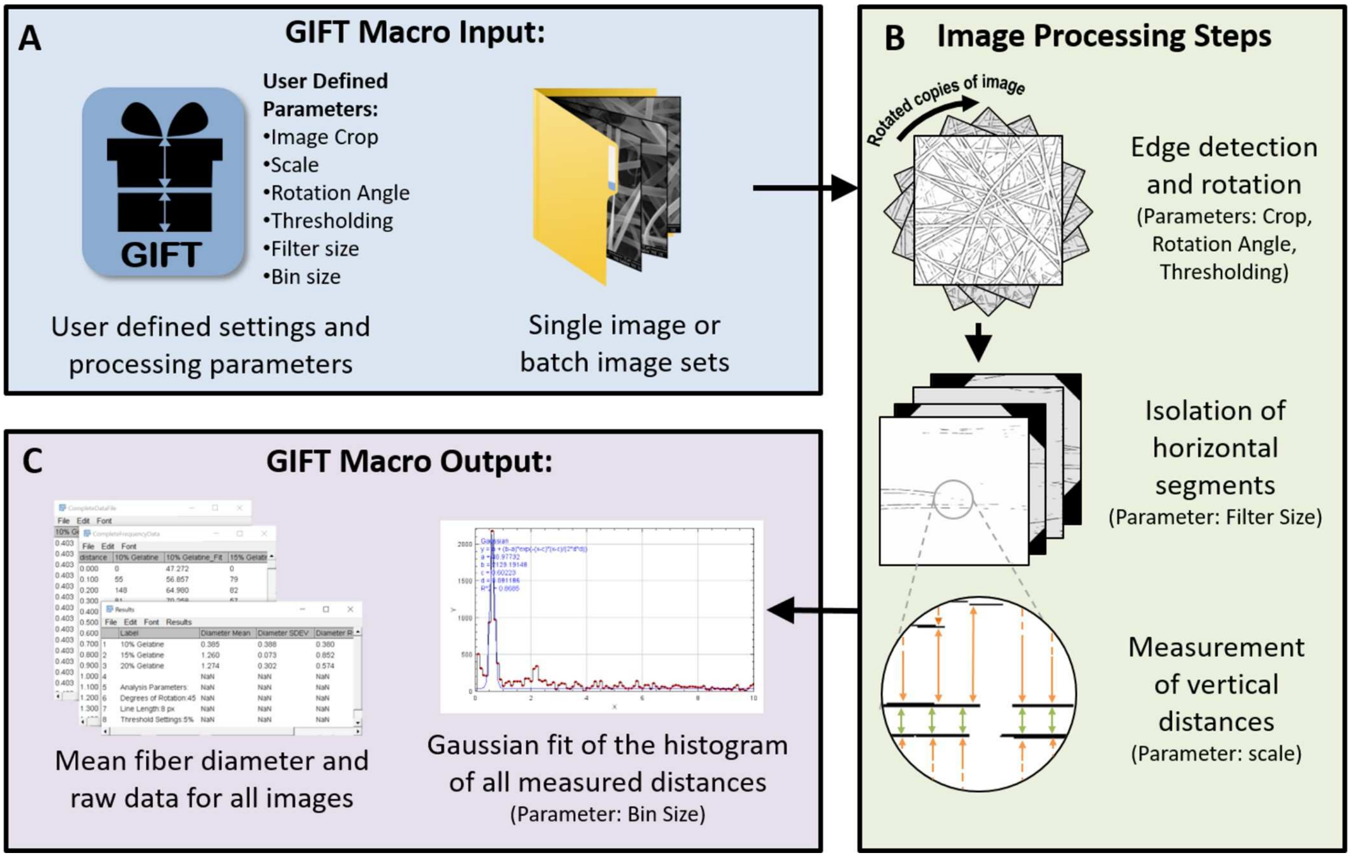

Fig 1. Diagram of image processing pathway of the GIFT macro. A) User-defined image processing parameters can be modified in the GIFT graphical user interface. These parameters are applied either to a single image or a batch of images in a single folder. B) Edge detection and thresholding is performed and then a set of rotated copies is made. An opening line filter is applied to isolate horizontal edge segments on each rotated image and the vertical distances between horizontal edge segments are measured. In the figure, the green arrows indicate the actual fiber diameter, which appears with a significantly high frequency in the image. Distances between fibers (orange arrows) are randomly distributed. C) Vertical distances are plotted as a histogram and a Gaussian fit is used to determine average fiber diameter. Users are provided with histograms and raw data for each image and a summary table with all average diameters.

https://doi.org/10.1371/journal.pone.0275528.g001

produce more consistent results when analyzing image sets with variable contrast or high blurriness (S1 and S2 Figs in S1 File).

From the binary image containing just the fiber edges (and the edges of any elements or objects in the image), a set of rotated copies of this image is created based on a user-specified angle of rotation (Fig 1B). A horizontal opening line filter is then applied to the all rotated copies using the separate ImageJ plug-in, MorphoLibJ [18]. The MorphoLibJ plug-in is automatically included in FIJI and must be installed when using ImageJ, however, the plug-in provided the filtering step that was initially done with the proprietary software Origin during the development of the GIFT method. The filtering operation isolates horizontal edge segments in each of the rotated copies which should include the parallel edges of fibers. In the next step, the macro scans through each pixel column of each rotated copy and identifies the maxima. Each maximum location corresponds to the presence of an edge in the original image. The vertical pixel distance between each maximum is measured and converted into a real distance based on the user-provided scaling factor. A histogram of all measured distances is plotted. Actual fiber diameters occur with significantly higher frequency and can be identified by applying a Gaussian fit to the data. The peak location of the Gaussian fit is used to determine the mean fiber diameter and the peak width is used to determine the standard deviation of fiber diameter.

The GIFT macro is designed for ease of use and can be run with minimal user input using the supplied default settings. Only the input of the file or file locations are required to run the macro. However, all of the key processing and output parameters can be modified in a single graphical user interface (GUI). Image cropping, scaling and threshold percent can additionally be determined interactively based on the first image in a given data set at the time of image processing. For additional applicability, users can choose to measure fiber orientation by running the existing plug-ins, OrientationJ or Directionality, in parallel with the GIFT macro and the orientation data is incorporated into the GIFT macro data output for streamlined data processing.

GIFT benchmarking against existing software with synthetic image set

The average error of the GIFT macro was measured using a set of synthetic images which had been created for the validation of the ImageJ plug-in, DiameterJ, and was published online for the purpose of future benchmarking experiments [19]. Average errors measured with this data set have already been published for the ImageJ-based DiameterJ histogram method and the Matlab-based image analysis tool, SIMPoly [16, 17]. These programs serve as suitable benchmarks as they were specifically designed for fiber measurement in SEM images. Additionally, both programs have varied image analysis methods but utilize fiber diameter histograms to determine the final average fiber diameter in a manner similar to GIFT. Two sets of synthetic test images were used. One composed of straight lines of a constant width spaced at regular intervals, but at variable angles (ordered synthetic images) and the other had randomly placed, curves lines of a constant width (disorder synthetic images). Each set has 3 images each for line widths of 3, 5, 7, 10, 15, 20, 25, 50, 75 and 100 px. Following the precedent set by the SIMPoly analysis, the first 20 px disordered synthetic image was not included due to the extreme incidence of overlapping line segments which made it a poor reference for line width. This image was included in the DiameterJ analysis but did not significantly affect the outcome. Both synthetic image sets were analyzed with the GIFT macro using 8 px filter line length, 1% threshold cutoff and either a 45˚ or 6˚ angle of rotation. The percent error was calculated based on the following equation:

$$\%\ error = \frac{|D_{Real} - D_{Calc}|}{D_{Real}} * 100$$

Where D_{Real} is the known line width in pixels and D_{calc} is the diameter in pixels measured by GIFT. The percent error was calculated for each image and the averages and standard deviations were reported. Average error was calculated separately for 3–7 px lines and 10–100 px lines for better comparison to the previously published error values.

Electrospun fiber measurement

A series of gelatin electrospun fibers were created as a real-world test set for the GIFT macro. Spinning solutions of 10, 15 or 20% w/v gelatin (Merck, Germany) in 2,2,2-Trifluoroethanol (TFE) were used. Electrospinning was performed at 22˚C and ~24% humidity with a Contipro (Dolní Dobrouč, Czech Republic) 4SpinC4S LAB2 device. Flow rates of 45–130 μl/ml and an applied voltage of 20–30 kV were used to deposit fibers on a cylindrical collector at a distance of 12–60 cm. Parameters were adjusted to ensure reliable fiber formation from each of the different gelatin solutions. Samples were imaged by scanning electron microscopy (SEM) on a Quanta FEG 250 (FEICompany, Germany). Manual measurement of the fiber diameters was performed by an experienced technician. Ten randomly selected fibers were measured on each image. DiameterJ (version 1.018) was also used to measure the images after cropping and based on the known scale. The fiber diameter histogram mean based on the M3 segmentation method was used for analysis. Because DiameterJ is not compatible with newer versions of ImageJ, this analysis was done using ImageJ 1.52a. SIMPoly was run in Matlab R2020b with the known scale supplied.

The images were batch processed using the GIFT macro using the default image analysis parameters (Line length = 8 px, threshold = 5%, angle of rotation = 45˚), a 0.1 bin size, the scale defined as 32.25 px/μm and the image height cropped to 875 px to remove scale bars.

GIFT macro parameter testing

The 10, 15 and 20% w/v gelatin electrospun fiber images were analyzed with the GIFT macro under many combinations of image analysis parameters to observe the sensitivity of the results to input parameters. A modified form of the GIFT macro code was used to quickly and automatically run through the various combinations of parameters and record the results. All combinations of filter line length (4–12 px) and threshold percent (2–8%) were tested using 90, 45 or 6˚ angles of rotation for each of the 3 images. These parameter ranges were centered around the default values for the GIFT macro. All analysis was done with a 0.1 bin size and the scale defined as 32.25 px/μm and the image height cropped to 875 px to remove scale bars. The fiber diameter results were graphed as heatmaps using Rstudio. Negative diameter results were graphed as zero. Additionally, two disordered synthetic images from the dataset used from benchmarking (with 10 and 100 pixel diameters) were analyzed with all combinations of 90, 45, 30, 18, 12 and 6˚ angles of rotation and 4–12 px line length. The threshold was kept at 1% because the synthetic images are composed of only black and white pixels.

Image processing speed measurements

The GIFT macro was tested on a Dell Latitude 5400 (Windows 10 Pro, 8 GB of RAM, Intel Core i5-8365U Processor). The macro was run as part of FIJI, using ImageJ 1.53n. The macro was used to analyze a single image or a set of 10 copies of the 15% Gelatin image shown in Fig 2 (1024x943 pixels) for consistency. Images were analyzed first using the default GIFT settings. To illustrate how some parameters can affect processing time, the same images were also analyzed with the addition of the orientation measurement option (via OrientationJ) or the images were analyzed with a 6˚ angle of rotation instead of 45˚ which increases the number of processed copies of each image from 4 to 30. Each test case was run n = 3 times and mean processing time and standard deviation was calculated.

Results

GIFT benchmarking with synthetic images

30 ordered synthetic and 29 disordered synthetic line images from a publically available dataset were analyzed using the GIFT macro [19]. The measured "fiber" diameters were compared to the known diameters and used to calculate average percent error. The percent error was calculated separately for images with fiber widths of 3–7 px and 10–100 px. The percent error generated by GIFT is given in Table 1 alongside the published percent error from measurements on the same dataset using DiameterJ and SIMPoly software. When measuring ordered synthetic images in the 10–100 px range, GIFT run with the default parameter settings had a higher average percent error (6.8±19.0%) than DiameterJ (2.5±1.9%) and SIMPoly (2.1±1.7%). However, the median error value of 1.2% was lower. Additionally, when the angle of rotation was

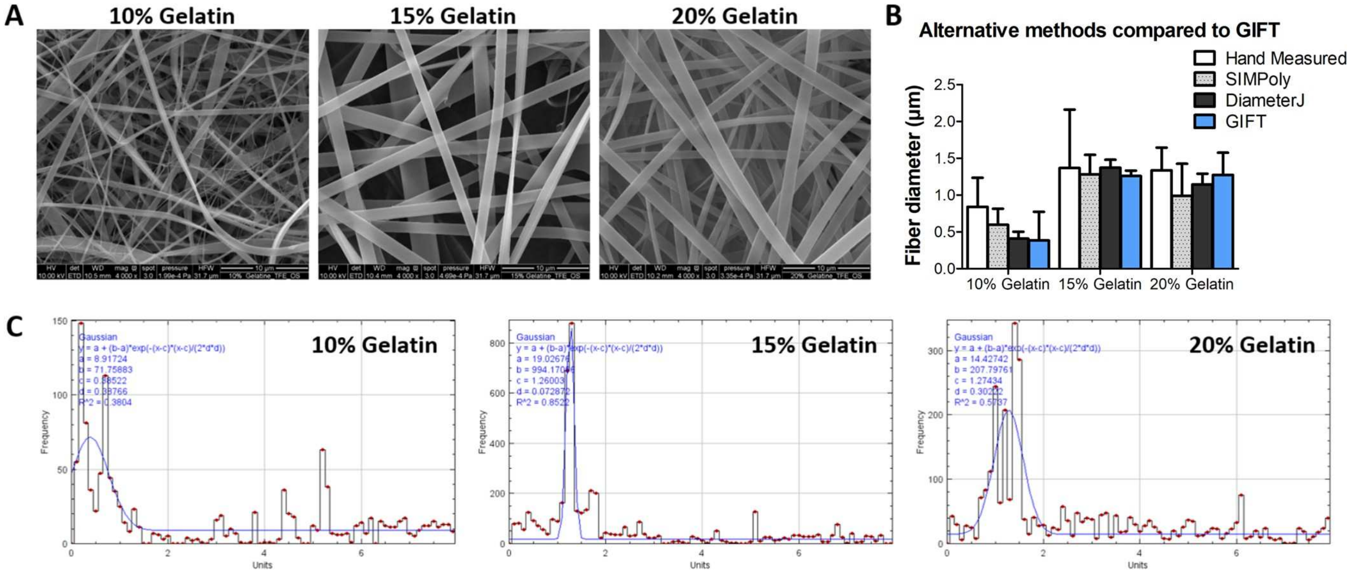

Fig 2. Real world image analysis. A) SEM images of electrospun fibers made from 10, 15 or 20% gelatin solutions. Manual fiber diameter measurements were made on 10 random fibers in each image. B) This SEM image set was also used to test the GIFT macro. The images were analyzed using default GIFT parameters. For comparison, the GIFT results were graphed with the results of hand measurement and DiameterJ and SIMPoly analysis of the same images. C) The fiber diameter histograms produced by the GIFT macro for each SEM image are shown. The x-axis units are µm. The blue line overlaid on the histograms represents the Gaussian fit curve. The parameters of the Gaussian fit are shown in the upper left corner.

https://doi.org/10.1371/journal.pone.0275528.g002

reduced to 6˚, the average percent error of GIFT (2.2±4.0%) was similar to the other two analysis methods. GIFT performed generally better when analyzing disordered synthetic images, which more closely mimic electrospun fibers. In the 10–100 px range, GIFT run with default parameter settings had an average percent error of 1.2±0.7% which was lower than the error from DiameterJ (4.7±1.4%) and SIMPoly (1.6±1.5%). Lowering the angel of rotation used when analyzing 10–100 px disordered synthetic images did not change the error. When analyzing 3–7 px sized synthetic images, GIFT was only compared to DiameterJ because the values were not published for SIMPoly. For both ordered and disordered synthetic images, GIFT with default settings (ordered: 6.8±6.5%, disordered: 6.0±3.0%) performed significantly better than DiameterJ (ordered: 12.6±3.4%, disordered: 20.9±4.3%).

Electrospun fiber measurement

10, 15 and 20% gelatin solutions were used to produce electrospun materials which were imaged with SEM (Fig 2A). These images were analyzed by hand and by GIFT. The GIFT macro was run using default parameters and was compared to manual measurements and results from DiameterJ and SIMPoly (Fig 2B). All methods produced similar results, with the

Table 1. Average percent errors based on analysis of synthetic image set with line widths between 3 and 100 px.

	Line diameter range (pixels)	Ordered Synthetic images	Disordered Synthetic images
Published DiameterJ average error (%) [19]	10–100	2.5±1.9	4.7±1.4
Published SIMPoly average error (%) [16]	10–100	2.1±1.7	1.6±1.5
GIFT average error (%), Default Settings	10–100	6.8±19.0 (median = 1.2)	1.2±0.7
GIFT average error (%), 6˚ angle of rotation	10–100	2.2±4.0 (median = 1.2)	1.2±0.7
Published DiameterJ average error (%) [19]	3–7	12.6±3.4	20.9±4.3
GIFT average error (%), Default Settings	3–7	6.8±6.5 (median = 4.6)	6.0±3.0

https://doi.org/10.1371/journal.pone.0275528.t001

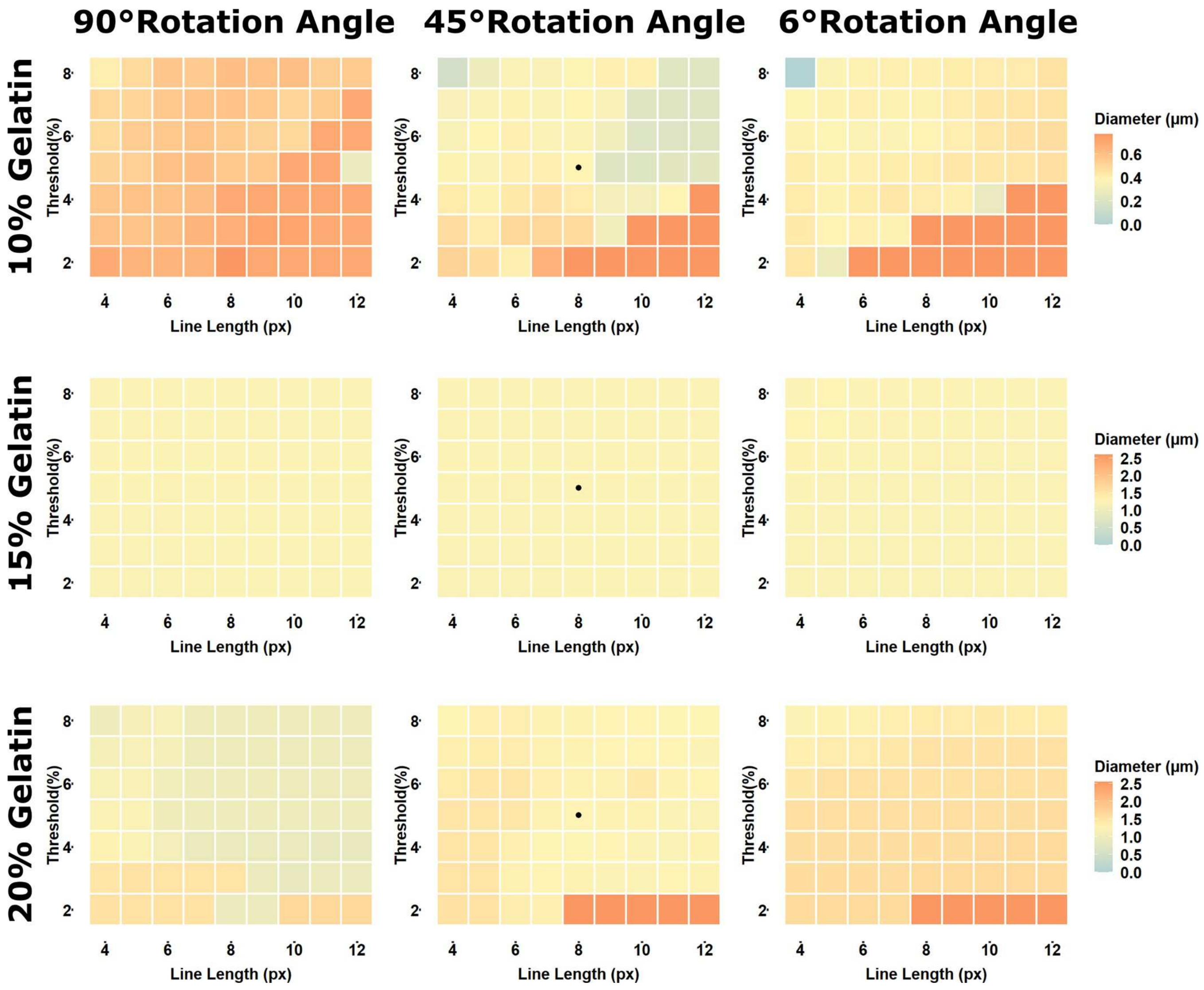

Fig 3. GIFT parameter sensitivity. SEM images of 10, 15 or 20% gelatin electrospun fibers were analyzed using the GIFT macro with 90, 45 or 6˚ angles of rotation and at all combinations of 4–12 pixel line length and 2–8% threshold parameters. The resulting fiber diameter measurements were graphed as heatmaps to visualize sensitivity of GIFT to changes in parameters. All graphs for each image (rows) have the same scale, with the fiber diameter measured with default parameters set as the midpoint of the scale bar (yellow color). Average diameters higher than the default are represented by increasingly red hues and diameter results lower than the default are increasingly blue in color. The black dots indicate the results under default parameters for reference.

https://doi.org/10.1371/journal.pone.0275528.g003

most noticeable difference in the values for the 10% gelatin image. The resulting fiber diameter histograms for GIFT are given in Fig 2C and show the distributions of measured distances from each image. The blue overlaid line on each histogram shows the Gaussian fit curve used to calculate the average fiber diameter. The Gaussian parameters are given in the top left corner of each graph. For comparison, the fiber diameter histograms for GIFT, SIMPoly and DiameterJ are provided in S5 Fig in S1 File.

GIFT parameter sensitivity

To assess the sensitivity of the GIFT macro to user input, SEM images of different gelatin electrospun fibers (Fig 2A) were analyzed using the GIFT macro with 90, 45 or 6˚ angles of

Table 2. GIFT macro processing time under different conditions.

	Default settings	Default settings + alignment analysis (OrientationJ)	Minimum angle of rotation (6˚)
1 Image	1.8 ± 0.1 s	3.3 ± 0.1 s	21.6 ± 0.9 s
10 Images	16.0 ± 0.5 s	22.6 ± 0.1 s	215.9 ± 1.0 s

https://doi.org/10.1371/journal.pone.0275528.t002

rotation (which corresponds to 2, 4 or 30 copies analyzed per image, respectively) and at all combinations of 4–12 pixel filter line length and with a 2–8% threshold. The resulting average fiber diameters from each parameter combinations were graphed as heatmaps (Fig 3). Heatmaps for the same image were graphed with a consistent color scale for easier comparison. In all cases, the scales were defined so that the average diameter measured by default parameters represents the midpoint of the scale bar which is set to a yellow color. Average diameters higher than the default are represented by increasingly red hues and diameter results lower than the default are increasingly blue in color. The 15% gelatin image results showed almost no sensitivity to changes in input parameters. The results of the 10 and 20% gelatin images, which represent more difficult images with multiple fibers sizes and lower contrast, respectively, show the most sensitivity to image analysis parameters, but still produce results in a fairly narrow range.

Similar analysis was done for two disorder synthetic images (S3 Fig in S1 File). The results show very little influence of the parameters on the results. With the synthetic images, a percent error can be calculated based on the known line width. The percent error for each set of parameters is shown in S3 Fig in S1 File and also shows very little change in the results based on parameter input.

Image processing speed measurements

The GIFT macro was tested for processing speed using the 15% gelatin SEM image (Fig 2A). The image was processed once or as a batch of 10 copies and the total processing times are presented in Table 2. The GIFT macro was run using default settings, with the addition of OrientationJ alignment analysis and with a 6˚ angle of rotation for comparison. Under default conditions, 1 image is processed in less than 2 seconds. When using a 6˚ angle of rotation GIFT, which requires processing 30 rotated copies of each image instead of the default 4, the single image processing time was significantly increased (21.6 ± 0.9 s). However, GIFT generally processes images much faster than DiameterJ, which reports a per image processing time of 20 to 60 seconds [17, 19].

Discussion

The gold standard for average fiber diameter measurement for electrospun materials is to image the material with an SEM and then measure the fiber size by hand, often with the aid of software such as ImageJ. The process of hand measurement is subjective, tedious and does not lend itself to applications which require high throughput analysis like large screening experiments or quality control for product manufacturing. Automated image analysis potentially offers a better alternative to the manual measurement of fibers. However, existing software is either limited by availability, cost, ease of use or accuracy. Our goal was to develop an open source tool that was more accurate than what was currently available and which has a low barrier to entry.

The presented GIFT macro is run through ImageJ, a freely available and popular image analysis software platform which is already familiar to many researchers and has extensive online resources and support. The GIFT macro user manual, available for download at the

Github website along with the program, outlines exactly how to download and open GIFT in ImageJ. To run GIFT, a user only needs to provide an input and output folder location into the single GUI. All other parameters have default values, so the software has a low learning curve. However, all key image processing parameters can be adjusted by the user if desired. Explanations and examples are given in the user manual. The GIFT macro saves image processing intermediates, raw data, fiber diameter histograms and summary data as outputs. Additionally, the GIFT macro has a 'single image' function to allow users to quickly run the analysis method on just one open image.

To assess the accuracy of the GIFT macro in its current form and as a way to benchmark our software with similar tools, we used the GIFT macro to batch analyze a set of synthetic test images specifically designed for validating fiber diameter measurement software. The synthetic test images contained white lines of a constant, known diameter on a black background and were of two types. Ordered images had straight and evenly-spaced lines and disordered images had curved and randomly oriented lines. The average error of the GIFT macro when measuring the line diameter in these images was compared to the previously published average errors for DiameterJ and SIMPoly based on the same dataset [16, 19]. Across the board, GIFT performs similarly or better than DiameterJ and SIMPoly when measuring disordered fibers, which are visibly very similar to the typical structure of electrospun fibers. Importantly, the number of rotations did not significantly affect the error for disorder synthetic images, indicating that, in most cases, there is no need to increase the number of rotated copies per image and subsequently the processing time. In the original DiameterJ paper, line sizes below 10 pixels had an average error over 10% and were not included in the main results, but the values were reported in the supplemental data. GIFT significantly out performs DiameterJ when analyzing the smallest sized lines (3–7 px) which indicates that GIFT may be particularly well-suited to analyzing nanoscale fibers and is not as limited when it comes to minimum measurable fiber size. GIFT had higher average error when analyzing the ordered synthetic images, which are similar in structure to aligned fibers. We believe that one of the strengths of GIFT is that it does not need to specifically identify fibers or background in an image and therefore avoids the need for complicated and potentially inaccurate methods of image segmentation. GIFT relies on the assumption that the segments of the background visible in the image are of random sizes and shapes. However, in the ordered synthetic images both the lines and the background are evenly spaced with parallel edges which means that the background essentially appears like a very wide line and leads to a peak in the fiber diameter histogram generated by GIFT. In these cases, GIFT may identify the repetitive size of the background as the fiber diameter. This did happen in the benchmarking test and impacted the average error for ordered images. However, it happened rarely and the median error was lower than the average error for both DiameterJ and SIMPoly. Additionally, reducing the rotation angle helped to avoid this issue and led to GIFT having an average error similar to the other software. This means that adjusting the rotation angle parameter in GIFT is a simple strategy for the analysis of samples with aligned fibers. Even when an error happens due to highly ordered structures, the actual fiber diameter will still be evident on the histogram, but GIFT currently cannot identify multiple peaks on a single histogram. Luckily, such strictly ordered structures are not typical in electrospun materials.

To test the GIFT macro on real-world images, a set of SEM images of gelatin electrospun fibers was chosen. We felt that the chosen SEM images represented a range of image types and situations that commonly occur. The 15% gelatin image represents an ideal SEM image of fibers. The image is clear, has high contrast and is composed of straight, consistently sized fibers. The 20% gelatin image is similar, but has a lower overall contrast. The 10% image contains a wide range of fiber sizes with the smallest fibers only being a few pixels wide. Therefore in analyzing just a few images we can demonstrate and assess GIFT's function in a variety of potentially challenging, but common situations. When compared to hand measurements of the same images, GIFT produced averages that were nearly identical. The average diameter measured by the GIFT macro for the 10% gelatin image was slightly lower than the value generated by hand measurement. This may be due in part to the presence of many very thin fibers, which are difficult to measure by hand and easily overlooked during manual measurement analysis. The diameter averages from GIFT were also comparable to the results generated by DiameterJ for the same image set. For some images, GIFT had slightly larger error measurements, however, we believe that this accurately reflects the characteristics of the fibers and that the larger standard deviation corresponding with a wider distribution of fiber sizes. This information can be useful in identifying electrospinning methods that require further optimization to achieve a more consistent fiber size. SIMPoly performed similarly to GIFT in the ideal case of the 15% gelatin image. However, SIMPoly produced different results when challenged with the extremely small fibers or poor contrast in the 10 and 20% images, respectively. The exact histograms generated by each program shown in S5 Fig in S1 File.

DiameterJ and SIMPoly also differ from GIFT in terms of dependence on user input, ease of use and accessibility. DiameterJ requires the selection of a segmentation method based on visual inspection of initial results and this segmentation method can significantly impacts the results (segmentation images shown in S4 Fig in S1 File and diameter results for all segmentation methods included in S1 Dataset). Furthermore, DiameterJ is no longer compatible with current versions of ImageJ which limits its accessibility and utility. SIMPoly runs through Matlab which is not freely available. While SIMPoly is not prone to user bias, it also has very little opportunity for user input and user control which may make it less flexible.

The effects of adjusting image analysis parameters was also evaluated. The GIFT macro has a set of defined default values for all parameters, but they are fully adjustable by the user. The heatmap plots in Fig 3 show how much influence the three main image processing parameters (filter line length, threshold percent and rotation angle), have on the results. In the case of the 15% gelatin image, the parameters have almost no effect on the outcome. Only extreme parameter values generate fiber diameter results which vary widely from those generated by the default settings. In this case, which is an image representative of most fiber SEM images, GIFT is extremely consistent, and not prone to user influence. In the other images, which represent more complicated images with a wide variety of fiber sizes and less ideal image contrast, there is more of an effect of the parameters on the results. However, this variability can be minimized by decreasing the rotation angle and using parameter values near the defaults. Even in these cases the effect on the final fiber size is minimal.

One major current limitation of the GIFT macro is that it is designed for analyzing nonwoven materials with single fiber diameters. The Gaussian fit used to identify the mean diameter from the fiber diameter histogram treats all distributions as if they have one peak. If applied to a bimodal distribution, the Gaussian distribution will only identify one peak or may find the average of 2 close peaks. An example of this can be seen in the fiber diameter histogram of the 10% gelatin fibers. It appears that there is not an even distribution of fiber sizes, but two peaks, one under and one just over 0.5 μm diameter and the Gaussian fit identifies an average between these two close peaks. This average is still a reasonable representation of fiber size, but it means that, in its current form, GIFT may not be ideal for nonwovens with two or more distinct fiber diameters like composite materials made with multiple nozzle or polymers. This limitation is largely because ImageJ is primarily designed for image manipulation and analysis and is not the ideal software environment for doing the more complicated data analysis necessary for analyzing multimodal distributions. That kind of analysis is better done in software that is specifically for statistical analysis. For this reason GIFT saves raw data and binned histogram data which could be transferred to other software for further analysis if desired. It should be noted that DiameterJ showed multi-peak data in their validation paper, but the multi-peak fitting was done in the separate paid software Igor-Pro. It may be possible in the future to integrate GIFT with external open-source statistical software or to have parallel analysis software developed to be specifically compatible with GIFT output for further analysis. However, this would more than likely not be as user friendly and have a much higher learning curve.

Additionally, GIFT is currently limited to only directly measuring fiber diameters. No other characteristic of the fibers or image is assessed. The GIFT macro can indirectly measure fiber orientation by running the existing plugins Directionality or OrientationJ in parallel to fiber size analysis, but this is a completely separate operation and adds a significant amount of processing time. One of the strengths of GIFT is that it has a very simple and streamlined method for fiber diameter measurement, however, this limits the information that can be mined from GIFTs raw data. There is currently no differentiation between fiber and background which could be used to identify things like pore size. DiameterJ can provide information related to fiber orientation, fiber length, intersection density and mesh hole area, but many of these measurements are based on incorporation of other existing plugins. It may be possible in the future to continue to incorporate more functionality with the GIFT macro by similarly integrating already existing methods.

Conclusions

The newly developed GIFT macro for ImageJ is a freely accessible and user friendly tool for determining fiber diameter from SEM images of nonwoven biomaterials. The new macro allows users to apply the previously validated GIFT method to large batches of images in a single-step process and has been benchmarked against existing software and tested on a real-word data set. Utilizing this novel method, the GIFT macro determines fiber diameters based on edge distance frequencies and outputs the mean fiber diameter in the image along with standard deviation. Additionally, all raw distance and frequency data is provided to the user for maximum transparency and flexibility. The GIFT macro was designed to maximize user control over image processing and output parameters, but users can start immediately with default settings. Examples and explanations of all image processing steps and parameters are included in the GIFT macro user guide. The macro integrates the existing popular plug-ins OrientationJ and Directionality so fiber orientation data can be collected at the same time as fiber diameter measurements. We believe that the GIFT macro is an easy to use tool with a low barrier to entry that produces reliable fiber diameter measurements and that this tool will be of great interest to researcher using electrospinning or similar techniques for the production of biomaterials.

Supporting information

S1 File. Supporting information for the manuscript.
(DOCX)

S1 Dataset. Raw data related to the manuscript.
(XLSX)

Acknowledgments

The authors would like to thank Katja Hahn and Beate Lyko for their technical assistance and contributions.

Author Contributions

Conceptualization: Jennifer Huling, Andreas Götz, Sabine Illner.

Data curation: Jennifer Huling.

Formal analysis: Jennifer Huling.

Software: Jennifer Huling, Andreas Götz.

Supervision: Niels Grabow, Sabine Illner.

Validation: Andreas Götz.

Visualization: Jennifer Huling.

Writing – original draft: Jennifer Huling.

Writing – review & editing: Jennifer Huling, Andreas Götz, Niels Grabow, Sabine Illner.

References

1. Xue J, Wu T, Dai Y, Xia Y. Electrospinning and Electrospun Nanofibers: Methods, Materials, and Applications. Chemical Reviews 2019; 119(8): 5298–415. https://doi.org/10.1021/acs.chemrev.8b00593 PMID: 30916938
2. Li Y, Zhu J, Cheng H, et al. Developments of Advanced Electrospinning Techniques: A Critical Review. Adv. Mater. Technol. 2021; 6(11): 2100410. https://doi.org/10.1002/admt.202100410
3. Luraghi A, Peri F, Moroni L. Electrospinning for drug delivery applications: A review. J Control Release 2021; 334: 463–84. https://doi.org/10.1016/j.jconrel.2021.03.033 PMID: 33781809
4. Omer S, Forgách L, Zelkó R, Sebe I. Scale-up of Electrospinning: Market Overview of Products and Devices for Pharmaceutical and Biomedical Purposes. Pharmaceutics 2021; 13(2). https://doi.org/10.3390/pharmaceutics13020286 PMID: 33671624
5. Naragund VS, Panda PK. Electrospun nanofiber-based respiratory face masks-a review. Emergent Mater 2022: 1–18. https://doi.org/10.1007/s42247-022-00350-6 PMID: 35098033
6. Chou S-F, Carson D, Woodrow KA. Current strategies for sustaining drug release from electrospun nanofibers. J Control Release 2015; 220(Pt B): 584–91. https://doi.org/10.1016/j.jconrel.2015.09.008 PMID: 26363300
7. Okuda T, Tominaga K, Kidoaki S. Time-programmed dual release formulation by multilayered drug-loaded nanofiber meshes. J Control Release 2010; 143(2): 258–64. https://doi.org/10.1016/j.jconrel.2009.12.029 PMID: 20074599
8. Badami AS, Kreke MR, Thompson MS, Riffle JS, Goldstein AS. Effect of fiber diameter on spreading, proliferation, and differentiation of osteoblastic cells on electrospun poly(lactic acid) substrates. Biomaterials 2006; 27(4): 596–606. https://doi.org/10.1016/j.biomaterials.2005.05.084 PMID: 16023716
9. Christopherson GT, Song H, Mao H-Q. The influence of fiber diameter of electrospun substrates on neural stem cell differentiation and proliferation. Biomaterials 2009; 30(4): 556–64. https://doi.org/10.1016/j.biomaterials.2008.10.004 PMID: 18977025
10. Narayanan N, Jiang C, Wang C, et al. Harnessing Fiber Diameter-Dependent Effects of Myoblasts Toward Biomimetic Scaffold-Based Skeletal Muscle Regeneration. Front. Bioeng. Biotechnol. 2020; 8: 203. https://doi.org/10.3389/fbioe.2020.00203 PMID: 32266234
11. Schneider CA, Rasband WS, Eliceiri KW. NIH Image to ImageJ: 25 years of image analysis. Nat Methods 2012; 9(7): 671–5. https://doi.org/10.1038/nmeth.2089 PMID: 22930834
12. Schindelin J, Arganda-Carreras I, Frise E, et al. Fiji: an open-source platform for biological-image analysis. Nat Methods 2012; 9(7): 676–82. https://doi.org/10.1038/nmeth.2019 PMID: 22743772
13. Narayanan G, Tekbudak MY, Caydamli Y, Dong J, Krause WE. Accuracy of electrospun fiber diameters: The importance of sampling and person-to-person variation. Polymer Testing 2017; 61: 240–8. https://doi.org/10.1016/j.polymertesting.2017.04.017
14. Götz A, Senz V, Schmidt W, Huling J, Grabow N, Illner S. General image fiber tool: A concept for automated evaluation of fiber diameters in SEM images. Measurement 2021; 177: 109265. https://doi.org/10.1016/j.measurement.2021.109265
15. Baheti S, Tunak M. Characterization of fiber diameter using image analysis. IOP Conf. Ser.: Mater. Sci. Eng. 2017; 254(14): 142002. https://doi.org/10.1088/1757-899X/254/14/142002

16. Murphy R, Turcott A, Banuelos L, Dowey E, Goodwin B, Cardinal KO. SIMPoly: A Matlab-Based Image Analysis Tool to Measure Electrospun Polymer Scaffold Fiber Diameter. Tissue Engineering Part C: Methods 2020; 26(12): 628–36. https://doi.org/10.1089/ten.TEC.2020.0304 PMID: 33256558

17. Hotaling NA, Bharti K, Kriel H, Simon CG. DiameterJ: A validated open source nanofiber diameter measurement tool. Biomaterials 2015; 61: 327–38. https://doi.org/10.1016/j.biomaterials.2015.05.015 PMID: 26043061

18. Legland D, Arganda-Carreras I, Andrey P. MorphoLibJ: integrated library and plugins for mathematical morphology with ImageJ. Bioinformatics 2016; 32(22): 3532–4. https://doi.org/10.1093/bioinformatics/btw413 PMID: 27412086

19. Hotaling NA, Bharti K, Kriel H, Simon CG. Dataset for the validation and use of DiameterJ an open source nanofiber diameter measurement tool. Data Brief 2015; 5: 13–22. https://doi.org/10.1016/j.dib.2015.07.012 PMID: 26380840

Supporting Information

S1 Table: Summary of GIFT macro changes. The GIFT macro was developed based on the published GIFT method [14], which was extensively reworked to create a macro with better functionality and which produced better outcomes. The main changes and upgrades are summarized.

Feature	Original Version	GIFT macro
Thresholding method	Constant pixel grayscale value used to threshold all images	A percent-based pixel value is calculated for each image individually
Gaussian fit	Fit performed in separate software (OriginPro)	Fit performed in ImageJ
Morphological Filter	Filtering step performed in separate software (OriginPro)	Morphological filtering (Erosion and Dilation) performed in ImageJ using the installed “Morphological Filter” Plugin.
User interface	No graphical user interface (GUI), parameters changed manually	A single GUI allows for control of all image-processing parameters. Additional control over file-saving options and fiber orientation analysis are available.
Output files	Manual file saving only	After analysis, the program prompts users to select the preferred file type for saving the data. Raw and summary data files are saved. Analysis parameters included in the summary data.
Interactive image analysis	Cropping and scale measurement determined manually in ImageJ before analysis	Users can interactively select the crop size, threshold level and scale bar length based on the first image in a batch during batch processing. These values are then automatically applied to all images in the batch.

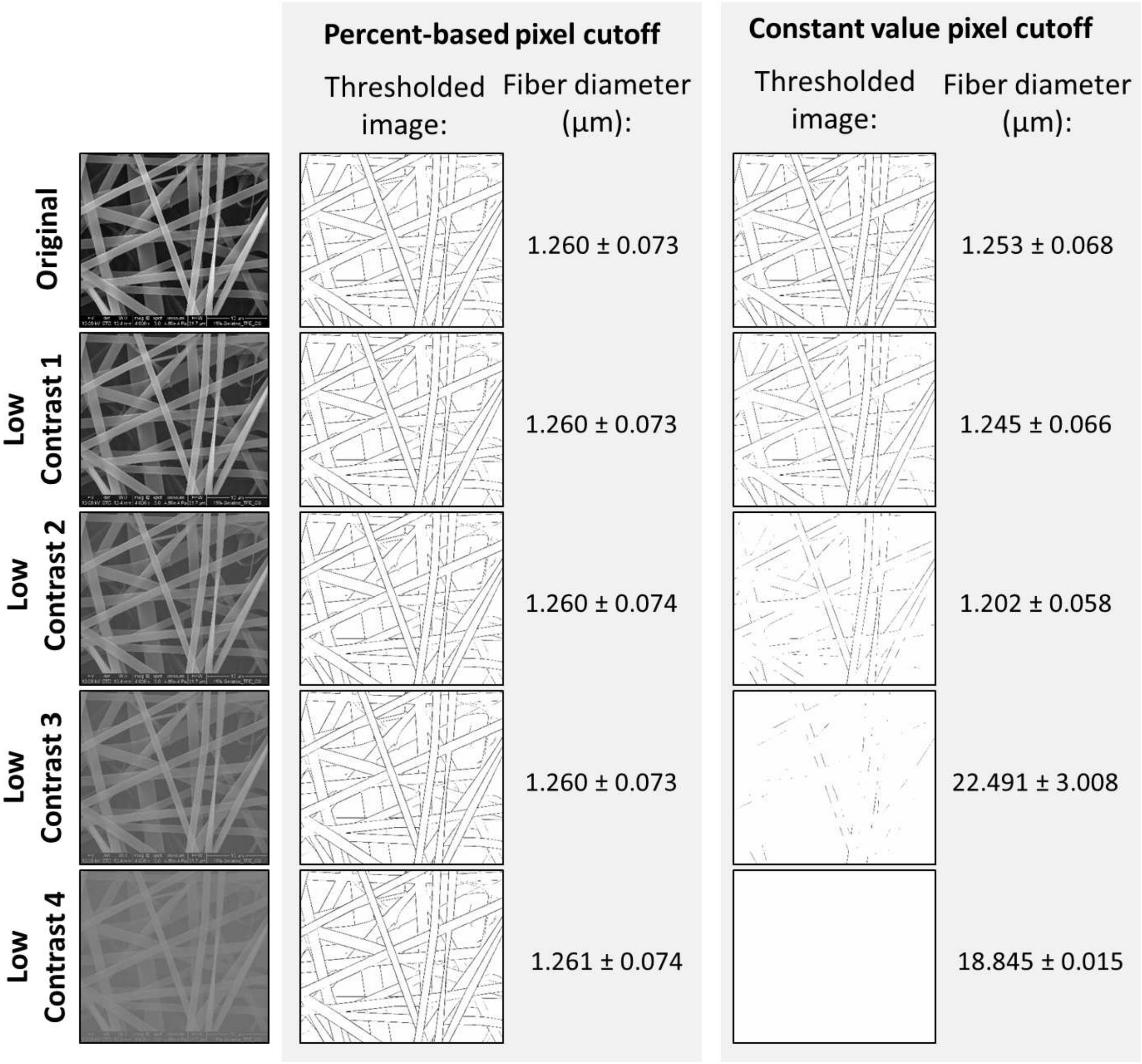

S1 Fig. Testing thresholding methods with low contrast images. A set of test images was made using the 15% gelatin SEM fiber image. The original image was adjusted in ImageJ to have progressively lower contrast. These images were analyzed with the GIFT macro using either percent-based thresholding or a constant thresholding value. For the percent based analysis, the threshold cutoff was determined so that 5% of darkest pixels remained after thresholding and this was calculated for each image. For the constant value thresholding analysis, a cutoff grayscale value of 200 was used for all images. The original images are shown in the left-hand column. The results of the thresholding image analysis step and the resulting average fiber diameter measured in each case are shown for both thresholding methods. It is clear that the adaptive, percent-based method is more consistent when presented with a batch of images with variable contrast.

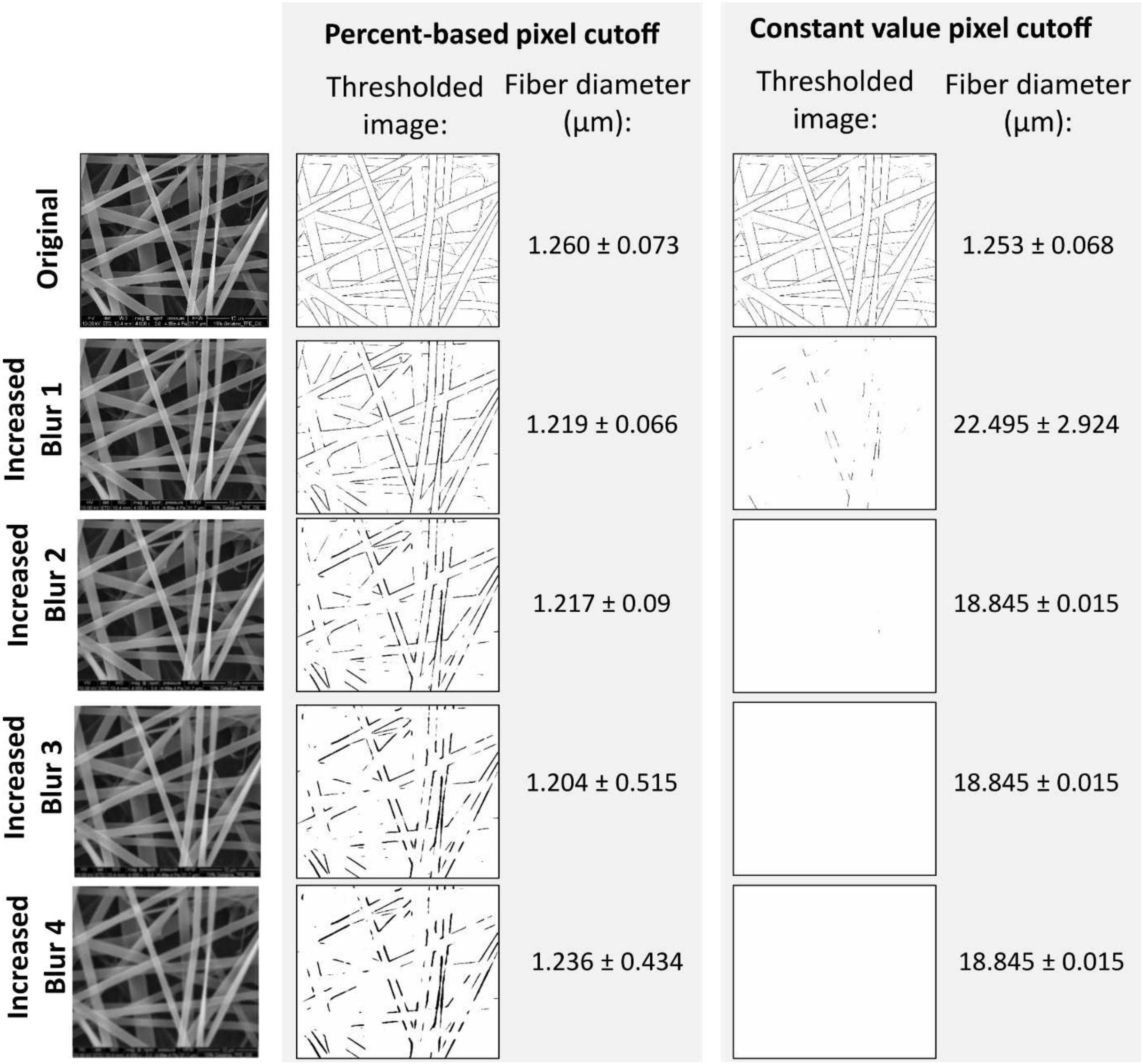

	Percent-based pixel cutoff: Fiber diameter (µm):	Constant value pixel cutoff: Fiber diameter (µm):
Original	1.260 ± 0.073	1.253 ± 0.068
Increased Blur 1	1.219 ± 0.066	22.495 ± 2.924
Increased Blur 2	1.217 ± 0.09	18.845 ± 0.015
Increased Blur 3	1.204 ± 0.515	18.845 ± 0.015
Increased Blur 4	1.236 ± 0.434	18.845 ± 0.015

S2 Fig. Testing thresholding methods with blurry images. A set of test images was made using the 15% gelatin SEM fiber image. The original image was adjusted in ImageJ to be increasingly blurry using the Gaussian Blur function. These blurred images were then analyzed with the GIFT macro using either percent-based thresholding or a constant thresholding value. For the percent based analysis, the threshold cutoff was determined so that 5% of darkest pixels remained after thresholding and this was calculated for each image. For the constant value thresholding analysis, a cutoff grayscale value of 200 was used for all images. The original images are shown in the left-hand column. The results of the thresholding image analysis step and the resulting average fiber diameter measured in each case are shown for both thresholding methods. The percent-based method is more consistent when presented with a batch of images with blurry edges.

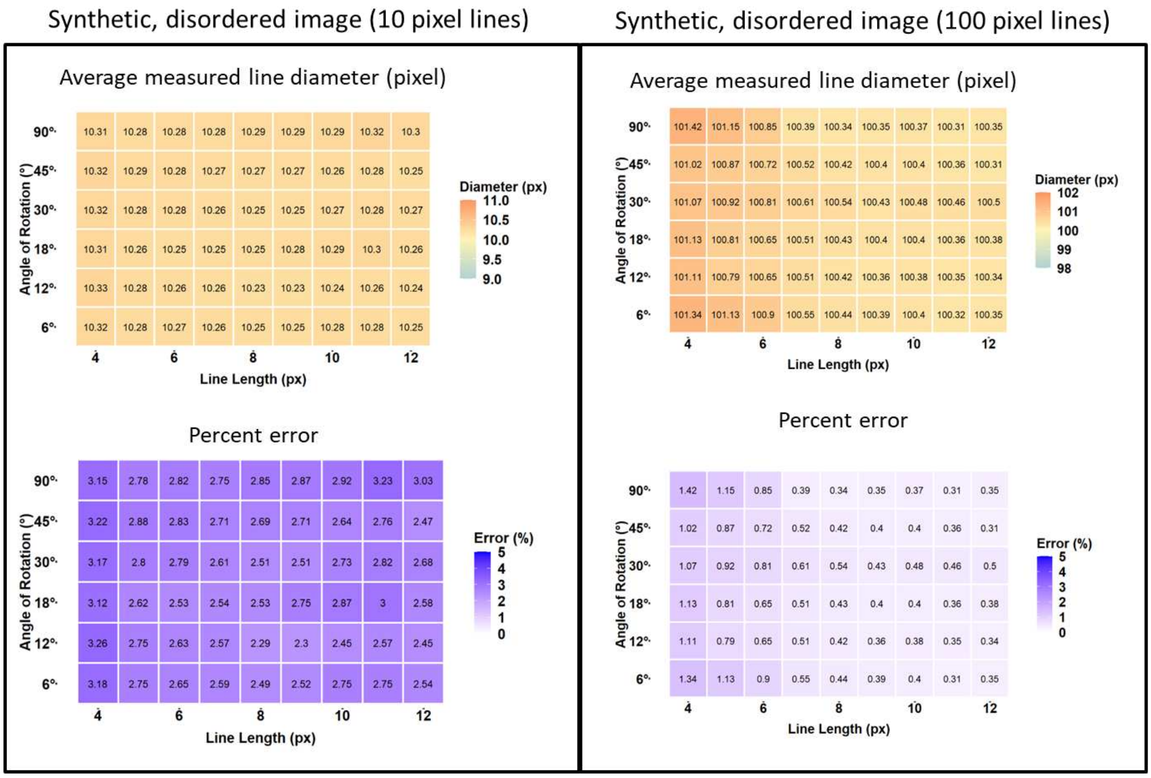

S3 Fig. Synthetic image parameter sensitivity. Disorder synthetic images with lines of 10 or 100 pixel diameter were analyzed using the GIFT macro with all combinations of 90, 45, 30, 18, 12 or 6° angles of rotation and 4-12 pixel line length. A 1% threshold was set because the synthetic images contain only black and white pixels. The top row of graphs showing the resulting fiber diameter measurements were graphed as a heat map to visualize the sensitivity of GIFT to changes in parameters when measuring a line with a known diameter. In the graphs of line diameter, the diameter measured with default parameters was set as the midpoint of the scale bar (yellow color). Average diameters higher than the default are represented by increasingly red hues and diameter results lower than the default are increasingly blue in color. The actual measured value is written on each point. The bottom row of graphs shows the percent error based on the known diameter of the lines at each combination of parameters.

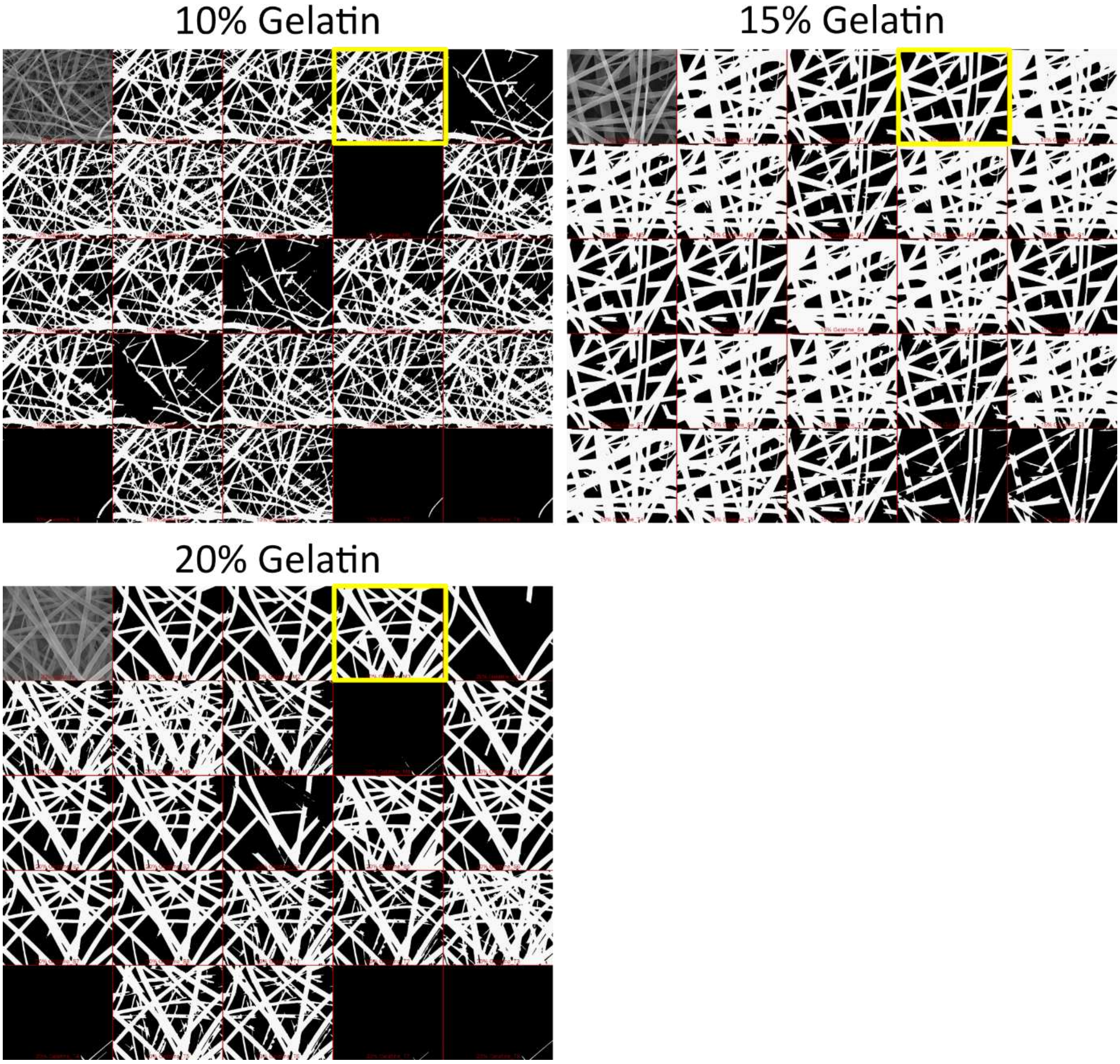

S4 Fig. Segmentation images from DiameterJ. During analysis, DiameterJ runs 24 segmentation methods and requires the user to select the best method before proceeding with diameter measurement. The montage of all segmentation images created by DiameterJ is shown here for the three analyzed SEM images of gelatin fibers. The top left image in each case is the original image and the selected segmentation method (M3) for this study is highlighted in yellow. Significant differences between segmentation methods can be seen.

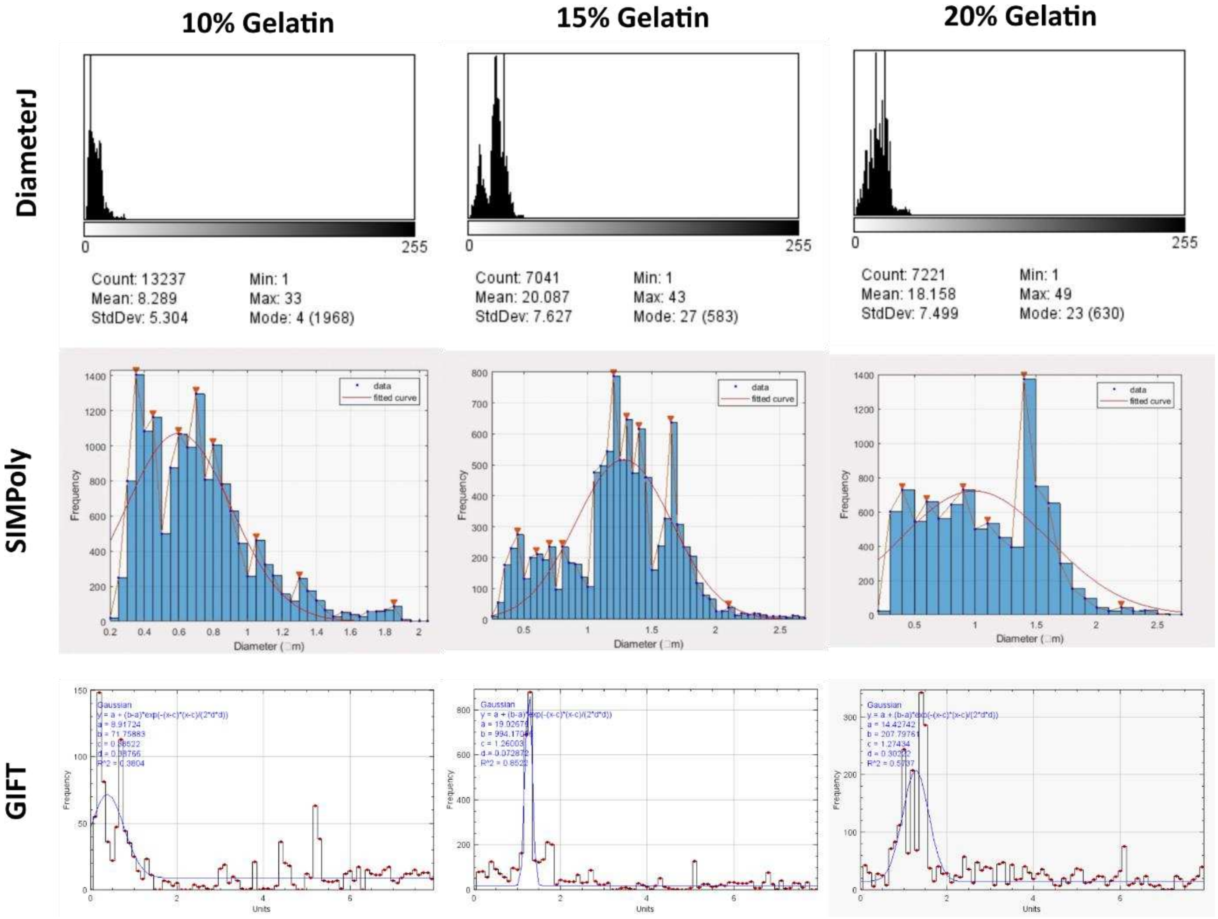

S5 Fig. Histograms from all tested software. DiameterJ, SIMPoly and GIFT all create histograms based on fiber width measurements and then use a Gaussian fit to determine a mean fiber diameter. This figure shows the histogram generated for the three SEM images of electrospun gelatin fibers for direct comparison. The DiameterJ graphs shown measurements in pixels, the measurements represent the fiber radii and the results are based on the results from the M3 segmentation method. The SIMPoly and GIFT graphs show measurements in µm based on the provided scale and default analysis parameters.

journal of the mechanical behavior of biomedical materials 140 (2023) 105720

Contents lists available at ScienceDirect

Journal of the Mechanical Behavior of Biomedical Materials

journal homepage: www.elsevier.com/locate/jmbbm

Detection of acoustic emission from nanofiber nonwovens under tensile strain – An ultrasonic test setup for critical medical device components

Andreas Götz [*], Volkmar Senz, Wolfram Schmidt, Daniela Koper, Niels Grabow, Sabine Illner

Institute for Biomedical Engineering, University Medical Center Rostock, Friedrich-Barnewitz-Str. 4, 18119, Rostock, Germany

ARTICLE INFO

Keywords:
In-situ
Fiber failure
Nanofibrous fabrics
Medicine
Invisible material defect
Ultrasound

ABSTRACT

In the biomedical field, nanofiber materials are gaining increasing application. For material characterization of nanofiber fabrics, tensile testing and scanning electron microscopy (SEM) are established standards. However, tensile tests provide information about the entire sample without information about single fibers. Conversely, SEM images examine individual fibers, but cover only a small section near the surface of the sample. To gain information on failure at the fiber level under tensile stress, recording of acoustic emission (AE) is a promising method, but challenging due to weak signal intensity. Using AE recording, beneficial findings can be obtained even on "invisible" material failure without affecting tensile tests. In this work, a technology for recording weak ultrasonic AE of tearing nanofiber nonwovens is presented, which uses a highly sensitive sensor. Functional proof of the method using biodegradable PLLA nonwoven fabrics is provided. The potential benefit is demonstrated by unmasking significant AE intensity in an almost imperceptible bend in the stress-strain curve of a nonwoven fabric. AE recording has not yet been performed on standard tensile tests of unembedded nanofiber material intended for safety-related medical applications. The technology has the potential to enrich the spectrum of testing methods, even those not confined to medical field.

1. Introduction

Fibrous materials are often superior to solid materials and are therefore used in a wide range of medical and industrial applications. One type of fibrous materials, called nonwovens or nanofiber fabrics, consists of fibers randomly arranged in a layer. This is in marked contrast to woven fabrics in which the fibers or yarns are connected in a precisely defined sequence. Numerous researchers are working on electrospun nanofiber nonwovens for medical implants as they are biomimetic, easy to fabricate, and can be spun from a variety of polymers and biopolymers. Nonwovens can be adapted to suit various applications through incorporation into composites (Jiang et al., 2018), or by post-modification (Kowalczyk, 2020). An interesting application area for embedded fiber implants is load bearing applications.

Since the 1960s, AE sensing has been an integral part of materials analysis, process and structural monitoring, and materials science in general (Hamstad, 1986; Mehan and Mullin, 1971; Williams and Lee, 1978). Professional societies monitor developments in the field and promote professional exchange, e.g. the Acoustic Emission Working Group (AEWG) (Vallen Jochen, 2021). Several researchers work on theoretical models to comprehensively describe failure behavior of fiber networks (Silberschmidt, 2022). However, AE recording has long been common practice and offers benefit for quality assurance and research in biomedical and industrial field (Bao et al., 2001; Sodomka, 2004).

In the medical field, current research related to AE is focused on bone fracture (Arun et al., 2014), soft tissue (Buis et al., 2018; Sánchez-Molina et al., 2015), early detection of failure modes of implants (Lee et al., 2021), bone cement (Qi et al., 2012), and teeth cracking (Wang et al., 2021). Advanced AE related test methods are particularly relevant for implants subjected to mechanical stress. AE related research typically focuses on fibers or filaments at the submillimeter range of yarns or skeins of wool. For example, Bao et al. mounted the AE sensor directly on the textile sample, whereas Wu et al. used an air-coupled design at a distance less than 5 mm (Bao et al., 2001; Wu et al., 2015). For AE testing of cotton fiber bundles a condenser microphone can be attached to the sample (Velu et al., 1999). Single bamboo fibers can be investigated using a two sensor setup mounted on the clamps (Alam et al., 2017), also an air-coupled setup at 7 mm distance is useable for single

---

[*] Corresponding author.

E-mail addresses: andreas.goetz@uni-rostock.de (A. Götz), volkmar.senz@uni-rostock.de (V. Senz), wolfram.schmidt@uni-rostock.de (W. Schmidt), daniela.koper@uni-rostock.de (D. Koper), niels.grabow@uni-rostock.de (N. Grabow), sabine.illner@uni-rostock.de (S. Illner).

https://doi.org/10.1016/j.jmbbm.2023.105720
Received 15 July 2022; Received in revised form 6 February 2023; Accepted 8 February 2023

synthetic polymer fibers (Ellison and Dai, 1996). Several previous studies have described that the mechanical properties of electrospun fibers often depend on their diameter (Baji et al., 2010; Papkov et al., 2013). But, in academic literature no relevant study about AE testing of bare nanofiber nonwovens was found.

To reliably and completely characterize nonwoven material properties, multiple test methods are needed. Besides SEM imaging and tensile tests, there are numerous microscopic, diffraction, nuclear magnetic resonance, chemical, mechanical and other characterization techniques for nanofiber nonwoven fabrics established (Ko and Wan, 2014; Russell, 2007). Structural characterization of bare nanofiber nonwovens is difficult due to small size of the structures, which requires highly sensitive technologies. For instance, the size of nanofibers is in the range of visible light wavelengths, posing a challenge for optical methods and precluding conventional cameras. Mechanical forces from tearing single nano or microfibers are hardly quantifiable, and noises produced by ruptures are not audible for the human ear. Computed tomography (CT) of sufficient spatial resolution at submicrometer scale is possible, but too complex and expensive for routine testing (Liu et al., 2018; Rack et al., 2008). Extending the spectrum of test methods as well as testing standards is of great importance (Padhye and Nayak, 2016), specifically to the requirements of bare nanofiber nonwovens. Standardization can bridge that gap in available methods. Therefore, specific AE related test methods are worth developing, which potentially could be developed into standards. Currently, there are no relevant standards available from DIN, CEN or ASTM. A number of testing standards already exists for fiber reinforced materials. In contrast, our work is focused on unembedded nanofiber nonwovens. The main challenge of AE recording at the nanoscale is the signal weakness of tearing nanofibers. Due to the lack of comparable data in other publications and the inaudibility of rupturing nanofibers, this study focused on a method with signal conversion that allows auditory control of the expected signals. A single tearing nanofiber produces a weak ultrasonic signal, but a highly sensitive instrument can detect it. After frequency conversion into the audible range “listening” in the failing sample is conceivable.

In general, not all material properties or failure processes are understood in detail in the study of nanofiber fabrics. There is a need for widening the spectrum of established test methods to gain more comprehensive insights into material characteristics. Our research group routinely applies a set of various testing methods for material characterization, e.g. mechanical testing (Fiedler et al., 2021), and physico-chemical tests (Arbeiter et al., 2021). Drug distribution and release are investigated (Reske et al., 2021; Wulf et al., 2020). Fibrous nonwovens are characterized using different thermal and mechanical tests (Arbeiter et al., 2020; Illner et al., 2021), as well as biocompatibility studies (Khaimov et al., 2021; Matschegewski et al., 2022). The focus of the current work is to obtain a more comprehensive understanding of the material characteristics by combining test methods in a novel way for nanofiber characterization. Tensile tests on nonwovens are known to provide information about the entire specimen. However, the question remains as to why stress-strain curves often show unexpected features. Accordingly, the visualization of material failure at the level of individual fibers motivated the development of the method presented here. A hidden defect is defined here as a pre-existing material deviation that remains undetected by common testing methods. To the best of our knowledge, this novel setup appears to be the first study on contactless AE recording of breaking bare nanofiber nonwovens.

Initial tensile tests in combination with AE recording are carried out using different fiber diameters. Poly-L-lactide acid (PLLA) from the class of polylactic acid (PLA) is often used as a common implant coating material in the medical field and in electrospinning is used to produce nonwovens with randomly oriented fibers. In order to provide a general proof of functionality of the method combination and to investigate a possible signal dependence on the fiber diameter in parallel, fibers of different thicknesses are electrospun from equivalent material. Surprising insights into conventional tensile curves have emerged.

2. Materials and Methods

2.1. Fiber material fabrication

Nonwovens of different average fiber diameters S, M, L (small, medium, large) were prepared by electrospinning. The fiber size was controlled by adjusting the polymer solution and individual electrospinning parameters, such as distance and feed rate. Different molecular weights of PLLA material were purchased to obtain different fiber diameters. Resomer L210 (M_W ~320.000 g/mol, Evonik, Essen, Germany) was used to obtain nonwovens with small (PLLA*S) and medium fibers (PLLA*M) by electrospinning 4.5 wt% and 5 wt% polymer solutions, respectively. Electrospinning of a 10 wt% Resomer L207 (M_W ~60.000 g/mol, Evonik, Essen, Germany) solution was used to create nonwovens with larger fibers (PLLA*L). Molecular weights were calculated based on the average intrinsic viscosity (Schindler and Harper, 1979). All polymer solutions were prepared by dissolving the polymer in chloroform and 2,2,2-trifluoroethanol (ratio 1:4, v/v) at 37 °C with 100 rpm shaking for 1–2 days. A device of Contipro, the 4SPIN C4S LAB2 (Dolní Dobrouč, Czech Republic), which includes a custom-built rotating continual collector, was used for the electrospinning process. All different PLLA nonwovens were processed using varied parameter sets and a multi-capillary emitter system. The emitter-collector distance was kept at 20–25 cm and a voltage of 26–28 kV and a feed rate of 120–220 μL/min were applied. The electrospinning process was performed in an ambient temperature of 22–24 °C, and humidity of 30–39%.

2.2. Test setup for recording of AE under tensile experiment

An air-coupled design was chosen for several reasons, which are listed here, for details see Supporting Information 1:

- The test specimen is very fragile, a sensor cannot be attached.
- Very strong disturbing signal is generated by friction, if the sensor is pressed against the specimen.
- The signal of fiber fracture is strongly attenuated and deformed during transmission through the sample.
- Further strong attenuation is expected at the transition into the clamp.
- Further loss of intensity is expected at the transition into the attached sensor.

As no comparable literature with corresponding signal patterns is available and measurements are made beyond the audible spectrum, the signals were converted into the audible range. This enabled the operator to listen in real time and to intuitively decide whether the detected signals are caused by real fiber tears or merely represent undefinable interfering noise. The typical crackling in the down-mixed signal resembles the audible sound of tearing textile samples and therefore is assessed as "real" signal. No undefined background or machine noise shall be misinterpreted as the desired signal. Due to frequency conversion, the signal differs from the original (Dvornikov et al., 2022). Focusing on the proof of principle, this circumstance is deliberately accepted here. The same frequency conversion concept is used in medical Doppler ultrasound examination. Here, a high frequency ultrasound signal is also mixed down to obtain an audible Doppler shift.

A self-developed device containing a slightly modified narrowband ultrasonic sensor MA40S4R (Murata Manufacturing Co., Ldt. Kyoto, Japan), electronic components including a CD2003 mixer integrated circuit, battery case, and electromagnetic shielding was used to generate a synthetic down-mixed difference signal. The sensor is very sensitive and inexpensive, its narrow bandwidth was seen as an advantage here to minimize any disruptive signals that might be present. The initial ultrasonic signal was detected by the sensor, then amplified and directed to the mixer IC which simultaneously received also the oscillator signal. The down-mixed output (difference signal) was amplified again and transmitted to three receivers: (i) digital oscilloscope PicoScope 2004A (Pico Technology, St Neots Cambridgeshire, United Kingdom) with PicoScope 6 - PC-Oszilloskop-Software Version: 6.14.36.5676, (ii) the capacitively decoupled signal to Microsoft audio recorder version 10.2005.1672.0, which recorded the audio signal with 178 kBit/s, and (iii) the capacitively decoupled signal to an active loudspeaker (Fig. 1). The difference signal specifies the down-mixed output signal, whereas the audio signal defines its alternating component after decoupling. The sensor cannot detect signals in audible range, and the loudspeaker does not emit ultrasonic noise, hence signals do not interfere. Using this method, the data will not be impaired. Due to the high sensitivity and amplification gain, electromagnetic shielding of the electronic parts was required. For recording the difference signal, an oscilloscope with a sample rate of 40 kHz was chosen. Audio data were processed with Audacity(R) version 3.0.0 (Mazzoni, 2021). The color representation of audio spectrum was set with Gain (0 dB), Range (120 dB), and Frequency Gain (0 dB/dec). For the graphic display, the displayed difference signal was reduced to a sample rate of 10 kHz. For normalized graphical representations the maximum value was set equal to 1, with all other values linear proportional. Data processing was performed with OriginPro version 2020 SR1 (OriginLab Corporation, Northampton, USA). The frequency-response characteristics of the ultrasonic sensor horn and the electronic device input are displayed in Figs. 2 and 3. In a flowchart of Fig. 1 the signal processing is visualized. The intensity of the difference signal was evaluated at specific regions in dataset, of which the signal-to-noise ratio (SNR) was calculated from sequences of 500 ms duration each.

The frequency-response characteristic of the sensor and the electronic device input were measured. Two frequency ranges were investigated for an overview and for the relevant range. The data are presented in Figs. 2 and 3. The natural resonance of the sensor horn is plotted in blue. For comparison, the signal at the device input, created by exposing the system to a broad band noise, is plotted in green. For details, see Supporting Information 2. The measurement agrees with the frequency-response characteristic provided in the manufacturer's data sheet. The oscillator frequency of approximately 42.7 kHz was adjusted close to maximum sensitivity. An oscilloscope sample rate of 40 kHz was chosen for recording, which, according to the Nyquist–Shannon sampling theorem, allows original ultrasonic frequencies in a range of the oscillator frequency ± 20 kHz to contribute to the recorded signal, i.e. 42.7 ± 20 kHz. The highest sensitivity of the device is within that range. Hence, the whole range of detected information was recorded (Fig. 3).

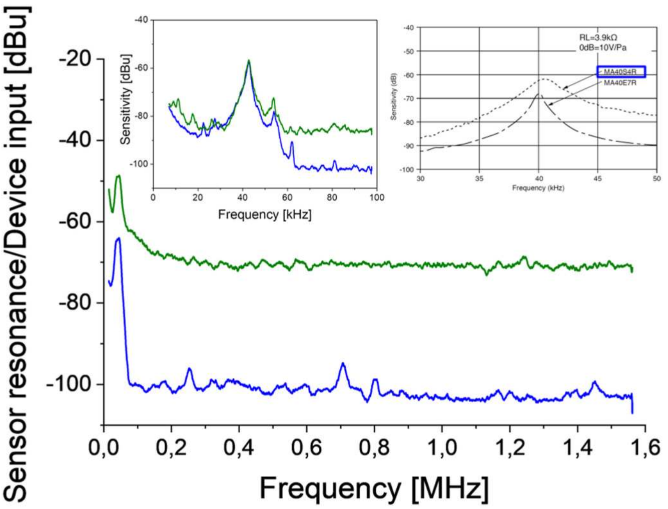

Fig. 2. Sensitivity. The frequency-response characteristic of the ultrasonic sensor (blue) and the device input (green) is displayed. The graphs show smoothed curves generated from data of the digital oscilloscope in frequency modus using a Blackman window, three measurements were averaged each. The sensitivity was measured for two frequency ranges (large graph, and upper left inset). The manufacturer's information (data sheet) is displayed in upper right inset.

2.3. Tensile experiment

Testing of nonwovens PLLA*S, PLLA*M, and PLLA*L (n = 6, each) was carried out using the uniaxial tensile test machine Zwicki ZN 2.5 (Zwick/Roell, Ulm, Germany). Samples were cut into dumbbell-shaped specimens with effective dimensions of 12 mm × 2 mm according to DIN EN ISO 527-2 1BB standards. The tests were conducted with a 10 N load cell. In order to create equal conditions, after reaching a pre-force of

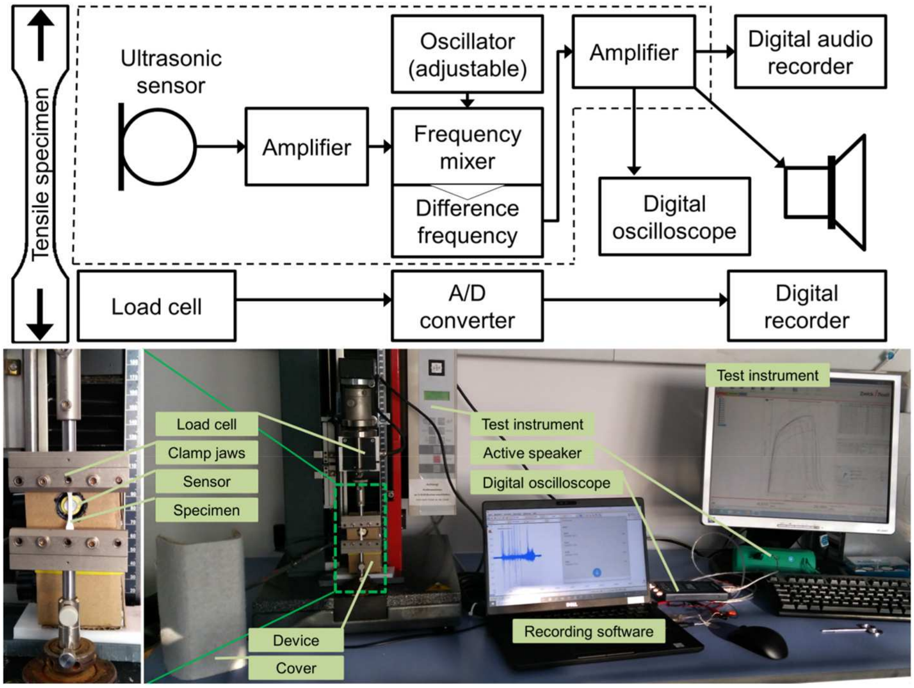

Fig. 1. Test setup as flow chart (top) and laboratory assembly (bottom). The weak ultrasonic acoustic emission from rupturing nanofibers was detected, amplified, and then mixed with an oscillator signal. The down-mixed differential signal (difference frequency) was amplified and transmitted to recording devices and audio output, simultaneously a load cell detected the tensile force. The ultrasonic sensor was placed 10 mm behind the specimen, which was fixed between clamps. A cover was placed in front of the specimen to reduce possible background noise.

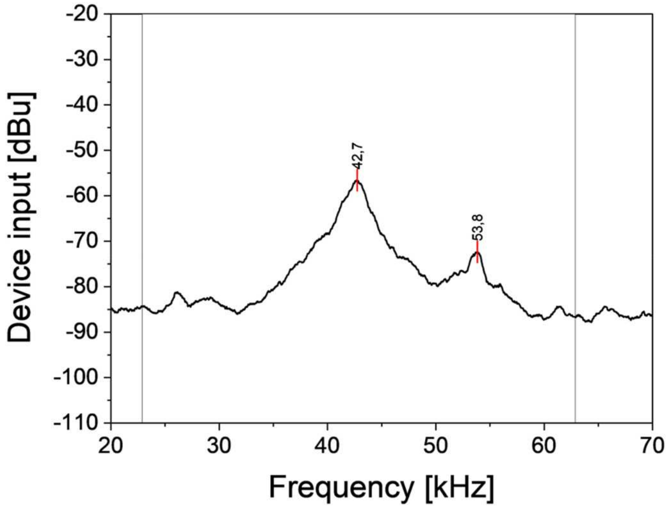

Fig. 3. Sampled frequency range. The frequency-response characteristic to a noise signal of the device input is displayed. The graph shows smoothed curves generated from data of the digital oscilloscope in frequency modus using a Blackman window, three measurements are averaged. Two frequencies of highest sensitivity in the recorded frequency band are marked. Due to 40 kHz sampling and generating of difference signals an original frequency range of approximately 23 kHz up to 63 kHz contributes to the recorded dataset.

0.005 N, the machine ran with a crosshead speed of 25 mm/min. Machine movement was stopped at a force drop of 95% of the maximum force. All tests were performed at room temperature. Young modulus was calculated by regression of corresponding subsections of the tensile curve. To synchronize oscilloscope and audio data, at each machine start three click signals were set, which ended before reaching the pre-force, hence they do not appear in graphs. Here, sample breaking refers to failure of the entire specimen, while tearing or rupturing relates to individual fibers.

In addition to testing until complete breaking, samples (n = 3) of PLLA*M nonwoven were stretched until specific points for investigation of the fiber morphology. Specially designed clip frames ($\text{Ø}_i = 8$ mm, $\text{Ø}_o = 25$ mm, Fig. 3 A, B) were used to fix the samples at specific moments during the tensile loading. The samples, still in the frames, were SEM imaged on the same day to retain some residual tension. Samples were fixed at three different points during tensile loading. The first point was after passing the yield point (Fig. 4 C), which is recognizable by bending of tensile curve at low elongation. The second point was defined some seconds after onset of large separated spikes in the AE signal (Fig. 4 D). The third point was defined at breaking of the entire sample under decreasing force (Fig. 4 E). After reaching these points, the test machine was stopped and the samples were fixed and gold sputter coated.

2.4. Porosity

Test specimens of type 1BB were punched out according to standard ISO 527–2:2012(E) and weighed with ultra-microbalance MYA 0.8/3.4Y (Radwag Waagen GmbH, Hilden, Germany). Six type 1BB pieces of each nonwoven were weighed together, and then averaged. For specimens of type 1BB, the geometry is not strictly defined, calculations were done with a sample area of 85.6 mm^2. Sample thickness was measured using a dial gauge (Mitutoyo Absolute, Mitutoyo Deutschland GmbH, Neuss, Germany). The static force on the plunger of approx. 0.25 N caused a sample compression of approx. 0.012 N/mm^2, not leading to relevant sample deformation. The density of solid polymer was defined according to literature, where a probable value for PLA basic grade of 1.25 g/cm^3 was presumed (Sin et al., 2012). Density and porosity of the nonwovens were then calculated, whereas porosity is defined as air fraction of the nonwoven sample according to equations (1) and (2)

$$Density = \frac{m}{A * t} \tag{1}$$

$$Porosity = \left(1 - \left(\frac{\frac{m}{A * \rho}}{t}\right)\right) * 100\% \tag{2}$$

where m is the mass of the sample, A denotes the sample area, t is the sample thickness, and ρ is the density of solid polymer.

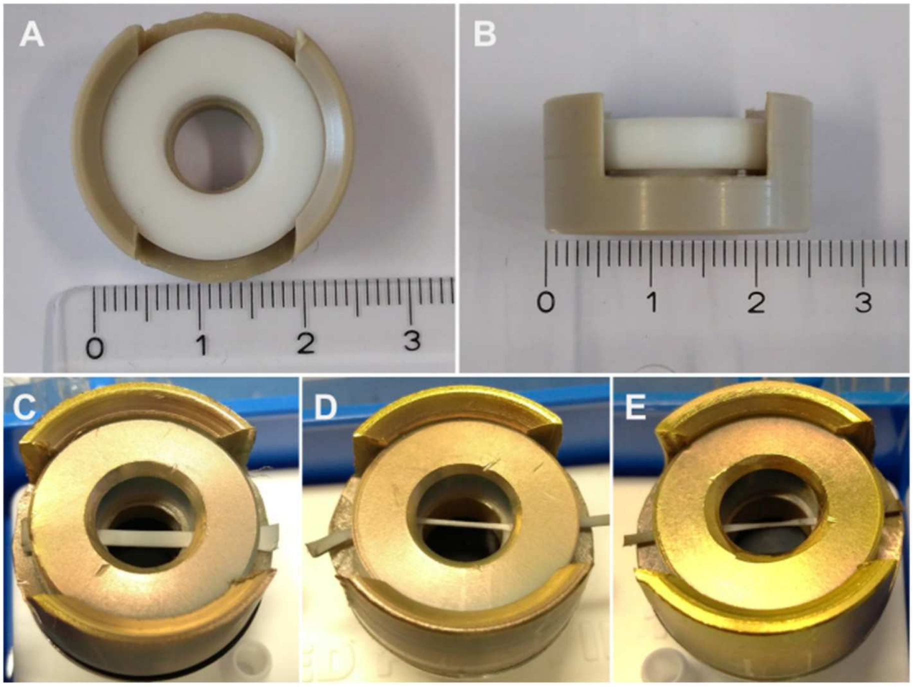

Fig. 4. Clip frames were used to fix samples of PLLA*M as they were stretched until specific points (A: clip frame in top view, and B: side view) Samples at each of the 3 investigated points during tensile testing (C: yield point, D: onset of large spikes, E: at sample breaking).

2.5. *Scanning electron microscopy (SEM)*

For investigation of fiber morphology before and after tensile testing, SEM was executed on a QUANTA FEG 250 device (FEI Company, Dreieich, Germany) operating in high vacuum and 10 kV voltage, using an Everhart-Thornley detector (ETD) in secondary electron mode. The nonwoven samples or clip frames were fixed on aluminum carriers using conductive carbon pads. Gold sputter coating was achieved using an AGAR Sputtercoater (Agar Scientific Ltd, Stansted, Essex, UK) under Argon atmosphere of 0.2 mbar pressure and a current of 25 mA for 240 s. SEM images were taken from one sample of each PLLA*S, PLLA*M, and PLLA*L nonwoven before and after tensile experiment. Three partly stretched PLLA*M samples, fixed in clip frames, were imaged additionally. According to previous work (Götz et al., 2021), fiber diameters were measured applying the GIFT-method, which statistically evaluates numerous automatic measurements of distances of fiber edges in images. Thereby the GIFT method omits bias by human operators as all fibers in the images are analyzed without any pre-selection.

3. Results

3.1. *Specific polymer properties before and after tensile test*

Tensile experiments with simultaneous recording of AE signals of PLLA nanofiber nonwovens of different fiber sizes were performed. For comparison and as a general overview of the nonwoven structures, fiber morphology and mechanical properties, numerical values and sample parameters were collated in Table 1. Fiber diameters were measured in SEM images before and after tensile testing. Mechanical data were obtained and calculated basing on tensile experiments. The term delamination refers to the disintegration of the sample by separation into some partial layers.

3.2. *Evaluation of AE signal during tensile tests*

The signals of breaking nanofiber nonwovens revealed different AE characteristics depending on fiber size as well as particular sections during the tensile test. A representative PLLA*L tensile test showed smooth tensile curves, clearly distinguishable sections of AE signal, and increasing AE activity towards sample breaking (Fig. 6, right). To give further insight, the whole dataset and detailed views of four characteristic sections of the AE signal for an example of PLLA*L is displayed in Fig. 5.

Table 1
Morphological, physical and mechanical properties of different PLLA nonwovens (averaged values, n = 6, each).

	Nonwoven type		
	PLLA*S	**PLLA*M**	**PLLA*L**
Nonwoven thickness [μm]	140 ± 15	175 ± 20	250 ± 25
Sample mass [mg]	2.251 ± 0.002	2.720 ± 0.002	3.421 ± 0.002
Density [kg/m^3]	188 ± 23	182 ± 22	160 ± 19
Polymer fraction [%]	15.0 ± 1.8	14.5 ± 1.7	12.8 ± 1.5
Porosity [%]	85 ± 10	85 ± 10	87 ± 10
Fiber diameter (unloaded) [nm]	650 ± 130	810 ± 160	1050 ± 260
Fiber diameter (loaded) [nm]	520 ± 200	720 ± 230	570 ± 320
Young modulus [N/mm^2]	38.0 ± 3.7	14.7 ± 1.2	13.9 ± 4.7
Yield point [N/mm^2] at elongation [%]	n.d.	3 ± 0.5 30 ± 6	0.7 ± 0.2 12 ± 8
Max. tensile strength [N/mm^2] at elongation [%]	6.45 ± 0.65 93 ± 14	5.11 ± 0.11 187 ± 17	2.05 ± 0.15 137 ± 19
Elongation at break [%]	133 ± 48	205 ± 25	144 ± 24
Remark	sample delamination, large variability	smooth stress-strain curve with slight knee curve	lowest ultimate strength, smooth stress-strain curves

According to audible output, a low background noise (A) was always present before starting the machine. At the start of each recording three click signals were used to later synchronize oscilloscope and audio data, whereas machine noise (motor) was never heard. A quiet, nonspecific signal (B) was detected during sample stretching at low elongation. At higher elongation single AE events (C) with increasing frequency towards maximal tensile force were audible. The signal turned into a loud, continuous crackling noise (D) during sample breaking. After machine stop (force drop of 95% of the maximum force) an immediate decrease in signal intensity was detected, resulting from single residual fibers. The signal intensity at specific locations was compared to background noise value (Fig. 5 A). Machine noise was evaluated closely after three synchronization clicks at machine start. Here the motor runs, but very low signal from sample was expected. Hence, it can be stated that the measurement was not impaired by machine noise with a SNR of about 0.01 dB. The quiet unspecified signal (Fig. 5 B) as well as single cracks (Fig. 5 C) revealed similar intensity of 2.3 dB SNR. Much higher signal intensity of more than SNR >20 dB was recorded from loud crackling signal (Fig. 5 D).

3.3. *Correlation of stress-strain diagram and AE signal*

To compare AE signals and mechanical data of different nonwovens, these have been assembled into various graphs, the results of a representative sample of PLLA*M (Fig. 6, left) and PLLA*L (Fig. 6, right) each are compared.

The difference signal shows the output signal of the electronic device, whereas the audio signal displays its decoupled alternating component. The cumulative curves indicate the highest slope in areas of the highest signal intensity, thus a correlation to the stress-strain curves provides meaningful insights. The audio spectra in this work show the difference frequency of the down-mixed signal. Characteristic changes in the audio signal can be associated with specific sections in the stress-strain curve. The PLLA*M and PLLA*L nonwovens revealed similar mechanical behavior and different AE activity, whereas PLLA*S showed mechanical delamination and an AE signal similar to PLLA*M (Fig. S 2). Nonwoven PLLA*M showed little AE activity after the yield point and the onset of strong spike signals after approximately 25 s at elongation of 80%. Breaking of the samples occurred concurrently with elevated AE intensity. For comparison, the AE signal of PLLA*L is already described above. PLLA*M and PLLA*L revealed distinct yield points, a relatively linear tensile curve prolongation, and steep curve slopes during sample breaking. Due to the distinctive features in AE measurements of PLLA*M, the tensile curves were subjected to a closer inspection. With the onset of strong spike signals, a weak stress-strain curve bending could be identified in some samples. This barely visible knee curve appeared at approximately 80%–100% elongation. At this point, however, there is a clear increase in the cumulative AE signal curve. Afterwards some background AE accompanied by lots of strong spike signals, whose frequency decreased towards sample break. Breaking of both nonwovens (PLLA*M and PLLA*L) occurred at the same time as raised AE intensity, PLLA*L was somewhat louder. During sample breaking a falling-rising tone was audible and remarkable in audio spectrum for most samples. Delamination was never seen in PLLA*M or PLLA*L samples. In contrast, PLLA*S nonwovens revealed no remarkable yield point, a slightly bent curve under prolongation with some basic AE accompanied by frequent strong spike signals, curve flattening with increasing basic AE intensity, breaking under general raised AE intensity. Delamination occurred in all PLLA*S samples. After first step of delamination the emergence of strong spike signals was reduced or not

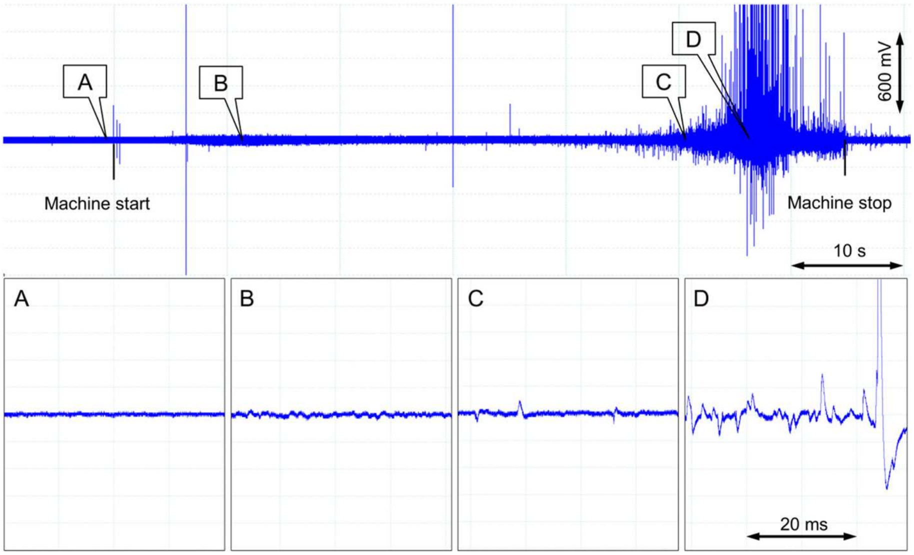

Fig. 5. Example of difference signal for a PLLA*L sample. The oscilloscope screenshots display the whole recorded dataset (Top) and sequences of 40 ms duration (bottom), the vertical range of all graphics is ± 1 V. A: background noise before machine start, B: quiet unspecified signal without distinctive features, C: single large spikes and higher wider peaks sticking out of low signal, D: loud crackling during sample breaking, single events were not reliably identifiable or countable.

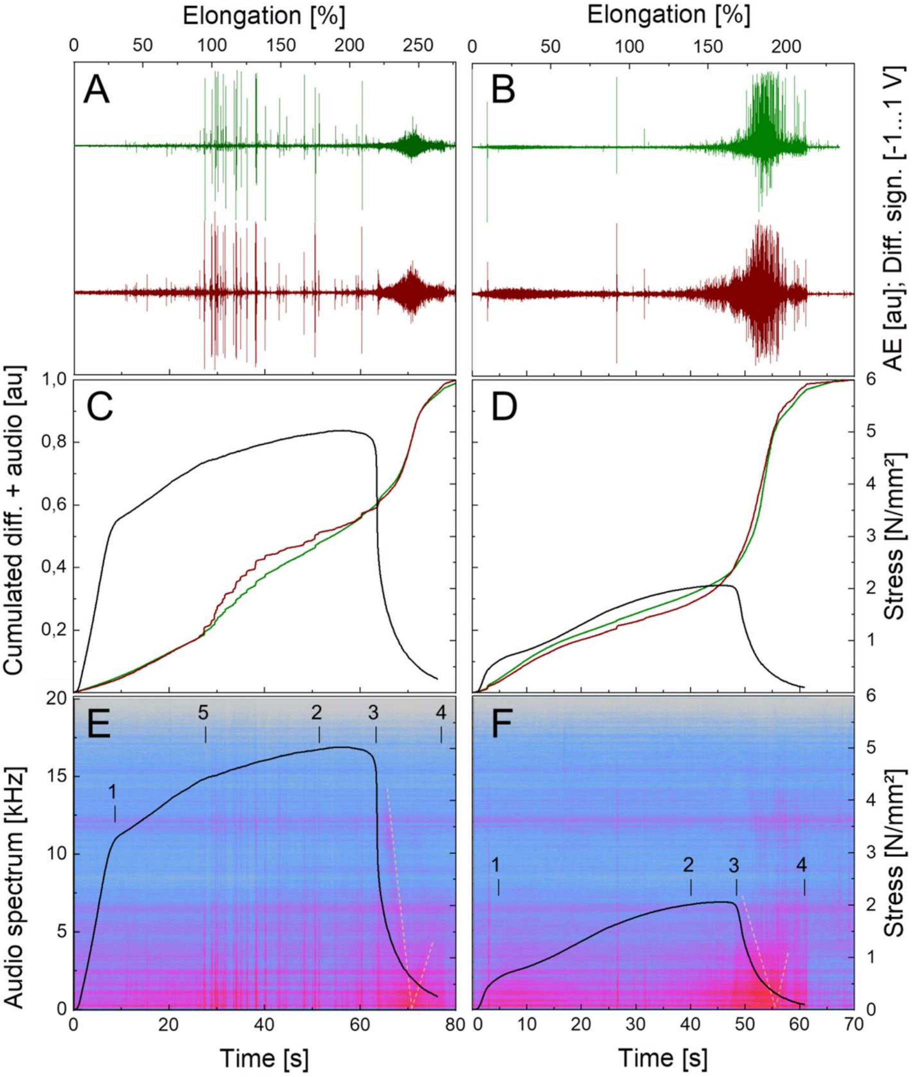

Fig. 6. AE signal during tensile stress recorded for PLLA*M (left) and PLLA*L (right) nonwovens. A and B: difference signal (green) in the range of ±1 V and normalized audio signal (dark red), C and D: Stresss-strain curves (black), normalized cumulative difference signal (green) and cumulative AE (dark red), E and F: stress-strain curves (black) and audio spectrum from 0 Hz (bottom) up to 20 kHz (top) in linear scaling with correlation of characteristic points, 1: yield point, 2: curve flattening, 3: sample breaking, 4: tensile machine stop, 5: slight knee curve. A falling-rising tone was audible and visible in audio spectrum during sample breaking (dotted lines, orange). PLLA*M revealed a relatively smooth stress-strain curve, but a remarkable uneven increase from point 5 in the cumulative signal is apparent. PLLA*L showed smooth stress and cumulative curves.

visible. Owing to the difficulty of comparison with the other nonwovens due to structural insufficiency the results of PLLA*S are presented in Supporting Information, see Fig. S 2 and Fig. S 3.

3.4. *Morphological fiber analysis by SEM imaging*

In Fig. 7, SEM images of the nonwovens before and after tensile loading are compared for morphological differences. Native nonwovens showed round fibers with smooth surface, low interconnection and very little damage. Nonwoven PLLA*S revealed some fiber bundles and slightly inhomogeneous fiber structure. On nonwoven PLLA*M, a few thick fibers were found, and PLLA*L showed a homogeneous structure. After the stress test, fibers showed necking (abrupt change in diameter), general thinning and some ruptures (not displayed here). Fibers were mostly oriented in the loading direction after tensile testing and due to relaxing and curling after rupture some fibers were randomly oriented.

3.5. *Correlation of morphology and AE signal for PLLA*M*

In the stress-strain curves of nonwoven PLLA*M an abrupt onset of strong spikes in the AE signal occurred on all samples. For investigation of the fiber morphology during tensile testing, three samples were stretched until specific points: A – after yield point for detection of first permanent deformation effects, B – after onset of individual large spike events (slight knee curve) to investigate the source of this AE signal, and C – at sample breaking to investigate a sample at failure (Fig. 8). At point A fibers were randomly oriented and some single fibers were ruptured. Point B clearly showed alignment and more ruptured fibers, but no dislocation of end pieces. At point C highly aligned and curled fibers were found as well as broken end pieces. Fiber diameters of stretched PLLA*M samples were measured in SEM images by the GIFT method, at point A 790 ± 240 nm (n = 21 images), at point B 590 ± 250 nm (n = 18 images), and at point C 620 ± 330 nm (n = 16 images).

4. Discussion

For PLLA nanofiber nonwovens of different average fiber diameters (PLLA*S, PLLA*M, PLLA*L) tensile testing with simultaneous recording of AE signal were performed. Subdivided according to fiber size, the most important characteristics of the individual fiber types are discussed.

4.1. *Correlation of morphological, tensile, and AE results*

In SEM images of nonwoven PLLA*S some fiber bundles are seen, but fiber interconnections are not found. In tensile experiments, continuous AE starts with low intensity and then at approximately 30%–40% elongation the onset of strong spike signals is detected. The bundled fibers bundles do not separate (necked bundle at bottom of Fig. 7 C). We expect them to rupture entirely, which is the most probably cause of the strong spike signals. Additionally, some insufficiently connected sublayers of the nonwoven are able to slide under tensile stress, which is defined as delamination. Nonwoven PLLA*S revealed several delamination steps. After first delamination the occurrence of strong spike signals is remarkably reduced. During delamination and sample breaking in 5 of 6 samples, a falling-rising frequency of sound is audible and partly visible in the spectrogram, which is indicated in Fig. S 2. The high AE intensity which occurs during the falling stress curve is assumed to be a combination of tearing and sliding fibers. Structural deficiency in coincidence with strong spike signals in every sample is an indication for a suboptimal manufacturing process and necessitates further modification of the parameters. In addition, a yield point is not clearly definable. Despite comparable porosity to the other nonwovens, due to delamination under tensile stress and some fiber bundles detected by SEM analysis, the PLLA*S fabric does not comply with our internal quality requirements for medical use.

PLLA*M nonwovens contain very few thick fibers in SEM images. Before the yield point no remarkable AE is audible, however, after the yield point some crackling signal occurs. Strong spike signals appear

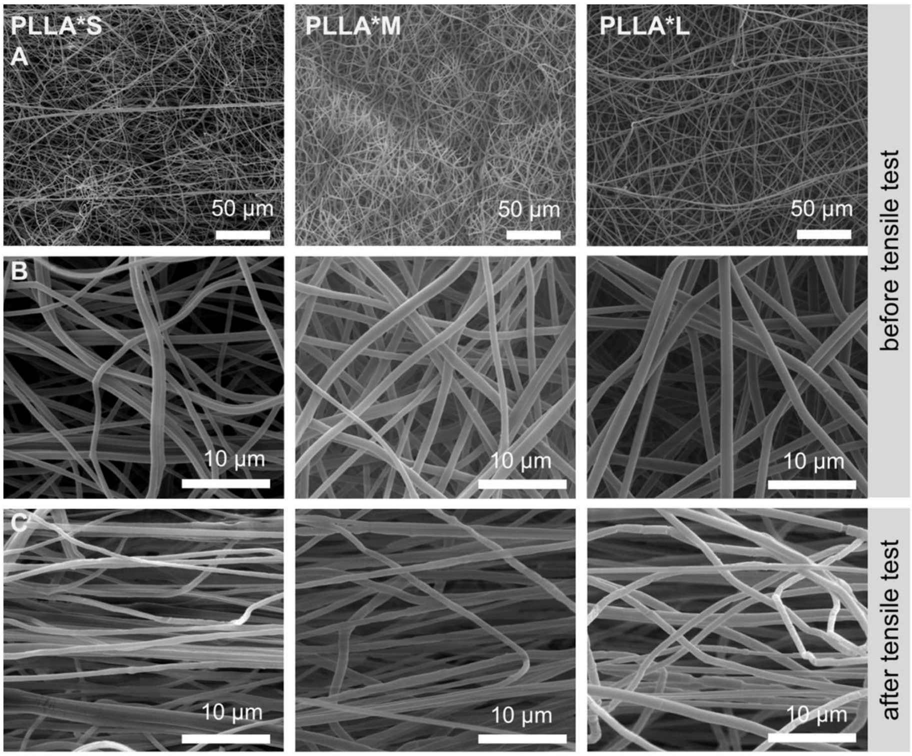

Fig. 7. SEM of PLLA*S, M, L fibers at different magnifications and stress conditions. Native unloaded nonwovens A: at 1000× magnification each, and B: at 4000× magnification each. C: Loaded nonwovens after tensile test at 4000× magnification each with noticeable thinning and necking of the fibers.

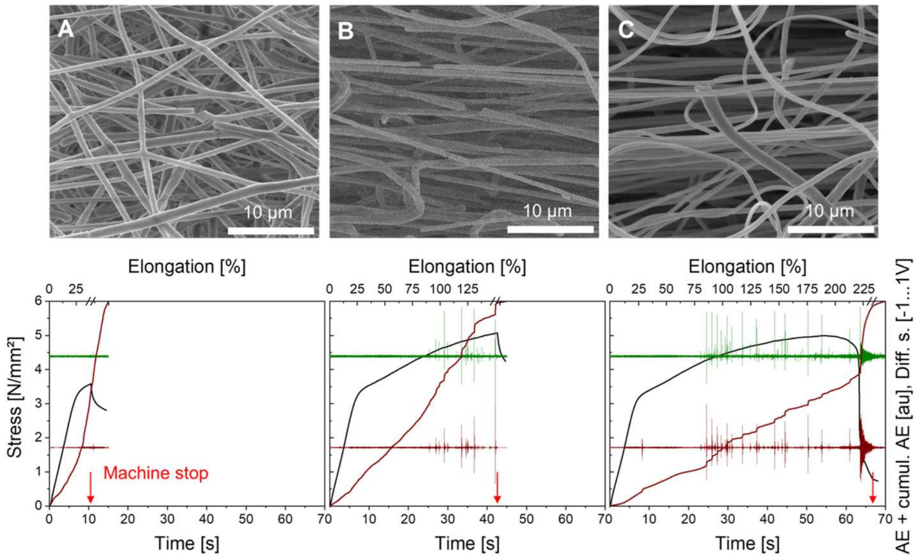

Fig. 8. Partially stretched samples of PLLA*M nonwoven. The machine was stopped at specific points, A: after yield point, B: after onset of strong spikes (slight knee curve), and C: shortly before complete breaking. In the top row representative SEM images are presented. The graphics in bottom row display combined diagrams of stress-strain curve (black), difference signal (green), and direct as well as cumulative normalized AE signal (dark red). The red arrow indicates the moment of machine stop.

concurrently with a slight knee curve in some stress-strain curves at an elongation of approximately 80–100%, and cause a clearly visible slope increase in the cumulative AE curves (Figs. 6 C, Fig. 8 B, C). The most common assumption is that this indicates the onset of tearing of individual thick fibers. The frequency of strong spike signals decreases slightly towards the maximal tensile strength. These strong spikes are not found during sample breaking. At maximum of the stress-strain curve, which occurs at approximately 200% elongation, a low constant signal becomes audible, which turns in strong AE activity during sample breaking. The samples break during AE noise with a falling-rising tone. Towards complete breaking the AE signal takes on a crackling quality. In spite of the same material and similar porosity, delamination, such as that observed in PLLA*S nonwovens, was never seen. The central region of the stress-strain curve for PLLA*M is very smooth and some samples show a barely noticeable knee curve. The increased AE signal at this knee curve demonstrates that the AE signal indicates mechanical events that are not clear from the stress-strain curve alone. This means an additional gain in information and confirms the meaningfulness of the method. In this case, we see hidden material defects occurring in the PLLA*M samples, which only emerge in AE signal.

In contrast, nonwoven PLLA*L revealed the most thinning of fiber diameter during tensile testing, with a nearly halved average diameter (54%), as well as clearly discernible necking. In SEM images no fiber bundles were found. Very few or no strong spike signals were detected in AE. This is also evidence to suggest the absence of thicker fibers or bundles. After passing the yield point, rising AE activity of low intensity is concomitant with the smooth rising of the stress curve (Figs. 5 B, Fig. 6 B). We cannot be certain of the source of this noise, but fiber sliding in these relatively thick and porous samples is conceivable. Some fiber necking may contribute to that signal. At the maximum of the stress-strain curve, rising AE intensity seems to be in good agreement with the increasing number of rupturing fibers (Figs. 5 C, Fig. 6 D). The highest AE intensity corresponds to the falling stress-strain curve with breaking of the entire sample (Figs. 5 D, Fig. 6 F). In addition, a falling-rising frequency is audible and partly visible in the spectrogram for most samples (e.g. Fig. 6 F). The characteristics of PLLA*L show generally high mechanical stability and support continued investigation or application.

4.2. Information gained from audio spectrum

An audio spectrum visualizes the current signal intensity (color) of a spectral band over time. A characteristic pattern was observed in most of the samples (for all three nonwovens) with a falling and rising pitch during breaking. In the spectrogram as well as audible output that pattern appears as a remarkable decrease and increase of frequency in the sound signal (dotted lines in Fig. 6 E, F, and Fig. S 2 B). Another aspect worth mentioning is that the frequency decrease/increase means a continuous sweep of the frequency band, with the reversal point corresponding to the set oscillator frequency. We assume that after a fiber break, part of the energy is released by the rapidly retracting fiber ends, and the surrounding fibers are excited to vibrate. Analogous to a guitar string, the resulting frequency depends on the force, cross section, density and free length of the resonating fibers (Tsuji and Müller, 2022). From this, we can conclude that the pattern is related to changing fiber tension, because the more tension a fiber is under, the higher the tone it produces. Furthermore, preceding considerations have led to a correct estimation of the frequency range of expected signals (Supporting Information, section 1), our AE setup is sensitive in a relevant frequency band. But the spectrogram alone does not allow any conclusions about the frequency progression in the ultrasonic AE signal of rupturing fibers. Considering the stress-strain curve shows the technical instead of the real tension. Due to fewer and thinner fibers having to bear the stress, a permanently increasing real tension is suggested, and consequently the frequencies of the original ultrasonic AE signal permanently increase. Unfortunately, due to the down-mixing and the narrow bandwidth of the input signal, interesting signal components may be lost (Dvornikov et al., 2022). Nevertheless, despite the limitations, it was possible to indirectly prove the course of the frequency increase due to the increasing fiber tension. In general, the strong spike signals appear as broad bands in the audio spectrum, whereas non-spike signals of delamination or specimen breaking show a narrower frequency range. That does not necessarily imply that the spectrum of strong spike signals is of a broader band, as it may be a misleading artifact due to the high signal intensity.

4.3. Relevance of AE recording of unembedded fiber materials in medical field

AE recording can be easily implemented in existing testing procedures of nanofibrous biomaterials and is especially relevant for load-bearing implants. The performance of biomedical implants is of the highest significance. Knowledge of their failure behavior down to single fibers provides beneficial information and may help to improve implant safety. For instance, in the cardiovascular system implants, for example heart valves (Capulli et al., 2016) and vascular grafts (Jirofti et al., 2018), have to endure multitudes of load cycles. . Load-bearing fibers are used in further areas. Besides monofilaments, multiple nanofiber systems are also used for surgical meshes (Baylón et al., 2017). Surgical meshes degrade by erosion, unraveling, and creep. More work and methods are needed to quantify this phenomenon (Schmidt and Taylor, 2021) and AE measurements may provide an option in these cases. In regenerative medicine helical microtissue is supposed to mimic stretchable tissues (Li et al., 2019b). AE investigation of the failure behavior of fibrous scaffolds or artificial tissues may generate relevant findings. Surgical yarns for tendon surgery (Ye et al., 2018), or yarns for general use or tissue scaffolds (Sara Asghari Mooneghi et al., 2019), as well as twisted yarns (Fakhrali et al., 2016) are a common focus of current research. Scaffolds made of core-shell-fibers can be used as drug loading platform for tissue engineering (Li et al., 2019a). Advanced development of existing testing methods by combining them with modern camera technology and AE can improve quality assurance, and potentially lead to improved screening methods for the identification of new fiber structures in the future.

4.4. Limitations

The air-coupled setup does not record the original broadband signal. It uses a narrow band sensor and frequency conversion. Due to the sensor's directional characteristics (Fig. S 1) and the length of a stretched sample, the intensity of received AE signal depends on distance and angle relating to the sensor. Events happening not directly in front of the sensor will contribute a weaker signal. However, given the high number of fibers, relevant events will be recorded even when using only one sensor. This can also be seen as an advantage, as a defined region of the sample can be brought into focus.

Conventional AE setups measure structure-borne sound with sensors mounted on the sample or the clamp. A signal corresponding to the mechanical fracture energy cannot be measured with the presented air-coupled system. Instead, air flows into the space pre-occupied by the tearing fiber and thereby generates a part of the sound signal. Another signal component is generated by vibrations of remaining fibers. Their frequency increases with tension, as explained above. These signals are neither comparable to conventional AE signals, nor are they accessible to traditional AE equipment. Thus, conclusive comparison with the scientific literature is limited. However, air-coupled signals may have the potential to expand the horizon of AE. Because of the narrow band sensor sensitivity, most of original AE signal is undetected. Additional down-mixing lowers the information content and may change the waveform limiting the value of spectral analysis. Nevertheless, single events are clearly detectable. Due to being sensitive to air-borne sound, the tensile testing instrument should not be placed in a loud noisy industrial environment, so a calm laboratory is advantageous. As AE data on tensile behavior of bare nanofiber nonwovens appears to be absent in the current literature, no valid data comparison or verified statements about failure modes can be provided within this study.

5. Conclusions and Outlook

This initial work introduces a methodology to detect and record weak ultrasonic AE signals of unembedded nanofibers exemplified on PLLA nonwovens during tensile testing. Ultrasonic signals are frequency converted, then directed to recording and audible output in a specially developed setup. The methodology is able to process weak input signals, avoid acoustical feedback, exclude most background noise, and does not influence the tensile experiment. Shown on representative PLLA electrospun nanofiber nonwovens with varied fiber diameters, AE activity corresponding with tensile measurements was detected. AE signals in direct or cumulative representation offer substantially more information than can be provided from stress-strain curves only. AE recording showed evidence of hidden material defects in PLLA nonwovens, which are not evident in stress-strain curves, such materials with undetected defects may pass through quality control systems. It is difficult to decide via visual monitoring whether the electrospinning process has run correctly, AE supplies valuable data for additional process control. The AE sensing method is useful in several research fields, and can help to improve quality assurance in industrial production processes of fibrous materials that are intended for medical purposes. Due to the increasing importance of nanofiber materials in medical applications, significant attention should be paid to the further development of testing methods. Mechanical properties of implant materials are often relevant for safety, durability, and stability. The contactless air-coupled AE method for nanofiber nonwovens uses air-borne signals, providing information content not accessible to established solid-borne setups. It appears suitable for gaining knowledge about material failure at the nanoscale. Currently, the method presented here consists of a preliminary laboratory setup with the potential for further upgrades. A more advanced setup could feature broadband sensors, direct signal recording, recording of signals from multiple sensors and inclusion of non-acoustic information, such as video recording and measurement of local deformation. Data analysis using spectral filtering, pattern detection and evaluation of signal energy could provide new and meaningful insights. Further studies are suggested to investigate the influence of mechanical test parameters, such as cross-head speed and temperature, as well as material properties and microstructure of the nonwoven samples. Investigation of suitable nano standards or test specimens supports the validity of the method. Further work needs to address AE sensing of mechanical deformation of nanofibrous implants in water or saline solution. While such liquid setups mimic biomedical application conditions, new acoustic challenges are to be expected. The system may be of particular interest for manufacturers of testing machines or accessories, for material scientists, as well as for QA in medical device manufacture. In particular, engineering of nanofiber covered implants or other mechanically stressed porous or fibrillary structures may benefit, for example enabling prediction of the fiber level micromechanics of material failure. The weak ultrasonic AE signals of unembedded breaking nanofiber nonwovens have been successfully recorded during tensile tests; the method is effective and unlocks great potential for establishing it as a standard for material testing.

Funding

Funding: Partial financial support by the European Regional Development Fund (ERDF) and the European Social Fund (ESF) within the excellence research program Card-ii-Omics and the collaborative research between economy and science of the state Mecklenburg-Vorpommern and by the Federal Ministry of Education and Research (BMBF) within RESPONSE "Partnership for In-novation in Implant Technology" is gratefully acknowledged.

Impact statement

AE recording is not yet a standard test for bare nanofiber materials. It provides additional information to the tensile test which is routinely performed. The technique can prove beneficial by detecting hidden material defects, especially for fibrous materials intended for medical use. This technique holds great potential for the future development of testing methods for nanofibers.

CRediT authorship contribution statement

Andreas Götz: Writing – original draft, Visualization, Validation, Methodology, Investigation, Formal analysis. **Volkmar Senz:** Writing – review & editing, Resources, Investigation. **Wolfram Schmidt:** Writing – review & editing, Conceptualization. **Daniela Koper:** Writing – review & editing, Conceptualization. **Niels Grabow:** Project administration, Funding acquisition, Conceptualization. **Sabine Illner:** Writing – review

& editing, Visualization, Resources, Conceptualization.

Declaration of competing interest

The authors declare that they have no known competing financial interests or personal relationships that could have appeared to influence the work reported in this paper.

Data availability

Files are available in Mendeley repository, doi: 10.17632/3cv9mvckkh.2.

Acknowledgements

The authors acknowledge technical assistance of Jonathan Ortelt, Manfred Strotmeier, Katja Hahn and Babette Hummel, as well as a word of thanks to Jennifer Huling for proofreading.

Appendix A. Supplementary data

Supplementary data to this article can be found online at https://doi.org/10.1016/j.jmbbm.2023.105720.

References

Alam, M.S., Gulshan, F., Ahsan, Q., Wevers, M., Pfeiffer, H., van Vuure, A.-W., Osorio, L., Verpoest, I., 2017. Development of methodology to assess the failure behaviour of bamboo single fibre by acoustic emission technique. J. Inst. Eng. India Ser. D 98 (1), 9–17. https://doi.org/10.1007/s40033-016-0118-8.

Arbeiter, D., Oschatz, S., Illner, S., Grabow, N., 2020. Study of poly(L-lactide) using fast scanning calorimetry. Curr. Dir. Biomed. Eng. 6 (3), 422–425. https://doi.org/10.1515/cdbme-2020-3109.

Arbeiter, D., Reske, T., Teske, M., Bajer, D., Senz, V., Schmitz, K.-P., Grabow, N., Oschatz, S., 2021. Influence of drug incorporation on the physico-chemical properties of poly(l-lactide) implant coating matrices-A systematic study. Polymers 13 (2). https://doi.org/10.3390/polym13020292.

Arun, M.W.J., Yoganandan, N., Stemper, B.D., Pintar, F.A., 2014. A methodology to condition distorted acoustic emission signals to identify fracture timing from human cadaver spine impact tests. J. Mech. Behav. Biomed. Mater. 40, 156–160. https://doi.org/10.1016/j.jmbbm.2014.08.023.

Baji, A., Mai, Y.-W., Wong, S.-C., Abtahi, M., Chen, P., 2010. Electrospinning of polymer nanofibers: effects on oriented morphology, structures and tensile properties. Compos. Sci. Technol. 70 (5), 703–718. https://doi.org/10.1016/j.compscitech.2010.01.010.

Bao, G., Kronick, P.L., Marmer, W.N., 2001. Nondestructive measurement of mechanical properties of wool fabrics by an acoustic emission method. Textil. Res. J. 71 (3), 255–260. https://doi.org/10.1177/004051750107100311.

Baylón, K., Rodríguez-Camarillo, P., Elías-Zúñiga, A., Díaz-Elizondo, J.A., Gilkerson, R., Lozano, K., 2017. Past, present and future of surgical meshes: a review. Membranes 7 (3). https://doi.org/10.3390/membranes7030047.

Buis, A., Guarato, F., Law, J., Ralston, Z., Courtney, A., 2018. A feasibility study to investigate if there is a correlation between soft tissue deformation and acoustic emission. Can. Prosthet. Orthot. J. https://doi.org/10.33137/cpoj.v1i1.30354.

Capulli, A.K., MacQueen, L.A., Sheehy, S.P., Parker, K.K., 2016. Fibrous scaffolds for building hearts and heart parts. Adv. Drug Deliv. Rev. 96, 83–102. https://doi.org/10.1016/j.addr.2015.11.020.

Dvornikov, S.V., Kryachko, A.F., Velmisov, I.A., Zatuchny, D.A., 2022. Amplifiers in Radio Receivers: Characteristics, Operating Principles, and Efficiency, first ed. Springer Nature Singapore; Imprint Springer, Singapore, p. 249 (Chapter 6) Frequency Converters.

Ellison, M.S., Dai, J., 1996. Description and application of an acoustic pulse detector to nylon 6 and polypropylene single fiber fracture. Textil. Res. J. 66 (5), 295–299. https://doi.org/10.1177/004051759606600502.

Fakhrali, A., Ebadi, S.V., Gharehaghaji, A.A., Latifi, M., Moghassem, A., 2016. Analysis of twist level and take-up speed impact on the tensile properties of PVA/PA6 hybrid nanofiber yarns. E-Polymers 16 (2), 125–135. https://doi.org/10.1515/epoly-2015-0248.

Fiedler, N., Arbeiter, D., Oschatz, S., Grabow, N., Lebahn, K., 2021. Definition of test parameters for dynamic mechanical testing of polymeric implant materials. Curr. Dir. Biomed. Eng. 7 (2), 684–687. https://doi.org/10.1515/cdbme-2021-2174.

Götz, A., Senz, V., Schmidt, W., Huling, J., Grabow, N., Illner, S., 2021. General image fiber tool: a concept for automated evaluation of fiber diameters in SEM images. Measurement 177, 109265. https://doi.org/10.1016/j.measurement.2021.109265.

Hamstad, M.A., 1986. A review: acoustic emission, a tool for composite-materials studies. Exp. Mech. 26 (1), 7–13. https://doi.org/10.1007/BF02319949.

Illner, S., Sühr, M., Fiedler, N., Arbeiter, D., Götz, A., Schmitz, K.-P., Grabow, N., 2021. Fiber composite materials via coaxial, dual or blend electrospinning. Curr. Dir. Biomed. Eng. 7 (2), 680–683. https://doi.org/10.1515/cdbme-2021-2173.

Jiang, S., Chen, Y., Duan, G., Mei, C., Greiner, A., Agarwal, S., 2018. Electrospun nanofiber reinforced composites: a review. Polym. Chem. 9 (20), 2685–2720. https://doi.org/10.1039/C8PY00378E.

Jirofti, N., Mohebbi-Kalhori, D., Samimi, A., Hadjizadeh, A., Kazemzadeh, G.H., 2018. Small-diameter vascular graft using co-electrospun composite PCL/PU nanofibers. Biomed. Mater. 13 (5), 55014 https://doi.org/10.1088/1748-605X/aad4b5.

Khaimov, V., Klußmann-Fricke, B.-J., Illner, S., Siewert, S., Schmitz, K.-P., 2021. In vitro biocompatibility testing of polymeric nanofiber scaffolds: fine-tuning for a better prediction of the in vivo behaviour. Curr. Dir. Biomed. Eng. 7 (2), 621–624. https://doi.org/10.1515/cdbme-2021-2158.

Ko, F.K., Wan, Y., 2014. Characterization of nanofibers. In: Ko, F.K., Wan, Y. (Eds.), Introduction to Nanofiber Materials. Cambridge University Press, Cambridge, ISBN 978-0-521-87983-5, pp. 101–145.

Kowalczyk, T., 2020. Functional micro- and nanofibers obtained by nonwoven post-modification. Polymers 12 (5). https://doi.org/10.3390/polym12051087.

Lee, C., Zhang, L., Morris, D., Cheng, K.Y., Ramachandran, R.A., Barba, M., Bijukumar, D., Ozevin, D., Mathew, M.T., 2021. Non-invasive early detection of failure modes in total hip replacements (THR) via acoustic emission (AE). J. Mech. Behav. Biomed. Mater. 118, 104484 https://doi.org/10.1016/j.jmbbm.2021.104484.

Li, T., Tian, L., Liao, S., Ding, X., Irvine, S.A., Ramakrishna, S., 2019a. Fabrication, mechanical property and in vitro evaluation of poly (L-lactic acid-co-ε-caprolactone) core-shell nanofiber scaffold for tissue engineering. J. Mech. Behav. Biomed. Mater. 98, 48–57. https://doi.org/10.1016/j.jmbbm.2019.06.003.

Li, Y., Guo, F., Hao, Y., Gupta, S.K., Hu, J., Wang, Y., Wang, N., Zhao, Y., Guo, M., 2019b. Helical nanofiber yarn enabling highly stretchable engineered microtissue. Proc. Natl. Acad. Sci. U.S.A. 116 (19), 9245–9250. https://doi.org/10.1073/pnas.1821617116.

Liu, J., Li, F., Chen, L., Guan, Y., Tian, L., Xiong, Y., Liu, G., Tian, Y., 2018. Quantitative imaging of Candida utilis and its organelles by soft X-ray Nano-CT. J. Microsc. 270 (1), 64–70. https://doi.org/10.1111/jmi.12650.

Matschegewski, C., Kohse, S., Markhoff, J., Teske, M., Wulf, K., Grabow, N., Schmitz, K.-P., Illner, S., 2022. Accelerated endothelialization of nanofibrous scaffolds for biomimetic cardiovascular implants. Materials 15 (6). https://doi.org/10.3390/ma15062014.

Mazzoni, D., 2021. Audacity: Free, Open Source, Cross-Platform Audio Software. https://www.audacityteam.org/. (Accessed 27 April 2021).

Mehan, R.L., Mullin, J.V., 1971. Analysis of composite failure mechanisms using acoustic emissions. J. Compos. Mater. 5 (2), 266–269. https://doi.org/10.1177/002199837100500213.

Mooneghi, Sara Asghari, , Ali Akbar Gharehaghaji, Hosseini-Toudeshky, Hossein, Torkaman, Giti, 2019. Effect of fatigue loading on wicking properties of polyamide 66 nanofiber yarns. J. Appl. Polym. Sci. 136 (11), 47206 https://doi.org/10.1002/app.47206.

Acoustic textiles. Chapter:. In: Padhye, R., Nayak, R. (Eds.), 2016. Acoustical Test Methods for Nonwoven. Springer, Singapore, p. 242.

Papkov, D., Zou, Y., Andalib, M.N., Goponenko, A., Cheng, S.Z.D., Dzenis, Y.A., 2013. Simultaneously strong and tough ultrafine continuous nanofibers. ACS Nano 7 (4), 3324–3331. https://doi.org/10.1021/nn400028p.

Qi, G., Fan, M., Lewis, G., Wayne, S.F., 2012. An innovative multi-component variate that reveals hierarchy and evolution of structural damage in a solid: application to acrylic bone cement. J. Mater. Sci. Mater. Med. 23 (2), 217–228. https://doi.org/10.1007/s10856-011-4481-6.

Rack, A., Zabler, S., Müller, B.R., Riesemeier, H., Weidemann, G., Lange, A., Goebbels, J., Hentschel, M., Görner, W., 2008. High resolution synchrotron-based radiography and tomography using hard X-rays at the BAMline (BESSY II). Nucl. Instrum. Methods Phys. Res. Sect. A Accel. Spectrom. Detect. Assoc. Equip. 586 (2), 327–344. https://doi.org/10.1016/j.nima.2007.11.020.

Reske, T., Wulf, K., Illner, S., Eickner, T., Grabow, N., Schmitz, K.-P., Siewert, S., Khaimov, V., 2021. Non-destructive analysis of drug distribution in nonwovens as drug-delivery systems for biomedical applications. Curr. Dir. Biomed. Eng. 7 (2), 504–506. https://doi.org/10.1515/cdbme-2021-2128.

Russell, S.J. (Ed.), 2007. Handbook of Nonwovens. CRC Press, Boca Raton, ISBN 9781855736030, p. 530.

Sánchez-Molina, D., Martínez-González, E., Velázquez-Ameijide, J., Llumà, J., Rebollo Soria, M.C., Arregui-Dalmases, C., 2015. A stochastic model for soft tissue failure using acoustic emission data. J. Mech. Behav. Biomed. Mater. 51, 328–336. https://doi.org/10.1016/j.jmbbm.2015.07.002.

Schindler, A., Harper, D., 1979. Polylactide. II. Viscosity–molecular weight relationships and unperturbed chain dimensions. J. Polym. Sci. Polym. Chem. Ed. 17 (8), 2593–2599. https://doi.org/10.1002/pol.1979.170170831.

Schmidt, A., Taylor, D., 2021. Erosion of soft tissue by polypropylene mesh products. J. Mech. Behav. Biomed. Mater. 115, 104281 https://doi.org/10.1016/j.jmbbm.2020.104281.

Silberschmidt, V.V. (Ed.), 2022. Mechanics of Fibrous Networks. Elsevier, San Diego, ISBN 978-0-12-822207-2.

Sin, L.T., Rahmat, A.R., Rahman, W.A.W.A., 2012. Polylactic Acid: PLA Biopolymer Technology and Applications. William Andrew, Oxford, ISBN 9781437744590.

Sodomka, L., 2004. Application of acoustical emission as a new effective diagnostic tool in the textile fields. Eur.Work. Group Acoust. Emiss. 26 (1), 783–790.

Tsuji, K., Müller, S.C., 2022. Physics and Music: Essential Connections and Illuminating Excursions. Springer, Cham, Switzerland, p. 424.

Vallen Jochen, 2021. Acoustic Emission Working Group. http://www.aewg.org/index.html. (Accessed 14 April 2021).

Velu, Y.K., Ellison, M.S., Dai, J., Rogers, C.D., 1999. Single fiber acoustic emission and tensile properties from cotton bundle fracture tests. Textil. Res. J. 69 (8), 616–620. https://doi.org/10.1177/004051759906900811.

Wang, L., Cao, S., Jiang, X., Salje, E.K.H., 2021. Cracking of human teeth: an avalanche and acoustic emission study. J. Mech. Behav. Biomed. Mater. 122, 104666 https://doi.org/10.1016/j.jmbbm.2021.104666.

Williams, J.H., Lee, S.S., 1978. Acoustic emission monitoring of fiber composite materials and structures. J. Compos. Mater. 12 (4), 348–370. https://doi.org/10.1177/002199837801200402.

Wu, G., Zhong, Y.Q., Yu, W.D., 2015. Evaluating tensile properties of wool fibers based on the waveform of acoustic emission. KEM 671, 391–396, 10.4028/www.scientific.net/KEM.671.391.

Wulf, K., Arbeiter, D., Matschegewski, C., Teske, M., Huling, J., Schmitz, K.-P., Grabow, N., Kohse, S., 2020. Smart releasing electrospun nanofibers—poly: L.lactide fibers as dual drug delivery system for biomedical application. Biomed. Mater. 16 (1), 15022 https://doi.org/10.1088/1748-605x/abbec8.

Ye, Y.-J., Zhou, Y.-Q., Jing, Z.-Y., Liu, Y.-Y., Yin, D.-C., 2018. Electrospun heparin-loaded core-shell nanofiber sutures for achilles tendon regeneration in vivo. Macromol. Biosci. 18 (7), e1800041 https://doi.org/10.1002/mabi.201800041.

Supporting Information

1. Detailed background considerations of the method
2. Sensitivity
3. Nonwoven PLLA*S
4. AE activity of all samples
5. Stress-strain-curves of all samples

1. Detailed background considerations of the method

For detection and recording of weak ultrasonic signals of tearing nanofibers, a method of technical implementation has been successfully identified, considering the following issues.

No.	Issues
0	AE sensing methods in the tensile unit directly, to detect tiny force changes, were considered, but not further pursued. Likewise optical imaging or diffraction methods, to detect fiber thinning and rupture, or gaining information about the inner microstructure, were considered, but not further pursued.
1	The main challenge is the low energy of a rupturing nanofiber, resulting in a weak signal and the need for a highly sensitive sensor as well as shielding from disturbances.
2	Background noise has to be suppressed and acoustic feedback is to avoid.
3	Without being embedded in hard material, AE of breaking nonwoven samples are expected in a frequency range below 100 kHz due to less mechanical coupling to air and their lower sound velocity.
4	Due to the difficult audibility of breaking nonwovens, the small fiber diameters and a low mass inertia, AE can be expected in a frequency range that lies above the audible spectrum.
5	Following issues 3 and 4, AE of breaking nanofiber nonwovens are expected in ultrasonic frequencies at a few tens of kilohertz. Assuming string vibration theory (Tsuji and Müller, 2022), this frequency range can be confirmed.
6	The weak ultrasonic AE from rupturing nanofibers is expected as pop signal in a wide frequency band. FFT spectra of fiber-break signals cover a broad frequency band (Gorman, 2011).
7	Considering issues 5 and 6, a part of the AE signal can be detected by a narrowband ultrasonic sensor.
8	The main focus of this work is on qualitative statements, less on quantitative measurements, considering that energy techniques do not necessarily have an advantage over counting techniques (Harris and Bell, 1977).
9	A contactless method is chosen to avoid any influence to the mechanics of the tensile test. Therefore the sensor is placed some millimeter behind the tensile specimen without direct contact.
10	Due to a lack of sufficient comparisons from the literature, it is very challenging to properly interpret recorded graphs and distinguish between a real signal, disturbing signal, and background noise only on the data basis. Audible output improves the appraisal and plausibility of the results.
11	Considering issue 10, in this work, a signal transformation is chosen that allows the signal to be made audible without much loss of information. To transform the ultrasonic sound signal into an audible sound signal the high frequency sound signal is mixed with an oscillator generated signal which is adjusted close to the maximal sensitivity of the sensor. The down-mixed differential frequency signal (synthetic audio signal) is further amplified for recording and audible output.
12	From issues 7 and 11 follows, that most background noise as well as potential acoustical feedback is eliminated.

An air-coupled design was chosen for several reasons. The sample is very fragile, has a clamping length of about 2 cm and must not be mechanically affected by sensor mounting. The sensor membrane horn has a diameter of 7mm and sits in a larger housing. If attached directly on the sample, noise would be generated due to friction between sample and sensor horn, superimposing the actual measurement signal. Therefore, direct attachment to the specimen is neither possible nor practical. The nonwoven sample consists of numerous individual fibers with undefined connection. Hence, individual fiber breaking may result in dissipation of fracture energy by friction between loose interfiber connections. Transmission of the fracture pulse through numerous loose frictional contacts and elastically stretched fiber elements attenuates the signal considerably. Additionally, the information about the shape of the waveform is lost. If attaching the sensor directly to the clamp, further strong attenuation is expected at the transition into the clamp with its relatively large inertial mass (relative to the torn fiber) and small contact area (due to high sample porosity), as well as at the transition into a bonded acoustic sensor (impedance drop). Hence, positioning of an air-coupled sensor at a short distance from the sample appears reasonable.

2. Sensitivity

The frequency-response characteristic is described in section 2.2. Here, the following additional information is provided: The natural resonance of a vibrating system depends on shape, mass and material elasticity, and can be excited by a suitable energy supply. The sensor has the highest sensitivity at the resonance frequency, as this requires the least energy for excitation. To measure the natural resonance of the sensor, it was exposed to a moderate air stream. An illustrative example is vibrations in a spider web due to a relationship between fiber length and frequency (Su et al., 2022). Another example is a tree in the wind: leaves shake quickly, the whole tree swings slowly, both excited by the same air stream. In our setup, the sensor membrane vibrates in the ultrasonic range.

Sound causes a forced oscillation of the sensor membrane with the exciting frequency. Consequently, sounds falling outside the resonance frequency are also transmitted, but with less signal intensity. Various broadband noise from different sound sources (containing audible and ultrasonic frequencies) was used for testing the device input, e.g. friction noise on paper, cardboard, textiles, hissing of compressed air through a small vent. All produced consistent signals in terms of frequency response (Figs. 2 and 3).

The sensitivity of the sensor also depends on the orientation to the sound source. This angle dependency is shown in Fig S 1.

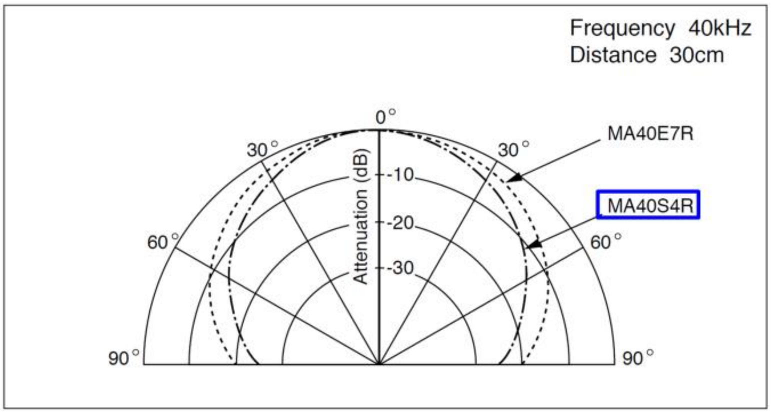

Fig S 1. Directional receiving pattern. manufacturer’s sensor information (data sheet).

3. Nonwoven PLLA*S

Due to delamination in tensile experiment and therefore inadequate comparability to the other nonwovens PLLA*S was excluded from main analysis and is presented in Supporting Information. The results are presented in Fig S 2 and Fig S 3.

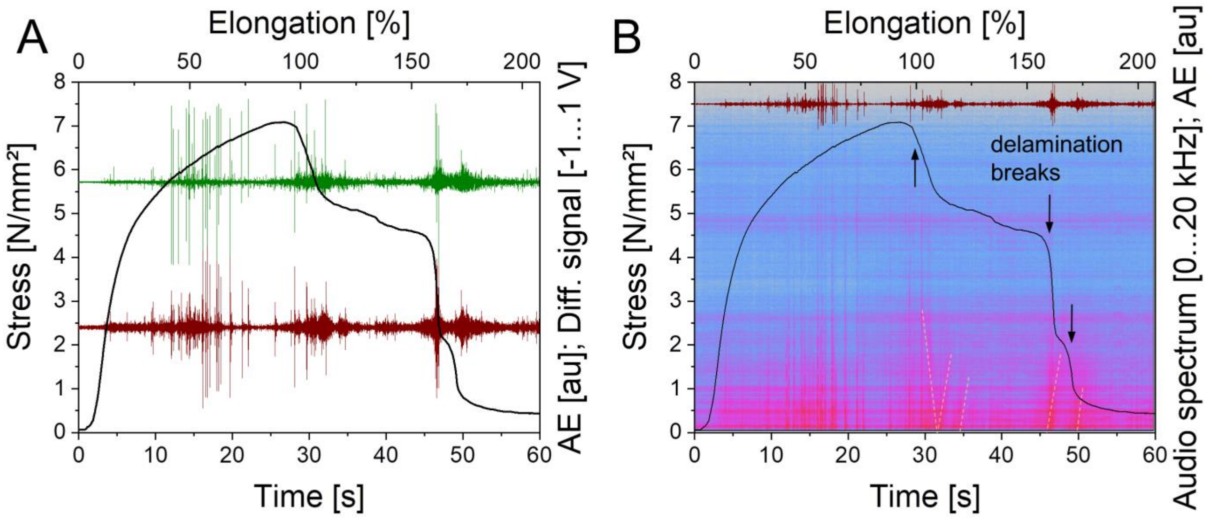

Fig S 2. Tensile experiment AE and spectrum of nonwoven PLLA*S. A: Combined diagram of tensile stress curves (n = 6). AE of one illustrative sample is displayed, difference signal in the range of ± 1V (green), audio signal (dark red), and audio spectrum from 0 Hz (bottom) up to 20 kHz (top) in linear scaling. PLLA*S revealed a tensile strength of approximately 6 MPa, the samples broke at elongation of 80% to 120%, and the breaking occurred in stages over several delaminations. B: The main delamination breaks are indicated by arrows. A falling-rising tone was audible and visible in audio spectrum during sample breaking, the dotted lines indicate these distinct decreasing-increasing sounds.

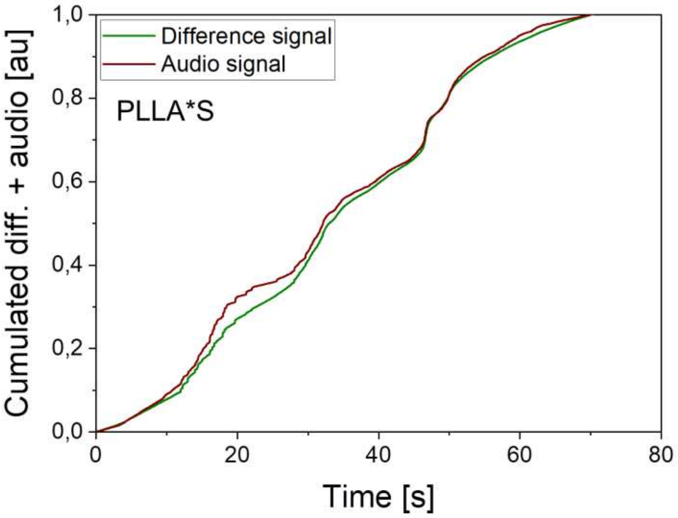

Fig S 3. Cumulative normalized signals of nonwoven PLLA*S. comparison of cumulative difference signal (green) and cumulative AE (dark red).

4. AE activity of all samples

AE recordings of all nonwoven samples (n = 6 each) are displayed in Fig S 4, Fig S 5, and Fig S 6. For presentation in the main part of this work these samples were selected: PLLA*L sample 3, PLLA*S sample 1, and PLLA*M sample 5.

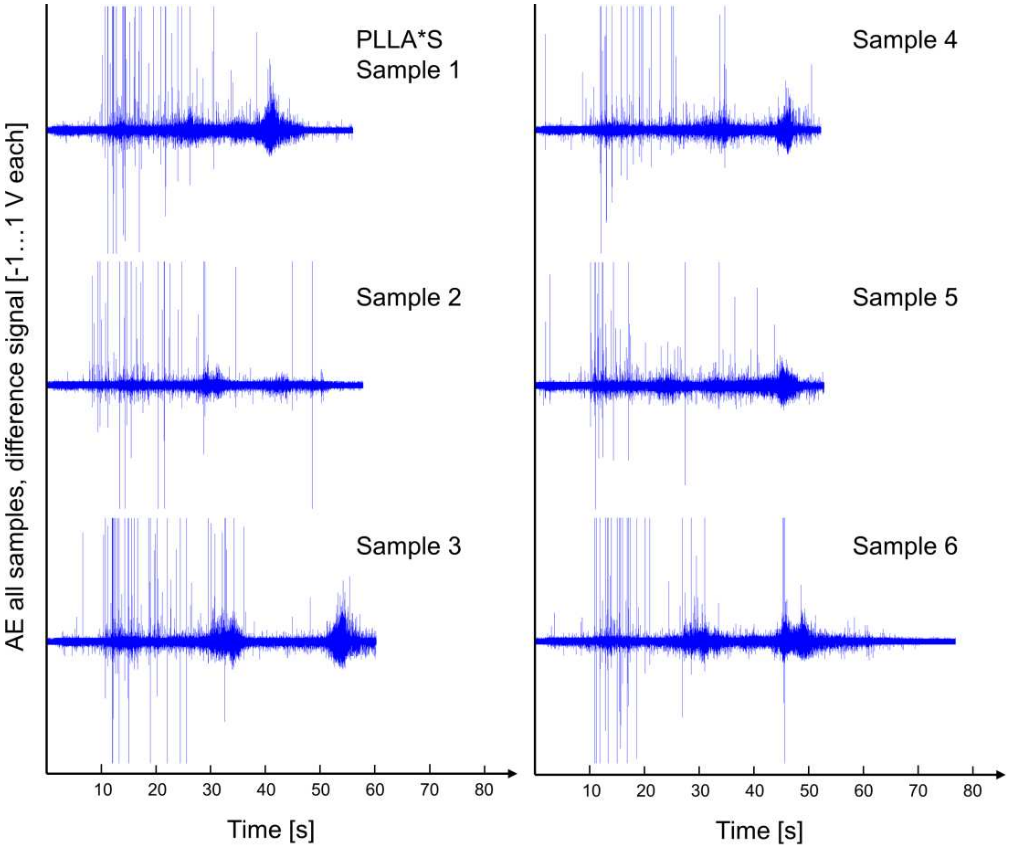

Fig S 4. AE of all samples. Comparison, difference signal of all samples of nonwoven PLLA*S.

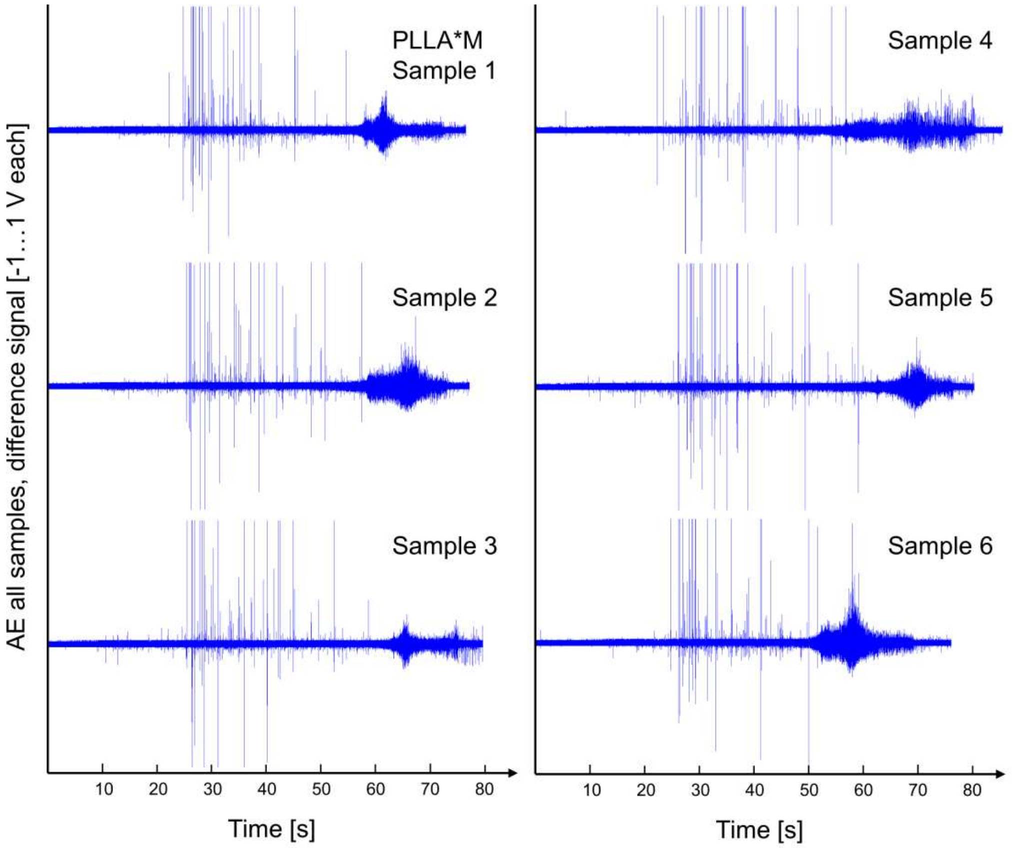

Fig S 5. AE of all samples. Comparison, difference signal of all samples of nonwoven PLLA*M.

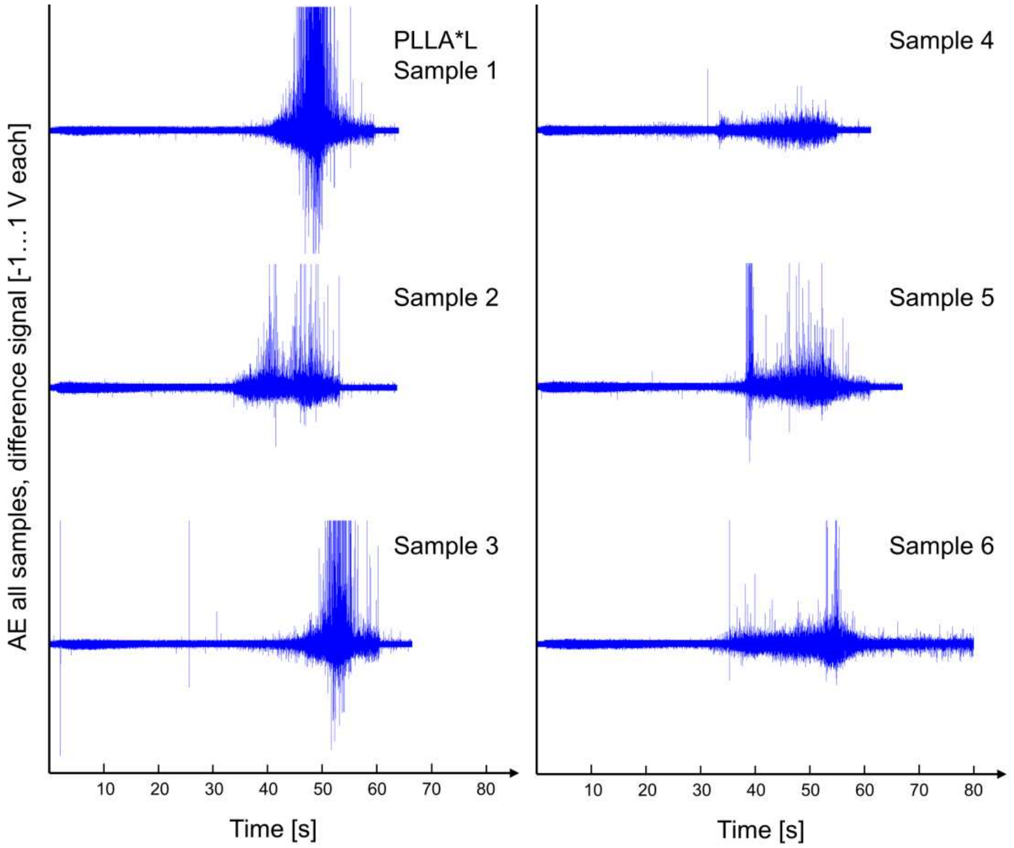

Fig S 6. AE of all samples. Comparison, difference signal of all samples of nonwoven PLLA*L.

5. Stress-strain curves of all samples

Recordings of tensile testing of all nonwoven samples (n = 6 each) are displayed in Fig S 7.

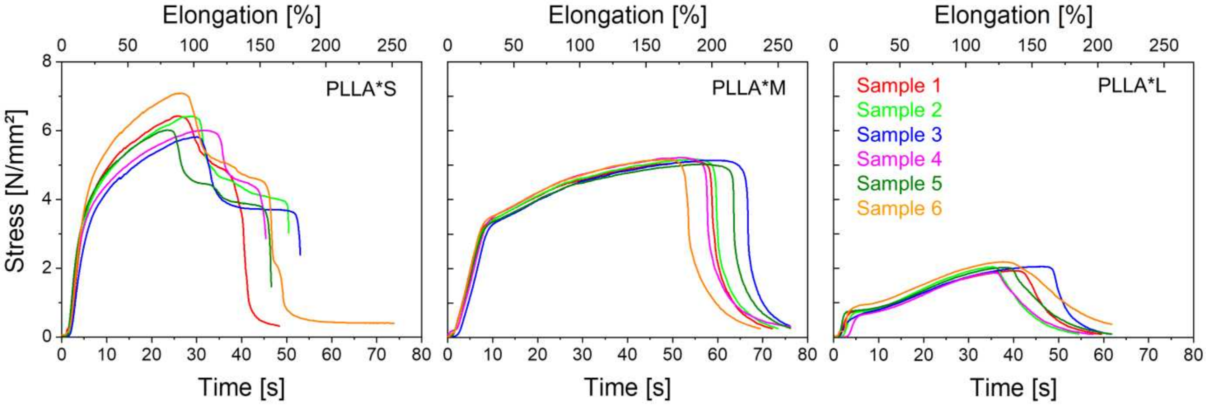

Fig S 7. Tensile test of all samples. Comparison of stress-strain curves, the sample numbers correspond to Fig S 6, Fig S 4, and Fig S 5.

References

Gorman, M.R., 2011. Modal AE analysis of fracture and failure in composite materials, and the quality and life of high pressure composite pressure vessels. Journal of Acoustic Emission 29.

Harris, D.O., Bell, R.L., 1977. The measurement and significance of energy in acoustic-emission testing. Experimental Mechanics 17 (9), 347-353. 10.1007/BF02326321.

Su, I., Hattwick, I., Southworth, C., Ziporyn, E., Bisshop, A., Mühlethaler, R., Saraceno, T., Buehler, M.J., 2022. Interactive exploration of a hierarchical spider web structure with sound. J Multimodal User Interfaces 16 (1), 71-85. 10.1007/s12193-021-00375-x.

Tsuji, K., Müller, S.C., 2022. Physics and music: Essential connections and illuminating excursions. Springer, Cham, Switzerland, 424 pp.

Götz *et al. BioMedical Engineering OnLine* (2024) 23:124
https://doi.org/10.1186/s12938-024-01316-x

BioMedical Engineering
OnLine

RESEARCH

Open Access

Transcatheter bicuspid venous valve prostheses: fluid mechanical performance testing of artificial nonwoven leaflets

Andreas Götz[1*], Sabine Illner[1], Nicklas Fiedler[1], Julia Schubert[1], Jan Oldenburg[2], Heinz Müller[3], Wolfram Schmidt[1], Klaus-Peter Schmitz[2], Niels Grabow[1] and Kerstin Lebahn[1]

*Correspondence:
andreas.goetz@uni-rostock.de

[1] Institute for Biomedical Engineering, Rostock University Medical Center, Friedrich-Barnewitz-Str. 4, 18119 Rostock, Germany
[2] Institute for ImplantTechnology and Biomaterials e.V., Friedrich-Barnewitz-Str. 4, 18119 Rostock, Germany
[3] CORTRONIK GmbH, Friedrich-Barnewitz-Str. 4a, 18119 Rostock, Germany

Abstract

Background: Chronic venous insufficiency (CVI) is a common disease with a high prevalence. Incompetent venous valves are considered as one of the main causes. Besides compression therapy, various surgical therapies are practiced, whereby the reconstruction of valves is of central importance. There is an unmet clinical need, no valve prosthesis is commercially available to date. This work introduces two versions of a patented prosthetic bicuspid valve design made of electrospun thermoplastic silicone polycarbonate polyurethane (TSPCU) nanofiber leaflets attached in a nitinol stent, and their performance in static and pulsatile operation.

Results: The valves mainly fulfill the requirements widely accepted in literature. Valves of both versions were functional in the physiological pressure range up to 50 mmHg with design specific differences.

Conclusions: The here introduced design versions act as a platform technology and can be tailored for an intended implantation site. Evaluation of the original and modified valve concept demonstrated efficacy, with limitations at higher loads for original design. At the current state, the modification is preferable for fabrication, as one processing step is eliminated. Moreover, specific design recommendations could be drawn for valves of similar basic structure. Future work will focus on long-term performance and biocompatibility prior to the initiation of preclinical in vivo studies.

Keywords: CVD, CVI, Venous valve, Chronic venous disease, Valve implant, Testing, Forward flow, Reflux

Introduction

Chronic venous insufficiency (CVI), chronic venous disease (CVD), or chronic deep venous insufficiency (DVI) are often synonymously used terms, which describe principally a vascular disorder in which venous return is compromised. CVI is a persistent, progressive and often underestimated condition that is prevalent in the general population and has a huge socio-economic, physical and psychological impact.

The clinical presentation is accompanied by severe manifestations of edema, skin changes or leg ulcers. Prevalence data of CVI vary widely from around 1–40% in women and around 1–17% in men [1]. There are two pathogeneses universally accepted, primary valvular incompetence and primary congenital vein wall weakness [2]. Furthermore, there are numerous genetic candidate loci, but still rudimentarily understood [3].

Therapeutic methods for CVI demonstrate a wide variety. The standard initial treatment is compressing therapy, supported by medication [2]. Besides, there are several surgical treatment concepts, such as interventional therapies, occlusion, or venoplasty [2, 4]. For example, the "BlueLeaf" system is a minimally invasive technique to form fully autogenous deep endovenous valves using an expandable dissection tool [5]. The recurrence of varicose veins after surgery is a frequent phenomenon, which may be caused by the so called "hemodynamic paradox" [6, 7].

Venous valve prostheses are supposed to address the shortcomings of reconstruction surgery. In general, valve prostheses consist of a support structure, which in most cases is a stent, and the actual valve, which is designed as a single or multi leaflet. The stent is usually made of nitinol and the leaflet material can consist of natural or polymeric fiber mats. New generation of biostable medical polyurethane elastomers with favorable bio- and hemocompatibility is thermoplastic silicone polycarbonate urethanes (TSPCU), which can be additionally modified [8–12]. For example, polyhedral oligomeric silsesquioxanes–polycarbonate urethane (POSS–PCU) nanocomposites showed good biocompatibility, mechanical durability, tear resistance, and better thrombosis resistance than other common polymeric valve materials such as polytetrafluoroethylene (PTFE) [13–15]. In contrast, bioresorbable, co-growing and minimally invasive venous valve concepts with degradable polymers such as polycaprolactone (PCL), polydioxanone (PDS), polylactide (PLA) and polyglycolide (PGA) are also gaining ground [10, 16]. However, the associated research effort is considerably more complex, particularly with regard to inflammation, tissue regeneration processes and degradation rates. In general, published studies regarding artificial valve materials and designs are difficult to compare due to their individuality in terms of limits or technical parameters. Various models are being developed from concept studies [17], over animal studies (e.g. "SailValve", "BVV1"–"BVV3") [18–20], to clinical testing (e.g., "VenoValve", "enVVe", and "Innovein") [21–26]. In addition, there are currently limited data to support vein reconstruction and no consensus on the characteristics of an ideal prosthesis [27–30] and no international "gold standard" in terms of operating conditions and performance requirements for venous valve prostheses. Ideally, the implant should allow free blood flow towards the heart, but prevent flow in retrograde direction. However, this point of view is still controversial, as a leakage in the valve can promote the long-term patency of the design by preventing thrombosis [19, 20].

In the development of new venous valve prostheses, generally recognized requirements, especially physiological conditions and several design aspects have to be considered to ensure safe operation. Cardiac output at rest is about 5 L/min and may reach 20 L/min at strong exercise [31, 32]. Unilateral lower limb venous blood flow is in a range of 420–450 mL/min in relaxed condition [33, 34], 400–800 mL/min at normal walking [35], 1600 mL/min at standing ankle flexion [36], and 2000 or 2450 mL/min at exercise of 40 W [37, 38] or 65 W [34], respectively. The blood flow in the legs does not differ between age groups when cycling at low intensity (20–40 W), but is significantly attenuated in older compared to younger subjects when the exercise intensity increases [39]. The anaerobic threshold describes the highest possible continuous intensity of exertion and is specified as 30–40 W for untrained older people [40].

The venous pressure at relaxed upright position depends mostly on gravitational pressure, and may reach 100 mmHg [27]. Activation of the calf muscle pump by walking removes the blood within some steps, ideally without reflux. The constantly incoming fresh blood does not fill the complete vein within one step, this creates a balance with low average pressure of 22–24 mmHg between the blood pumped out and the blood flowing in [41]. The normal operating pressure of a valve in the thigh is estimated with approximately 50 mmHg, in case no competent valve exists proximal. During coughing, sneezing, jumping or similar actions, short-term pressure surges up to 300 mmHg are transmitted from the abdomen to the legs, but in the same way to the arterial and venous system [42–45].

The vein size differs individually in a wide range as reported by various authors. Diameters of the common femoral vein are indicated with varying values of 11–12 mm [46], 6–21 mm [47], 10 mm [36], or for the proximal femoral vein of 4–16 mm [47], 8–16 mm [48], and for the distal femoral vein of 3–13 mm [47], or 3–10 mm [48]. However, vein diameters change not only due to exertion, but also with age and throughout the day. The femoral veins dilate by a few millimeters from morning to the afternoon, as indicated by 1.3–3.3 mm [49]. Suggested implant sites are 5–10 cm proximal to the saphenofemoral junction or in V. saphena parva [48]. The mid-thigh region of the femoral vein is likewise suitable [23].

From the physiological considerations further venous valve design requirements are derived. A minimal invasive surgery type is preferred and the valve design needs to ensure a blood flow similar to the native valves [29]. The orifice area should be larger than 30% of the vessel cross-sectional area [13, 50]. Leakage and reflux are controversially discussed, the valve can be considered functional when the leakage is less than 10% of the forward blood volume [51], or less than 3 mL/min [27]. Since native vein valves typically open with a pressure gradient of less than 5 mmHg, the opening pressure of prosthetic valves should be similar [27, 35, 51]. Tilting of the valve should be prevented from a fluidic perspective to keep patency and avoid thrombosis as main complication [29, 52].

Oversizing is a suitable method for secure fitting the implant in the vein, size mismatch of protheses and vein should be less than 15% [53], which means stent oversizing in the range of 1–2 mm. A rarely specified but crucial factor is which condition was used as the basis to calculate oversizing for determining the implant diameter to take account of the varying vein diameters under different load situations. Further anti-displacement techniques such as barbs are a common and effective solution to prevent valve migration, in sheep model barb penetration through the vein wall was seen in 56% of cases [54].

Recently, our group has reported on a novel prosthetic venous valve concept [55]. Main objective of the current study is to further improve this concept regarding the prevention of tilting and downstream migration, as well as maximization of effective orifice area (EOA). As part of this approach, two valve design embodiments were systematically assessed in vitro in an effort to establish more robust design and testing requirements for prosthetic venous valves. For the oversizing values, the inner diameters of the test attachments were applied as base value and set in relation to the uncompressed stent diameters. Systematic experimental testing is conducted to identify design strengths and weaknesses. The evaluation and comparison of valve performance is used to demonstrate the impact of design changes, to identify key elements for future implant developments.

Results

Artificial bicuspid venous valves

In both designs, the electrospun nanofiber nonwovens were assembled in the stents as an inwardly folded, double-layered sandwich. Both sandwich layers, inside and outside of the stent structure, are thermally spot welded in the center of the rhomboid stent cells allowing clearance and load distribution, thus enabling structural flexibility during the entire load history and avoiding critical load peaks. In the welding points fibers were melted together and no longer recognizable as individual fibers. Some details of manufacturing and bonding method are presented in Fig. 1. Morphologically, the TSPCU leaflets consisting of nanofiber nonwovens showed a smooth surface and slightly sticked together. The fiber diameters of the nanofibrous leaflets were 870 ± 140 nm of valve A14, 720 ± 140 nm for valve B12, and 770 ± 110 nm for valve B13. The leaflet thicknesses were 100 ± 15 µm for valve A14, 90 ± 10 µm for valve B12, and 146 ± 15 µm for valve B13.

Performance in static operation

The valve performance was tested for both directions, open (forward flow) and closed valves (reflux). Water pressure equivalent to 1, 3, and 5 mmHg for forward flow, as

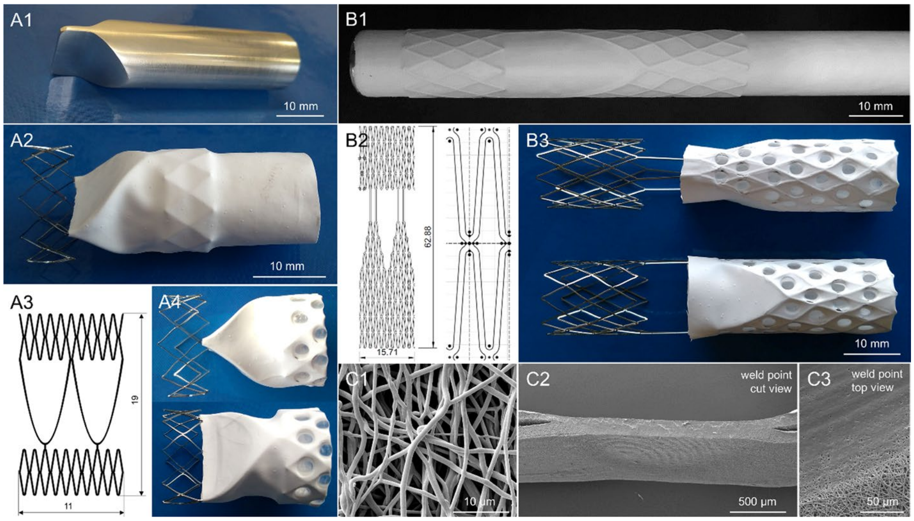

Fig. 1 Valve versions. **A1**: aluminium mold for electrospinning of version A nonwovens, **A2**: version A, stent enclosed with electrospun cover and protruding part for fixation, **A3**: sketch of version A stent, **A4**: assembled valve of version A in front and side view, **B1**: electrospun layer on version B stent mounted on metal cylinder, **B2**: sketch of version B stent as whole and a basic element, **B3**: assembled valve of version B in front and side view, **C1**: SEM image of nanofiber material, **C2**: SEM image of a cut weld point in side view, **C3**: SEM image of a weld point in top view

well as 20 up to 140 mmHg for reflux was achieved by adjusting water levels of distinct height (see Fig. 6). Maximum possible flow values were measured using attachments without valves. Valve A14–17 allowed about 1/3 of these maximum flow to pass through, with valves of version B approximately 2/3 of maximal flow values were observed, see Fig. 2A, C. The results of reflux are displayed in Fig. 2B.

Valve A14–17 revealed a reflux less than 310 mL/min for the physiological pressure range of 30–50 mmHg. Considerably increased reflux was observed at a pressure of more than 80 mmHg with a maximum of 2420 mL/min at 140 mmHg. After the experiment, the valve was found to be deformed and tilted, see Figure S16. The valves of version B12–9 and B12–20 revealed a reflux of less than 225 mL/min and 180 mL/min for the physiological pressure range, respectively. Considerably increased reflux was observed at a pressure of more than 80 mmHg (B12–9) and 100 mmHg (B12–20). A maximum reflux of 1510 mL/min (B12–9) and 890 mL/min (B12–20) resulted. The valve B13 revealed a reflux flow less than 905 mL/min (B13–8) and 290 mL/min (B13–18) for the physiological pressure range, respectively. Reflux was considerably increased at a pressure of more than 80 mmHg (B13–18). In contrast, for B13–8 a pressure proportional increase of reflux was observed with a maximum of 2635 mL/min.

Performance in pulsatile operation

To illustrate the valve performance at a representative working condition, a typical operating pressure of 50 mmHg imitating moderate physical exertion is compared here for both valve versions. The complete data series mimicking different exertions are provided in supporting information 4. Experimental results of pulse duplicator testing of valve A14–17 at 60 bpm revealed valve opening at 0.21 s, forward flow until 0.66 s, maximal flow at 0.4 s of about 3.5 L/min, and valve closing at 0.7 s with some post-pulse oscillation, see Fig. 3. A total reflux of 1.75 mL per cycle was measured. The calculated effective orifice area (EOA) was 0.27 cm^2, i.e. 24% of attachment cross-sectional area.

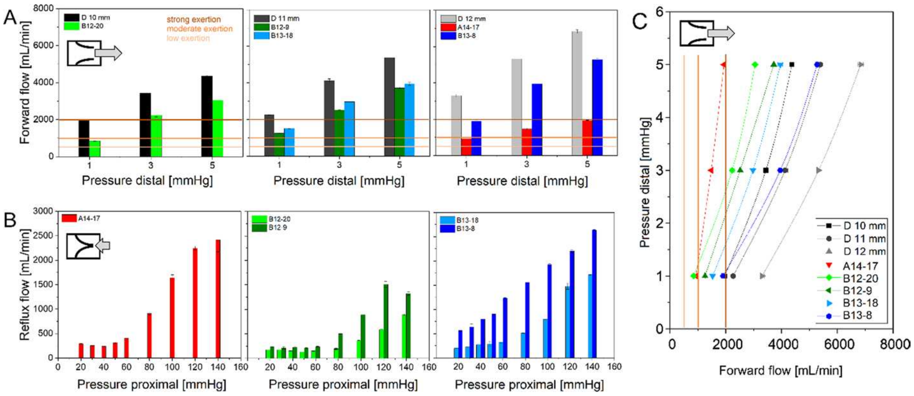

Fig. 2 Static test results. **A** Open valves (under distal pressure) with inner attachment diameter of D 10 mm (left), D 11 mm (mid), and D 12 mm (right), black/gray color: attachments without valve, red: valve version A14, green: version B12, blue: version B13, **B** closed valves (under proximal pressure), version A14 (left, red), version B12 (mid, green), version B13 (right, blue), **C** comparison of pressure-flow characteristics (under distal pressure) of valves and attachments, *n* = 3 measurements each. **A**, **C** Indicator lines for low (light orange), moderate (orange) and strong exertion (dark orange)

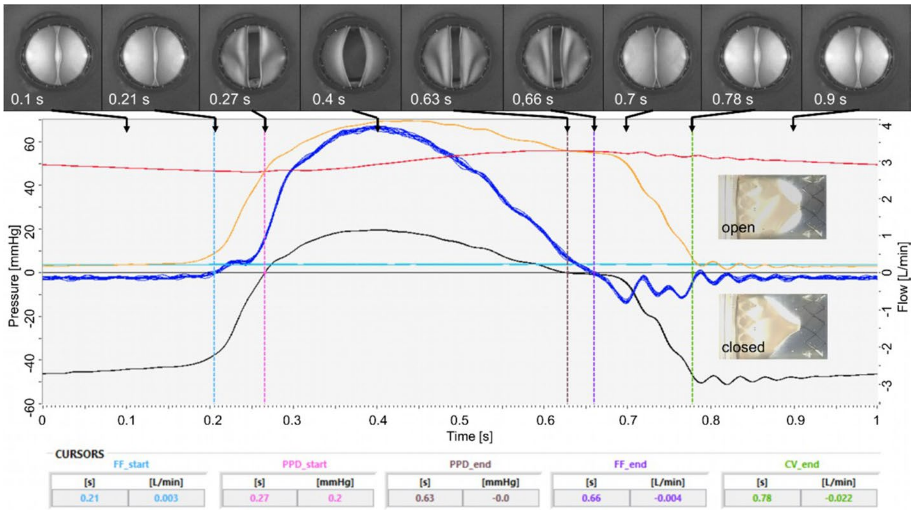

Fig. 3 Pulsatile experiment, valve version A14–17, 60 bpm, 1 L/min, 50 mmHg. Curves ($n = 10$): red—pressure proximal to the valve, yellow—pressure distal to the valve, black—difference pressure, dark blue—flow, light blue—pre-pressure at water reservoir, cursors: FF—forward flow, PPD—positive pressure difference, CV—closing volume, Images: from proximal inline camera at points in time as specified, and photographs from outside of open and closed state

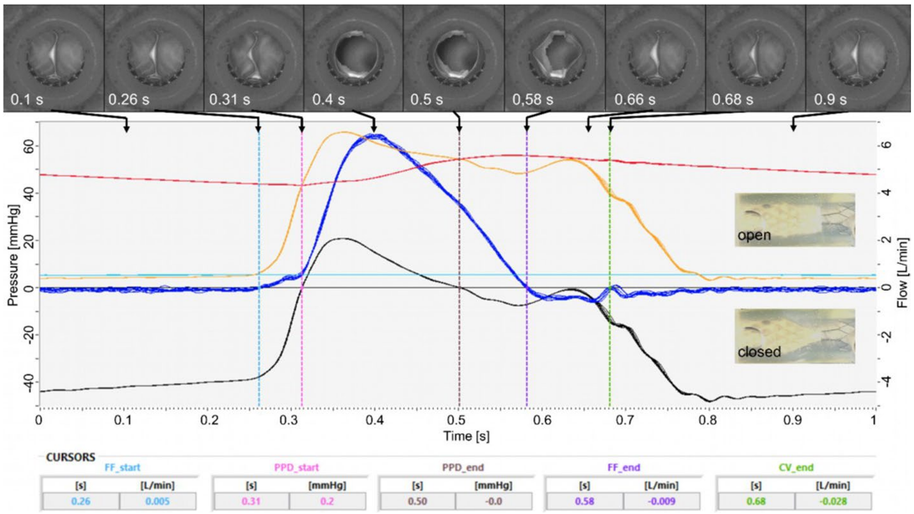

Fig. 4 Pulsatile experiment, valve version B12–9, 60 bpm, 1 L/min, 50 mmHg. Curves ($n = 10$): red—pressure proximal to the valve, yellow—pressure distal to the valve, black—difference pressure, dark blue—flow, light blue—pre-pressure at water reservoir, cursors: FF—forward flow, PPD—positive pressure difference, CV—closing volume. Images: from proximal inline camera at points in time as specified, and photographs from outside of open and closed state

Pulsatile testing of valve B12–9 at 60 bpm revealed valve opening at 0.31 s, forward flow until 0.58 s, maximal flow at 0.4 s of almost 6.5 L/min, and valve closing at 0.66 s, see Fig. 4. A total reflux of 1.68 mL per cycle was measured. The calculated EOA was 0.49 cm^2, i.e. 51% of attachment cross-sectional area.

Characteristic flow parameters and three simulated physiological conditions at operating pressure of 50 mmHg are summarized in Fig. 5. Similar PPD values were consistently

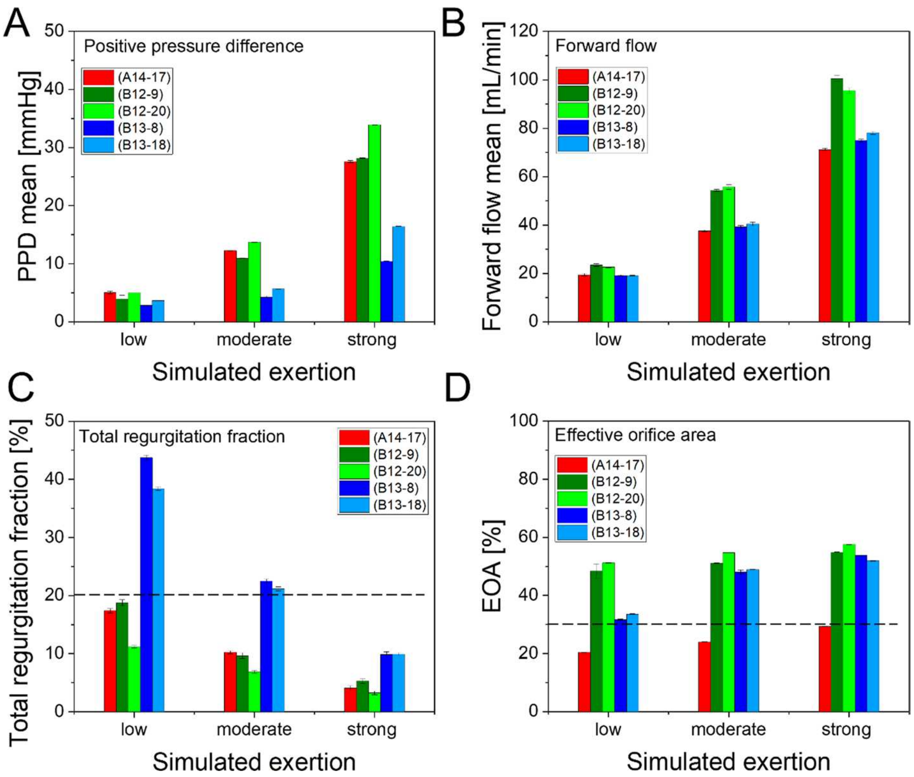

Fig. 5 Representative pulsatile performance data at operating pressure of 50 mmHg. Simulated exertion as indicated: low (0.5 L/min at 40 bpm), moderate (1 L/min at 60 bpm), strong (2 L/min at 80 bpm), tests: $n = 10$, each. **A** positive pressure difference (PPD), **B** forward flow, **C** normalized total regurgitation fraction, dashed reference line at 20% indicating acceptable reflux [56], **D**: effective orifice area (EOA) normalized to circular cross section, dashed reference line at 30% as recommended minimum value [13]

observed for versions A14 and B12 across all simulated exertions. The leaflets opened and closed simultaneously on both sides evenly and symmetrically for both versions (see supporting information 5, especially Figure S17 and Figure S18). In contrast, version B13 required approximately half pressure at simulated moderate and strong exertion. The mean forward flow of version B12 was noticeable higher than versions A14 and B13, which revealed similar values. The total regurgitation fraction decreased with increased simulated exertion, for all tested valves. A significant higher regurgitation fraction was observed for valve B13. Version A revealed an increasing EOA of about 20–30% of circular cross section with rising simulated exertion. The EOA of version B12 also slightly increased with twice as large values (compared to version A14) of 50% to almost 60%. In difference, the EOA of version B13 increased from 30% to about 50% with rising simulated exertion.

Discussion

Physiological load of standing upright is simulated by static testing

Assuming that the EOA at static flow conditions is comparable to pulsatile operation, the difference in forward flow ratios of empty and valve loaded attachments, between the valve versions can be explained. For proximal pressure up to 60 mmHg all valves (except

B13–8) revealed nearly constant reflux, over 80 mmHg the reflux considerably increased with pressure, which indicates functionality with some safety reserve. The proportionally to pressure increasing reflux of version B13–8 can be seen as hint for insufficient oversizing and leakage, despite proper valve function in pulsatile operation. Consequently, 8% oversizing revealed as insufficient sealing in this experimental setup. Hence, version B revealed functional with safety reserves in the physiological pressure range and beyond, if sufficiently oversized. A larger stent diameter allows slightly increased flow at a given vessel diameter (versions B), but the EOA has a significantly greater influence on the flow (version A vs. B).

Version A revealed limited performance due to significant higher flow resistance as a fluid dynamic deficit, which may be a potential risk factor for thrombosis. However, the static condition is more theoretical than practical, muscle activity is always necessary for upright standing. Small amounts of blood of different volumes are continuously pushed towards the heart by the muscle pump, which in reality means semi-pulsatile valve operation.

Physiological load of walking is simulated by pulsatile testing

All valves are functional in acute testing conditions showing an almost constant operating behavior over the tested pressure and flow ranges, see Figures S1–S15, there is no concerning drifting out of line. The mean PPD of version B13 at simulated moderate and strong exertion was almost half the values of versions A14 and B12 (with similar forward volume per cycle), this indicates significantly less flow resistance or longer time duration. For versions A14 and B13 similar mean forward flow was observed, but with half pressure for B13, i.e. version B13 is of less flow resistance. Due to similar PPD values (A14 and B12) the higher forward flow indicated less flow resistance of version B12. The flow resistance of A14–17 is more than double the value of B12–9, which can be explained by different EOA. If the standard for heart valves is considered as a guideline, reflux in the range of 10–20% are described as acceptable (Table S2) [56]. The tested constellations except B13–8 fulfil this requirement. For natural saphenous veins a closing pressure of 2–5 mmHg at flow of 12–32 mL/min is reported [57]. Both versions appear applicable under physiological conditions. However, without any flow or pressure, the valves of both versions are slightly open and allow slow blood flow without considerable resistance, e.g. horizontally lying person.

Risk of valve displacement

Valve migration was not observed in the experiments presented here. As the inner surface and the compliance of a real vein differ from 3D printed material, no valid statement can be drawn. Due to pressure difference within the valve, a force is generated in the axial direction, which the implant has to resist to avoid displacement. Nevertheless, rough estimation of axial force can be calculated with circular cross section area and proximal pressure for the closed valve. In forward direction, with increasing valve opening the axial forward force decreases, a suction effect due to the wake turbulence may also pull on the valve. Additionally, due to irregular leg movements, mass inertia of blood, and hydrodynamic conditions maximal axial short-term forces of about some Newton are realistic. Radial force distribution of oversized stents is not uniform due to anatomical environment or possibly uneven calcification [58]. However, recommendations for avoiding valve displacement require complex considerations including axial force, radial force, surface properties, and the anatomical–biological environment.

In contrast to the arterial system, vein diameter is not constant in different load situations and due to postural changes of the body, causing permanent changes in hydrostatic pressure and systemic conditions. Therefore, comparably high oversizing and a high compliance is essential for venous stent-based implants, to accommodate to the vessel diameter changes and achieve secure fixation. To avoid migration of the stent in the vein, oversizing of 1–4 mm (10–20%) is recommended [19, 59]. In general, veins show lower maximum stresses and Young's moduli, but higher maximum strains compared to arteries, indicating that the thin venous wall can tolerate more extensive dilatation without rupture [60–62]. Nevertheless, permanent high overexpansion of the venous wall should be prevented, as it could affect neointimal growth [63]. High radial force can cause inflammatory response and fibrosis [59].

Implant migration or tilting can also be prevented by surgical suture or additional elastic stent elements. One further option is the utilization of barbs, which are for example used for inferior vena cava (IVC) filters [64], these are not further discussed here.

Compliance with general recommendations

Considering the general recommendations derived from literature, following respects can be stated. Both versions are designed to being crimped for minimal invasive implantation. Secure fixation should be ensured, but permanent overexpansion of the vein wall should be prevented. The bicuspid design mimics blood flow similar to natural valves, version A causes higher flow velocity and thus washout of region behind leaflets, version B allows a high orifice area with less dead space. The orifice of an open venous valve is always elliptical, never circular [57], hence, natural flow conditions are achieved when the valve is not fully open. These are theoretical considerations, monocuspid valves are also under development, which imitate natural blood flow less conforming. Tilting and deformation occurred with the valve of version A below 80 mmHg in both scenarios (static and pulsatile), which could be prevented by the double strut of version B, no displacement was observed here. Manufacturing leaflets from material of the group of polycarbonate urethane is promising to us in regard of biocompatibility and thrombosis triggering, but in vivo tests were not performed in this study. Reflux was observed in the range of 1–4 mL/min in physiological pressure range at pulsatile testing, which is less than 10% of forward flow in most cases and fits mainly the recommended range. Valves of both versions open at a pressure gradient below 5 mmHg relating to natural conditions. The ratio of implant length to diameter is controversial, a short implant is less burden for the vein wall and easier to handle, but is of increased tendency for tilting. A long implant shows less tendency for migration, but has to withstand bending [60]. That ratio is for version A 1.6, and for version B 4.6. Version can be designed differently by adapting the number of cell (rhomboid) rings and changing the length of double struts (keeping the mid part) without impairing its performance. The EOA of version A14–17 revealed less than the recommended area of 30% of vessel cross-sectional area [50], valves of version B fulfil this requirement. The long-term performance of the valves was not yet investigated, the focus was on functional testing prior enduring studies. The long-term requirements are estimated as followed: when a hypothetic patient slowly walks 1 h a day with a cadence of 40 steps per minute, the valve performs 2400 cycles per day or 0.9 million steps per year, Sathe et al. recommend durability for at least 500.000 cycles [35].

Depending on the stage of CVI disease, the vascular situation can be diverse in terms of venous dilation and deformation. An advanced therapy concept may comprise several implantation sites for valve prostheses. A possible therapy approach that takes into account superficial and deep implantation sites, in consideration of the hemodynamic paradox [7] as an example, could work with differently designed valves that are tailored to the respective conditions. For this advanced therapy, valve prosthesis of version A (shorter, more flexible) seem to be more suitable for peripheral system, and valves of version B (longer, more sturdy) are well suited for central veins. Summing up, the intended positive effects of version B have been confirmed in the experimental findings.

Further aspects for the application of venous valve prostheses

The utilization of non-magnetic or non-metallic material is advantageous in order not to limit the spectrum of available diagnostic examinations or therapy options for a patient, e.g. MRI ("MR-safe" or "MR-conditional"), and radiothermy. Further, a concept for diagnosing the current state of the implant itself is also recommended, regarding to wear, aging, structural failure. This can be achieved e.g. through accessibility for ultrasound, radiopaque elements, sensing wires, or microelectronic components. Sonography is limited in metallic stents, but in the here presented design the leaflets are accessible. A prospective special biologized valve that prevents both neointima and intimal hyperplasia and improves the functionality of the valves could be achieved with tissue engineering, e.g. seeding with endothelial cells [18].

In addition, durability and crimpability for minimal invasive implantation of the whole implant will be investigated in forthcoming work. Further, studies on different stent materials (stainless steel, cobalt chrome alloys, or nonmetallic or polymeric material) are intended.

Venous valve design recommendations

Considering the testing results, also concerning to generally accepted commendations of other authors, we derive design recommendations for prosthetic venous valves as listed below, see Table 1.

Limitations

From valve version A only one size was available, due to the aforementioned deficiencies and the consequently design of version B, no further sizes of version A were manufactured. The influence of leaflet thickness cannot be clearly distinguished from other design effects, in consideration the other findings a subordinate role is presumable. In static and pulsatile conditions, the whole flow was measured, discriminating perivalvular leak fraction from the flow fraction through the valves was not possible. Based on the inline camera video recordings at high pressure levels, no gaps or incomplete radial stent apposition were apparent, so that only minor influence of perivalvular leakage was assumed. The long-term performance of the valves has yet to be investigated, as

Table 1 Recommendations for new version of bicuspid venous valve design and testing conditions

	Parameter/aspect	Recommendation	Explanation based on our test results
Advances in similar valve designs	Stent oversizing 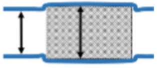	10–20% of vessel diameter	Vessel dilation should be considered 8% revealed as too small, 9% is the limit in tests without vessel deformation More than 20% may injure the vein wall [19, 59]
	Stent fixation	Additional elastic stent retaining structures	Prevention of dislocation E.g. hooked barbs may penetrate venous wall
	Stent structure 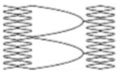	2–3 cell rings (e.g. rhomboid) at the top and bottom	Acceptable implant length Sufficient stability Single rings showed tendency to rocking motion
	Cell ring connector	Double struts between leaflet and upper cell ring	Increase stability Prevention of deformation and tilting
	Stent length/diameter 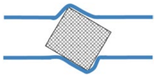	Ratio (L/D) more than 2	Prevention of tilting Shorter ring connection reduces implant length
	Stent sidewall 	Filled with cells (e.g. rhomboids)	Prevention of inward bulging of wall material Version A vs. version B, see also Fig. 1
	Effective orifice area (EOA) 	Large (maximum)	Less flow resistance Larger than 30% of the vessel cross-sectional area [13, 50]
	Leaflet fixation	Fixation of leaflet in cells (rhomboids) of sidewall	Prevention of leaflet sliding down Improved sealing to vessel wall
	Leaflet material	Flexible, biocompatible, antithrombotic, long-term stable, non-biological origin	Artificial (synthetic) material has no variations in quality, texture, durability, etc. compared to natural material Less complexity in testing (in vitro, in vivo)
Specific test parameters	Pressure range	Runing up to at least twice the physiologically expected pressure values	Discovering hidden weaknesses Safety reserve
	Opening/closing pressure	Opening and closing at low pressure difference (below 5 mmHg)	Performance close to natural valves
	Flow range for vessels (Ø > 10 mm)	Capability to operate at flow of 2 L/min	No failure under high operational load
	Frequency	60 bpm (minimum)	Simulation of realistic exertion scenario
	Reflux 	< 20% of forward flow (pulsatile operation)	Sufficient functionality

the focus of the present study was on functional testing prior to enduring studies. The crimpability of version B has not yet been investigated to determine whether the leaflet structure has been damaged, but this will be done in future work. The inner surface of a natural vein differs from attachments made of 3D-printed material, and the compliance of the vein wall depends on the tension of smooth muscles. Therefore, statements about oversizing are of limited validity.

Conclusion

In this study, a modified venous valve concept was comparatively compared to the original design by performance testing under static and pulsatile flow conditions. The valve leaflets were fabricated of electrospun TSPCU nanofiber nonwoven, due to favorable biocompatibility and simple processability. It could be shown that the ES parameters can be adapted to both setups of versions A and B, without any particular advantage of one concept over the other. However, version B is far easier to produce, eliminating the elaborate process step of nonwoven transfer from an ES mold, while also improving leaflet thickness homogeneity and maximizing EOA. Regarding stent design, version B improved stent anchoring and leaflet fixation. In terms of material selection, the approach of using low Shore hardness TSPCU material could be substantiated.

Both valve versions performed under different simulated physiological conditions, whereas version A revealed a tendency to reach its limits in the situation of higher operational loads earlier. It can be summarized that the design modifications in version B demonstrated the intended positive effects on valve performance, but the modified stent design is initially a test platform rather than a final implant, it points the way to more suitable venous valve implants. The evaluation demonstrate the impact of design changes identifying key elements for future implant developments. Specific design and testing recommendations were drawn.

Future work will focus on long-term functionality, which will be investigated by endurance testing and comprehensive biocompatibility testing of various leaflet materials in vitro and in vivo is intended.

Materials and methods

Bicuspid prosthetic venous valves designs

The initially developed design is in the following named “version A” [55], the modified design is named “version B”. In light of the aforementioned requirements, two bicuspid valve concepts with valve leaflets made of thermoplastic silicone polycarbonate urethane (TSPCU) nanofiber nonwoven material were investigated. The valve leaflets are attached to nitinol stents consisting of two cell rings (rhomboid) and a leaflet support in between the cell rings, see Fig. 1. Version A consists of two cell rings with ten rhomboid-shaped elements, which are connected by two arched struts in between. The leaflet structure is attached to the lower ring, and the commissure of the leaflet matches the support structure, so the valve remains in its shape. The results of preparatory experimental studies on version A have encouraged the development of version B, which modifications are following:

- The rhomboid rings consist of three rows each instead of one, to avoid rocking motion.
- The side walls are filled with rhomboids for three reasons: (1) fixing the leaflets to prevent migration from stent attachments, (2) prevent inward bulging, (3) improved sealing to the vessel wall.
- Double struts were added between leaflet and upper rhomboid ring to improve stability and prevent tilting. In neutral position, the valve leaflets are to be slightly open.
- Application of leaflets with a cylindrical shape and a diameter according to the stent diameter for three reasons: (1) fully open cross-sectional area with lowest possible flow resistance, (2) no mold for electrospinning is needed, (3) possibility of using simple tube-shaped wrought material valves, which are not directly electrospun on the stent.

Fabrication of testing specimens

Stent samples

Stent A was designed using the CAD software Creo Parametric 6.0.3.0 (Parametric Technology Corp., Needham, MA, USA). Stent B was designed in Fusion 360 2.0.17721 (Autodesk GmbH, München, Germany). The stents were manufactured from a nitinol tube with a diameter of 5 mm and a wall thickness of 0.24 mm (Euroflex GmbH, Pforzheim, Germany). The stents were laser cut using a StarCut Tube system (Coherent Corp., Saxonburg, PA, USA) with a pulsed laser source Monaco 1035-80-60, frequency 500 kHz, pulse duration 300 fs, pulse energy 10 µJ, argon atmosphere with supply pressure 15 bar, and cutting velocity of 1.5 mm/s. Stent A was expanded in two steps with increasing diameter to 14 mm in a convection oven KLS 05/13 (Thermconcept GmbH, Bremen, Germany) with an annealing temperature of 512 °C for 15 min at each step. The stents of version B were expanded in three steps to final diameters of 12 and 13 mm, respectively, with 8 min annealing time per step. A polishing step followed afterwards.

Valve leaflet samples

A homogenous polymer solution of 7.5wt% TSPCU (Shore 80A) was obtained by dissolving in chloroform ($CHCl_3$), *N,N*-dimethylformamide (DMF) and 2,2,2-trifluoroethanol (TFE), (ratio of 3/1/1). All polymers, chemicals and solvents were used as received. In brief, electrospinning was performed using an experimental spinning setup equipped with a single jet capillary emitter (G21 cannula) and a rotating mold or cylinder, see Fig. 1. Following parameters were set: working distance of 160 mm, rotation of 4000 rpm, flow of 1 mL/min, linear traversing motion, room temperature. A high voltage of 6 kV (collector) and 22 kV (emitter) was applied and processing time was fixed at 7200 s. A layer thickness of 100 µm was targeted for both versions. For valve version A, CNC machined aluminum molds (Haas Automation, Inc–CNC Machine Tools, Oxnard, CA, USA) were coated with electrospun TSPCU nonwoven as described in [65]. The stents of version B were directly coated on the metal cylinder.

Assembly of valves

The electrospun nonwoven was removed from the mold and transferred to stent A, or removed from the cylinder with stent B. For fixing valves of both versions on the stents, the protruding part of the nonwoven was turned inwards and spot-welded in all rhomboids using an in-house developed device [66], see Fig. 1.

The nonwoven thickness ($n = 10$, each) was measured using a dial gauge Mitutoyo 543–394B with associated stand (Mitutoyo Corporation, Kawasaki, Japan).

The fiber morphology of leaflet and welded points were investigated using a scanning electron microscope (SEM) QUANTA FEG 250 device (FEI Company, Dreieich, Germany) operating in high vacuum and 10 kV voltage, using an Everhart–Thornley detector (ETD) in secondary electron mode. The nonwoven samples were fixed on aluminum carriers using conductive carbon pads. Gold sputter coating was achieved using an AGAR Sputtercoater (Agar Scientific Ltd, Stansted, Essex, UK). The fiber diameters were measured for quality control applying the GIFT-method [67, 68].

Testing fixtures

Attachments, which are simplified representations of vessels for experimental tests, were designed in three sizes with inner diameters (D10 mm, D11 mm, and D12 mm) using CAD software Fusion 360. Digital light processing (DLP) technology was used to create annular attachments of photopolymeric resin Ultracur3D FL 300 (BASF 3D Printing Solutions GmbH, Heidelberg, Germany) on an Asiga Pro 4K45 printer (Asiga, Alexandria, Australia), for details see supporting information 1.

Experimental test setup for performance testing

For preconditioning and removing of potentially existing solvent residues the assembled valves were stored in ultrafiltrated water at room temperature for at least 2 days before testing. Under immersed conditions, little material shrinking was observed. Before testing, the valves were crimped by hand at 0 °C in ice water, then implanted in the attachments. The test configurations are introduced in Table 2.

The valves were oversized by 1 or 2 mm in relation to the attachment diameter, as recommended in [19]. Regarding the experimental design, valve of version A (A14–17), available from previous work with a diameter of 14 mm has only been tested in a 12 mm attachment with 2 mm oversize. Preparatory studies revealed insufficient performance of valve A with 1 mm oversizing; hence, it was not pursued further for this work. In

Table 2 Test configurations, abbreviations for tested experimental arrangements specify the valve version, stent size, and the oversize in millimeters (O.S) resulting from the attachment, and oversizing percentage in brackets

Valve version	Stent diameter	Sample abbreviation in attachment (Ø$_{tube}$) and oversizing (O.S)					
		Ø10 mm	**O.S**	**Ø11 mm**	**O.S**	**Ø12 mm**	**O.S**
A	Ø14 mm	X		X		**A14–17**	2 (17%)
B	Ø12 mm	**B12–20**	2 (20%)	**B12–9**	1 (9%)	X	
B	Ø13 mm	X		**B13–18**	2 (18%)	**B13–8**	1 (8%)

contrast, two version B stents (B12, B13) were tested in attachments with two different diameters each.

For performance testing of the different valves, static testing and pulsatile testing was done. An operating pressure of 50 mmHg was estimated for a valve in the thigh. In general, the tests were run up to more than double operating pressure (worst case) to be on the safe side and detect possible trends in performance.

Static testing

The valves were implanted in different attachments, and testing was performed in forward and backward direction using water. The forward flow was measured at 1 mmHg, 3 mmHg, and 5 mmHg by gravimetric measurement of water mass, which flowed through the test specimens, at room temperature for a time interval of 30 s using a scale Sartorius MSE4202-000-D0 (Sartorius AG, Göttingen, Germany). Additionally the flow through empty attachments without valves was investigated ($n = 3$, each). The reflux was measured at 20–60 mmHg in 10 mmHg steps, and 80–140 mmHg in 20 mmHg steps by gravimetric measurement of water mass ($n = 3$, each). The values for pressure-equalized water column were calculated using a density value for water and mercury of 998.21 kg/m^3 at 20 °C [69], and the density of mercury (13,545.89 kg/m^3) [70] respectively, see Fig. 6 and Table S1.

Pulsatile testing

To investigate the fluid dynamics of venous valves under pulsatile, physiological, and pathological pressure and volume flow conditions, a fluid dynamic circulation model was used, shown in Fig. 7 and Figure S16, for details see supporting information 3.

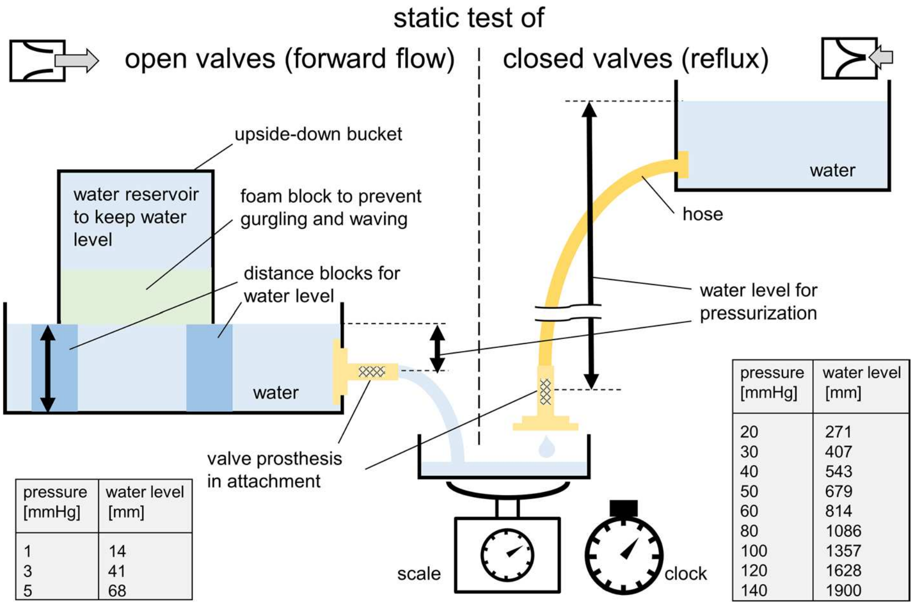

pressure [mmHg]	water level [mm]
1	14
3	41
5	68

pressure [mmHg]	water level [mm]
20	271
30	407
40	543
50	679
60	814
80	1086
100	1357
120	1628
140	1900

Fig. 6 Static testing. Gravimetric measurement of water mass per time interval was performed for open valves (conditions: constant water pressure was generated by distance blocks under a reservoir) and closed valves (conditions: different height levels and a flexible hose between valve and water container were utilized)

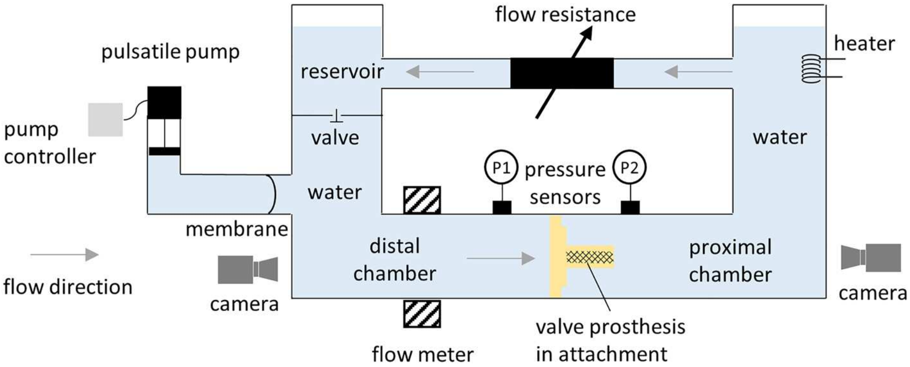

Fig. 7 Pulse duplicator system (schematic drawing)

The test series were performed with flow rates of 0.5 L/min at 40 bpm to imitate slow walking or low exertion, 1 L/min at 60 bpm for moderate exertion, and 2 L/min at 80 bpm for strong exertion. The test setup, initially designed for testing aortic and mitral valves (HDTi-6000, Biomedical Device Consultants and Laboratories, Wheat Ridge, USA), consists of two fluid compartments coupled via a flexible membrane: the pump circuit and the test circuit.

Testing was performed using 0.9% saline at 37 °C. The valves were tested with ballasting pressure in ranges of 20–60 mmHg (A14) and 20–140 mmHg (B12, B13), increased in 10 mmHg steps. For simulation of different exertion conditions, frequencies and flow parameters of 40 bpm with 0.5 L/min each, 60 bpm with 1 L/min each, and 80 bpm with 2 L/min each were adjusted. The pressures distal and proximal to the valve were measured, as well as the flow through the valve loaded testing attachment. To achieve specific flow at definite proximal pressure values, the mutually affecting parameters of displacement volume of the pulsatile pump, as well as flow resistance were controlled.

Supplementary Information

The online version contains supplementary material available at https://doi.org/10.1186/s12938-024-01316-x.

Supplementary Material 1

Acknowledgements
The authors thank Katja Hahn, Manfred Strotmeier, Babette Hummel, Falk Reinhardt, Dalibor Bajer, Eric Bohne, and Jens Großmann for their expert technical assistance and skillful work.

Author contributions

AG: Conceptualization, methodology, validation, formal analysis, investigation, writing—original draft, writing—review and editing, visualization. SI: Conceptualization, methodology, writing—original draft, writing—review and editing. NF: investigation, writing—review and editing. JS: Conceptualization, writing—review and editing. JO: Investigation, writing—review and editing. HM: Conceptualization, writing—review and editing. WS: Writing—review and editing. KS: Supervision, project administration, funding acquisition. NG: Supervision, project administration, funding acquisition, writing—review and editing. KL: Conceptualization, methodology, writing—original draft, writing—review and editing.

Funding
Open Access funding enabled and organized by Projekt DEAL. No funding.

Availability of data and materials

No datasets were generated or analysed during the current study.

Declarations

Ethics approval and consent to participate

Not applicable.

Consent for publication

Not applicable.

Competing interests

The authors declare no competing interests.

Generative AI

Generative AI and AI-assisted technologies were only used in the writing process to improve the language and readability. Generative AI and AI-assisted tools were not used in data evaluation, images and artwork.

Received: 12 July 2024 Accepted: 15 November 2024

References

1. Beebe-Dimmer JL, Pfeifer JR, Engle JS, Schottenfeld D. The epidemiology of chronic venous insufficiency and varicose veins. Ann Epidemiol. 2005;15:175–84. https://doi.org/10.1016/j.annepidem.2004.05.015.
2. Gujja K, Kayiti T, Sanina C, Wiley JM. Chronic venous insufficiency. In: Dangas GD, Di Mario C, Thiele H, Barlis P, editors. Interventional cardiology: principles and practice. 3rd ed. Newark: John Wiley & Sons Incorporated; 2022. p. 835–43. https://doi.org/10.1002/9781119697367.ch87.
3. Baylis RA, Smith NL, Klarin D, Fukaya E. Epidemiology and genetics of venous thromboembolism and chronic venous disease. Circ Res. 2021. https://doi.org/10.1161/CIRCRESAHA.121.318322.
4. Azar J, Rao A, Oropallo A. Chronic venous insufficiency: a comprehensive review of management. J Wound Care. 2022. https://doi.org/10.12968/jowc.2022.31.6.510.
5. Vasudevan T, Robinson DA, Hill AA, Ouriel K, Holden A, Gagnon J, et al. Safety and feasibility report on nonimplantable endovenous valve formation for the treatment of deep vein reflux. J Vasc Surg Venous Lymphat Disord. 2021;9:1200–8. https://doi.org/10.1016/j.jvsv.2020.12.073.
6. Recek C. The hemodynamic paradox as a phenomenon triggering recurrent reflux in varicose vein disease. Int J Angiol. 2012;21:181–6. https://doi.org/10.1055/s-0032-1325168.
7. Recek C. Calf pump activity influencing venous hemodynamics in the lower extremity. Int J Angiol. 2013;22:23–30. https://doi.org/10.1055/s-0033-1334092.
8. Liu Z, Liu B, Li C, Xiao Y, Wei H, Zhou J, Feng Z. Zwitterionic modification: a strategy to enhance the mechanical properties, lubricity and hemo- and biocompatibility of silicone poly(carbonate urethane urea). React Funct Polym. 2024;203: 106007. https://doi.org/10.1016/j.reactfunctpolym.2024.106007.
9. Wei S, Wu J, Gu X, Shen S, Ma M, Shi Y, et al. Low protein adsorption and high cellular activity of PEG-based silicone polyurethane for artificial heart valves. Mater Today Commun. 2024;39: 109357. https://doi.org/10.1016/j.mtcomm.2024.109357.
10. Wang Y, Fu Y, Wang Q, Kong D, Wang Z, Liu J. Recent advancements in polymeric heart valves: from basic research to clinical trials. Mater Today Bio. 2024;28: 101194. https://doi.org/10.1016/j.mtbio.2024.101194.
11. Dempsey DK, Carranza C, Chawla CP, Gray P, Eoh JH, Stacy Cereceres S, Cosgriff-Hernandez EM. Comparative analysis of in vitro oxidative degradation of poly(carbonate urethanes) for biostability screening. J Biomed Mater Res, Part A. 2014;102:3649–65. https://doi.org/10.1002/jbm.a.35037.
12. Bachtiar EO, Erol O, Millrod M, Tao R, Gracias DH, Romer LH, Kang SH. 3D printing and characterization of a soft and biostable elastomer with high flexibility and strength for biomedical applications. J Mech Behav Biomed Mater. 2020;104: 103649. https://doi.org/10.1016/j.jmbbm.2020.103649.
13. Zong Q, Liu J, Chen Y, Kong Y, Dang Y, Wang Z. Prosthetic venous valves for chronic venous insufficiency: advancements and future design directions. Med Novel Technol Devices. 2024;21: 100288. https://doi.org/10.1016/j.medntd.2024.100288.
14. Kidane AG, Burriesci G, Edirisinghe M, Ghanbari H, Bonhoeffer P, Seifalian AM. A novel nanocomposite polymer for development of synthetic heart valve leaflets. Acta Biomater. 2009;5:2409–17. https://doi.org/10.1016/j.actbio.2009.02.025.
15. Kannan RY, Salacinski HJ, de Groot J, Clatworthy I, Bozec L, Horton M, et al. The antithrombogenic potential of a polyhedral oligomeric silsesquioxane (POSS) nanocomposite. Biomacromol. 2006;7:215–23. https://doi.org/10.1021/bm050590z.
16. Rocco KA, Maxfield MW, Best CA, Dean EW, Breuer CK. In vivo applications of electrospun tissue-engineered vascular grafts: a review. Tissue Eng Part B Rev. 2014;20:628–40. https://doi.org/10.1089/ten.TEB.2014.0123.
17. Oberdier MT, Rittgers SE. The design, development, and evaluation of a prototypic, prosthetic venous valve. BioMed Eng OnLine. 2008;7:1–16. https://doi.org/10.1186/1475-925X-7-25.
18. Pavcnik D, Uchida B, Kaufman J, Hinds M, Keller FS, Rösch J. Percutaneous management of chronic deep venous reflux: review of experimental work and early clinical experience with bioprosthetic valve. Vasc Med. 2008;13:75–84. https://doi.org/10.1177/1358863X07083474.
19. Borst GJ, Moll FL. Percutaneous Venous Valve Designs for Treatment of Deep Venous Insufficiency. J Endovasc Ther. 2012;19:291–302. https://doi.org/10.1583/11-3766R.1.
20. Boersma D, Vink A, Moll FL, de Borst GJ. Proof-of-concept evaluation of the sailvalve self-expanding deep venous valve system in a porcine model. J Endovasc Ther. 2017;24:440–6. https://doi.org/10.1177/1526602817700120.

21. Cifuentes S, Ulloa JH, Rasmussen TE. An implantable bioprosthetic venous valve to establish deep vein competence for post-thrombotic syndrome. JAMA Surg. 2023;158:316–7. https://doi.org/10.1001/jamasurg.2022.6362.
22. Ulloa JH, Glickman M. One-year first-in-human success for venovalve in treating patients with severe deep venous insufficiency. Vasc Endovasc Surg. 2022;56:277–83. https://doi.org/10.1177/15385744211073730.
23. Ulloa JH, Glickman M. Human trial using the novel bioprosthetic VenoValve in patients with chronic venous insufficiency. J Vasc Surg Venous Lymphat Disord. 2021;9:938–44. https://doi.org/10.1016/j.jvsv.2020.10.017.
24. enVVeno Medical Corporation, Irvine, CA (US). Transcatheter valve system and method for venous insufficiency;US20230363900A1; 16.11.2023.
25. Innovein, Inc., San Carlos, CA (US). Venous valve prosthesis; US 2017/0056175 A1; 25.08.2016.
26. Innovein, Inc., San Carlos, CA (US). SBIR Phase II: Venous Valve Prosthesis as a Cure for Chronic Venous Insufficiency. 08.07.2024. https://www.sbir.gov/sbirsearch/detail/1644629.
27. D'Addario J, Smeds MR, Wittgen C. Surgical treatment of deep venous insufficiency and requirements for novel interventions. JVS-Vascular Insights. 2023;1: 100011. https://doi.org/10.1016/j.jvsvi.2023.100011.
28. Wilson NM, Rutt DL, Browse NL. Repair and replacement of deep vein valves in the treatment of venous insufficiency. Br J Surg. 1991;78:388–94. https://doi.org/10.1002/bjs.1800780404.
29. Zervides C, Mahdi H, Staub RA, Jouni H. Prosthetic venous valves: short history and advancements from 2012 to 2020. Phlebology. 2021. https://doi.org/10.1177/0268355520962451.
30. Zervides C, Giannoukas AD. Historical overview of venous valve prostheses for the treatment of deep venous valve insufficiency. J Endovasc Ther. 2012;19:281–90. https://doi.org/10.1583/11-3594MR.1.
31. Bombardini T. The venous contribution to cardiovascular performance: from systemic veins to left ventricular function: a review. Scr Med. 2021;52:299–308. https://doi.org/10.5937/scriptamed52-35083.
32. Brandes R, Lang F, Schmidt RF. Physiologie des Menschen. Berlin: Springer, Berlin Heidelberg; 2019.
33. Rudolphi PB, Recke A, Langan EA, Hunold P, Kahle BK. Are sonographically measured vascular haemodynamic parameters reproducible using magnetic resonance imaging? Eur J Vasc Endovasc Surg. 2016;52:665–72. https://doi.org/10.1016/j.ejvs.2016.08.004.
34. Jorfeldt L, Wahren J. Leg blood flow during exercise in man. Clin Sci. 1971;41:459–73. https://doi.org/10.1042/cs0410459.
35. Sathe RD, Ku DN. Flexible prosthetic vein valve. J Med Devices. 2007;1:105–12. https://doi.org/10.1115/1.2736393.
36. Rittgers SE, Oberdier MT, Pottala S. Physiologically-based testing system for the mechanical characterization of prosthetic vein valves. BioMed Eng OnLine. 2007;6:1–12. https://doi.org/10.1186/1475-925X-6-29.
37. Tschakovsky ME, Saunders NR, Webb KA, O'Donnell DE. Muscle blood-flow dynamics at exercise onset: do the limbs differ? Med Sci Sports Exerc. 2006;38:1811–8. https://doi.org/10.1249/01.mss.0000230341.86870.4f.
38. MacDonald MJ, Shoemaker JK, Tschakovsky ME, Hughson RL. Alveolar oxygen uptake and femoral artery blood flow dynamics in upright and supine leg exercise in humans. J Appl Physiol. 1998. https://doi.org/10.1152/jappl.1998.85.5.1622.
39. Koch DW, Newcomer SC, Proctor DN. Blood flow to exercising limbs varies with age, gender, and training status. Can J Appl Physiol. 2005. https://doi.org/10.1139/h05-141.
40. Posner JD, Gorman KM, Klein HS, Woldow A. Exercise capacity in the elderly. Am J Cardiol. 1986;57:C52–8. https://doi.org/10.1016/0002-9149(86)91027-1.
41. Pollack AA, Wood E. Venous pressure in the saphenous vein at the ankle in man during exercise and changes in posture. J Appl Physiol. 1949. https://doi.org/10.1152/jappl.1949.1.9.649.
42. Iqbal A, Haider M, Stadlhuber RJ, Karu A, Corkill S, Filipi CJ. A study of intragastric and intravesicular pressure changes during rest, coughing, weight lifting, retching, and vomiting. Surg Endosc. 2008;22:2571–5. https://doi.org/10.1007/s00464-008-0080-0.
43. Cobb WS, Burns JM, Kercher KW, Matthews BD, James Norton H, Todd HB. Normal intraabdominal pressure in healthy adults. J Surg Res. 2005;129:231–5. https://doi.org/10.1016/j.jss.2005.06.015.
44. Smith JA, Aliverti A, Quaranta M, McGuinness K, Kelsall A, Earis J, Calverley PM. Chest wall dynamics during voluntary and induced cough in healthy volunteers. J Physiol. 2012;590:563–74. https://doi.org/10.1113/jphysiol.2011.213157.
45. Schattner A. The wide-ranging spectrum of cough-induced complications and patient harm. Am J Med. 2020;133:544–51. https://doi.org/10.1016/j.amjmed.2019.12.044.
46. Fronek A, Criqui MH, Denenberg J, Langer RD. Common femoral vein dimensions and hemodynamics including Valsalva response as a function of sex, age, and ethnicity in a population study. J Vasc Surg. 2001;33:1050–6. https://doi.org/10.1067/mva.2001.113496.
47. Keiler J, Seidel R, Wree A. The femoral vein diameter and its correlation with sex, age and body mass index - an anatomical parameter with clinical relevance. Phlebology. 2019;34:58–69. https://doi.org/10.1177/0268355518772746.
48. Keiler J, Schulze M, Claassen H, Wree A. Human femoral vein diameter and topography of valves and tributaries: a post mortem analysis. Clin Anat. 2018;31:1065–76. https://doi.org/10.1002/ca.23224.
49. Salles-Cunha SX, Shuman S, Beebe HG. Planning endovascular vein valve implantation: significance of vein size variability. J Vasc Surg. 2003;37:984–90. https://doi.org/10.1067/mva.2003.245.
50. Sathe RD. Design and development of a novel implantable prosthetic vein valve [master thesis]. Georgia: School of Mechanical Engineering; May 2006.
51. Fernández-Colino A, Jockenhoevel S. Advances in engineering venous valves: the pursuit of a definite solution for chronic venous disease. Tissue Eng Part B Rev. 2021;27:253–65. https://doi.org/10.1089/ten.TEB.2020.0131.
52. Pavcnik D, Kaufman J, Uchida B, Correa L, Hiraki T, Kyu SC, et al. Second-generation percutaneous bioprosthetic valve: a short-term study in sheep. J Vasc Surg. 2004;40:1223–7. https://doi.org/10.1016/j.jvs.2004.08.027.
53. Tien W-H, Zhao X, Chen HY, Berwick ZC, Krieger JF, Chambers S, et al. Role of vessel-to-prosthesis size mismatch in venous valve performance. J Vasc Surg Venous Lymphat Disord. 2017;5:105-113.e1. https://doi.org/10.1016/j.jvsv.2016.08.004.
54. Pavcnik D, Uchida BT, Timmermans HA, Corless CL, O'Hara M, Toyota N, et al. Percutaneous bioprosthetic venous valve: a long-term study in sheep. J Vasc Surg. 2002;35:598–602. https://doi.org/10.1067/mva.2002.118825.

55. Stiehm M, Schmidt W, Grabow N, Keiler J, Reumann M, Wree A, et al. Venous Valve Prosthesis, US020230372103A1; 09.04.2021.
56. DIN EN ISO 5840. DIN EN ISO 5840: 2021-05, Herz- und Gefäßimplantate- Herzklappenprothesen- Teil 1, 2, 3 2021. Berlin: Beuth Verlag GmbH. https://doi.org/10.31030/3180290.
57. Thubrikar MJ, Robicsek F, Fowler BL. Pressure trap created by vein valve closure and its role in graft stenosis. J Thorac Cardiovasc Surg. 1994;107:707–16. https://doi.org/10.1016/s0022-5223(94)70326-4.
58. Egron S, Fujita B, Gullón L, Pott D, Schmitz-Rode T, Ensminger S, Steinseifer U. Radial Force: An Underestimated Parameter in Oversizing Transcatheter Aortic Valve Replacement Prostheses: In Vitro Analysis with Five Commercialized Valves. ASAIO J. 2018;64:536–43. https://doi.org/10.1097/MAT.0000000000000659.
59. Massi I, Zamboni P. What are the ideal characteristics of a venous stent? Veins and Lymphatics. 2021. https://doi.org/10.4081/vl.2021.9739.
60. Taha MA, Busuttil A, Bootun R, Thabet BA, Badawy AE, Hassan HA, et al. Clinical outcomes and overview of dedicated venous stents for management of chronic iliocaval and femoral deep venous disease. Vascular. 2022;30:320–30. https://doi.org/10.1177/1708538121989860.
61. Camasão DB, Mantovani D. The mechanical characterization of blood vessels and their substitutes in the continuous quest for physiological-relevant performances. A critical review. Mater Today Bio. 2021;10: 100106. https://doi.org/10.1016/j.mtbio.2021.100106.
62. Karimi A, Navidbakhsh M. A comparative study on the uniaxial mechanical properties of the umbilical vein and umbilical artery using different stress-strain definitions. Australas Phys Eng Sci Med. 2014;37:645–54. https://doi.org/10.1007/s13246-014-0294-5.
63. Yamaguchi M, Sugimoto K, Zamora CA, Takahashi T, Hayashi Y, Sugimura K. Placement of self-expanding stents with different diameters in the porcine venous system: an experimental study. J Vasc Interv Radiol. 2006;17:113–9. https://doi.org/10.1097/01.RVI.0000186951.22050.3D.
64. Mahnken AH, Pfeffer J, Stanzel S, Mossdorf A, Günther RW, Schmitz-Rode T. In vitro evaluation of optionally retrievable and permanent IVC filters. Invest Radiol. 2007;42:529–35. https://doi.org/10.1097/RLI.0b013e318036b42b.
65. Schubert J, Arbeiter D, Götz A, Lebahn K, Schmidt W, Grabow N, Illner S. Investigations on physico-chemical properties of TSPCU nonwoven for application as prosthetic venous valve. CDBME. 2021;7:613–6. https://doi.org/10.1515/cdbme-2021-2156.
66. Tautorat C, Lebahn K, Oschatz S, Arbeiter D, Schmitz K-P, Grabow N, Schmidt W. Thermal welding of polymeric biomaterials: development of a novel device for temperature controlled local application. CDBME. 2021;7:660–3. https://doi.org/10.1515/cdbme-2021-2168.
67. Götz A, Senz V, Schmidt W, Huling J, Grabow N, Illner S. General image fiber tool: a concept for automated evaluation of fiber diameters in SEM images. Measurement. 2021;177: 109265. https://doi.org/10.1016/j.measurement.2021.109265.
68. Huling J, Götz A, Grabow N, Illner S. GIFT: an ImageJ macro for automated fiber diameter quantification. PLoS ONE. 2022;17: e0275528. https://doi.org/10.1371/journal.pone.0275528.
69. Tanaka M, Girard G, Davis R, Peuto A, Bignell N. Recommended table for the density of water between 0 C and 40 C based on recent experimental reports. Metrologia. 2001;38:301–9. https://doi.org/10.1088/0026-1394/38/4/3.
70. Cook AH, Stone NWB. Precise measurements of the density of mercury at 20°C I. Absolute displacement method. Philos T R Soc A. 1957;250:279–323. https://doi.org/10.1098/rsta.1957.0022.

Publisher's Note

Supporting Information

Transcatheter bicuspid venous valve prostheses: fluid mechanical performance testing of artificial nonwoven leaflets

Andreas Götz* 1, Sabine Illner 1, Nicklas Fiedler 1, Julia Schubert 1, Jan Oldenburg 2, Heinz Müller 3, Wolfram Schmidt 1, Klaus-Peter Schmitz 2, Niels Grabow 1, and Kerstin Lebahn 1

1) Institute for Biomedical Engineering, Rostock University Medical Center, Friedrich-Barnewitz-Str. 4, 18119 Rostock, Germany
2) Institute for Implant Technology and Biomaterials e.V., Friedrich-Barnewitz-Str. 4, 18119 Rostock, Germany
3) CORTRONIK GmbH, Friedrich-Barnewitz-Str. 4a, 18119 Rostock, Germany

Corresponding author: Andreas Götz, andreas.goetz@uni-rostock.de

Table of Contents

---

1. 3D printing process

All 3D printing processes were performed with an Asiga Pro 4K45 printer (Asiga, Alexandria, Australia) using digital light processing (DLP) technology. The LED projectors (UV-light, λ = 385 nm) xy-resolution in 4K-mode is 32 µm with a build platform of 122 x 68 mm² installed. A base plate with a height of 0.400 mm was used as a supporting structure to ensure adequate built platform adhesion. The base plate was built using a layer resolution in z-direction (layer height) of 100 µm per layer, exposed for 30.210 s. Further layers of the parts were built using a layer height of 100 µm per layer, exposed for 8.934 s.

Attachments for experimental hydrodynamic testing were printed using flexible photopolymeric resin Ultracur3D FL 300 (BASF 3D Printing Solutions GmbH, Heidelberg, Germany). Burn-in layers and subsequent layers were sliced in 100 µm and exposed for 6.968 s and 1.675 s respectively.

Printed flexible attachments for hydrodynamic testing were washed twice for 5 min in an isopropanol (Sigma-Aldrich, Steinheim, Germany) filled ultrasonic bath and post-cured for 3000 flashes each side (6000 flashes in total) submerged in glycerol (Sigma-Aldrich, Taufkirchen, Germany). UV curing unit Otoflash G171 (NK Optik GmbH, Baierbrunn, Germany) was used for post-curing of all 3D-printed parts.

2. Pressure equivalent water levels

Table S1: Pressure equivalent water levels

Pressure [mmHg]	1	3	5	20	30	40	50	60	80	100	120	140
Water level [mm]	14	41	68	271	407	543	679	814	1086	1357	1628	1900

3. Pulse duplicator system

Device: HDTi-6000 (Biomedical Device Consultants and Laboratories, Wheat Ridge, USA). The pump circuit employs a piston pump (PD-1100, Biomedical Device Consultants and Laboratories, Wheat Ridge, USA), whose oscillating piston movements generate a pulsatile volume flow. The piston position is defined over time by a modified sinusoidal function, allowing the adjustment of the durations of systole and diastole as well as stroke volume and frequency. The system primarily consists of the pump chamber and three interconnected fluid chambers: the distal chamber, the proximal chamber, and the reservoir chamber, which hold 3 L, 7 L, and 11 L of test fluid, respectively. A valve between the reservoir and distal chambers prevent fluid backflow to the reservoir, thus enabling pressure increase in the distal chamber during piston advance. By adjusting the flow resistance and fill volume in the proximal and reservoir chambers, the mean system pressure and pressure amplitudes during pulsatile testing can be regulated. During piston advance, the test fluid flows through the venous valve model, with the volume flow measured immediately upstream of the model using a bidirectional in-line volume flow sensor (PXN25, Transonic Systems Inc., Ithaca, USA). The flow sensor was calibrated for 0.9% sodium chloride solution at a temperature of 37°C within the measurement range of −25 to 25 L/min. For these specifications, the absolute accuracy of the measurements is ± 4%. The kinematics of the venous valves were recorded using high-speed cameras (Basler acA1300-200um with ON Semiconductor PYTHON 1300 CMOS sensor, Basler AG, Germany). The high-speed cameras are equipped with fixed focal length lenses (50mm C Series Fixed Focal Length Lens f/2.0, Edmund Optics Inc., USA). This configuration produces images at a frame rate of 200 s^{-1} with a resolution of 1280 x 1024 pixels, thus allowing adequate characterization of valve kinematics. The cameras are synchronized with the piston pump. For pressure measurement up- and downstream of the venous valve, two identical relative pressure sensors (PendoTECH, Princeton, USA) are included. These differential pressure sensors have a maximum measurement deviation of ± 0.9 mmHg and a maximum relative deviation of 0.29% of the measured value within the range of 0 – 310 mmHg.

4. Results of pulsatile testing

The results of pulsatile test series are displayed in following bar charts, further explanations are included in each graphic.

Explanation of terms:

- Forward flow volume: forward flowed fluid volume, per cycle
- Closing volume: visualized in section 6 (Standards), per cycle
- Leakage volume: visualized in section 6 (Standards), per cycle
- Total regurgitation volume: sum from closing volume and leakage volume, per cycle

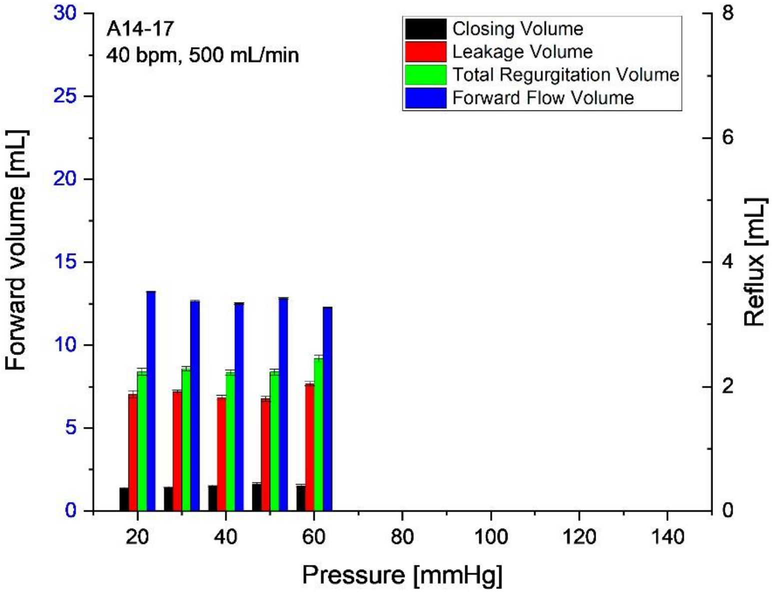

Figure S1: valve A14-17, test series imitating low exertion

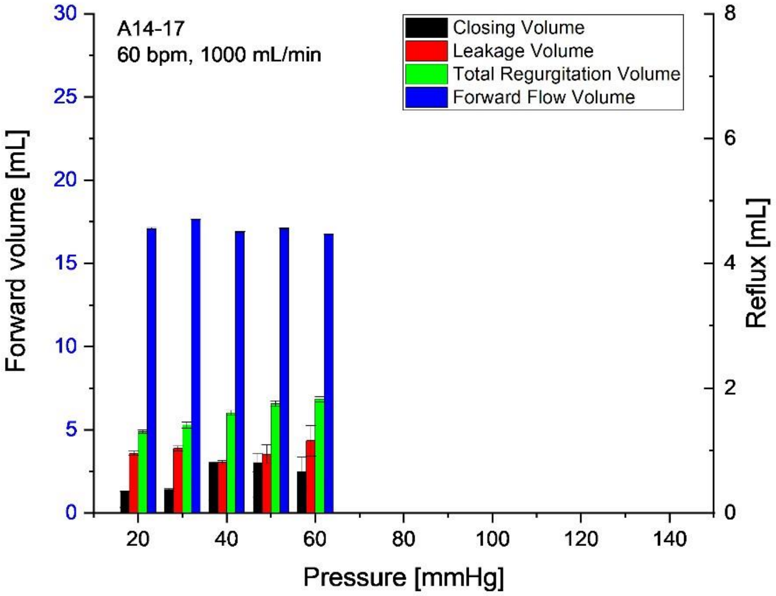

Figure S2: valve A14-17, test series imitating moderate exertion

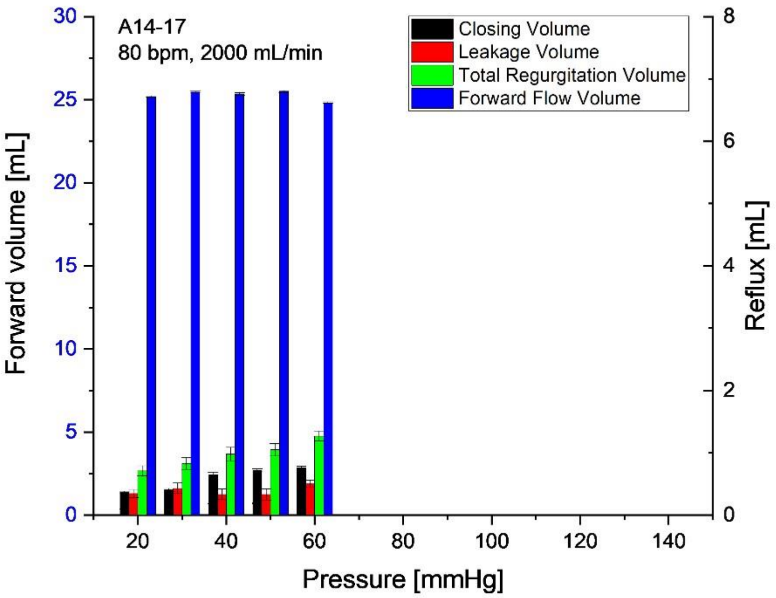

Figure S3: valve A14-17, test series imitating strong exertion

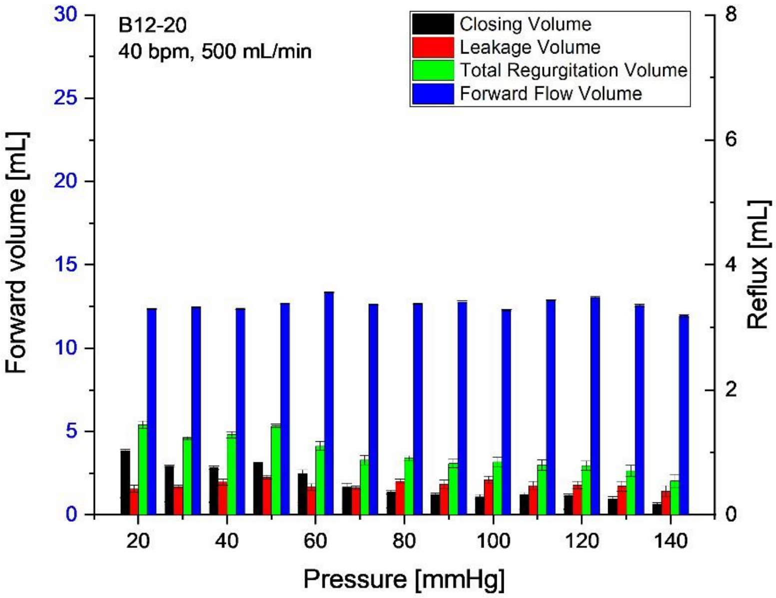

Figure S4: valve B12-20, test series imitating low exertion

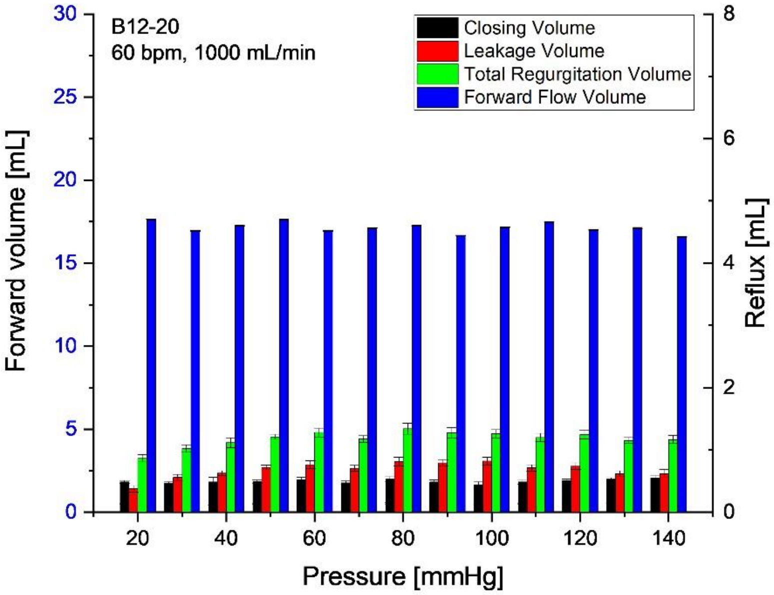

Figure S5: valve B12-20, test series imitating moderate exertion

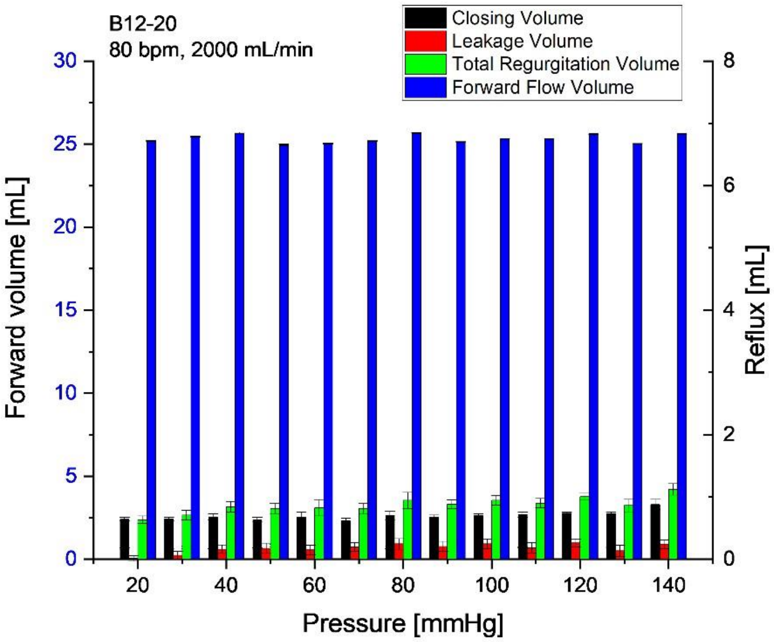

Figure S6: valve B12-20, test series imitating strong exertion

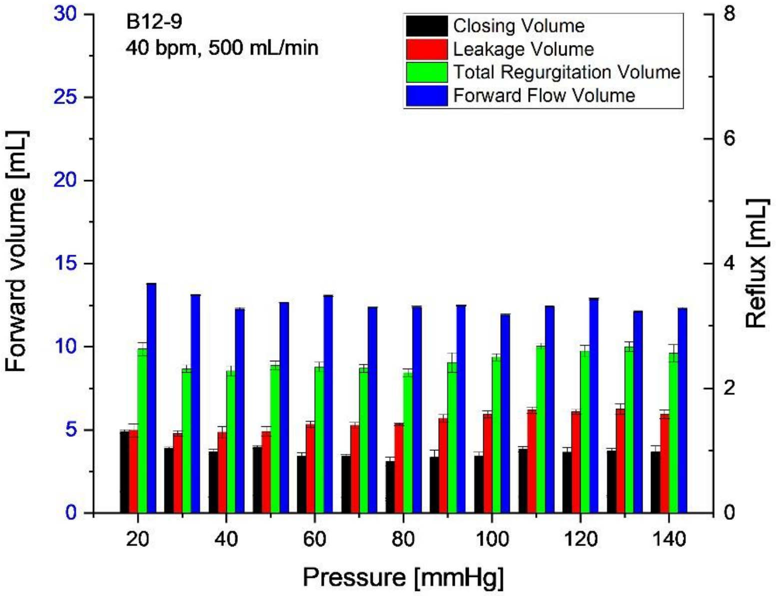

Figure S7: valve B12-9, test series imitating low exertion

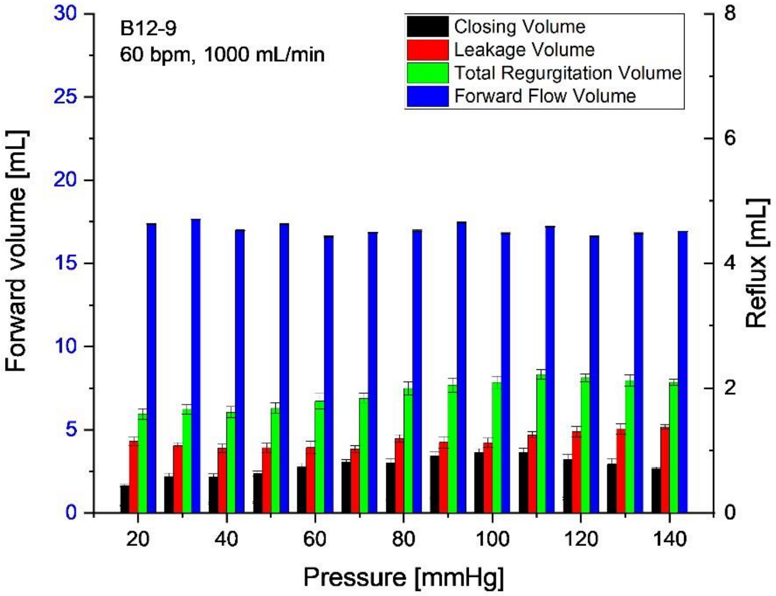

Figure S8: valve B12-9, test series imitating moderate exertion

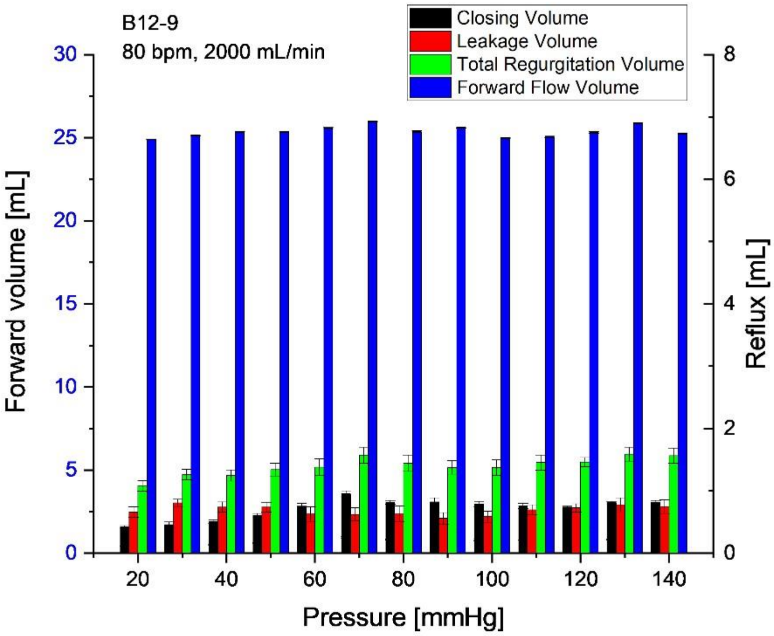

Figure S9: valve B12-9, test series imitating strong exertion

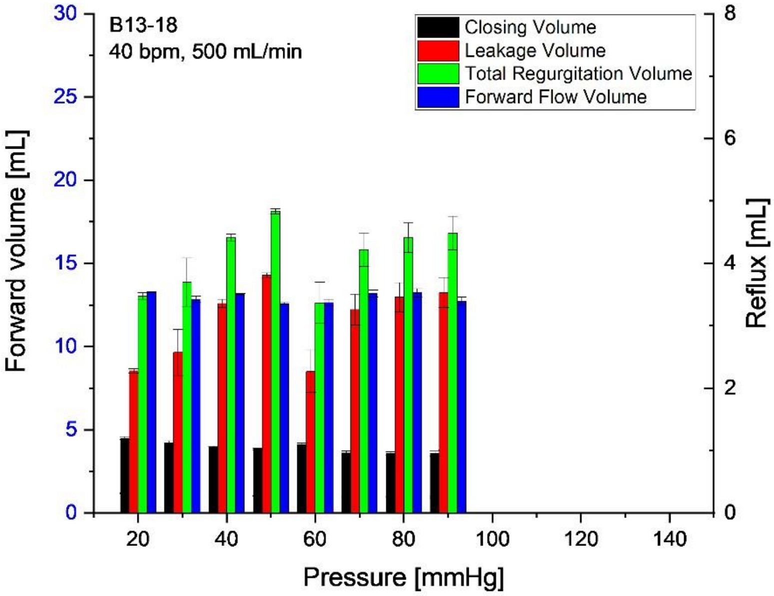

Figure S10: valve B13-18, test series imitating low exertion

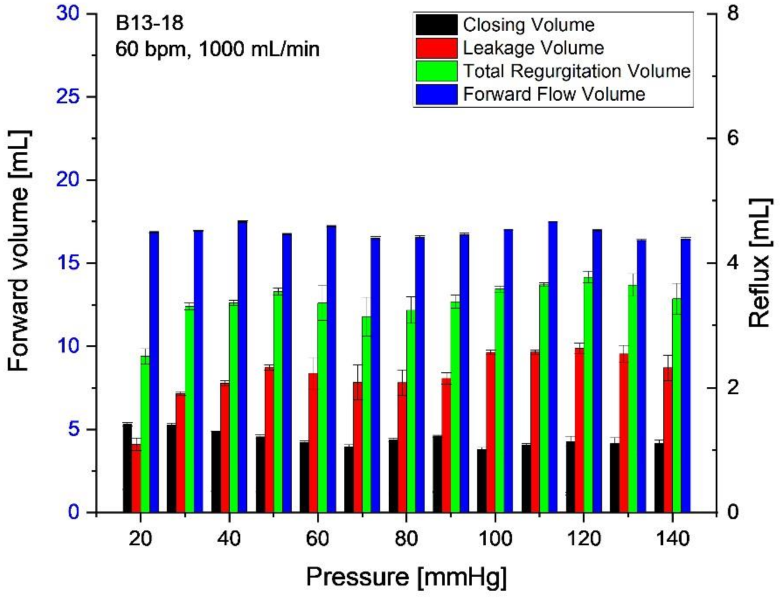

Figure S11: valve B13-18, test series imitating moderate exertion

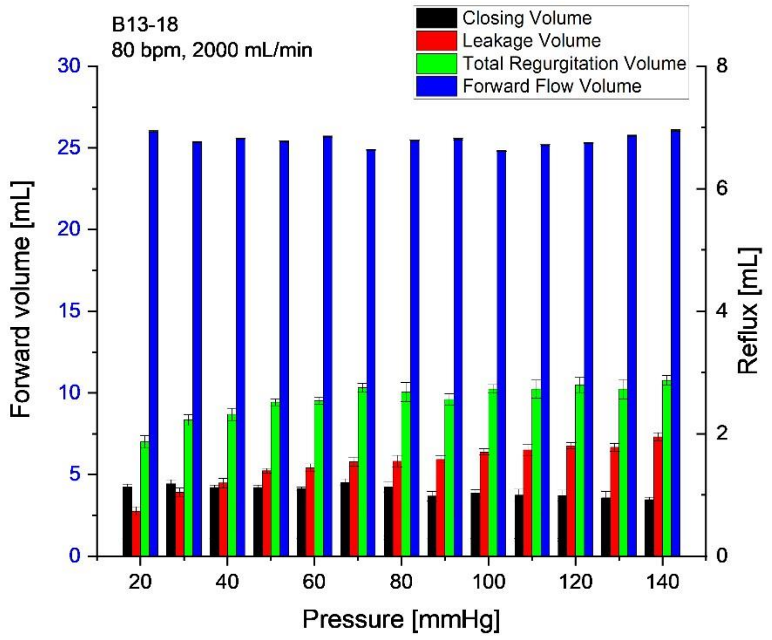

Figure S12: valve B13-18, test series imitating strong exertion

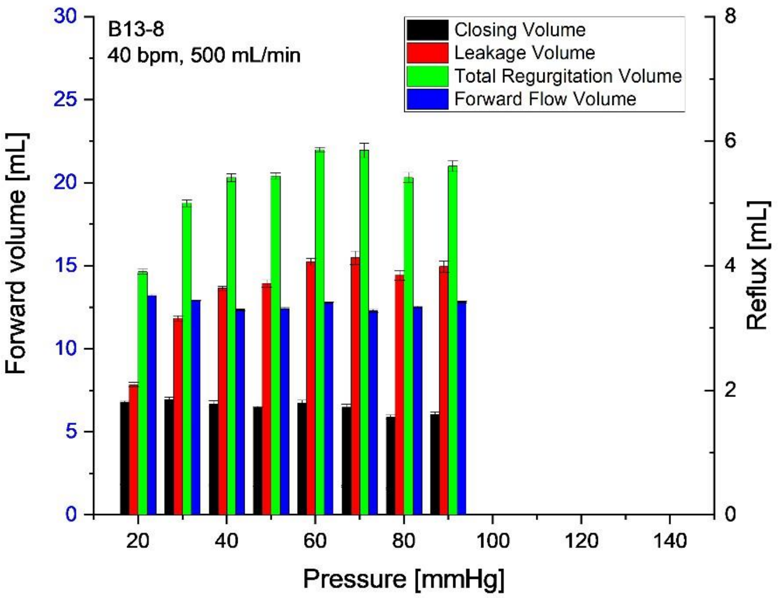

Figure S13: valve B13-8, test series imitating low exertion

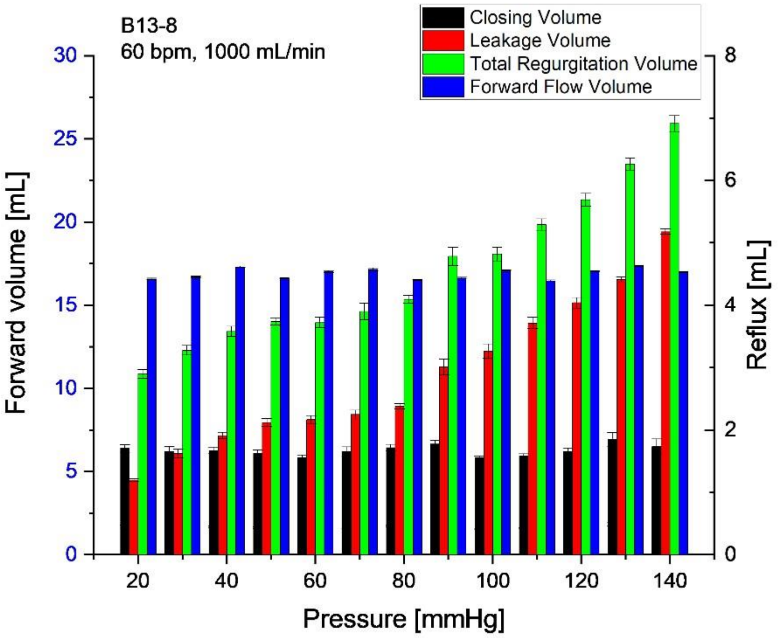

Figure S14: valve B13-8, test series imitating moderate exertion

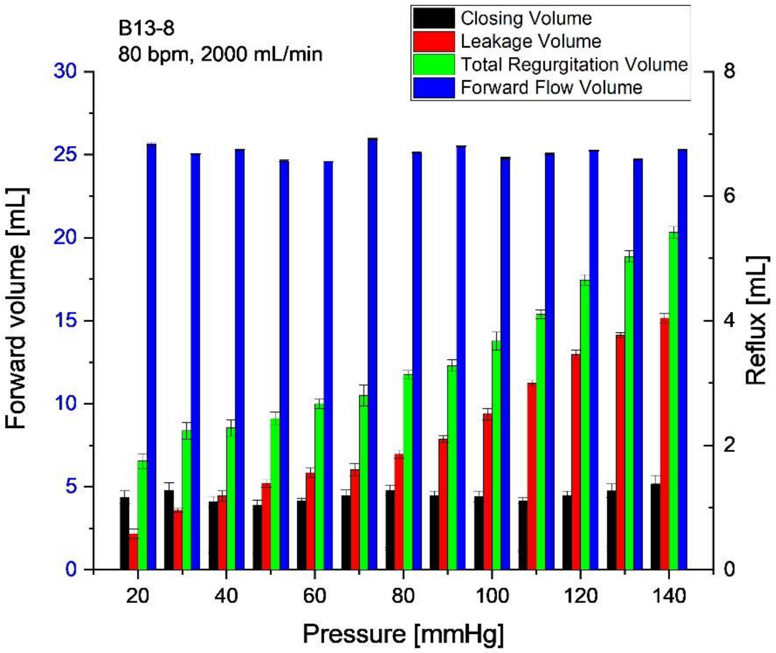

Figure S15: valve B13-8, test series imitating strong exertion

The valves were fixed in attachments, which were connected to a water basin (distal pressure forward flow) or a hose (proximal pressure, reflux) for static testing. For pulsatile testing the valve loaded attachments were fixed in the pulse duplicator system, see Figure S 16. As mentioned above, valve A14-17 tilted in static testing at proximal pressure between 60 and 80 mmHg, photographs are displayed in Figure S 16.

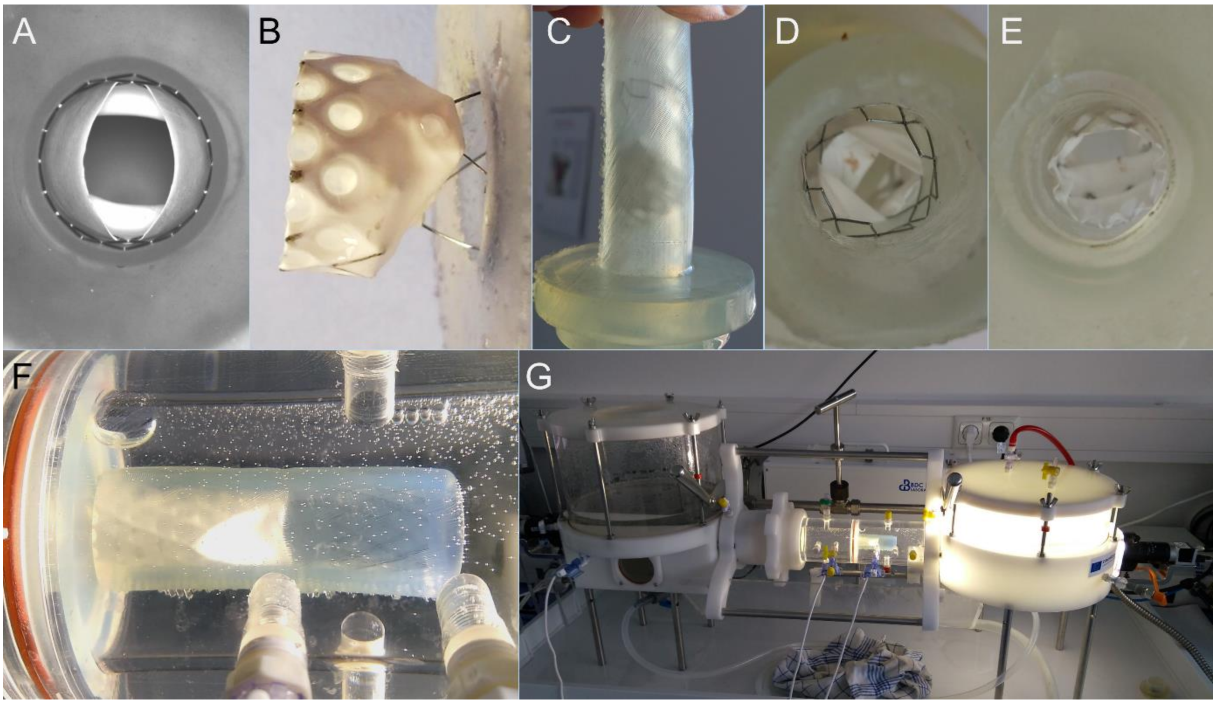

Figure S 16: Implanted valves. A: valve A14-17 proximal view on open valve, B: valve A14-17 moved out of the attachment over an additional support ring with leaflets slipped back, C, D, E: valve A14-17 tilted during static testing, in proximal view (D) and distal view (E), F, G: valve B12-9 in pulse duplicator system.

5. Leaflet deformation

The leaflet deformation (movement) was visualized according the idea of comparing subsequent images of a video sequence of the inline camera. Areas of the images, which differ from previous image, were highlighted, and unchanged areas were not accentuated (dark). Videos were recoded with 200 frames per second, i.e. a time interval of 5 ms between subsequent images. The video sequences of the inline camera were converted to sequences of single grayscale images of 8 bit depth. For difference image generation each pair of subsequent images were subtracted. The difference images were displayed as heat map using the Look-Up Table <Fire= Image processing was performed using the software ImageJ, version 1.53n (National Institutes of Health, USA). This method allows the visualization of local leaflet deformation, but no numerical information about the total movement can be derived from these images.

At opening of valve A14-17 the leaflets bulged on both sides evenly and symmetrically, see Figure S17. The valve showed a post-pulse oscillation approximately 0.1 s after closing corresponding to the dark blue flow-curve in **Fehler! Verweisquelle konnte nicht gefunden werden.**.

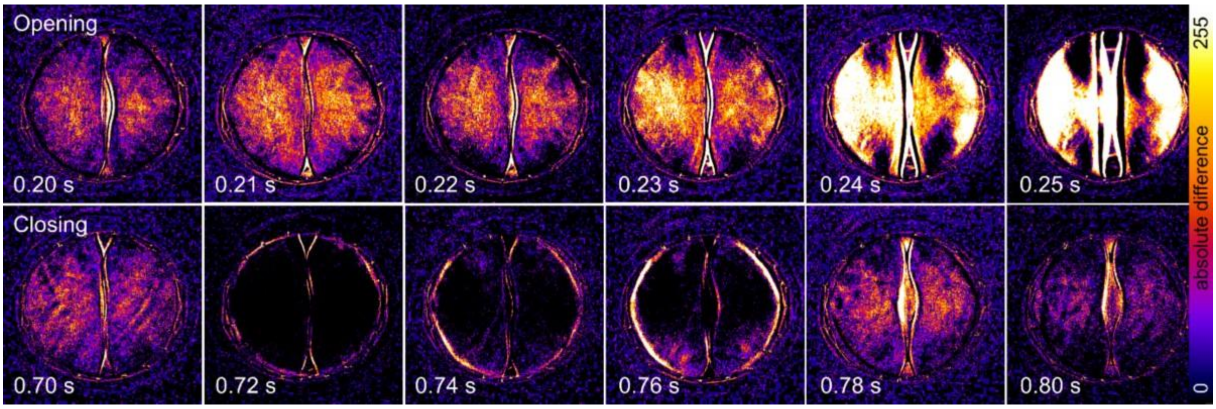

Figure S17: Visualization of leaflet deformation of valve A14-17. The difference of pixel values between two subsequent inline camera images of an interval of 5 ms at the indicated time points is displayed as a heat map, no numerical information about the total movement can be derived. At closing a post-pulse oscillation at about 0.8 s appeared.

At opening of valve B12-9 the leaflets bulged symmetrically on both sides and opened simultaneously. A post-pulse oscillation after closing was not observed, see Figure S18.

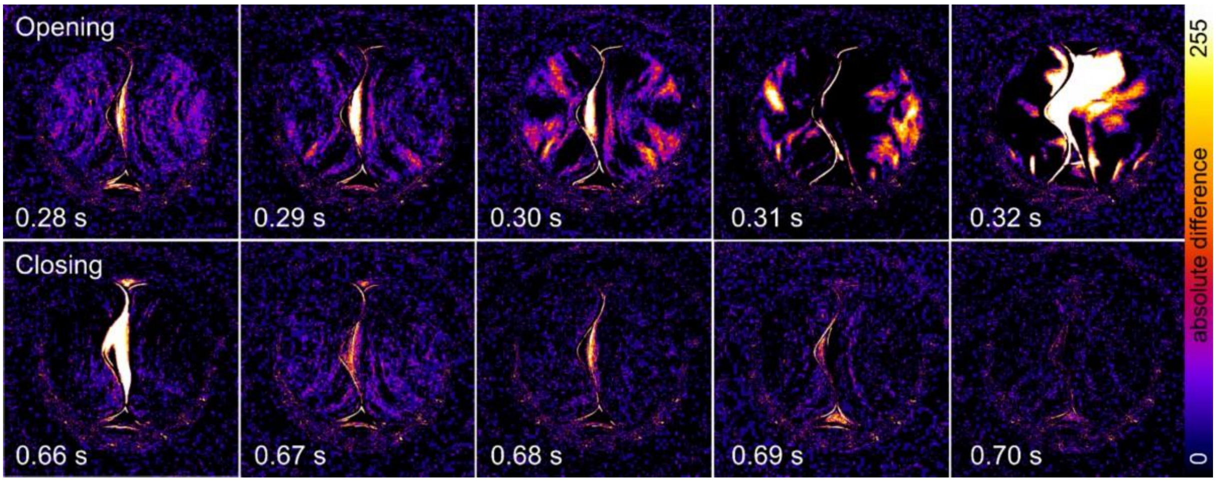

Figure S18: Visualization of leaflet deformation of valve B12-9. The difference of pixel values between two subsequent inline camera images of an interval of 5 ms at the indicated time points is displayed as a heat map, no numerical information about the total movement can be derived.

6. Standards

There are no standards for in vitro testing of prosthetic venous valves, but standards for heart valves can give orientation, see DIN EN ISO 5840-1 [56].

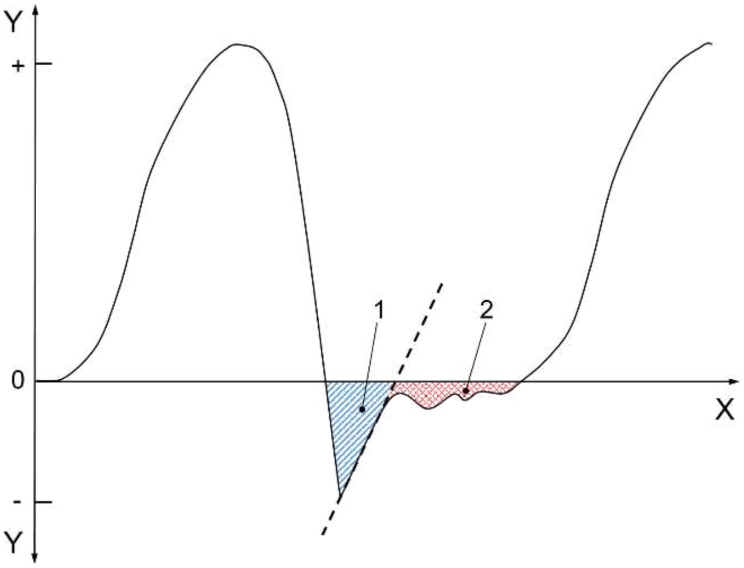

Figure S19: Test cycle, X – time, Y – flow, 1 – closing volume, 2 – leakage volume, adapted figure from DIN EN ISO 5840-1 [58]

According to the standard DIN EN ISO 5840-1 [56], the following formula is used for effective orifice area (EOA):

$$\mathrm{A}_{eo} = \frac{q_{\mathrm{vRMS}}}{51{,}6 \times \sqrt{\frac{\Delta p}{\rho}}}$$

- Aeo - effective valve opening area (cm^2);
- q_{vRMS} - effective value of the forward flow (mL/s) during the positive differential pressure phase
- Δp the mean pressure difference (measured during the positive differential pressure) (mmHg)
- ρ is the density of the test liquid (g/cm^3)

with:

$$q_{\mathrm{v}_{\mathrm{RMS}}} = \sqrt{\frac{\int_{t_1}^{t_2} q_{\mathrm{v}}\,(t)^2 dt}{t_2 - t_1}}$$

- $q_{\mathrm{v}_{\mathrm{RMS}}}$ - effective value of the forward flow during the phase of positive differential pressure
- qv(t) - instantaneous flow rate at time (t)
- t_1 - time at the beginning of the positive differential pressure phase
- t_2 - time at the end of the positive differential pressure phase

Table S2: Selected information from the standard [56].

Standard	Table name (translated)	Selected information
DIN EN ISO 5840-1 (Table 3)	Recommended pressure values for the in vitro test for the left side of the heart - adult population	The peak differential pressure across the closed valve for normal condition is specified with 100 mmHg.
DIN EN ISO 5840-2 (Table 1)	Minimum requirements for implant performance, aortal	The maximum total regurgitation fraction (% of forward flow volume) is specified with 10% for small valves (17 mm) up to 20% for large valves (31 mm).
DIN EN ISO 5840-3 (Table 1)	Minimum requirements for hydrodynamic in-vitro implant performance, aortal	The maximal regurgitation fraction is specified with 20% for all sizes, including the closing volume, the leak volume across the valve and the paravalvular leak volume.